

Fiscal Year 2020: First Quarter

Progress Reports:  
**Advanced Battery Materials Research  
(BMR) Program  
&  
Battery500 Consortium**

**Released April 2020  
for the period of October – December 2019**

*Approved by*

Tien Q. Duong, Program Manager  
Advanced Battery Materials Research Program & Battery500 Consortium  
Vehicle Technologies and Electrification Program  
Energy Efficiency and Renewable Energy

## TABLE OF CONTENTS

### A Message from the Manager:

**Advanced Battery Materials Research Program and Battery500 Consortium ..... xx**

### Advanced Battery Materials Research Program

#### **Task 1 – Liquid/Polymer Solid-State Electrolytes..... 1**

Task 1.1 – Advanced Lithium-Ion Battery Technology: High-Voltage Electrolyte (Joe Sunstrom, Ron Hendershot, and Alec Falzone, Daikin) .....	4
Task 1.2 – Multi-Functional, Self-Healing Polyelectrolyte Gels for Long-Cycle-Life, High-Capacity Sulfur Cathodes in Lithium-Sulfur Batteries (Alex Jen and Jihui Yang, University of Washington) .....	7
Task 1.3 – Dual Function Solid-State Battery with Self-Forming, Self-Healing Electrolyte and Separator (Esther Takeuchi, Stony Brook University) .....	11
Task 1.4 – Characterization and Modeling of Li-Metal Batteries: Characterization of Li <sup>+</sup> Transport in Polyelectrolytes (Bryan D. McCloskey, University of California at Berkeley) .....	15
Task 1.5 – Advanced Polymer Materials for Batteries (Zhenan Bao and Yi Cui, Stanford University) .....	18
Task 1.6 – Improving the Stability of Lithium-Metal Anodes and Inorganic-Organic Solid Electrolytes (Nitash Balsara, Lawrence Berkeley National Laboratory) .....	24
Task 1.7 – Development of Thin, Robust, Lithium-Impenetrable, High-Conductivity, Electrochemically Stable, Scalable, and Low-Cost Glassy Solid Electrolytes for Solid-State Lithium Batteries (Steve Martin, Iowa State University of Science and Technology) .....	27
Task 1.8 – Composite Solid Ion Conductor with Engineered Lithium Interface (Kyler Carroll and Cam Peebles, Wildcat Discovery Technologies) .....	31
Task 1.9 – Single-Ion Conducting Electrolyte Extended to Cathode for All-Solid-State Lithium-Ion Batteries (Nianqiang (Nick) Wu, University of Massachusetts Amherst).....	34
Task 1.10 – Physical and Mechano-Electrochemical Phenomena of Thin-Film Lithium-Ceramic Electrolyte Constructs (Jeff Sakamoto, University of Michigan).....	37
Task 1.11 – Lithium Dendrite-Free Li <sub>7</sub> N <sub>2</sub> I-LiOH Solid Electrolytes for High-Energy Lithium Batteries (Chunsheng Wang, University of Maryland).....	39
Task 1.12 – Hot Pressing of Reinforced Li-NMC All-Solid-State Batteries with Sulfide Glass Electrolyte (Thomas Yersak, General Motors) .....	45

Task 1.13 – Low Impedance Cathode/Electrolyte Interfaces for High-Energy-Density Solid-State Batteries (Eric Wachsman, University of Maryland) .....	49
Task 1.14 – Developing an <i>In Situ</i> Formed Dynamic Protection Layer to Mitigate Lithium Interface Shifting: Preventing Dendrite Formation on Metallic Lithium Surface to Facilitate Long Cycle Life of Lithium Solid-State Batteries (Deyang Qu, University of Wisconsin Milwaukee) .....	52
Task 1.15 – Molecular Ionic Composites: A New Class of Polymer Electrolytes to Enable All-Solid-State and High-Voltage Lithium Batteries (Louis Madsen, Virginia Polytechnic Institute and State University) .....	55
Task 1.16 – All-Solid-State Batteries Enabled by Multifunctional Electrolyte Materials (Pu Zhang, Solid Power, Inc) .....	58
Task 1.17 – Developing Materials for High-Energy-Density Solid-State Lithium-Sulfur Batteries (Donghai Wang, Pennsylvania State University) .....	61
<b>Task 2 – Diagnostics .....</b>	<b>65</b>
Task 2.1 – Characterization and Modeling of Li-Metal Batteries: Model-System Synthesis and Advanced Characterization (Guoying Chen, Lawrence Berkeley National Laboratory) .....	66
Task 2.2 – Interfacial Processes – Diagnostics (Robert Kostecki, Lawrence Berkeley National Laboratory) .....	69
Task 2.3 – Advanced <i>In Situ</i> Diagnostic Techniques for Battery Materials (Xiao-Qing Yang and Seong-Min Bak, Brookhaven National Laboratory) .....	72
Task 2.4 – <i>In Situ</i> Diagnostics of Coupled Electrochemical-Mechanical Properties of Solid Electrolyte Interphases on Lithium-Metal Rechargeable Batteries (Xingcheng Xiao, General Motors; Brian W. Sheldon, Brown University; Yue Qi, Michigan State University; and Y. T. Cheng, University of Kentucky) .....	75
Task 2.5 – Probing Interfacial Processes Controlled Electrode Stability in Rechargeable Batteries (Chongmin Wang, Pacific Northwest National Laboratory) .....	78
Task 2.6 – Integrated Atomic-, Meso-, and Micro-Scale Diagnostics of Solid-State Batteries (Yi Cui, William Chueh, and Michael Toney; Stanford University/SLAC National Accelerator Laboratory) .....	81
Task 2.7 – Investigating the Stability of Solid/Solid Interface (Zonghai Chen, Argonne National Laboratory) .....	83
Task 2.8 – Fundamental Understanding of Interfacial Phenomena in Solid-State Batteries (Xingcheng Xiao, General Motors) .....	86
Task 2.9 – Multidimensional Diagnostics of the Interface Evolutions in Solid-State Lithium Batteries (Yan Yao, University of Houston) .....	88

<b>Task 3 – Modeling</b> .....	<b>91</b>
Task 3.1 – Characterization and Modeling of Li-Metal Batteries: First-Principles Modeling and Machine Learning (Kristin Persson, Lawrence Berkeley National Laboratory) .....	92
Task 3.2 – Understanding and Strategies for Controlled Interfacial Phenomena in Lithium-Ion Batteries and Beyond (Perla Balbuena and Jorge Seminario, Texas A&M University; Partha Mukherjee, Purdue University).....	94
Task 3.3 – Electrode Materials Design and Failure Prediction (Venkat Srinivasan, Argonne National Laboratory).....	97
Task 3.4 – Dendrite Growth Morphology Modeling in Liquid and Solid Electrolytes (Yue Qi, Michigan State University).....	100
Task 3.5 – Modeling of Amorphous Solid-State Conductors (Gerbrand Ceder, Lawrence Berkeley National Laboratory).....	103
Task 3.6 – Characterization and Modeling of Li-Metal Batteries: Force Field Theory and Lithium-Sulfur Battery Simulations (Lin-Wang Wang, Lawrence Berkeley National Laboratory) .....	106
Task 3.7 – <i>In Situ</i> and <i>Operando</i> Thermal Diagnostics of Buried Interfaces in Beyond Lithium-Ion Cells (Ravi Prasher, Lawrence Berkeley National Laboratory).....	109
Task 3.8 – Multi-Scale Modeling of Solid-State Electrolytes for Next-Generation Lithium Batteries (Anh Ngo, Larry A. Curtiss, and Venkat Srinivasan, Argonne National Laboratory).....	112
Task 3.9 – Integrated Multi-Scale Modeling for Design of Robust 3D Solid-State Lithium Batteries (Brandon Wood, Lawrence Livermore National Laboratory) .....	115
Task 3.10 – First-Principles Modeling of Cluster-Based Solid Electrolytes (Puru Jena, Virginia Commonwealth University) .....	119
Task 3.11 – Predictive Engineering of Interfaces and Cathodes for High-Performance All-Solid-State Lithium-Sulfur Batteries (Badri Narayanan, University of Louisville) .....	122
<b>Task 4 – Metallic Lithium</b> .....	<b>127</b>
Task 4.1 – Lithium Dendrite Prevention for Lithium Batteries (Wu Xu and Ji-Guang Zhang, Pacific Northwest National Laboratory) .....	129
Task 4.2 – Composite Electrolytes to Stabilize Metallic Lithium Anodes (Nancy Dudney and X. Chelsea Chen, Oak Ridge National Laboratory).....	132
Task 4.3 – Enabling Solid-State Batteries through Characterization and Modeling (Nenad M. Markovic and Larry A. Curtiss, Argonne National Laboratory) .....	136
Task 4.4 – 3D Printing of All-Solid-State Lithium Batteries (Jianchao Ye, Lawrence Livermore National Laboratory) .....	139

Task 4.5 – Interfacial Studies on Lithium Thiophosphate Based Solid Electrolytes and Cathodes (Jagjit Nanda, Oak Ridge National Laboratory) .....	142
Task 4.6 – Prelithiation of Silicon Anode for High-Energy Lithium-Ion Batteries (Yi Cui, Stanford University) .....	145
<b>Task 5 – Sulfur Electrodes .....</b>	<b>147</b>
Task 5.1 – Novel Chemistry: Lithium Selenium and Selenium Sulfur Couple (Khalil Amine, Argonne National Laboratory) .....	149
Task 5.2 – Development of High-Energy Lithium-Sulfur Batteries (Dongping Lu and Jun Liu, Pacific Northwest National Laboratory) .....	152
Task 5.3 – Nanostructured Design of Sulfur Cathodes for High-Energy Lithium-Sulfur Batteries (Yi Cui, Stanford University).....	155
Task 5.4 – Investigation of Sulfur Reaction Mechanisms (Enyuan Hu, Brookhaven National Laboratory; Deyang Qu, University of Wisconsin at Milwaukee).....	157
Task 5.5 – New Electrolytes for Lithium-Sulfur Battery (Gao Liu, Lawrence Berkeley National Laboratory) .....	160
<b>Task 6 – Air Electrodes/Electrolytes.....</b>	<b>162</b>
Task 6.1 – Rechargeable Lithium-Air Batteries (Ji-Guang Zhang and Wu Xu, Pacific Northwest National Laboratory).....	164
Task 6.2 – Lithium-Air Batteries (Khalil Amine and Larry A. Curtiss, Argonne National Laboratory) .....	167
Task 6.3 – Lithium Oxygen Battery Design and Predictions (Larry A. Curtiss/Anh Ngo, Argonne National Laboratory; Amin Salehi-Khojin, University of Illinois at Chicago).....	170
<b>Task 7 – Sodium-Ion Batteries .....</b>	<b>173</b>
Task 7.1 – Exploratory Studies of Novel Sodium-Ion Battery Systems (Xiao-Qing Yang and Enyuan Hu, Brookhaven National Laboratory).....	174
Task 7.2 – Development of a High-Energy Sodium-Ion Battery with Long Life (Chris Johnson and Khalil Amine, Argonne National Laboratory) .....	177
Task 7.3 – High-Capacity, Low-Voltage Titanate Anodes for Sodium-Ion Batteries (Marca Doeff, Lawrence Berkeley National Laboratory) .....	180
Task 7.4 – Electrolytes and Interfaces for Stable High-Energy Sodium-Ion Batteries (Ji-Guang Zhang, Pacific Northwest National Laboratory) .....	182
<b>Battery500 Consortium Program</b>	
<b>Innovation Center for Battery500</b> (Jun Liu, Pacific Northwest National Laboratory; Yi Cui, Stanford University) .....	<b>185</b>

## TABLE OF FIGURES

Figure 1. Example calibration curves for major components seen in commercial Li-ion battery pouch cells. Concentration ranges were identified based on previously reported qualitative data (FY 2017/2018).....	5
Figure 2. Gassing kinetics data for NMC-811 cells compared to previously studied NMC-622 and NCA cathodes. Baseline hydrocarbon electrolyte (left), fluoroether containing (middle), and fluoroether / fluoroethylene carbonate (FEC) formulation (right).....	5
Figure 3. Cycling performances of cells with sulfur cathodes with (a) PENDI-350 / polyethylene oxide (PEO) as binder (3.71 mgS/cm <sup>2</sup> ) and (b) PENDI-350/triPy/PEO (PPP) as binder (2.91 mgS/cm <sup>2</sup> ). All cells were cycled with C rate of C/10 in the first 5 cycles and then 1C in the remaining cycles. (c) Image of sulfur cathode using PPP as binder (5.04 mgS/cm <sup>2</sup> ).....	8
Figure 4. (a) Cathode with PPP binder immersed in organic electrolyte after 48 hours. (b) Cathode with PPPVDF binder immersed in organic electrolyte after 48 hours. (c) Cycling performances of cathodes with PPPVDF binder at different sulfur loading (the cells were cycled at C/20 rate at 1 <sup>st</sup> cycle and C/2 at remaining cycles). (d) Cycling performances of cathodes with PPPVDF at different C rate (4.4 mgS/cm <sup>2</sup> ). (e) Cycling performances of cathodes with PPPVDF with -SH surface modified carbon. (f) The first discharge (at C/20 rate) and first charge (at C/2) performance of cathode with PVDF as binder.....	9
Figure 5. Mean Lil particle diameter with standard deviation for the three new electrolyte processes compared to the control. ....	12
Figure 6. Comparison of the first cycle galvanostatic profiles for the new electrolyte process(es). ....	12
Figure 7. Electrochemical impedance spectroscopy of the Process III composite Lil with Lil(3-hydroxypropionitrile) <sub>2</sub> cells in cell configuration SS, Li, and Li+CNT before initial charge (a) and after charging to 0.5% of the theoretical capacity (b). ....	13
Figure 8. Comparison of the first-cycle galvanostatic profiles for the electrode interface modification. Arrow indicates drop in polarization. ....	13
Figure 9. Comparison of the electrochemical response of cell type B I under 30°C and 40°C. (a) Galvanostatic discharge profile. (b) Electrochemical impedance spectroscopy as a function of temperature. ....	14

Figure 10. Diffusion coefficient of Li <sup>+</sup> as measured via nuclear magnetic resonance normalized to the monomer diffusion coefficient of sulfonated polysulfone polyions in two different solvent systems: DMSO and water. In DMSO where the backbone is well solvated, diffusion coefficients drop rapidly at high concentration, whereas this trend is not observed for the aqueous solutions where the polymer backbone is poorly solvated.....	16
Figure 11. Li <sup>+</sup> transference number as measured by the Balsara-Newman method for LiPF <sub>6</sub> in EC:EMC (3:7 w/w). Error bars represent ± 1 standard deviation. ....	17
Figure 12. Molecular dynamics simulations showing relationship between the rate and morphology with the deposition probability. ....	20
Figure 13. (a) Schematic showing the structure of ionic polymer coated on the Li-metal electrode. The ionic polymer comprises of x: PFPE-DMA backbone, y: PETMP crosslinker, and z: STFSI-Li salts. (b) Comparison of peak heights obtained from 1H nuclear magnetic resonance measurements showing the relative content of the methyl groups in the polymer backbone and the tethered anions (spectra referenced to residual protons in CD <sub>3</sub> OD). (c) Infrared spectroscopy measurements for polymer networks with varying salt content. The shaded region at 2550 cm <sup>-1</sup> , indicates the –SH group in PETMP, while at 1650 cm <sup>-1</sup> is for C=C bond in Li-STFSI. ....	21
Figure 14. (a) <sup>7</sup> Li chemical shift measured for different ionic polymer networks, showing a downfield shift with increasing salt concentration. (b) Lithium diffusivity and transference number obtained from pulse field gradient nuclear magnetic resonance measurements. (c) Nyquist plot showing the impedance measurement in symmetric lithium cell, where the electrode was coated with and without polymer networks. (d) Comparison of the interfacial resistances measured using impedance spectroscopy of symmetric lithium cells. In (a/b), the solvent used was EC/DEC, and in (c/d), the bulk liquid electrolyte utilized was 1 M LiTFSI in EC/DEC. ....	22
Figure 15. Chemical structure of PEO-POSS diblock and POSS-PEO-POSS triblock copolymer.....	25
Figure 16. Chemical structure of PEO-POSS-PSTFSILi.....	26
Figure 17. The ISU-4 glass of composition 0.90 [0.61Li <sub>2</sub> S + 0.39SiS <sub>2</sub> ] + 0.10 [0.74LiPO <sub>3</sub> + 0.26LiPON] has a 25°C Li <sup>+</sup> -ion conductivity of 7 x 10 <sup>-4</sup> S/cm (a), gains essentially no weight in contact with air (b), shows only nanoamp levels of electronic conductivity in blocking cells against metallic lithium and shows oxidative voltage stability up to 4 V (c), shows no crystallization when scanned in temperature until T is more than 100°C above the softening point, T <sub>g</sub> , of the glass (d), and is stable against metallic lithium in symmetric Li GSE Li cells (e) and can cycle against lithium up 1.5 mA/cm <sup>2</sup> for hundreds of cycles (f). ....	28

Figure 18. (a) The old impure version of SiS <sub>2</sub> that is badly contaminated with unreacted silicon. (b) The new SiS <sub>2</sub> produced this quarter that is perfectly white and has no unreacted silicon particles. (c) Close inspection shows the open porosity of the SiS <sub>2</sub> that is formed when the sulfur evaporates away from the SiS <sub>2</sub> .	29
Figure 19. Differential scanning calorimetry (DSC) scans of three different samples of Iowa State University glassy solid electrolytes showing reproducibility of the glass properties. This figure shows the T <sub>g</sub> determined by DSC.	30
Figure 20. (a) The Wildcat high throughput trilayer sandwich cell and equivalent circuit models for AC impedance fitting. (b) Nyquist plots of LTAP ceramic pellet, polymer electrolyte, and trilayer cells. (c) Area-specific resistance of the trilayer cell and the sum of the LTAP pellet and polymer electrolyte. (d) The calculate R <sub>interface</sub> for the trilayer cell.	32
Figure 21. Representative cycling plots for various test vehicles under investigation. Test vehicles include (a) Li/NMC half cells, (b) Li/LTO half cells, (c) Li/Li symmetric cells, and (d) Li/Cu half cells. The cycling rate, current density (CD), and operating temperature for each test vehicle are given. All test vehicles used a standard carbonate-based electrolyte (1.0 M LiPF <sub>6</sub> in EC:EMC 4:6 wt/wt.).	33
Figure 22. (a) Electrochemical impedance spectroscopy of UiO-66-LiSS with different amount of EC+PC measured at room temperature. (b) Ionic conductivity of UiO-66-LiSS with different amount of EC+PC. (c) DC polarization curve of symmetric Li UiO-66-LiSS-50% EC/PC Li cell.	35
Figure 23. Fourier transform infrared spectra of lithium salt-grafted LLAZO nanofibers, bare LLAZO nanofibers, and reactant (4-[2 (trimethoxysilyl)ethyl]benzene-1-sulfonyl chloride).	36
Figure 24. Thin-film construct (TFC) and precision lithium reference electrode experience. (a) TFC consisting of 20- $\mu$ m thick lithium and 100- $\mu$ m thick LLZO. (b) 18- $\mu$ m tape cast and densified LLZO. (c) Demonstrated precision Li-metal reference electrode integration. Normalized potential of the three-electrode cell design; < 10 <sup>-3</sup> , avoids occurrence of electrochemically driven reactions over the reference electrode (c). (d) The experience with TFC fabrication and reference electrode integration demonstrates feasibility of TFC with reference electrodes.	38
Figure 25. (a) Digital photo of the as-assembled Li <sub>7</sub> N <sub>2</sub> I-LiOH pellet and its corresponding (b) crystal structure. X-ray diffraction of the synthesized (c) Li <sub>7</sub> N <sub>2</sub> I-LiO and (d) Li <sub>3</sub> YCl <sub>6</sub> solid-state electrolytes.	40
Figure 26. Scanning electron microscopy of the synthesized Li <sub>7</sub> N <sub>2</sub> I-LiOH solid-state electrolytes.	40
Figure 27. Energy dispersive X-ray spectroscopy of cross-section of the Li <sub>7</sub> N <sub>2</sub> I-LiOH/Li <sub>3</sub> YCl <sub>6</sub> bi-layered electrolyte fabricated using suspension casting method.	41

Figure 28. Electrochemical characters of $\text{Li}_7\text{N}_2\text{I}$ and $\text{Li}_3\text{YCl}_6$ solid-state electrolytes. (a) Electrochemical impedance spectroscopy (EIS) of $\text{Li}_7\text{N}_2\text{I}$ -LiOH and $\text{Li}_3\text{YCl}_6$ solid-state electrolyte. (b) Cyclic voltammetry curve from -0.1 to 1.0 V at the scan rate of 1 mV/s. (c) EIS of $\text{Li}_7\text{N}_2\text{I}$ -LiOH at different temperatures. (d) Arrhenius plot of $\text{Li}_7\text{N}_2\text{I}$ -LiOH solid-state electrolyte. ....	41
Figure 29. Cycle voltammetry of $\text{Li} \text{Li}_7\text{N}_2\text{I}$ -LiOH- $\text{Li}_3\text{YCl}_6$   solid-state cells at a scan rate of 1 mV/s. ....	42
Figure 30. Schematic of physical and chemical stable interface for dendrite suppression. Schematic illustration of the (a) current amplification effect between lithium and unstable SSEs interface, and (b) lithium dendrite suppression mechanism. ....	43
Figure 31. (a) Density functional theory calculated phase diagram. (b) Grand potential phase diagram. (c) Electrochemical windows; the oxidation potential to fully delithiate $\text{Li}_7\text{N}_2\text{I}$ is marked by the dashed line. ....	43
Figure 32. (a) Scanning electron microscopy image. Atomic force microscopy (AFM) topographic height image (b) and corresponding AFM current image (c) of a conventional cathode composed of $\text{LiMn}_2\text{O}_4$ , PVDF binder, and C65 conductive agent. ....	43
Figure 33. Cross section of a baseline composite cathode prepared by hand mixing. Severe solid-state electrolyte aggregation is evident. Sample cross section was prepared by Ar-ion milling. ....	46
Figure 34. Electrochemical performance of NMC-811@ $\text{LiNbO}_3/\beta\text{-Li}_3\text{PS}_4/\text{Li}_x\text{In}$ battery at room temperature: (a) voltage profile and (b) rate capabilities. ....	47
Figure 35. Decomposition of LLZ with lithiated and delithiated (prefix "d-") LCO and NMC-111. Phase equilibria of each reaction at the minimum decomposition energy for the pseudobinary of LLZO and cathode are written at right. ....	50
Figure 36. Stability heatmap of lithiated and delithiated (prefix "d-") NMC-111 ( $\text{LiMn}_{0.3}\text{Co}_{0.3}\text{Ni}_{0.3}\text{O}_2$ ) and NCA ( $\text{LiAl}_{0.05}\text{Co}_{0.15}\text{Ni}_{0.8}\text{O}_2$ ) cathodes compared to $\text{LiNiO}_2$ , $\text{LiCoO}_2$ , and other high-voltage cathodes. ....	50
Figure 37. Electrochemical cell for <i>in situ</i> mass spectroscopic (MS) experiments (i). The gas generated during the cycling can be monitored in real-time with a gas analyzer (MS). The design of the <i>in situ</i> cell eliminates the influence of the carry-over residual gases, so the gas amount and composition can be determined either at various voltage or various charging time (iii). An example of analysis data is shown in (ii). ....	53
Figure 38. (i) Optical electrochemical cell for <i>in situ</i> electrochemical observations during the discharge and recharge of a lithium anode. (ii) Photo of the set-up for the <i>in situ</i> electrochemical optical experiments, including laser confocal microscope, optical cell, and electro-chemical workstation. Surface morphology and dendrite growth can be observed in real-time. Examples are shown in (iii). ....	53

Figure 39. Initial molecular ionic composite (MIC) electrolyte films. (a) Chemical structures of PBDT polymer and ionic liquid Pyr <sub>14</sub> TFSI. (b) Large area as-cast 80-mm thick MIC film. (c) Scanning electron microscopy image of MIC film after Li-Li electrochemical cell cycling (pinhole free). .....	56
Figure 40. Dynamic mechanical analysis of molecular ionic composite electrolyte films. The red curve shows storage modulus for 20 wt% PBDT / 80% Pyr <sub>14</sub> TFSI electrolyte film, and the black curve shows the same for 20 wt% PBDT / 80% EMIM TfO (an initial pilot material). Similar analysis of Li-loaded films is under way. These films have tensile storage modulus > 1 GPa over a wide temperature range and show no evidence of decomposition (also with TGA – not shown) to well above 200°C. ....	57
Figure 41. (left to right) Ball mill for powder synthesis; X-ray diffraction for powder structure analysis; cryo focused ion beam and scanning transmission electron microscopy energy dispersive X-ray facility for material characterization; and cell assembly station. ....	59
Figure 42. Lithium ionic conductivity of solid-state electrolyte (SSE) at various temperatures. A promising multifunctional SSE shows $5 \times 10^{-3}$ S/cm at 25°C, 10 times higher than the LPS baseline.....	59
Figure 43. Cycle life of Li-metal solid-state cells with NMC cathode materials containing 60%, 70%, and 85% nickel, respectively. The cells were cycled at 2.5-4.3 V, C/10 rate, and 70°C. ....	60
Figure 44. X-ray diffraction patterns of 75Li <sub>2</sub> S·25P <sub>2</sub> S <sub>5</sub> glass solid electrolyte prepared by (a) dry ball milling process and (b) wet ball milling process.....	62
Figure 45. Arrhenius plot for measured ionic conductivity of LPS glass synthesized by wet ball milling process.....	62
Figure 46. Scanning electron microscopy images of dry-ball-milling synthesized (a) 75Li <sub>2</sub> S·25P <sub>2</sub> S <sub>5</sub> and (c) Li <sub>6</sub> PS <sub>5</sub> Cl glass solid electrolytes and of wet-ball-milling synthesized (b) 75Li <sub>2</sub> S·25P <sub>2</sub> S <sub>5</sub> and (d) Li <sub>6</sub> PS <sub>5</sub> Cl glass solid electrolytes.....	63
Figure 47. (a) Rate performance of sulfur cathode at 60°C. (b) Corresponding charge/discharge voltage profiles.....	64
Figure 48. (a) Rate performance of sulfur cathode using TiS <sub>2</sub> as solid additive at 60°C. (b) Corresponding charge/discharge voltage profiles.....	64
Figure 49. (a-b) Scanning electron microscopy images of Al-LLZO particles prepared using the molten-salt method and (c-d) refinement of X-ray diffraction patterns collected on as-synthesized (garnet tetragonal phase) and proton exchanged Al-LLZO particle after annealing (garnet cubic phase). ....	67

Figure 50. (a-b) Scanning electron microscopy images and (c) X-ray diffraction patterns of Al-LLZO samples obtained from the recrystallization process and solid-state synthesis method. ....	67
Figure 51. (a) Schematic illustration of the fabrication of the <i>in situ</i> cell with graphene window to study electrode/electrolyte interfaces. (b) Fourier transform infrared (FTIR) absorption spectrum of PEO+ LiTFSI mixtures at EO/Li ratios of 10:1. (c) Scattered near-field infrared amplitude image in a region where graphene window is in contact with the solid-state electrolyte in the cell. (d) Nano-FTIR spectra collected at locations marked by blue and red dots mark points. ....	70
Figure 52. Depth profile X-ray photoelectron spectroscopy (XPS) spectra of as-synthesized NCA collected in the CO <sub>2</sub> environment (1.6 Torr). (a) Li 1S, (b) O 1S, and (c) Ni 2p XPS spectra of NCA measured at 1200, 1500, and 1800 eV in the CO <sub>2</sub> environment. ....	73
Figure 53. (a) Illustration of Li-atom diffusion mechanism among layer 1 (L1) to layer 4 (L4) of Li/Li <sub>2</sub> O interface. Red: oxygen atom; Green: lithium atom. (b) Energy barriers to fill lithium vacancy at L1 to L4, respectively, for left (Li/Li <sub>2</sub> O) and right (Li/LiF) interfaces. (c) Kinetic Monte Carlo simulation of void evolution from time = 0 sec to time = 1.48E-06 sec (100 K steps). Left panel: Li/Li <sub>2</sub> O; right panel: Li/LiF. ....	76
Figure 54. The atomic force microscope – environmental transmission electron microscope (AFM-ETEM) solid open-cell setup for the study. (a) Schematic of experimental setup prior to lithium deposition. (b) Schematics illustrating that a growing lithium whisker will push the AFM cantilever, which leads to measurement of the force that the growing whisker can potentially exert on an obstacle. ....	79
Figure 55. The lithium whisker formation during the electrochemical deposition of lithium in CO <sub>2</sub> environment. (a-c) Sequential transmission electron microscopy snapshots of lithium particle nucleation. (d-f) Whisker growth process. (g) Whisker collapse. Red arrow in (f) indicates that the lithium whisker sprouts up from the whisker-electrolyte interface. Blue dotted lines indicate the nucleus. Red dotted lines highlight the side surface and shape of the lithium whisker. (h) Deflection of atomic force microscopy (AFM) tip and vertical growth rate of whisker during the process. (i-j) Lithium particle in another nucleation case and corresponding electron diffraction pattern. Spring constant of the AFM cantilever is ~ 0.4 N·m <sup>-1</sup> . The scale bar is 200 nm. ....	79
Figure 56. (a) A typical Rietveld refinement result showing that the materials can well be described using a three-phase model; evolution of lattice parameter <i>c</i> (b) and <i>a</i> (c) of NMC-622 during the co-sintering process; and (d) the evolution of lattice parameter of LLTZO during the co-sintering process. ....	84
Figure 57. (a-b) X-ray diffraction scan of NMC on Al <sub>2</sub> O <sub>3</sub> and on Au/Al <sub>2</sub> O <sub>3</sub> substrates, respectively. ....	87

Figure 58. The thin-stack solid-state cell. (a) The schematic illustration of the thin cell stack. (b) Charge–discharge curve of the thin-stack all-solid-state full cell. The specific capacity reaches 150 mAh/g (based on the mass of LiCoO <sub>2</sub> ). Inset: capacity stays stable after about 50 cycles. ....	89
Figure 59. Cross-section polishing result of the cell. (a) Cryogenic polishing of a Li-metal anode. (b) The cathode composite fabricated as shown in Figure 58a. ....	89
Figure 60. (top) Residence time plotted as function of concentration. (middle) Characteristic diffusion length $L^c = \sqrt{6D\tau^{res}}$ is shown as function of concentration. (bottom) Ratio of the average time a Li <sup>+</sup> spends around at least one anion to the residence time (one specific anion), $\frac{\tau^{bound}}{\tau^{res}}$ . ....	93
Figure 61. (a) Phenomenon of reduced dendrite height at ~350K (compared to morphologies at 300K and 325K). (b) Obtained metal morphologies at 300K, 350K, and 400K. (c) Phase maps summarizing electrodeposition morphologies obtained at various operating temperatures. (d) Contrasting morphologies: simulations predict that for operating temperature of 300K, a local hot spot temperature of 325K is sufficient to trigger aggravated dendrite growth. (e) Homogenizing internal thermal field (~ 350K) helps effective dendrite suppression. ....	95
Figure 62. (a) Concentration-dependent partial molar volume of lithium within NMC cathodes. (b) Partial molar volume of lithium within LCO cathodes. It is evident that within the range of operation, NMC and LCO demonstrate positive and negative partial molar volumes with respect to lithium, which impacts their performance. ....	98
Figure 63. (a) Performance curves demonstrated by NMC cathodes with LLZO electrolytes. Substantial delamination-induced impedance rise observed during charge, which leads to capacity fade during discharge. (b) Charge/discharge performance curves experienced by the LCO cathodes with LLZO electrolytes. Major delamination-induced impedance rise, and subsequent capacity fade, occurs during the discharge process. (c) LLZO grain size dependent discharge capacity fade experienced by NMC and LCO cathodes. Smaller grains help to minimize the delamination-induced capacity fade in both the cathode materials. ....	98
Figure 64. Morphologies of lithium plating under different conditions. ....	101
Figure 65. (a) Part of Li-P-S phase diagram. Stable and unstable phases are written in black and blue font, respectively. Each arrow depicts substitution from PS <sub>4</sub> <sup>3-</sup> to a different anion block. (b) Arrhenius plots of <i>ab initio</i> molecular dynamic simulation on the Li-P-S systems with different compositions, that is, substitution from PS <sub>4</sub> <sup>3-</sup> to P <sub>2</sub> S <sub>7</sub> <sup>4-</sup> (the third arrow). ....	104
Figure 66. The interaction of sulfur and Li-S with carbon nanotube with and without internal filling with lithium. ....	107

Figure 67. The electrostatic potential in ethylene carbonate electrolyte with LiPF <sub>6</sub> salt. The Li <sup>+</sup> and PF <sub>6</sub> <sup>-</sup> can induce long-range electric field. (a) Full electrostatic potential. (b) Electrostatic potential after removing the fitting charge density electrostatic potential. ....	107
Figure 68. (a) 3ω sensor for analysis of lithium symmetric cell based on thermal signal. Sensitivity analysis of symmetric cells with (b) 50-μm and (c) 100-μm Li-metal anode, assuming Rb <sub>Li-LLZO</sub> = 3 × 10 <sup>-5</sup> m <sup>2</sup> K/W. (d) Peak sensitivity to Rb <sub>Li-LLZO</sub> as a function of Rb <sub>Li-LLZO</sub> .....	110
Figure 69. (a) 3ω sensor for analysis of Li-metal cells using wet electrolyte based on thermal signal. Sensitivity analysis of cells with (b) 20-μm, (c) 50-μm, and (d) 100-μm Li-metal anode. Peak sensitivity to Rb <sub>Li-LLZO</sub> as a function of Rb <sub>Li-LLZO</sub> for cells with 50-μm Li-metal anode. ....	111
Figure 70. Energy barrier obtained from the DFT analysis as a lithium atom travels from an LBCO coating material to a LLZO electrolyte. The magnitude of ΔG obtained from the PBE-GGA calculation is 0.68 eV. ....	113
Figure 71. Analyzed critical temperatures (T <sub>crit</sub> ) as a function of the grain boundary (GB) diffusion property for simulated effective ionic conductivities of systematically varied LLZO microstructures. T <sub>crit</sub> variation (a) with D <sub>0</sub> <sup>GB</sup> for different grain sizes; (b) with D <sub>0</sub> <sup>GB</sup> for different GB width; (c) with E <sub>a</sub> <sup>GB</sup> for different grain sizes; and (d) with E <sub>a</sub> <sup>GB</sup> for different GB width.....	116
Figure 72. Interfacial structures of LCO/LLZO from three LCO orientations. (a-c) Density functional theory relaxed structures followed by initial construction of the interfaces. (d-f) Quenched structures from <i>ab initio</i> molecular dynamics trajectories that are equilibrated at 2000K for 2 ps. The green, blue, yellow, purple, and red spheres represent lithium, cobalt, lanthanum, zirconium, and oxygen in the LCO/LLZO structures, respectively.....	117
Figure 73. Demonstration of a physical model for electrochemical impedance spectroscopy for a simple two-phase microstructure. ....	117
Figure 74. Demonstration of some of the cluster-ions used in the study. They exhibit different shapes, sizes, and compositions.....	120
Figure 75. Two typical cluster-based solid electrolyte structures identified from the extensive structure search. Cluster-ions are shown in tetrahedron, rod and cage configurations. Li-ions are shown in blue. ....	120
Figure 76. Liquid phase synthesis of lithium argyrodites solid electrolytes. (top) Scheme of solution-based synthesis method. (lower left) X-ray diffraction shows as-produced electrolytes are high-purity and possess high crystallinity. (lower right) Measured ionic conductivity of various halide-doped sulfide electrolytes produced by liquid phase method. ....	123

- Figure 77. *Ab initio* molecular dynamics (AIMD) simulations to understand Li<sup>+</sup> ion transport and structural evolution at anode/sulfide-electrolyte interfaces. (a) Unit cells of various Li<sub>6</sub>PS<sub>5</sub>FaX<sub>1-a</sub> (X = Cl, Br, I) compounds. (b) Mean-squared displacement of lithium atoms over 150 ps of AIMD simulations at 450K. (c-d) AIMD snapshots showing evolution of lithium (001) || Li<sub>6</sub>PS<sub>5</sub>F(001) interface at 450K..... 124
- Figure 78. Development of the deep neural network (DNN) model. (a) Data: Distribution of data used in training the neural network (NN). (b) Model: Schematic representation of the NN that takes 50 translationally/rotationally invariant features of a configuration and outputs its energy. The input layer of the network holds these coordinates, which are represented by G1 and G2. G1 and G2 are radial and angular symmetry functions, respectively. The network contains two hidden layers in each of the 10 compute nodes. All the compute nodes in the network are labeled as f(x). b1, b2, and b3 are biased nodes, which hold a constant value of one. {W<sub>i</sub>} represents the weights between nodes of the i<sup>th</sup> and (i.1)<sup>th</sup> layers. (c) Optimization-mean absolute energy during the training of the NN is plotted as a function of the training cycle for training and validation datasets..... 125
- Figure 79. (a) Low- and (b) high-magnification transmission electron microscopy images of small (~ 3 nm) carbon nanocages impregnated with sulfur. (c) high-angle annular dark field – scanning transmission electron microscopy image and (d) corresponding elemental map of this sample..... 126
- Figure 80. (a) Ionic conductivity of P(EO)<sub>n</sub>LiFSI polymer-in-salt electrolytes with different [EO]/[Li<sup>+</sup>] molar ratio. (b) Temperature dependence of ionic conductivity of P(EO)<sub>1</sub>LiFSI-xPyr14FSI polymer-in-salt composite electrolytes at 60°C. .... 130
- Figure 81. (a) A free-standing interconnected composite film made of LICGC<sup>TM</sup> ceramic and crosslinked polymer electrolyte (TC composite). (b) A cross-sectional scanning electron microscopy image of the film. Note the presence of thin layers of polymer protecting both surfaces of the ceramic. (c-d) Pictures of the composite electrolyte film after being in contact with lithium. (c) The part where there was no surface polymer layer turned black. (d) With the surface polymer layer, no sign of ceramic reacting with lithium was observed..... 133
- Figure 82. Lithium symmetrical cell cycling using interconnected composite film. (a) Cycling at 80°C with very little plasticizer in the film. (b) Cycling at 70°C with the polymer phase containing 50:50 TEGDME plasticizer/polymer by weight. (c) Impedance spectra of the cell in (b) before cycling and after 5 cycles..... 133
- Figure 83. Charge and discharge curves of the cells at cycle 1, 10, and 20. Dimensions of cell components are: Li (3/8) PE (5/8) LFP (1/2), Li (1/2) PE (5/8) LFP (3/8), Li (1/2) PE (5/8) LFP (1/2), and Li (1/2) PE (1/2) LFP (1/2)..... 134
- Figure 84. X-ray photoelectron spectroscopy (XPS) data of SiO<sub>2</sub> control sample (a), after lithium deposition (b), and after heating (c). XPS data of neat PEO (d), after lithium deposition (e), and after heating (f)..... 137

Figure 85. (a) Density of LLZTO-Al pellets with different atomic layer deposition (ALD) cycles of $\text{Al}_2\text{O}_3$ coating after sintering at $900^\circ\text{C}$ (black) and $1100^\circ\text{C}$ (red). (b) Scanning electron microscopy image of LLZTO-1Al with 1 cycle of $\text{Al}_2\text{O}_3$ sintered at $900^\circ\text{C}$ . Inset is a zoom-in image showing the existence of a low-z phase between LLZTO grains. (c) Electrochemical impedance spectroscopy of LLZTO-1Al sintered at $900^\circ\text{C}$ . Inset is an optical image of a disassembled Li/LLZTO-1Al/Li cell with the interface exposed. Arrow indicates the black color formed after contact between lithium and LLZTO-1Al above the lithium melting point. ....	140
Figure 86. Raman spectra of solution phase $\text{Li}_2\text{S} : \text{P}_2\text{S}_5$ (molar ratio 1:1) solvate complexes in AN, MA, TEGDME, DME, and THF. ....	143
Figure 87. (a) Raman spectra for solution phase solvate complex in AN. (b) The same complex vacuum dried at $140^\circ\text{C}$ for 24 h (still containing $\sim 3$ wt% strongly coordinated AN). (c) The same complex heated to $270^\circ\text{C}$ to remove the remaining AN. (d) Raman spectra of sample (c) re-dissolved in AN. ....	143
Figure 88. X-ray diffraction patterns of the same solvate complexes described in Figure 87. ....	144
Figure 89. X-ray photoelectron spectra for the same solvate complexes analyzed in Figures 87-88. ....	144
Figure 90. (a) Schematic illustration of one-step solvent-free prelithiation method for silicon anodes. (b-c) Scanning electron microscopy images of silicon anode before prelithiation (b) and after (c) prelithiation. ....	146
Figure 91. (a) Brunauer–Emmett–Teller result. (b) Transmission electron microscopy (TEM) image of new carbon host for $\text{SeS}_x$ cathode. (c) Representative TEM Image. (d) X-ray diffraction patterns. (e) Thermogravimetric analysis curve. (f) S 2p X-ray photoelectron spectroscopy result of $\text{SeS}_x$ -C composite. (g) Cycling performance of $\text{SeS}_x$ -C composites of $\text{SeS}_x$ with different selenium doping. (h) Cycling performance of $\text{SeS}_x$ -C with 10 wt% selenium doping in HFE and DME electrolytes, respectively, at $200 \text{ mA g}^{-1}$ with $2.5 \text{ mg cm}^{-2}$ sulfur loading. ....	150
Figure 92. Scanning electron microscopy images of integrated Ketjen Black (IKB) particles with different particle sizes: (a) $< 20 \mu\text{m}$ and (b) $> 70 \mu\text{m}$ . Brunauer–Emmett–Teller absorption isotherms of (c) IKB and (d) IKB/S particles with different particle sizes. Electrochemical properties of sulfur cathode using IKB particles with size (e) $< 20 \mu\text{m}$ , and (f) $> 70 \mu\text{m}$ . Sulfur electrode loading $> 4 \text{ mg/cm}^2$ , $E/S = 4 \mu\text{L/mg}$ , $I = 0.1\text{C}$ , and electrolyte: $1 \text{ M LiTFSI/DOL/ DME} + 0.3 \text{ M LiNO}_3$ . ....	153

- Figure 93. Design of high-performance all-solid-state Li-S battery. (a) Schematic diagram of battery architecture and cycling reaction for the solid-state Li-S battery with Li-metal anode, polymer solid electrolyte, and Li<sub>2</sub>S composite cathode. (b) Cross-sectional scanning electron microscopy images of as-prepared solid-state Li<sub>2</sub>S-Li cell. (f) Zoomed-in image of polymer-polymer composite electrolyte and cathode/electrolyte interface. (d) Charge-discharge voltage profiles of Li<sub>2</sub>S@TMDs and bare Li<sub>2</sub>S cathodes at 0.1 C (1 C = 1,166 mA g<sup>-1</sup> Li<sub>2</sub>S)..... 156
- Figure 94. (a) X-ray absorption spectroscopy of pristine polymeric sulfur. Major peaks corresponding to characteristic unoccupied molecular orbitals are labeled. (b) X-ray fluorescence of pristine polymeric sulfur collected at energies of 2469 eV, 2475 eV, and 2480 eV. .... 158
- Figure 95. The charge and discharge curves of a polymeric sulfur cathode (left); cycle life (right). .... 159
- Figure 96. (a) The molecular structures of the amphiphilic additives and fluorocarbon solvent. (b) Micelle size characterized by small angle X-ray scattering as a function of lithium salts and additives..... 161
- Figure 97. (a-c) Voltage profiles of Li-O<sub>2</sub> cells with the three electrolytes at selected cycles at a current density of 0.2 mA cm<sup>-2</sup> under a capacity limited protocol of 1.0 mAh cm<sup>-2</sup>. (d-f) Cross-sectional scanning electron microscopy images of Li-metal anodes from cycled Li-O<sub>2</sub> cells. (a/d) 1 M LiTf in G4. (b/e) HCE. (c/f) LHCE..... 165
- Figure 98. (a) Galvanostatic test of the Li-O<sub>2</sub> batteries with Na<sup>+</sup> additives. The cell consists of a lithium anode, carbon fiber paper cathode, glass fiber separator, and metal triflate salts in TEGDME electrolytes including 1.0 M Li<sup>+</sup> (red), 1.0 M Li<sup>+</sup> + 0.1 M Na<sup>+</sup> (green), and 1.0 M Li<sup>+</sup> + 0.5 M Na<sup>+</sup> (violet). (b) Scanning electron microscopy images of the discharged and charged cathodes based on the three electrolytes. The scale bar in the inset is 1 μm. (c) X-ray diffraction of pristine carbon cathode, discharged cathode, and charged cathode. (d) Raman spectra of triflate salt, pristine carbon cathode, discharged cathode, and charged cathode. .... 168
- Figure 99. (left) Charge and discharge profiles comparing LiClO<sub>4</sub> and LiNO<sub>3</sub> in the 100<sup>th</sup> cycle. (right) Comparison of battery capacity retention with four salts over 100 cycles. .... 171
- Figure 100. *In situ* X-ray absorption spectrum (XAS) of NaCr<sub>2/3</sub>Ti<sub>1/3</sub>S<sub>2</sub> at (a) chromium, (b) titanium, and (c) sulfur K-edges. (d) Corresponding voltage profiles for the first charge. The divided *in situ* XAS K-edge XAS spectra of three stages as marked in the bottom inset during the first charge process. The inset in the bottom part is converted R space of *ex situ* sulfur K-edge extended X-ray absorption fine structure (EXAFS) for pristine and full charged samples..... 175
- Figure 101. (a) Cyclic voltammogram at 0.1 mV s<sup>-1</sup>. (b) *In situ* high-energy X-ray diffraction (HEXRD) in the first cycle at 0.1 C of black phosphorus-Ketjenblack (BPC) anode. (c) *Ex situ* HEXRD. (d) <sup>31</sup>P nuclear magnetic resonance spectra of BPC anode at different charge/discharge states. .... 178

Figure 102. Representative charge/discharge curves. (b) Cycle performance at 12 mA g <sup>-1</sup> . (c-d) Rate performance of Na <sub>0.66</sub> Ni <sub>0.26</sub> Zn <sub>0.07</sub> Mn <sub>0.67</sub> O <sub>2</sub> /P cell with electrolyte of 1 M NaPF <sub>6</sub> /PC with 2 vol% fluorinated ethylene carbonate additive. ....	179
Figure 103. Initial charge and discharge profiles of a Na/Na <sub>0.7</sub> Ti <sub>1.825</sub> O <sub>4</sub> cell. The structure of the material is shown in the inset. ....	181
Figure 104. Capacity as a function of cycle number for Na/Na <sub>0.7</sub> Ti <sub>1.825</sub> O <sub>4</sub> cells cycled at different current densities. ....	181
Figure 105. (a) Cycling stability and (b) Coulombic efficiency (CE) of Na  O3- NaCu <sub>1/9</sub> Ni <sub>2/9</sub> Fe <sub>1/3</sub> Mn <sub>1/3</sub> O <sub>2</sub> cells with different molar ratio of NaFSI / triethyl phosphate (TEP) electrolyte. (c) Cycling stability and (d) CE of Na  O3- NaCu <sub>1/9</sub> Ni <sub>2/9</sub> Fe <sub>1/3</sub> Mn <sub>1/3</sub> O <sub>2</sub> cells with different diluents at the same TEP to diluent ratio. (e) Cycling stability and (f) CE of Na  O3-NaCu <sub>1/9</sub> Ni <sub>2/9</sub> Fe <sub>1/3</sub> Mn <sub>1/3</sub> O <sub>2</sub> cells with different amount of TTE diluent in NaFSI/TEP/TTE electrolyte.....	183
Figure 106. Charge/discharge curves of pristine NMC-811 and Nb-O modified NMC-811 heated from 300°C to 800°C.....	186
Figure 107. Cycling stability of a cell with PVDF-only binder (baseline) and a 5:1 PVDF:PANI binder blend (left) in both the cathode and anode and (right) in the cathode only or anode only. ....	186
Figure 108. PANI changing color after HF exposure (left). HF scavenging and improved SEI formation (right). ....	187
Figure 109. Cathode time-of-flight secondary ion mass spectrometry (TOF-SIMS) data with normalized signal intensities for cells with (left) no PANI and (middle) PANI after 1,000 cycles. (Right) <i>Ex situ</i> X-ray diffraction (XRD) patterns of the cathode (top) without PANI and (bottom) with PANI after 1,000 cycles. Both the TOF-SIMS and XRD characterizations were performed on pouch-cell electrodes. ....	187
Figure 110. Three-dimensional X-ray absorption near-edge structure tomography of (left) LiNi <sub>0.92</sub> Co <sub>0.06</sub> O <sub>2</sub> (NC) and (right) LiNi <sub>0.92</sub> Co <sub>0.06</sub> Al <sub>0.02</sub> O <sub>2</sub> (NCA) after 70 cycles at a cut-off voltage of 4.8 V. ....	188
Figure 111. The transient simulation of electrolyte diffusion and redistribution in a large-size pouch cell on cycling. (a) Schematic illustration of the electrode dimension selected for the simulation with an electrolyte diffusion coefficient of 1 × 10 <sup>-10</sup> m <sup>2</sup> s <sup>-1</sup> . Electrolyte distribution at half of the electrode thickness (0.073 mm) after different reaction time: (b) t = 0 h, (c) t = 50 h, (d) t = 100 h, (e) t = 150 h, and (f) t = 200 h. Electrolyte content (%) variation at different times and locations: (g) at long line of (x, 0 mm, 0.073 mm) and (h) at short line of (0 mm, y, 0.073 mm). ....	190

---

Figure 112. Comparison of cycling performance of SPAN electrodes in different electrolytes. (a-c) Thick SPAN electrode with areal capacity loading of $6 \text{ mAh cm}^{-2}$ , at $1.2 \text{ mA cm}^{-2}$ (C/5). (b) Voltage profiles of thick SPAN electrode in conventional carbonate electrolyte. (c) Voltage profiles of thick SPAN electrode in novel ether electrolyte. ....	191
Figure 113. Schematic showing different types of risk associated with use of lithium metal, preparation of Li-metal batteries, and cycling of Li-metal batteries. ....	192
Figure 114. (a) Cells using carbon-only cathode cannot reach the upper cutoff potential and only deliver a very limited amount of discharge capacity under the lean electrolyte condition, even during C/20 formation. (b) Discharge/charge profiles of NiO-carbon and $\text{Ni}_3\text{S}_2$ -carbon materials at the first cycle under the lean electrolyte condition; their discharge capacities are 690 and 1128 mAh/g, respectively. (c) CV curves shown for various cathode materials. (d) Cycling performance. (e-f) Retention (normalized to discharge capacity of first aging cycle) of capacities for upper-plateau ( $Q_H$ ) and lower-plateau ( $Q_L$ ) regions of the NiO@Ni-carbon and $\text{Ni}_3\text{S}_2$ @Ni-carbon cells.....	193

---

## TABLE OF TABLES

Table 1. Composition of various PEO-POSS diblock and POSS-PEO-POSS triblock copolymers. The molecular weight of the POSS block ( $M_{\text{POSS}}$ ) was estimated from nuclear magnetic resonance. ....	25
Table 2. Composition of the triblock terpolymer PEO-POSS-PSTFSiLi. The composition was determined by nuclear magnetic resonance spectra. The $r$ values denote the concentration of lithium ion in the polymer and are given by $r = [\text{Li}]/[\text{EO}]$ .....	26
Table 3. Prototype molecular ionic composite electrolyte film compositions, thicknesses, and room-temperature conductivities.....	56
Table 4. Process parameter design control factors (■ indicates baseline conditions developed in Q1).....	60

## A MESSAGE FROM THE MANAGER: ADVANCED BATTERY MATERIALS RESEARCH PROGRAM AND BATTERY500 CONSORTIUM

This document summarizes the efforts conducted from October 1, 2019, through December 30, 2019. A few notable achievements from the BMR investigators are summarized below.

- The **Stanford University** (Bao and Cui) group used a three-dimensional coarse-grained Brownian dynamics model of lithium deposition under an applied voltage to understand the effect of the Damköhler Number (Da) on lithium morphology. They found that decreasing Da can lead to more uniform lithium deposition at the cost of a lower charging rate for the same applied potential.
- The **Argonne National Laboratory** (Markovic and Curtis) team showed the interface reaction of lithium with PEO as determined by X-ray photoelectron analysis before and after lithium deposition and heating to 100°C under vacuum. New features in the O 1s, C 1s, and Li 1s spectra reveal evidence for lithium dissolution in the PEO and reaction forming organolithium (LiCR) and lithium alkoxide (LiOR) species.
- The **Argonne National Laboratory** (Johnson and Amine) team studied the (de)sodiation reaction mechanism of phosphorus anodes using *in situ* high-energy X-ray diffraction, <sup>31</sup>P solid-state nuclear magnetic resonance, and electrochemical methods. They observed that reversibility is tied to a nanostructure stable amorphous state that is amiable to volume changes. A full cell using a phosphorus anode and a P<sub>2</sub>-type Zn-doped Ni-Mn layered cathode demonstrated very good cycling reversibility and life (100 cycles) with less than 10% capacity loss.
- The **Pacific Northwest National Laboratory** (Zhang) team optimized the nonflammable phosphate-based localized high-concentration electrolyte with a composition of NaFSI:TEP:TTE (1:1.5:2 in molar ratio). The new combination leads to a high Coulombic efficiency of 99.78% for sodium deposition/stripping.

Highlights from the Battery500 consortium team include the following:

- **Keystone Project 1 (Materials and Interfaces):** Brookhaven National Laboratory compared LiNi<sub>0.94</sub>Co<sub>0.06</sub>O<sub>2</sub> (NC) and LiNi<sub>0.92</sub>Co<sub>0.06</sub>Al<sub>0.02</sub>O<sub>2</sub> (NCA) that were cycled to a high voltage (4.8 V). Using 3-dimensional X-ray absorption near-edge structure tomography, the team showed reduced cracking and a more even distribution of nickel valence states in the Al-doped cathode.
- **Keystone Project 2 (Electrode Architectures):** The University of California at San Diego conducted simulations of lithium deposition at three rates using reactive molecular dynamics to investigate the evolving morphological development of Li-metal deposits. Using this technique, the sensitivity of the deposition rate on morphological features, including film density, surface roughness, porosity, defect (1-D dislocations, 2-D grain boundaries, to 3-D voids) formation and density was well captured.
- **Keystone Project 3 (Cell Fabrication and Testing, and Diagnosis):** The Idaho National Laboratory made recommendations on the safe handling of lithium metal. Guidance was published in the *Journal of the Electrochemical Society*.

Fifteen new solid-state electrolyte projects were added to the Advanced Battery Materials Research Program this quarter. Replacing organic liquid electrolytes with a solid-state Li<sup>+</sup> conductor would improve battery safety and potentially allow integration of next-generation electrode materials. Unfortunately, solid electrolyte suffers from many issues, including low conductivity, poor stability at anodic and cathodic potentials, and inadequate mechanical properties. The new efforts listed below seek to tackle these challenges. They focus on: (1) discovery of new solid-state electrolytes and novel electrode and cell architectures, (2) development

of *in situ* microscopy and spectroscopy, and associated *ex situ* tools, capable of identifying the physical and chemical changes of Li-metal-based battery components during charge and discharge, and (3) development of advanced models to assess Li-metal-based batteries to gain a better understanding of these challenges and suggest potential solutions.

Affiliation	Principal Investigator	Project Title
Iowa State University of Science and Technology	Steve Martin	Development of Thin, Robust, Lithium-Impenetrable, High-Conductivity, Electrochemically Stable, Scalable, and Low-Cost Glassy Solid Electrolytes for Solid-State Lithium Batteries
Wildcat Discovery Technologies	Kyler Carroll	Composite Solid Ion Conductor with Engineered Lithium Interface
University of Massachusetts, Amherst	Nianqiang "Nick" Wu	Single-Ion Conducting Electrolyte Extended to Cathode for All-Solid-State Lithium-Ion Batteries
University of Michigan	Jeff Sakamoto	Physical and Mechano-Electrochemical Phenomena of Thin-Film Lithium-Ceramic Electrolyte Constructs
University of Maryland, College Park	Chunsheng Wang	Lithium Dendrite-Free Li <sub>7</sub> N <sub>2</sub> I-LiOH Solid Electrolytes for High-Energy Lithium Batteries
General Motors	Thomas Yersak	Hot Pressing of Reinforced Li-NMC All-Solid-State Batteries with Sulfide Glass Electrolyte
University of Maryland, College Park	Eric Wachsman	Low Impedance Cathode/Electrolyte Interfaces for High-Energy-Density Solid-State Batteries
University of Wisconsin, Milwaukee	Deyang Qu	Developing an <i>In Situ</i> Formed Dynamic Protection Layer to Mitigate Lithium Interface Shifting: Preventing Dendrite Formation on Metallic Lithium Surface to Facilitate Long Cycle Life of Lithium Solid-State Batteries
Virginia Polytechnic Institute and State University	Louis Madsen	Molecular Ionic Composites: A New Class of Polymer Electrolytes to Enable All-Solid-State and High-Voltage Lithium Batteries
Solid Power, Inc	Pu Zhang	All-Solid-State Batteries Enabled by Multifunctional Electrolyte Materials
Pennsylvania State University	Donghai Wang	Developing Materials for High-Energy-Density Solid-State Lithium-Sulfur Batteries
General Motors	Xingcheng Xiao	Fundamental Understanding of Interfacial Phenomena in Solid-State Batteries
University of Houston	Yan Yao	Multidimensional Diagnostics of the Interface Evolutions in Solid-State Lithium Batteries
Virginia Commonwealth University	Puru Jena	First-Principles Modeling of Cluster-Based Solid Electrolytes
University of Louisville	Badri Narayanan	Predictive Engineering of Interfaces and Cathodes for High-Performance All-Solid-State Lithium-Sulfur Batteries

We encourage you to follow our progress as we proceed. Our next report is expected to be available in May 2020.

Sincerely,

*Tien Q. Duong*

Tien Q. Duong  
Manager, Advanced Battery Materials Research Program & Battery500 Consortium  
Vehicle Technologies and Electrification Program  
Energy Efficiency and Renewable Energy  
U.S. Department of Energy

## TASK 1 – Liquid/Polymer Solid-State Electrolytes

### Summary and Highlights

The BMR Program goal is to develop long-life batteries superior to commercial Li-ion systems in terms of cost, vehicle range, and safety. The BMR Program addresses the fundamental problems of electrode chemical and mechanical instabilities that have slowed development of affordable, high-performance, automotive batteries. The aim is to identify electrode/electrolyte materials that yield enhanced battery performance and lead to greater acceptance of electric vehicles (EVs). Currently, the U. S. Department of Energy (DOE) Vehicle Technologies Office (VTO) supports 17 projects in the BMR Program under this Electrolytes Task. These projects can be categorized into four general topics:

- **Liquid.** The projects for liquid electrolyte aim to develop electrolyte formulations, based on fluoro-chemistries, to achieve significantly improved operating voltage, increased durability, and increased energy density of Li-ion batteries at a reasonable cost. Nonaqueous polyelectrolyte solutions with high Li<sup>+</sup> transference numbers will be developed to achieve high rate capabilities at room temperature. In addition, electrolytes with new polymer binders bearing a pentafluorophenyl group on the backbone will be designed, synthesized, and tested.
- **Polymer.** The targets of polymer electrolyte (PE) projects include inorganic/polymer and polymer/gel hybrid electrolytes that have flexibility, mechanical strength, thermal stability, high ionic conductivity, stable interfaces against lithium metal, and polysulfide-trapping capability enabling energy density Li-S batteries, with comparable cycle life.
- **Self-Forming & Self-Healing.** The self-forming, self-healing electrolyte projects are focused on developing and implementing Li-metal-based metal fluorite and metal iodide batteries, capable of energy densities > 400-500 Wh/kg and 1000 Wh/L.
- **Solid-State.** The solid-state projects are to develop high conductivities solid electrolytes / composite solid electrolytes that are scalable, are chemically and electrochemically stable, and will enable low-cost, high energy-density solid-state lithium batteries.

### Highlights

At Daikin (Sunstrom, Hendershot, and Falzone), significant efforts were focused on completing method development for molar quantification of components in commercial pouch cells. To increase resolution of low molecular weight components and permanent gases (CH<sub>4</sub>, CH<sub>3</sub>F, O<sub>2</sub>, etc.), a cryogenic cooler was installed on the Agilent gas chromatography – mass spectrometry (GC-MS) / thermal conductivity detector (TCD) system. This allows for better separation of components and shorter analytical methods. Gassing kinetics at 55°C in pouch cells using high nickel content charged to 4.6 V were studied using different electrolytes. They found that without the presence of fluoroethylene carbonate (FEC) in the electrolyte, gas generation is suppressed in all cathodes aside from NCA.

The University of Washington (UW) group (Jen and Yang) has fabricated test cells with S/C cathode using PENDI-350/poly(ethylene oxide) (PEO) with weight ratio = 3 : 1, the PENDI-350/triPy/PEO (PPP binder), and PENDI-350/PEO/polyvinylidene fluoride (PPPVDF) binders. They studied the effect of surface modification, the weight ratio of S/C in the cathode, electrode loading, etc., to achieve long cycle stability with high electrode loadings. They have provided test cells for performance evaluation at a designated DOE testing laboratory.

At Stony Brook University (SBU, Takeuchi), the group studied the resulting particle size, effect on electrochemical cycling, impact on electrode interfaces, and temperature effect of their new electrolyte processes. They found that the modified processing approaches aid in formation of lithium metal at the anode

and formation of the iodine cathode, as well as lower overall impedance for the cells. In addition, they found that modification of the interfaces aids in formation of both electrodes and further acts to stabilize cell configuration.

The University of California (UC) at Berkeley team (McCloskey) studied the conductivity, viscosity, and diffusion of model polysulfone-based polyelectrolyte solutions in dimethyl sulfoxide (DMSO) and water. This study suggests that tuning polymer backbone chemistry and therefore backbone-solvent interactions could help increase  $t_+$  without sacrificing ionic conductivity. These results were reported in the article listed in the Publications section. In addition, the team has focused on completing transport property characterization of total salt diffusion coefficients, thermodynamic factors, and non-ideal concentrated solution transference number measurements via the Balsara-Newman method originally developed for polymer and glyme electrolytes. Their initial results show that the analysis is extremely sensitive to fitting of concentration cell data as well as diffusion coefficient data.

The Stanford University group (Bao and Cui) used a three-dimensional (3D) coarse-grained Brownian dynamics model of lithium deposition under an applied voltage to understand the effect of the Damköhler Number (Da) on lithium morphology. They found that decreasing Da can lead to more uniform lithium deposition at the cost of a lower charging rate for the same applied potential. Based on these results, they designed polymer coating - perfluoropolyether-dimethacrylate (PFPE-DMA) as a polymer network backbone, pentaerythritol-tetrakis(3-mercaptopropionate) (PETMP) as the crosslinker, and lithium-styrene-trifluoromethanesulfonyl-imide (Li-STFSI) as the salt linker in different ratios. They further found that the coatings facilitate transport from the bulk electrolyte to the lithium electrode without significantly contributing to interfacial resistance.

The Lawrence Berkeley National Laboratory (LBNL) group (Balsara) has completed a milestone: a series of diblock and triblock organic-inorganic hybrid copolymers were synthesized to compare and contrast their electrochemical properties. The compositions of the polymers determined by nuclear magnetic resonance (NMR) spectra were reported.

The Iowa State University (ISU) group (Martin) started a new project last October. The project objective is to develop new  $\text{Li}^+$ -conducting mixed oxy-sulfide-nitride glassy solid electrolytes (MOSN GSEs) that are impermeable to lithium dendrites, have high conductivities, are scalable through low-cost glass manufacturing, are chemically and electrochemically stable, and will enable low-cost, high-energy-density solid-state lithium batteries. They have focused on two aspects: materials scale-up and reproducibility. They have developed synthesis techniques to produce hundred-gram quantities of  $\text{SiS}_2$ , needed for kilogram quantities of ISU-4 glass, and have made ISU-4 glass multiple times and measured the properties.

The Wildcat project (Carroll/Peebles) is new. They seek to develop composite polymer/ceramic electrolytes compatible with Li-metal anodes for an all-solid-state Li-metal battery that achieves the DOE requirements. They have focused on developing a high throughput workflow for screening the polymer/ceramic interface and Li-metal protection agents using baseline materials. In addition, they tested various cell architectures.

At University of Massachusetts (UMass, Wu), the team started synthesis of two types of poly(arylene ether)-based single-ion conducting multi-block copolymer electrolytes. At the same time, a new metal-organic framework (MOF) single Li-ion conductor (LIC) has been synthesized by covalently immobilizing anions to the skeleton of MOF structures. After incorporation of ethylene carbonate (EC) and propylene carbonate (PPC) into the MOF structure, its ionic conductivity reaches a remarkable value of  $7.8 \times 10^{-4} \text{ S/cm}$ . They also introduced lithium salt-grafted  $\text{Li}_{6.4}\text{La}_3\text{Al}_{0.2}\text{Zr}_2\text{O}_{12}$  (LLAZO) nanofiber into the crosslinked poly(ethylene glycol) dimethylacrylate (PEGDMA) to demonstrate the feasibility of fabricating a single-ion conducting composite solid electrolyte consisting of the lithium salt / silane-co-grafted LLAZO nanofiber/crosslinked multi-block copolymer.

The new project at University of Michigan (UM, Sakamoto) aims at discerning the physical and mechano-electrochemical phenomena that control the performance of cells consisting of thin  $\text{Li}_7\text{La}_3\text{Zr}_2\text{O}_{12}$  (LLZO,  $\sim 10\ \mu\text{m}$ ), thin lithium anodes ( $\sim 20\ \mu\text{m}$ ), and thin solid-state composite cathodes. This quarter, they completed the custom thin-film constructs design that will be cycled with reference electrodes.

The new University of Maryland (UMD, Wang) project is to develop Li-metal-based batteries that implement solid LICs equipped with  $\text{Li}_7\text{N}_2\text{I-LiOH}$  solid electrolyte capable of achieving cell performance of 350 Wh/Kg energy density for 1000 cycle life with a cost of  $\leq \$100/\text{kWh}$ . This quarter, the team synthesized, characterized, and optimized  $\text{Li}_7\text{N}_2\text{I-LiOH}$ ,  $\text{Li}_3\text{YCl}_6$ , and  $\text{Li}_7\text{N}_2\text{I-LiOH/Li}_3\text{YCl}_6$  bi-layer solid electrolytes. They also worked on lithium dendrite suppression criteria for solid electrolytes with some initial microscopy data.

The new project at General Motors (GM, Yersak) is to develop Li-NMC all-solid-state batteries (ASSBs) capable of achieving program performance metrics by implementing sulfide glass solid-state electrolytes (SSE) and hot press processing. The team successfully applied a  $\text{LiNbO}_3$  coating to NMC-811 (acquired from BASF) via a solution-based method. As the baseline catholyte, GM has chosen the BMR  $\beta\text{-Li}_3\text{PS}_4$  model SSE. The SSE prepared by GM has an ionic conductivity of approximately  $2 \times 10^{-4}\ \text{S/cm}$  at room temperature and acceptable anodic stability against cathode materials. They are also evaluating low-energy ball milling as a method to prepare baseline composite cathodes. Cycling data for a preliminary baseline cell (NMC-811@ $\text{LiNbO}_3/\beta\text{-Li}_3\text{PS}_4/\text{Li}_x\text{In}$ ) with a composite cathode prepared by ball milling exhibit a reversible capacity of 138 mAh/g with Coulombic efficiency (CE) of 73% in the first cycle at 0.05C-rate and decent cycling stability after a rate test.

At UMD (Wachsman and Mo), computational studies based on first-principles calculations have been initiated to (1) evaluate the thermodynamic interface stability of LLZO solid electrolytes for cathode materials using the thermodynamic analysis demonstrated in their previous studies and (2) identify the interface stability of LLZ solid electrolytes with NMC cathode in comparison to  $\text{LiCoO}_2$ . They also studied the coating layer on cathode materials as the first step to identify the promising coating layers between LLZO-NMC interfaces.

The new project at University of Wisconsin at Milwaukee (Qu) aims to develop Li-metal-based batteries that implement solid LICs equipped with a formed dynamic protection layer. This quarter, they modified and validated apparatus for the *in situ* electrochemical MS analysis and the *in situ* electrochemical optical analysis.

The new project at Virginia Polytechnic Institute and State University (Virginia Tech, Madsen) targets molecular ionic composites (MICs) as solid-state lithium conductors for use in transportation applications. The team has so far generated solid MIC electrolyte films with uniform thickness and with areas up to  $10 \times 10\ \text{cm}$ . These films contain the charged rigid-rod PBDT polymer along with mobile and non-volatile ions (lithium salt and ionic liquid). They have also performed preliminary dynamic mechanical-thermal analysis (DMTA) on MIC films made using the current casting process.

The new project at Solid Power (Zhang) and University of California at San Diego (UCSD, Meng) aims to develop Li-metal solid-state batteries (SSBs) enabled by multifunctional SSEs. A promising multifunctional SSE has demonstrated a conductivity of  $5 \times 10^{-3}\ \text{S/cm}$  at  $25^\circ\text{C}$ , 10 times higher than a baseline LPS electrolyte. Several lithium surface treatments are being evaluated to improve Li-metal stability, ranging from binary lithium compounds to polymers. In addition, the cycle life data of the three cathodes show that the 85% nickel material has the highest initial capacity but faded faster than the other two. The 60% nickel material showed slightly lower initial capacity but higher cycling stability than the 70% nickel material. The NMC-622 material has been down-selected for concept-proven demonstration in Year 1.

Another new project at Pennsylvania State University (PSU, Wang) is to develop advanced S/C composite materials, solid additives, and sulfide-based SSEs for Li-S ASSBs. The team has synthesized  $75\text{Li}_2\text{S}\cdot 25\text{P}_2\text{S}_5$  glass solid electrolyte by a dry ball milling process, and tested the ionic conductivity and morphology. In addition, rate performance of sulfur cathode was tested using LPS as solid-electrolyte membrane and Li-In alloy as anode at  $60^\circ\text{C}$ . A high specific discharge capacity of  $\sim 1200\ \text{mAh g}^{-1}$  at 0.1 C, although the rate performance and sulfur content of the sulfur cathode still need improvement.

## Task 1.1 – Advanced Lithium-Ion Battery Technology: High-Voltage Electrolyte (Joe Sunstrom, Ron Hendershot, and Alec Falzone, Daikin)

**Project Objective.** The project objective is to identify electrolyte formulations, based on fluoro-chemistries, that will allow significantly improved operating voltage, increased durability, and increased energy density of Li-ion batteries at a reasonable cost. The project seeks to understand the conditions under which the electrolyte degrades, the effect on battery performance, and solutions that can overcome current limitations of the electrolyte. Gassing in Li-ion batteries is one of the most common failure mechanisms and poses the greatest safety risk in consumer devices. This project aims to investigate gas composition as a function of cathode material, electrolyte formulation, and operating voltage, and proposes optimal cell compositions at decomposition voltages.

**Project Impact.** Developing an understanding of the operating conditions in which gasses form in Li-ion batteries enables the project to propose optimized cell compositions that operate at higher voltages for a longer period. Different fluorinated electrolyte components and additives may suppress and/or eliminate gas generation at or above hypothesized decomposition voltages. To investigate these topics, it is imperative that the project utilize multiple approaches, including, but not limited to, cathode material, electrolyte composition, operating voltage, and cycle number.

**Approach.** The evolving composition of the electrolyte in the battery will be examined by various analytical instruments to study volatiles (GC-MS/TCD), liquid [liquid chromatography MS (LC-MS)], and solid [time-of-flight secondary ion mass spectrometry (TOF-SIMS), thermogravimetric analysis MS (TGA-MS), X-ray photoelectron spectroscopy (XPS), and auger electron spectroscopy (AES)] electrolyte decomposition products during battery operation. In the first year, the team addressed the gas composition and kinetics for both hydrocarbon and fluorocarbon as a function of several charge/discharge conditions. In the second year, the project will transition into analysis of the SSE decomposition components of its tested batteries to obtain valuable information about solid electrolyte interphase (SEI) layer formation and how it manifests change in both the anode (graphite) and cathode (LCO and NMC). The third year is focused on measuring changes in the solid-state structure of the cathode following high-voltage operation. The project aims to quantify any dissolved metal ions originating from the cathode and deposited on the anode using inductively coupled plasma – mass spectrometry (ICP-MS). It will also study changes in the cathode structure using powder X-ray diffraction (XRD).

**Out-Year Goals.** Work will progress toward understanding how electrolyte formulation and cell operation affect stability of transition metals (TMs) in the cathode structure. The project aims to quantify metal ions, if any, dissolved into solution as a function of operating parameters (that is, voltage, time, etc.) and electrolyte formulation. In addition, measurements will be made using powder XRD to detect changes in the crystal structure of the cathode (LCO and NMC). Understanding effects on the solid-state structure in Li-ion batteries will provide valuable information on the required cathode chemistry for increased performance at high voltage.

**Collaborations.** The project has initiated a collaboration with Dr. J. Chan (University of Texas, or UT, at Dallas) for powder XRD measurements to investigate changes in cathode structure as a function of operating conditions.

### Milestones

1. *Go/No-Go Decision:* Interim cells achieve significant improvement at 4.6 V. (Q4, FY 2019; Complete)
2. Cathode structure versus time/voltage. (Q1, FY 2020; In progress)
3. Data compilation and selection of new electrolyte composition. (Q2, FY 2020; In progress)

## Progress Report

Significant efforts this quarter focused on completing method development for molar quantification of components in commercial pouch cells. To increase resolution of low molecular weight components and permanent gases ( $\text{CH}_4$ ,  $\text{CH}_3\text{F}$ ,  $\text{O}_2$ , etc.) a cryogenic cooler was installed on the Agilent GC-MS/TCD system. This component allows for better separation of components and shorter analytical methods. Figure 1 depicts select representative calibration curves for the major components in Li-ion battery pouch cells ( $\text{CH}_4$ ,  $\text{CH}_3\text{F}$ , and  $\text{CO}_2$ ). These three gases are the result of electrolyte decomposition at high voltage ( $> 4.2$  V), with carbon dioxide and methane originating from multiple components [for example, ethyl methyl carbonate (EMC), EC, and FEC). Fluoromethane is proposed to evolve from the degradation of FEC.

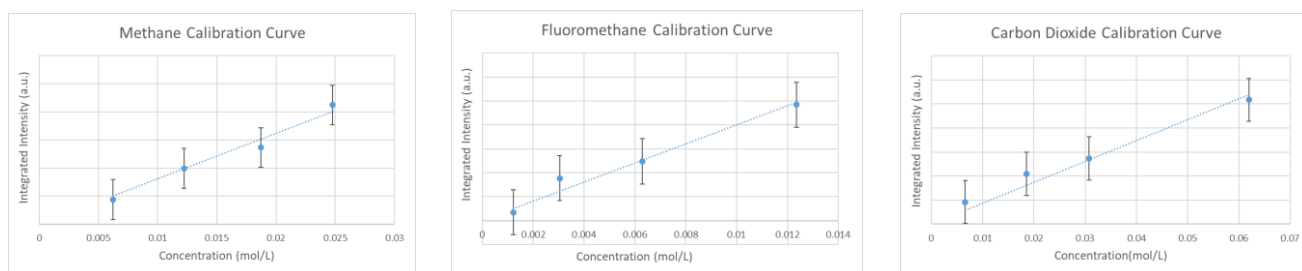


**Figure 1. Example calibration curves for major components seen in commercial Li-ion battery pouch cells. Concentration ranges were identified based on previously reported qualitative data (FY 2017/2018).**

Cell chemistries using NMC-811 are becoming more common as the industry moves to higher nickel content in the cathode. It is necessary to develop an understanding of performance of these cells at high voltage ( $> 4.2$  V). Figure 2 depicts gassing kinetics at  $55^\circ\text{C}$  in NMC-622, NMC-811, and NCA pouch cells charged to 4.6 V as a function of electrolyte.

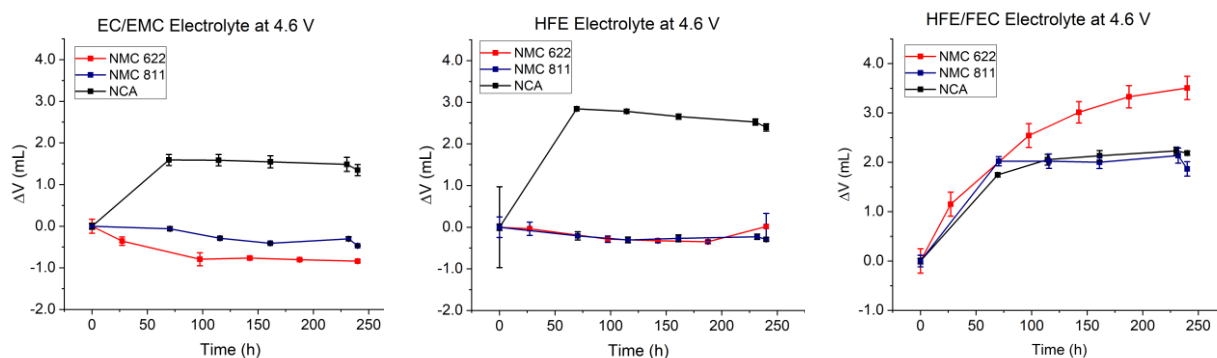


**Figure 2. Gassing kinetics data for NMC-811 cells compared to previously studied NMC-622 and NCA cathodes. Baseline hydrocarbon electrolyte (left), fluoroether containing (middle), and fluoroether / fluoroethylene carbonate (FEC) formulation (right).**

As reported previously with NMC-622 and NCA cells, most gas generation occurs in the first 48-72 hours at elevated temperature in NMC-811. Without the presence of FEC in the electrolyte, gas generation is suppressed in all cathodes aside from NCA.

Collaborative efforts with Dr. J. Chan continued this quarter to investigate solid-state structural changes at 100% state of charge (SOC) in NMC-532 cells. To study effects of Li-ion migration in the system as a function of voltage (4.2 V versus 4.6 V), diffraction patterns were collected on both edge and center portions of the cathode post-mortem. Data are being compiled and will be compared to the baseline diffraction patterns of untested cells that were reported last quarter.

In addition, results were obtained early this quarter from the interim cell submission to Idaho National Laboratory (INL), the *Go/No-Go* FY 2019 Milestone. These tests aimed to compare the best practice to date on electrolyte/cell chemistry to that at the start of the project. The baseline hydrocarbon cells have begun to fail at 4.5 V and 4.6 V; however, the fluorinated electrolyte cells are still testing ( $\geq 80\%$  capacity at 300 cycles for both voltages).

### Patents/Publications/Presentations

The project has no patents, publications, or presentations to report this quarter.

## Task 1.2 – Multi-Functional, Self-Healing Polyelectrolyte Gels for Long-Cycle-Life, High-Capacity Sulfur Cathodes in Lithium-Sulfur Batteries (Alex Jen and Jihui Yang, University of Washington)

**Project Objective.** The project objective is to develop self-healing and polysulfide-trapping polyelectrolyte gels containing room-temperature ionic liquid (RTIL) for the Li-S battery system. The Li-S battery design will be able to achieve gravimetric and volumetric energy densities of  $\geq 800$  Wh/kg and  $\geq 1000$  Wh/L, respectively.

**Project Impact.** The Li-S battery system is hampered by poor capacity retention, primarily caused by dissolution of polysulfide reaction intermediates in typical organic electrolytes, as well as poor electrical contact between insulating sulfur and the conductive carbon matrix. This project aims to produce a high-capacity, long-cycle-life Li-S battery system by using rational molecular design strategies to address each capacity loss mechanism directly. A long-cycle-life Li-S battery system capable of doubling Li-ion energy density would enable production of lighter, longer range EVs at a cost that is affordable to the average U. S. household.

**Approach.** The team will develop Li-S coin cells that utilize self-healing, interpenetrated ionomer gel electrolytes in both the cathode and separator. The team will synthesize necessary starting materials and fabricate components of these gels while testing their relevant electrochemical and mechanical properties. All components are combined into interpenetrating structures, which are being tested both alone and in cell configurations. Device performance data were collected and used to further optimize designs of both material and cell, culminating in an optimized Li-S battery design capable of doubling the energy density of traditional Li-ion batteries. The team has focused on (1) design and synthesis of various precursors for gel electrolytes, (2) fabrication and testing of both reference materials and novel materials made from these precursors, and (3) iterative validation and improvement of design principles through both materials and device testing.

**Out-Year Goals.** Work will progress toward developing structure-property relationships for the self-healing, interpenetrated gel ionomer electrolyte and its individual components, as well as successful incorporation of such an electrolyte into a working Li-S cell. The team plans to demonstrate significant improvements in both capacity and retention when using the project's developed materials, as compared to state-of-the-art reference systems.

**Collaborations.** This project funds work at UW. Dr. A. Jen, principal investigator (PI), focuses on design, synthesis, and testing of novel materials, as well as device-based verification of design principles. Dr. J. Yang (co-PI) focuses on optimizing device fabrication and testing, as well as investigating failure mechanisms in devices using novel materials. Pacific Northwest National Laboratory (PNNL) facilities are used for detailed material characterization study.

### Milestones

1. Provide detailed cell performance data for concept cells containing currently best materials designs, which should meet, or nearly meet, performance targets. (Q4, FY 2019; Completed)
2. Provide test cells for performance evaluation at a designated DOE testing laboratory: 12 baseline cells or half cells with a minimum capacity of 10 mAh, and 12 improved cells or half cells with a minimum capacity of 10 mAh. (Q1, FY 2020; Completed)
3. Suggest test procedures for the cells/half-cells evaluation. This should include discharge/charge voltage and current limits, number of test sequences, recommended cycling temperature, or other relevant test conditions as appropriate. (Q1, FY 2020; Completed)

## Progress Report

**Self-Healing Polymer Binders for S/C Composite Cathodes.** Previously, the team demonstrated physical integration of S/C cathode with PENDI-350 as a binder blended with PEO showing improved performance. As shown in Figure 3a, they have fabricated test cells with S/C cathode using PENDI-350/PEO (weight ratio = 3:1) as binder with sulfur loading of  $3.71 \text{ mgS/cm}^2$ . It shows that the cell capacity remains at  $718 \text{ mAh/g}$  after 100 cycles at 1C. The capacity retention was as high as 96% (based on the 10<sup>th</sup> cycle with capacity of  $750 \text{ mAh/g}$ ). The team attributes this improved capacity retention to the flexibility of long-chain PEO ( $M_w = 1000 \text{ K}$ ) as well as its good compatibility with PENDI-350 resulting in well dispersed polymer blends.

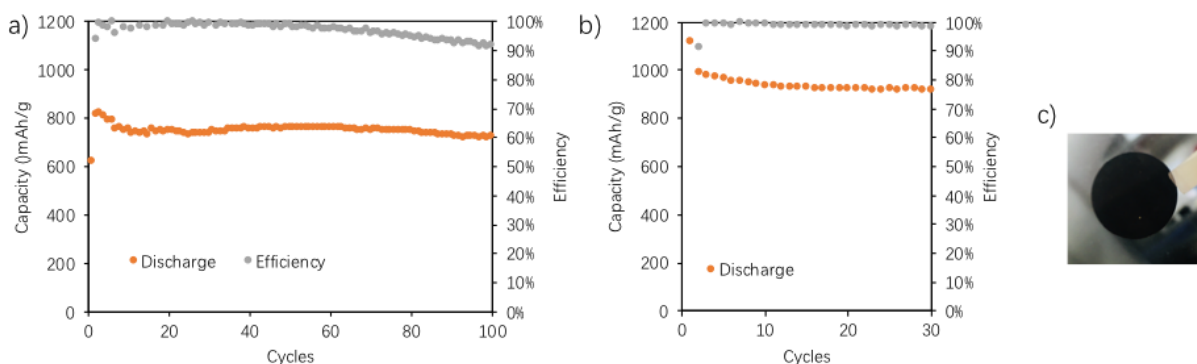


**Figure 3.** Cycling performances of cells with sulfur cathodes with (a) PENDI-350 / polyethylene oxide (PEO) as binder ( $3.71 \text{ mgS/cm}^2$ ) and (b) PENDI-350/triPy/PEO (PPP) as binder ( $2.91 \text{ mgS/cm}^2$ ). All cells were cycled with C rate of C/10 in the first 5 cycles and then 1C in the remaining cycles. (c) Image of sulfur cathode using PPP as binder ( $5.04 \text{ mgS/cm}^2$ ).

Despite excellent cycling stability, the cathode capacity needs additional improvement for practical application. An effective way to improve cathode capacity is to cast the slurry with greater thickness. However, thicker cathode can suffer from cracking issues due to increased volume expansion stresses during the cycles. To further improve the mechanical properties, the team has prepared composite binders with tri-Pyrene (Py) cross-linker with PENDI-350 based on quadrupolar aromatic pi-pi interactions between NDI and Py units in the cross-linker. In the PENDI-350/triPy/PEO (PPP binder) the flexible PEO chains could form interpenetrating network structures. As shown in Figure 3b, test cells with S/C cathode with a PPP (PENDI-350:triPy:PEO = 3:2:1 by weight) binder was fabricated with sulfur loading of  $2.91 \text{ mgS/cm}^2$ . The capacity remains around  $918 \text{ mAh/g}$  after 30 cycles, with relative capacity retention of 97% (based on 6<sup>th</sup> cycle with capacity of  $954 \text{ mAh/g}$ ). As shown in Figure 3c, the team has also fabricated Li-S cells with the S/C cathode with relatively high loading of  $5.04 \text{ mgS/cm}^2$  without cracking. However, the discharge capacity of the high loading cell can suddenly drop after 10 cycles, which may due to partial dissolution of the cross-linker tri-Py into the organic electrolyte. As shown in Figure 4a, when the cathode was immersed in organic electrolyte for 48 hours, the cathode with PPP binder tends to break into pieces. Significant volume expansion stress during cycling would accelerate the dissociation of NDI and Py units.

Finally, the team has designed and optimized the composites of PENDI-350/PEO/PVDF (PPPVDF) as binder for deliverable cells, possessing the following advantages: (1) the PENDI-350 impedes the diffusion of long-chain lithium polysulfides (LiPS) via electrostatic trapping and redox mediation of NDI units; (2) PVDF helps to improve the film forming property of the binder system; (3) long-chain PEO improves electrolyte wettability and compatibility between PVDF and PENDI-350. Consequently, sulfur loading higher than  $6 \text{ mgS/cm}^2$  was achieved by using S/MJ430 (weight ratio = 7:3) as C/S composite. Compared with PPP, cathode with the PPPVDF binder remains intact even after immersion in organic electrolyte (Figure 4b). Composition of optimized PPPVDF binder used in the deliverable cells is a composite of PENDI-350:PEO:PVDF = 2:1:1 in weight ratio. Test cells with sulfur loading of  $4.2 \text{ mgS/cm}^2$  were fabricated. The specific discharge capacity stabilized in a low level of around  $700 \text{ mAh/g}$  (Figure 4c), which implies low sulfur utilization. Overall, the

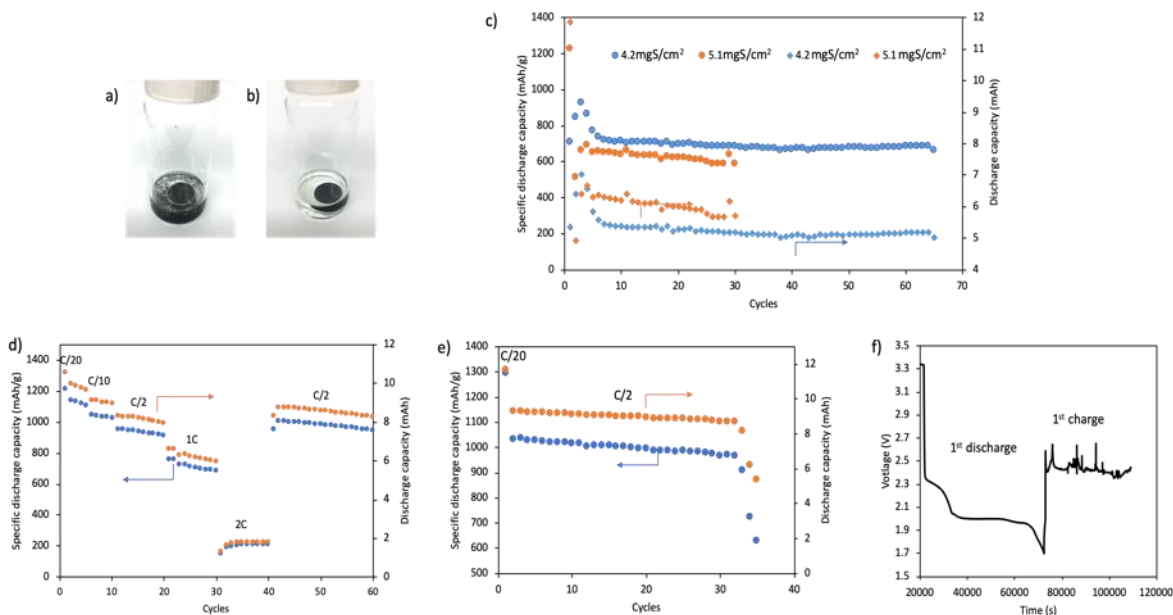


**Figure 4.** (a) Cathode with PPP binder immersed in organic electrolyte after 48 hours. (b) Cathode with PPPVDF binder immersed in organic electrolyte after 48 hours. (c) Cycling performances of cathodes with PPPVDF binder at different sulfur loading (the cells were cycled at C/20 rate at 1<sup>st</sup> cycle and C/2 at remaining cycles). (d) Cycling performances of cathodes with PPPVDF at different C rate (4.4 mgS/cm<sup>2</sup>). (e) Cycling performances of cathodes with PPPVDF with -SH surface modified carbon. (f) The first discharge (at C/20 rate) and first charge (at C/2) performance of cathode with PVDF as binder.

cells possess high capacity retention of 93% (from 10<sup>th</sup> cycle to 65<sup>th</sup> cycle). The utilization of sulfur on the 10<sup>th</sup> cycle is lower than 50%. The specific capacity drops further after increasing the sulfur loading amount to 5.1 mgS/cm<sup>2</sup>. A thicker cathode composite layer could encumber the diffusion of electrolyte. Meanwhile, the insulating short-chain LiPS formed during cycling may block the pores of mesoporous carbon and result in decrease of conductive surface. Therefore, the team has employed two additional strategies to resolve the poor ion and electron conductivity issues at higher sulfur loading. First, they modified the surface of mesoporous carbon (MJ430) with -SH (thiol) functional groups. The polar, surface thiol groups resulted in improved wetting of the electrode surface by the electrolyte due to the dipole-dipole interaction of the thiol groups with lithium ion in the electrolyte. Second, the weight ratio of S/C composite was adjusted from 70% to about 60%. Higher ratio of conductive mesoporous carbon would improve the conductive surface area and mitigate the blocking effect of insulating short-chain LiPS. As shown in Figure 4d, the resulting cell was tested under different C rates. The cathode capacity is close to 10 mAh at C/20 rate. The specific discharge capacity is around 945 mAh/g even after 60 cycles at C/2 rate. Capacity retention higher than 90% was achieved when the cell was cycled at a C/2 rate, as compared to the capacity at C/10. As shown in Figure 4e, at C/2 rate the cathode discharge capacity (C/20) is higher than 11 mAh in the first cycle. Even at C/2 rate, the cathode capacity remains at 8.7 mAh after 30 cycles. Meanwhile, the cathode capacity remains high with specific discharge capacity of 967 mAh/g after 30 cycles. However, the cell failed suddenly after around 35 cycles. The team attributes this to the failure of anode side. In the control cells using PVDF as a binder, the cells fail quickly due to shuttle effect, especially for cells with higher sulfur loading. Figure 4f shows the voltage profile of PVDF cathode with sulfur loading of ~ 5.5 mgS/cm<sup>2</sup>. The cells failed in the first charge cycle due to lack of LiPS trapping ability, demonstrating typical shuttle effect.

## Patents/Publications/Presentations

### Publications

- Lin, F. “Design and Synthesis of Organic Functional Materials for Energy Conversion and Storage Applications.” Ph.D. Thesis. University of Washington, Seattle, WA (September 2019).
- Hubble, D. “From Solvate to Cell: A Molecular Engineering Approach to the Li-S Battery.” Ph.D. Thesis. University of Washington, Seattle, WA (November 2019).

### Presentations

- University of Washington, Seattle, Washington (September 27, 2019): “Design and Synthesis of Organic Functional Materials for Energy Conversion and Storage Applications”; F. Lin. Dissertation defense.
- University of Washington, Seattle, Washington (November 22, 2019): “From Solvate to Cell: A Molecular Engineering Approach to the Li-S Battery”; D. Hubble. Dissertation defense.

## Task 1.3 – Dual Function Solid-State Battery with Self-Forming, Self-Healing Electrolyte and Separator (Esther Takeuchi, Stony Brook University)

**Project Objective.** The project objective is to demonstrate a solid-state rechargeable battery based on a Li-metal anode and iodine cathode with a self-forming, self-healing electrolyte and separator with high gravimetric and volumetric energy density.

**Project Impact.** This program will enable demonstration of the proposed rechargeable battery with improved power capability, high energy density, and a self-forming, self-healing SSE/separator. Technical insight will be gained regarding improved conductivity of the solid LiI based electrolyte, power capability of the proposed system, the self-healing nature of the LiI layer, the nature of the electrode-electrolyte interfaces, and feasibility of the system to reach the DOE targets.

**Approach.** The proposed concept is a dual function rechargeable SSB utilizing LiI combined with silver iodide (AgI) as the electrolyte, with lithium metal (and small quantities of silver metal) as the anode and iodine as the cathode and with a self-forming, self-healing separator/electrolyte. The battery will be assembled in the discharged state, where the anode and cathode will be created during the first formation (charge) step. Initially, silver ion ( $\text{Ag}^+$ ) will diffuse toward the negative electrode and be reduced to silver metal ( $\text{Ag}^0$ ), and iodine ion ( $\text{I}^-$ ) will be oxidized to elemental iodine ( $\text{I}_2$ ) at the cathode side. As the formation of the battery continues, lithium ion ( $\text{Li}^+$ ) will form a Li-metal layer at the anode, with generation of iodine at the cathode. LiI will remain and serve as both the separator and electrolyte.

**Out-Year Goals.** This is a multi-year program where the effort is divided into three major tasks.

- Year 1 involves electrolyte preparation and characterization including preparation of SSEs and conductivity measurements.
- Year 2 will focus on cell construction and testing including both *in situ* and *ex situ* analysis.
- Year 3 will focus on cell characterization. Under the program, cycle life, efficiency, energy density, and the functional capacity of cells will be determined.

**Collaborations.** This project collaborates with A. Marschilok and K. Takeuchi of SBU.

### Milestones

1. Determine cycling performance at elevated temperature. (Q1, FY 2020; Completed)
2. Determine behavior of conductivity as a function of temperature to determine resistance as well as fundamental thermodynamic parameters of the SSEs. (Q2, FY 2020)
3. Conduct destructive analysis of tested cells. (Q3, FY 2020)
4. Perform extended cycle life testing. (Q4, FY 2020)

## Progress Report

### Particle Size Analysis of New Electrolyte Process

Mean particle size diameter was determined with imageJ analysis of scanning electron microscopy (SEM) images of the individual powders on silicon wafers. Particle diameter decreases by more than half with further processing, going from  $5.56 \pm 1.74 \mu\text{m}^2$  to  $2.09 \pm 0.23 \mu\text{m}^2$  for the Control and Process III samples, respectively. Furthermore, processing reduces the standard deviation one order of magnitude, indicating a more uniform size. The median value for each sample is approximately the same as the mean, indicating there are not a significant number of outliers (Figure 5).

### Impact of the New Electrolyte Process on Cycling

Prior to cycling, all cells were charged to form the initial battery. Electrochemical cycling measurements were carried out on the Control and Process(es) I, II, and III, with the first galvanostatic charge (formation) and discharge voltage profile shown in Figure 6. During discharge, modified processing of the electrolyte material increases the voltage of the discharge plateau, indicating significantly reduced polarization in the cells. Less polarization allowed the cells to discharge longer, increasing from 1.2 h to 4.5 h under the same current density. These results affirm an improvement in cell kinetics with decreasing particle size. Similarly, the charge profile exhibits a lower voltage plateau with increased processing, also indicating less polarization. Clearly, the modified processing approaches aid in the formation of lithium metal at the anode and formation of the iodine cathode as well as lower overall impedance for the cells. Interestingly, the charging profile of the Control exhibits intermittent shorting behavior, as evidenced by the sharp drops in voltage and subsequent quick recovery. Despite these microsecond long shorts, the Control cell is able to recover and continue with charging successfully. Overall, the processed sample (Process III) displays the best electrochemical response of the group.

### Impact of Electrode Interface Modification on Electrochemistry

The electrochemical performance of Process III was further expanded with a study on the negative and positive electrode interfaces. Three variations were examined: (1) Interface A with no alteration to the interfaces, (2) Interface B with negative electrode interface modification, and (3) Interface C with negative and positive interface modification. ASSBs can exhibit performance loss due to interfacial issues resulting from inappropriate pore size, high tortuosity, and volume expansion/contraction resulting in loss of contact between active material, electrolyte, and current collector. Ionic conductivity can be significantly impacted, and thus the cells were tested with electrochemical impedance spectroscopy (EIS). The results revealed that further processing of the electrolyte indeed induced a decrease in the impedance of the pristine cells (Figure 7). Before charging (Figure 7a), the following trend in impedance emerges where Interface A > Interface C > Interface B. Interestingly, Interface C does not exhibit the typical diffusional tail, which is observed in both Interface A and

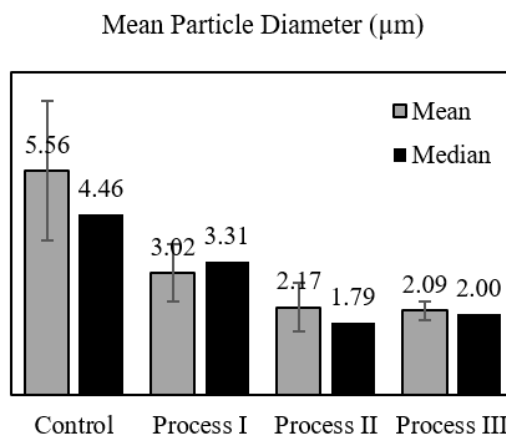


Figure 5. Mean Lil particle diameter with standard deviation for the three new electrolyte processes compared to the control.

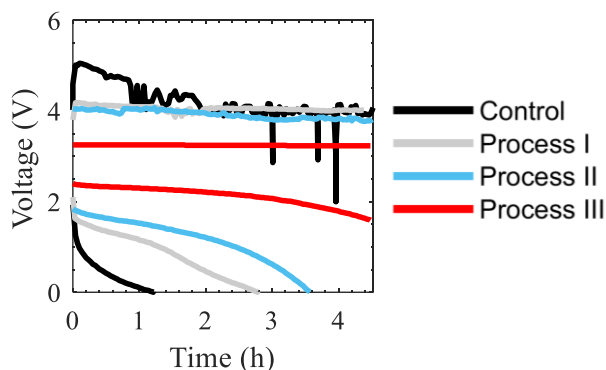


Figure 6. Comparison of the first cycle galvanostatic profiles for the new electrolyte process(es).

Interface B. The impedance spectra of Interface A reveal that, at intermediate frequencies, the impedance does not intersect the real axis as it does for both B and C designs. This may occur due to poor contact between the SSE and the current collectors used for EIS measurement, indicating that modifying the negative and positive electrode interfaces significantly improves contact with the current collectors. On charging to as little as 0.5% of the theoretical capacity, all cells show an order of magnitude decrease in impedance (Figure 7b), consistent with the formation of a more conductive  $\text{Li}^0$  layer at the negative electrode interface. Interestingly, Interface C exhibits two distinct flattened semicircles, consistent with the formation of two distinct electrodes. Modification of both interfaces aids in formation of both electrodes and further acts to stabilize this configuration.

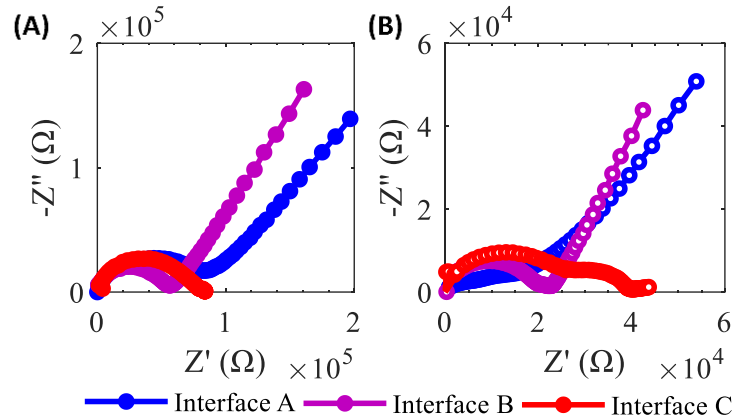


Figure 7. Electrochemical impedance spectroscopy of the Process III composite  $\text{LiI}$  with  $\text{LiI}(\text{3-hydroxypropionitrile})_2$  cells in cell configuration SS, Li, and Li+CNT before initial charge (a) and after charging to 0.5% of the theoretical capacity (b).

As mentioned for the new electrolyte processed cells above, all cells were charged to form the battery before testing.

Electrochemical cycling measurements were carried out on Interfaces A, B, and C, with the first galvanostatic voltage profile shown in Figure 8. During discharge, Interface C reaches a higher discharge loaded voltage at 2.6 V compared to 2.3 V reached by Interfaces A and B. This trend in polarization holds true for the subsequent charge as well, with Interface C having the lowest charge potential, followed by Interface B, and then Interface A. Additionally, at the start of charge, both B and C have a lower overpotential than A by  $\sim 0.25$  V, as indicated by the black arrow (Figure 8). The modification to the negative electrode was the same for both cells, indicating that more facile Li-metal plating is exhibited with this modification.

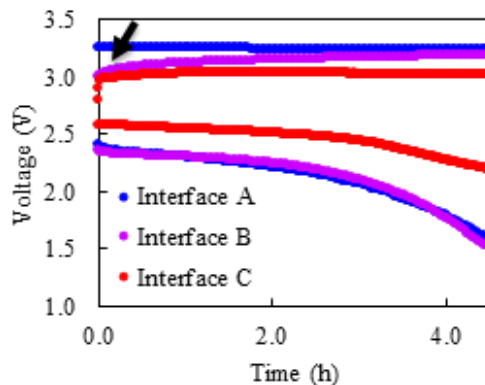


Figure 8. Comparison of the first-cycle galvanostatic profiles for the electrode interface modification. Arrow indicates drop in polarization.

temperatures stabilizing the current collector–electrode interface as well as increasing the conductivity of the solid electrolyte.

### Impact of Elevated Temperature on Impedance

As shown in Figure 9a, impedance measurements were carried out on cell type B I prior to charging, after charging, and when fully discharged after cycling at  $30^\circ\text{C}$  and  $40^\circ\text{C}$ . There is an observed increase in the loaded voltage at  $40^\circ\text{C}$  resulting from a decrease in cell polarization. Elevated temperatures increase mobility of the ion in the SSE. As temperature is increased, a precipitous decrease in impedance is observed. In general, an initial increase in temperature ( $30 > 40^\circ\text{C}$ ) by ten degrees produced an approximately five-fold decrease in impedance. A further  $10^\circ$  increase in temperature results in at least a ten-fold reduction in impedance. The decrease in impedance with rising temperatures has been attributed to the elevated

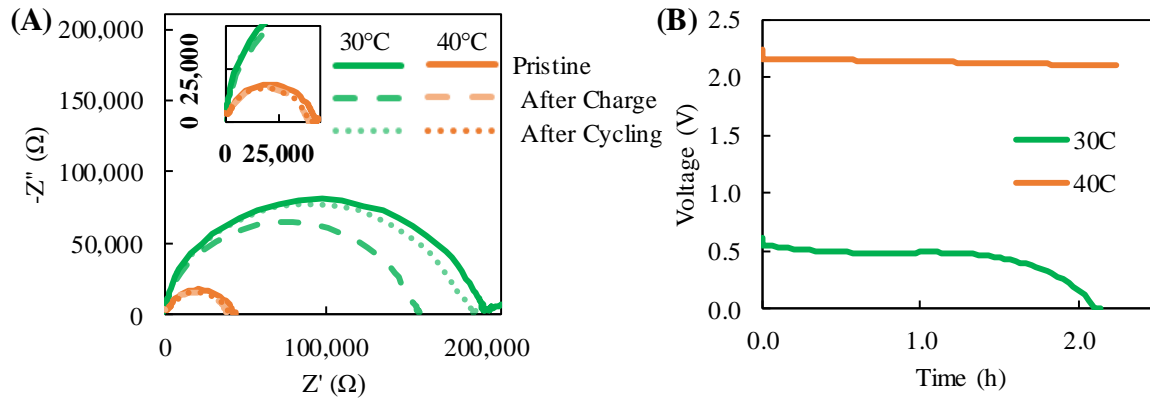


Figure 9. Comparison of the electrochemical response of cell type B I under 30°C and 40°C. (a) Galvanostatic discharge profile. (b) Electrochemical impedance spectroscopy as a function of temperature.

### Patents/Publications/Presentations

The project has no patents, publications, or presentations to report this quarter.

## Task 1.4 – Characterization and Modeling of Li-Metal Batteries: Characterization of Li<sup>+</sup> Transport in Polyelectrolytes (Bryan D. McCloskey, University of California at Berkeley)

**Project Objective.** This task aims to understand lithium plating and stripping in non-traditional electrolyte systems (specifically, polyelectrolyte solutions and concentrated binary salt electrolytes) that have been proposed to reduce dendrite formation during lithium stripping and plating due to their high Li<sup>+</sup> transference numbers ( $t_+$ ). The team will develop capabilities that allow them to understand how ion dynamics in these electrolytes impact macroscale transport properties and Li-metal plating and stripping.

**Impact.** Ultimately, this task will develop an understanding of how electrolyte composition and molecular interactions can be manipulated to positively impact ion transport of potential electrolytes for Li-metal batteries. This will provide a set of general design rules for novel electrolytes that enable stable, efficient high capacity Li-metal stripping and plating.

**Approach.** To understand various aspects of lithium plating and ion transport in these systems, the team will develop novel diagnostic and computational modeling techniques. Model polyelectrolytes, with pendant triflimide anions, will be used as polyanions, as their properties can be easily tuned via changes in the polymerization chemistry. Solution parameters that can be varied for both polyelectrolyte solutions and concentrated electrolytes include solvent and salt composition, additive inclusion, and the aforementioned polymer properties, all of which can have a profound impact on electrostatic interactions between charged species in solution, as well as interfacial stability and reaction kinetics of the lithium electrode. The team will develop capabilities that allow them to understand how molecular-level ion dynamics in these electrolytes impact macroscale transport properties and Li-metal plating and stripping. These computational simulations will be validated and refined by comparing results to experimentally measured transport properties of these electrolytes. They will optimize electrochemical methods for these electrolytes to evaluate relevant transport properties under the Newman Concentrated Solution Theory framework, which has never been performed on these non-traditional electrolytes. <sup>1</sup>H and <sup>19</sup>F NMR diffusometry will also be used to measure single-ion self diffusion coefficients without an applied electric field; solution viscosity measurements using a state-of-the-art rotating sphere viscometer can be performed under entirely air/water-free conditions. The team will develop capabilities to quantitatively understand degradation mechanisms of various electrolytes during Li-metal stripping and plating. Specifically, differential electrochemical MS will be used to study outgassing that occurs from electrolyte degradation processes.

**Out-Year Goals.** The ultimate goal of this project is to understand the influence of electrolytes with novel transport characteristics on the performance of Li-metal electrodes. Work will continue to build toward a complete understanding of Li-ion and counterion transport in polyelectrolyte solutions and concentrated electrolytes, as well as the impact of electrolyte transport properties on Li-metal uniformity during electrochemical stripping and plating. Outgassing measurements using differential electrochemical MS will be developed to further probe the interfacial reactivity of lithium metal with electrolytes created in this project.

**Collaborations.** Collaborators on this project include K. Persson (atomistic and coarse-grained modeling) at LBNL and Nitash Balsara (electrochemical characterization of polymer electrolytes) at LBNL

### Milestones

1. Complete study of solvent influence of transport in polysulfone-based polyelectrolyte solutions. (Q1, FY 2020; Completed)
2. Complete development and validation (using known liquid electrolytes) of electrochemical transport methods. (Q2, FY 2020)

- Complete synthesis and transport characterization of model triflimide-based polyion (pTFSI) solutions in symmetric cells with Li-metal electrodes. (Q3, FY 2020)
- Complete development of coarse-grained polyelectrolyte model to study the effect of polyelectrolyte composition on transport of model polyelectrolyte systems. Progress measure: publish an article describing scaling of transport properties of polyelectrolyte solutions as a function of polymer and solvent properties. (Q4, FY 2020)

## Progress Report

In prior quarters, the team showed that Li<sup>+</sup>-bearing polyelectrolyte solutions can achieve high conductivities and Li<sup>+</sup> transference numbers when the Li<sup>+</sup> is well-dissociated from the polymer-appended anions. Good dissociation was only observed in strong Lewis basic nonaqueous solvents that were inadequate for use in batteries (for example, DMSO). To further understand the role of solvent-backbone and solvent-ion interactions in the ultimate ion-transport properties of polyelectrolyte solutions, the team studied the conductivity, viscosity, and diffusion of model polysulfone-based polyelectrolyte solutions in DMSO and water. In both solvents, the polyion, sulfonated polysulfone, is readily soluble and the charged group is known to dissociate, but the neutral backbone polymer is only soluble in DMSO. The team observed marked differences in the transport behavior of polymer solutions prepared from the two solvents, particularly at high concentrations. Comparing this transport behavior to that of the monomer in solution demonstrates a larger decrease in lithium motion in DMSO than in water, even though the bulk viscosity in water increases far more rapidly. The team found that the combination of poor backbone solvation with good ionic moiety solvation allowed improved ion dissociation, while reducing polyanion mobility for polyelectrolyte solutions in water. This study suggests that tuning polymer backbone chemistry and therefore backbone-solvent interactions could help increase  $t_+$  without sacrificing ionic conductivity. These results were published in the article listed in the following Publications section. The team plans to further investigate these properties in the triflimide-based styrene and acrylate ionomer systems synthesized in previous quarters in battery-relevant solvent blends.

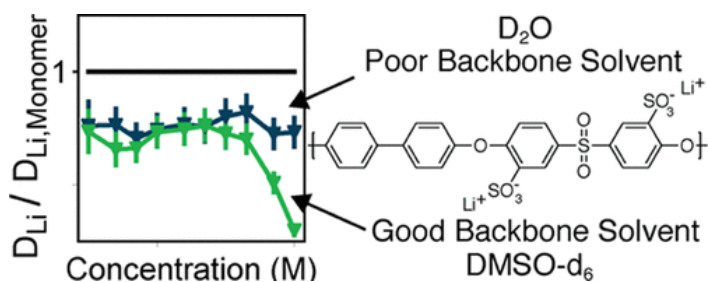


**Figure 10.** Diffusion coefficient of Li<sup>+</sup> as measured via nuclear magnetic resonance normalized to the monomer diffusion coefficient of sulfonated polysulfone polyions in two different solvent systems: DMSO and water. In DMSO where the backbone is well solvated, diffusion coefficients drop rapidly at high concentration, whereas this trend is not observed for the aqueous solutions where the polymer backbone is poorly solvated.

and non-ideal concentrated solution transference number measurements via the Balsara-Newman method originally developed for polymer and glyme electrolytes. LiPF<sub>6</sub> in EC:EMC (3:7 w/w) was chosen as a benchmark due to availability of data on this electrolyte from Hittorf method. The team performed full transport property measurements consisting of concentration cell measurements to measure the open circuit potential as a function of solution concentration ( $\frac{dU}{d\ln(m)}$ ), Bruce-Vincent steady state current measurements to capture ideal transference number ( $t_+^{id}$ ), restricted diffusion measurements (D), and conductivity measurements ( $\kappa$ ). The concentrated solution transference number ( $t_+^0$ ) and thermodynamic factor ( $1 + \frac{d\ln(\gamma_{\pm})}{d\ln(m)}$ ) were calculated according to Equations 1 and 2, respectively.

$$t_+^0 = 1 - \sqrt{\frac{\frac{F^2 D \tau c}{\nu \kappa R T} \left( \frac{1}{t_+^{id}} - 1 \right)}{1 + \frac{d \ln(\gamma_{\pm})}{d \ln(m)}}} \quad \text{Equation 1}$$

$$1 + \frac{d \ln(\gamma_{\pm})}{d \ln(m)} = \frac{\kappa \nu^+ z^+}{\nu R T D \tau c \left( \frac{1}{t_+^{id}} - 1 \right)} \left( \frac{dU}{d \ln(m)} \right)^2 \quad \text{Equation 2}$$

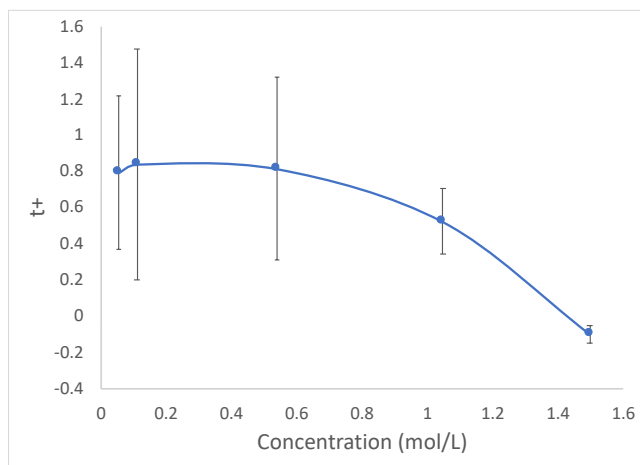


Figure 11. Li<sup>+</sup> transference number as measured by the Balsara-Newman method for LiPF<sub>6</sub> in EC:EMC (3:7 w/w). Error bars represent  $\pm 1$  standard deviation.

From Figure 11, there is significant uncertainty in the measurement, with an average uncertainty of 55% for solutions ranging in concentration from 0.05-1.5 M. The team is working on a full sensitivity analysis, but initial results show that the analysis is extremely sensitive to fitting of concentration cell data as well as diffusion coefficient data. The team aims to improve both fits by collecting more data points across the concentration range of interest. Furthermore, these issues are exacerbated by the instability of the Li-metal electrode in carbonate solutions, leading to large cell-to-cell variability in interfacial resistance. The team is testing lithium treatment methods, including electrode pressing and melting, to lower cell-to-cell variability. The team notes that the transference numbers obtained via the Balsara-Newman method differ significantly from those reported from the Hittorf method for LiPF<sub>6</sub> in

EC:EMC, where  $t_+^0$  is typically on the order of 0.3-0.4 across a broad range of concentrations. The team is still investigating the source of these deviations, although they have observed that the value of  $t_+^0$  is easily shifted depending on the fitting of concentration cell data. Next quarter, the team will focus on completing sensitivity analysis of the Balsara-Newman method for measuring standard liquid electrolytes as well as exploring other low-volume methods for measuring full transport properties of liquid electrolytes.

## Patents/Publications/Presentations

### Publication

- Diederichsen, K. M., R. C. Terrell, and B. D. McCloskey. “Counterion Transport and Transference Number in Aqueous and Nonaqueous Short-Chain Polyelectrolyte Solutions.” *Journal of Physical Chemistry B* 123 (2019): 10858–10867.

### Presentations

- American Institute of Chemical Engineers (AIChE) Annual Meeting, Orlando, Florida (November 10–15, 2019): “Influence of Backbone Solvation on Polyelectrolyte Solution Transport Properties”; Kyle Diederichsen.
- AIChE Annual Meeting, Orlando, Florida (November 10–15, 2019): “Charge Transport in Nonaqueous Polyelectrolyte Solutions for Li-Ion Batteries: Ion-Ion Correlations and the True Transference Number from Molecular Dynamics Simulations”; Kara Fong.

## Task 1.5 – Advanced Polymer Materials for Batteries (Zhenan Bao and Yi Cui, Stanford University)

**Project Objective.** This project will develop new polymer materials for batteries. The team will develop polymer coatings with specific mechanical properties that can accommodate the volume expansion and contraction of the Li-metal anode associated with deposition and stripping (charging and discharging).

**Project Impact.** The cycling stability and CE of Li-metal electrodes will be increased by implementation of a polymer-based protective layer that functions as an artificial SEI with desired properties. The improved performance will enable further development toward practical utilization of Li-metal anodes with higher cycling efficiency and less susceptibility to dendrite-based failure.

**Approach.** The project uses soft polymer coatings with dynamic crosslinking to give the resulting polymers liquid-like rheological properties and stretchable and self-healing properties. In previous work, the project has shown that such coatings resulted in uniform deposition/stripping of lithium metal and improved cycling stability of Li-metal electrodes. To understand the design rules for effective polymer coatings, the team chose a few representative polymers to systematically understand structure property relationships. Here, the team investigates the correlation between surface energy of the polymer and exchange current for lithium deposition.

**Out-Year Goals.** Work will progress toward the correlation between dielectric constant and exchange current. These findings will enable further understanding and development of various polymer coatings for protecting Li-metal anodes.

**Collaborations.** This quarter, the team is collaborating with J. Qin at Stanford University.

### Milestones

1. Analyze the solvation structure and lithium diffusivity of polymer/electrolyte using NMR, FTIR, electrochemical tests, and molecular simulations. (Q1, FY 2020; Completed)
2. Evaluate the polymer basic cycling performance: 0.5 and 1 mA/cm<sup>2</sup> conditions in Li|Li and Li|Cu cells using carbonate electrolyte. (Q2, FY 2020; In progress)
3. Self-healing polymer coated Li||NMC battery: Stable cycling at C/3 rate for 150 cycles using 15  $\mu$ l/mAh electrolyte. (Q3, FY 2020)
4. Self-healing polymer coated Li||NMC battery: Stable cycling at C/3 rate for at least 50 cycles using 50  $\mu$ m lithium. (Q4, FY 2020)

## Progress Report

Li-metal anode suffers from several instabilities during electrodeposition process in battery charging. Specifically, lithium deposition leads to inhomogeneous coverage on the electrode substrate, resulting in concentration of electric field at the tip of these deposits and ultimately resulting in dendritic growth that shorts the battery. The high surface area metal deposition also causes faster parasitic reactions between the lithium metal and organic electrolyte that is responsible for the rapid fade of battery capacity. According to a conventional understanding, the primary sources of instabilities in electrodeposition are diffusion limitations in ion transport processes, both in the bulk electrolyte and at the electrode-electrolyte interfaces. Consequently, many theoretical efforts have been focused on modeling dendritic growth in a purely diffusion limited condition by varying transport properties such as ion conductivity and relative mobility of anions and cations (transference number) and on studying their effect on electrolyte modulus or electrode geometry. Likewise, several experimental efforts have reported improved electrodeposition stability with electrolytes with high transference number, conductivity, or modulus. While ion transport and mechanics are important determinants of morphological evolution of the metal electrode, other coupled parameters such as electrochemical kinetics and electrostatic potential landscape can play a critical role. For example, several experimental findings have reported observation of fractal structures during electrodeposition of metallic lithium, even at rates much below the diffusion limited current density. This further indicates that transport parameters in the electrolyte may not be the sole determinant of morphological stability. The relative effect of electrochemical kinetics and ion transport is particularly important, considering the metal electrode does not have a smooth surface, which is aggravated even at earlier stages of deposition. The physical perturbations on the metal surface result in abrupt enhancement of local electric field, causing the ions to be preferentially directed toward the dendritic tips and ultimately leading to unstable growth. In addition, a major challenge in understanding this phenomenon is the fact that the transport and kinetics essentially rely on the same physical factors as ion concentration, viscosity, and temperature, among others. Here, the team leverages ultrafast scanning voltammetry and pulse-field gradient NMR to decouple the effects of kinetics and transport, respectively. Based on these analyses, they are designing a polymer interface that stabilizes electrodeposition by maintaining a uniform ion flux to the electrode. Subsequently, they intend to utilize the polymer interface to improve Li-metal battery cycling, both in Li||Cu and Li||NMC configurations.

### Molecular Simulations of Electrodeposition

In collaboration with the group of J. Qin at Stanford, the team used a 3D coarse-grained Brownian dynamics model of lithium deposition under an applied voltage to understand the effect of the Damköhler Number ( $Da$ ) on lithium morphology. This model accounts for both diffusive motion and drift driven by the electric field. The potential field is solved at every time step using the Poisson equation, with boundary conditions defined by positions of the existing lithium deposits, to accurately represent the effect of lithium morphology on the local electric field. When lithium cations contact a Li-metal surface or the current collector, they have a probability  $p$  of depositing. This is analogous to the exchange current density for the reaction ( $i_0$ ). In the limit of fast kinetics,  $p = 1$ , growth is extremely dendritic and porous (Figure 12). This is due to the electrostatic forces attracting ions to growing lithium tips. The uniformity of the deposits can be quantified by the ratio of deposited volume of lithium within the control volume to ideal close-packing for the same volume, defined as the normalized density. In the case of slow kinetics or low  $Da$ , growth is uniform, dense, and non-dendritic. Lithium is initially attracted to dendritic tips, but diffuses away before the reaction occurs, leading to randomized deposition. The rate of lithium deposition decreases at low  $Da$ , as expected. Therefore, decreasing  $Da$  can lead to more uniform lithium deposition at the cost of a lower charging rate for the same applied potential.

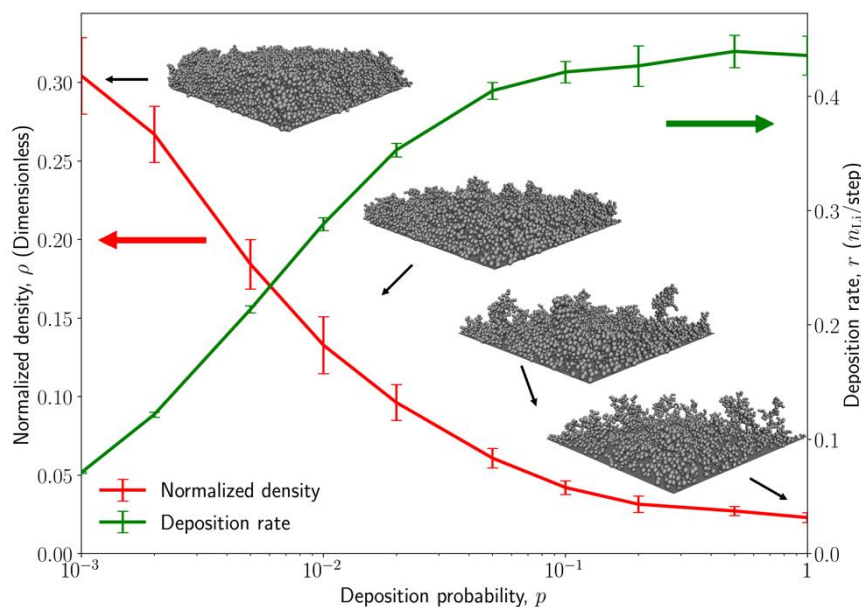
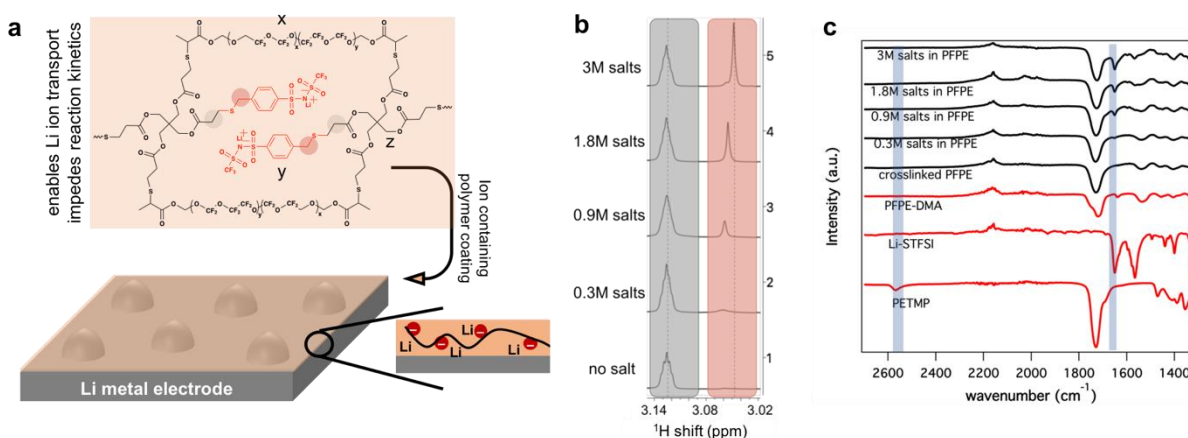


Figure 12. Molecular dynamics simulations showing relationship between the rate and morphology with the deposition probability.

## Polymer Coating Design

On the basis of the aforementioned theoretical understanding, the team proposes a design strategy to stabilize lithium electrodeposition, without significantly altering battery chemistry or architecture. Here, they incorporate a polymer interface based on crosslinked ionic networks between electrode and electrolyte. An ideal polymer interface is hypothesized to have the following characteristics: (1) chemically inert and unsusceptible to degradation by side reactions with lithium metal, (2) insoluble and chemically resistant liquid electrolyte accessibility to the metal electrode, (3) unhindered transport channels to facilitate high interfacial conductivity, and (4) regulated uniform charge transport on the electrode surface. The chemical design of the polymer network is shown in Figure 13a. Specifically, PFPE-DMA is used as polymer network backbone, PETMP as the crosslinker, and Li-STFSI as salt linker in different ratios. The PFPE polymer is known to be highly resistive to chemical corrosions, while the salt molecules are incorporated to facilitate ion transport. The variation in the salt content in the polymer is characterized using NMR and infrared spectroscopy (Fourier transform infrared, or FTIR). Figure 13b shows the varying  $^1\text{H}$  NMR peak intensities of the polymers for the specific methyl groups labeled in Figure 13a, where it is seen that as linkable Li-STFSI is increased in the feed, the immobilized salt content in the polymer network is progressively higher. The team further analyzed the IR-spectra of the ionic polymer networks as shown in Figure 13c, where they observe that on crosslinking, the representing vibrational mode of the thiol group ( $-\text{SH}$ ) at  $2550\text{ cm}^{-1}$  disappears for all the polymers synthesized here; thus, they can conclusively say that all the PETMP linkers are reacted. Also, the vibration modes of the double bonds ( $1650\text{ cm}^{-1}$ ) in the styrene molecule present in the Li-STFSI monomers were compared for different cases, and it is confirmed that increasing the Li-STFSI in the feed indeed leads to stronger intensity of this peak. Thus, the team is able to systematically vary the immobilized salt content in the polymer network that can ultimately lead to fundamental understanding of the effect of ionic polymers in stabilizing electrodeposition.



**Figure 13.** (a) Schematic showing the structure of ionic polymer coated on the Li-metal electrode. The ionic polymer comprises of x: PFPE-DMA backbone, y: PETMP crosslinker, and z: STFSI-Li salts. (b) Comparison of peak heights obtained from  $^1\text{H}$  nuclear magnetic resonance measurements showing the relative content of the methyl groups in the polymer backbone and the tethered anions (spectra referenced to residual protons in  $\text{CD}_3\text{OD}$ ). (c) Infrared spectroscopy measurements for polymer networks with varying salt content. The shaded region at  $2550\text{ cm}^{-1}$ , indicates the  $-\text{SH}$  group in PETMP, while at  $1650\text{ cm}^{-1}$  is for  $\text{C}=\text{C}$  bond in Li-STFSI.

### Ionic Properties of Polymer Coating

The Li-ion solvation environment and transport properties in these ionic polymer networks in presence of the solvent mixture ethylene carbonate/diethylene carbonate (EC/DEC) were analyzed using NMR. Figure 14a shows the  $^7\text{Li}$  NMR intensity profiles at different immobilized salt content. There are two important observations as the tethered salt content is varied: the peak intensity increases and also there is downfield (less-negative) shift. The progressive rise in the intensity indicates the increase in the tethered salt, while the downfield shift of  $^7\text{Li}$ -NMR peak implies a reduction of the solvation energy of lithium ions. This finding agrees with previous study that as the salt content is increased, the solvent molecules interact more with the anions rather than the lithium ions; thus, lithium experiences less ion pairing or a looser solvation shell. The team further measured self-diffusion characteristics of lithium and grafted STFSI ions. Figure 14b plots the Li-ion diffusivity in the left axis, measured using pulse-field gradient NMR, while the right axis reports the lithium transference number ( $t_{\text{Li}}$ ) for the corresponding ionic polymer networks. The lithium diffusivity across the different salt concentration is relatively high compared to the diffusivity values of lithium salts reported in the literature and also are similar for all concentrations measured in this study. For comparison, the lithium diffusivity using the same method for 1 M LiTFSI in EC / DEC is  $1.41 \times 10^{-6}\text{ cm}^2/\text{s}$ . Thus, it can be asserted that the Li-ion mobility in the ionic polymer network is similar to that of liquid electrolyte, which is essential to enable unhindered transport when used as polymer electrolyte or as electrode coating. The lithium transference number in Figure 14b is calculated using a simple formula:  $t_{\text{Li}} = \frac{D_{\text{Li}}}{D_{\text{Li}} + D_{\text{F}}}$ , where  $D_{\text{Li}}, D_{\text{F}}$  are the diffusivities obtained from the pulse field gradient NMR measurements. Owing to immobilization of the STFSI anions, the  $t_{\text{Li}} > 0.5$  ( $\sim 0.7$ ) for all the polymer networks, as compared to  $t_{\text{Li}} = 0.49$  for the liquid electrolyte (1 M LiTFSI in EC/DEC). The higher transference number polymer electrolytes can essentially eliminate space charge formation due to ion polarization, even at relatively high current densities as reported by several theoretical and experimental studies.

The team utilized the synthesized ionic polymer networks as an interfacial layer on the Li-metal electrodes in a symmetric cell configuration and analyzed interfacial impedance using a bulk electrolyte, 1 M LiTFSI in EC/DEC. Figure 14c shows the Nyquist plots for various ionic polymer networks, while interfacial resistance values are plotted in Figure 14d for the corresponding measurements. The resistance value for the neat electrolyte (without any coating) is the lowest, as expected, while that of one with salt-free polymer coating is the highest. Specifically, the interfacial resistance increases by  $\sim 8$  times when the electrode is coated by the crosslinked PFPE layer ( $1\text{-}\mu\text{m}$  thickness), implying that the coating significantly blocks the liquid electrolyte

access to the metal electrode. The team recently reported that mass transport limiting polymer interfaces can prevent continuous side reactions between the bulk electrolyte and Li-metal electrode that caused capacity fade in reactive metal batteries. While it is important to prevent or limit electrolyte access to the lithium electrode, the electrode-electrolyte interface should maintain unperturbed ion transport. The design strategy of incorporating tethered salt molecules in the polymer networks is useful to enable high interfacial ion conduction. As seen in Figure 14d, interfacial resistance progressively decreases as salt content in the network increases; in fact, for the 3M salt containing polymer coatings, resistance is under twice that of the bare electrodes. As previously observed using NMR analysis, ionic polymer networks can maintain high Li-ion mobility, and thus the coatings facilitate transport from the bulk electrolyte to the lithium electrode without significantly contributing to interfacial resistance. Next quarter, the team will analyze electrochemical properties such as the exchange current density of these coatings as well as applicability in suppressing side-reactions and dendrites during electrodeposition.

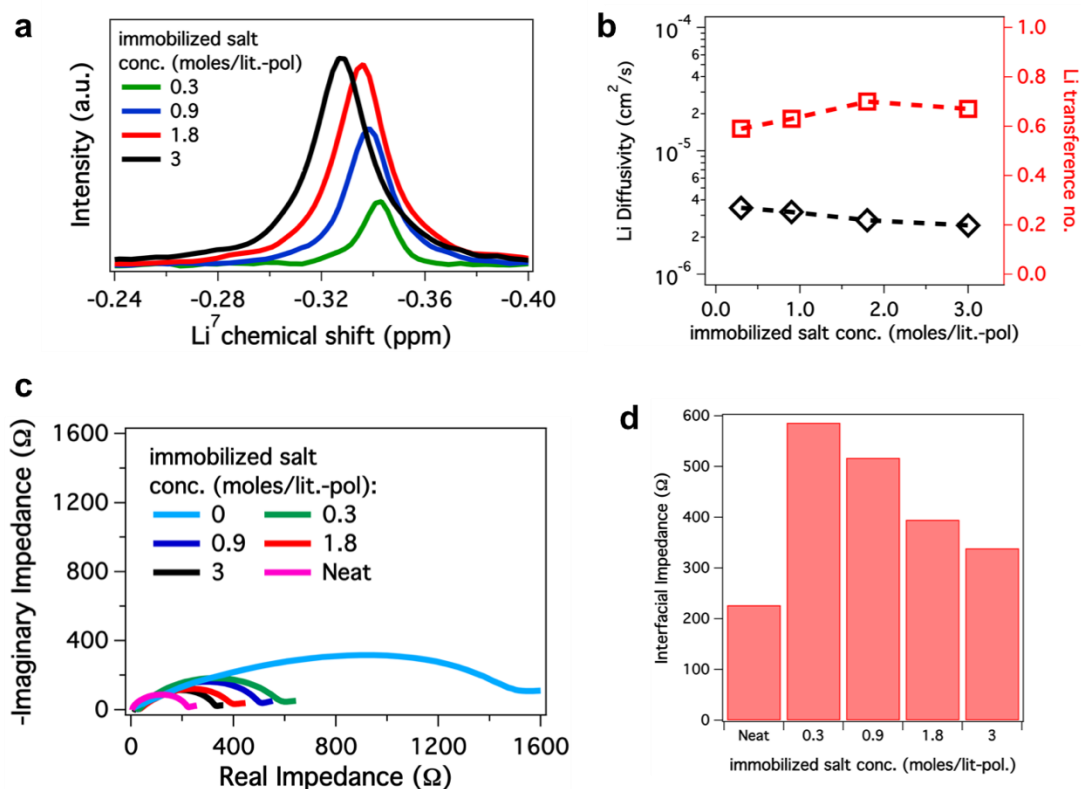


Figure 14. (a)  $^7\text{Li}$  chemical shift measured for different ionic polymer networks, showing a downfield shift with increasing salt concentration. (b) Lithium diffusivity and transference number obtained from pulse field gradient nuclear magnetic resonance measurements. (c) Nyquist plot showing the impedance measurement in symmetric lithium cell, where the electrode was coated with and without polymer networks. (d) Comparison of the interfacial resistances measured using impedance spectroscopy of symmetric lithium cells. In (a/b), the solvent used was EC/DEC, and in (c/d), the bulk liquid electrolyte utilized was 1 M LiTFSI in EC/DEC.

## Patents/Publications/Presentations

### Patent

- Bao, Z., Z. Yu, D. Feng, M. Lee, Y. Cui, and A. Pei. U. S. Application No.: 62/740,785, PCT Patent Application No.: PCT/US2019/054298, Ion-Conductive Organic Networks for Battery Applications.

### Publication

- Mackanic, D. G., X. Yan, Q. Zhang, N. Matsuhisa, Z. Yu, Y. Jiang, T. Manika, J. Lopez, H. Yan, K. Liu, X. Chen, Y. Cui, and Z. Bao. “Decoupling of Mechanical Properties and Ionic Conductivity in Supramolecular Lithium Ion Conductors.” *Nature Communications* 10 (2019): 5384.

### Presentations

- 2019 Stanford StorageX Symposium, Stanford, California (October 15, 2019): “Advanced Materials for Lithium Batteries”; Z. Bao. Poster session.
- 2019 AIChE Annual Conference, Orlando, Florida (November 8–15, 2019): “Structure-Property Relationships in Dynamic Polymer Networks for Electrochemical Applications”; S. Choudhury, Y. Cui, and Z. Bao.
- 2019 AIChE Annual Conference, Orlando, Florida (November 8–15, 2019): “Ion-Containing Polymers for Suppressing Electrochemical Instabilities in Metal Batteries”; S. Choudhury, Y. Cui, and Z. Bao.
- 2019 AIChE Annual Conference, Orlando, Florida (November 8–15, 2019): “Nonpolar-Based Electrolytes for Improved Lithium Metal Deposition and Stripping”; C. Amanchukwu, Y. Cui, and Z. Bao.
- 2019 AIChE Annual Conference, Orlando, Florida (November 8–15, 2019): “Scalable and Facile Preparation of Self-Healable Single-Ion Conducting Networks (SSN) for Lithium Metal Stabilization”; D. Mackanic, Z. Yu, Y. Cui, and Z. Bao.

## Task 1.6 – Improving the Stability of Lithium-Metal Anodes and Inorganic-Organic Solid Electrolytes (Nitash Balsara, Lawrence Berkeley National Laboratory)

**Project Objective.** The project objective is to establish a new hybrid electrolyte that will be stable against cells with a Li-metal anode.

**Project Impact.** Polymer electrolytes offer increased stability in lithium batteries in comparison to more widely used liquid electrolytes. Nanostructured electrolytes containing both soft, ion-conducting domains and rigid, nonconducting domains offer the opportunity to tune both mechanical and electrical properties separately. Such electrolytes are conveniently made by block copolymer self-assembly. Most of the block copolymer electrolytes studied thus far comprise organic polymer chains for both the conducting and rigid domains. The team hopes to synthesize new electrolytes that simultaneously have high transport properties and have greater stability against lithium in comparison to organic diblock copolymers.

**Approach.** First, the team synthesizes hybrid diblock copolymers by incorporating monomers that contain an inorganic component. Then, electrolytes are prepared by mixing these diblock copolymers with salt. Electrochemical and mechanical characterization of these materials is performed before carrying out cycling X-ray tomography (XRT) experiments. The combination of these approaches enables rational design of materials that exhibit improved stability against lithium metal.

**Out-Year Goals.** The project will synthesize a new hybrid electrolyte that is designed to be stable against lithium metal. The material is a block copolymer wherein acryloisobutyl polyhedral oligomeric silsesquioxane (POSS) is covalently bonded to the chain. The second block is a conventional polymer electrolyte, PEO. Electrochemical characterization of this polymer will include measurement of all transport properties including conductivity, diffusion coefficient, and the transference number. The stability against lithium metal will be evaluated by cyclic voltammetry (CV), while its applications as an electrolyte will be evaluated and visualized using cycling XRT experiments on symmetric Li-hybrid-Li cells.

**Collaborations.** There are no active collaborations this quarter.

### Milestones

1. Synthesize a series of POSS-containing block copolymer electrolytes for electrochemical studies. (Q1, FY 2020; Completed)
2. Create impurity-free lithium layers. (Q2, FY 2020)
3. Complete electrochemical characterization of POSS-containing block copolymer electrolytes. (Q3, FY 2020)
4. Provide cycling data for at least two POSS-containing block copolymer electrolytes. (Q4, FY 2020)

## Progress Report

The following milestone for this quarter was completed: A series of diblock and triblock organic-inorganic hybrid copolymers (as shown in Figure 15) was synthesized to compare and contrast electrochemical properties.

The polymerizations were carried out based on atom transfer radical polymerization (ATRP). Typically, POSS acrylate was polymerized using PEO-based mono or di-ATRP initiator and copper (I) bromide catalyst in toluene at 60°C for 24 h. After the reaction, the solution was passed through neutral alumina to get rid of the copper bromide. Pure polymer was obtained by reprecipitating three times from cold diethyl ether. The incorporation of POSS units in the block copolymers was confirmed via NMR spectra, and the purity was determined using GPC. Table 1 summarizes the composition of all the polymers.

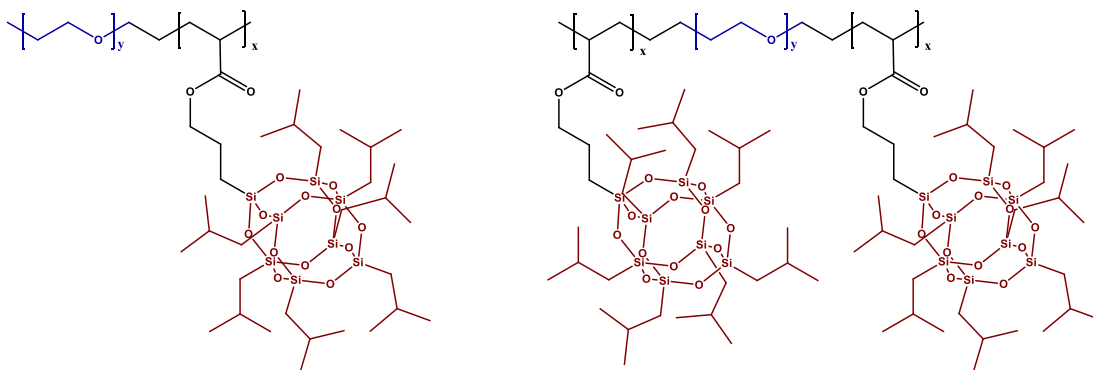


Figure 15. Chemical structure of PEO-POSS diblock and POSS-PEO-POSS triblock copolymer.

Table 1. Composition of various PEO-POSS diblock and POSS-PEO-POSS triblock copolymers. The molecular weight of the POSS block ( $M_{\text{POSS}}$ ) was estimated from nuclear magnetic resonance.

PEO-POSS	POSS units	$M_{\text{PEO}}(\text{Kg mol}^{-1})$	$M_{\text{POSS}}(\text{Kg mol}^{-1})$
<b>5-2</b>	2	5	1.9
<b>10-4</b>	4	10	3.7
<b>2-10-2</b>	4	10	3.7
<b>5-35-5</b>	10	35	9.2

In addition, single ion organic inorganic triblock terpolymer (Figure 16) was synthesized. These polymers were synthesized via nitroxide mediated polymerization (NMP) techniques. Typically, PEO-based macroalkoxamine was copolymerized with both POSS acrylate and lithium-4-styrenesulfonyl(trifluoromethane sulfonyl) imide, in one pot, in dimethyl formamide at 120°C for 24 h. After the reaction, the polymer was first precipitated from diethyl ether. It was then dialysed against deionized water for 72 h and dried to obtain the pure product. The composition of the polymer was determined by NMR spectra and is given in Table 2.

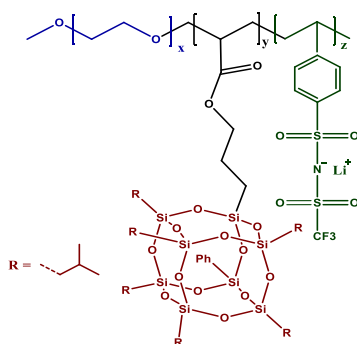


Figure 16. Chemical structure of PEO-POSS-PSTFSiLi.

Table 2. Composition of the triblock terpolymer PEO-POSS-PSTFSiLi. The composition was determined by nuclear magnetic resonance spectra. The  $r$  values denote the concentration of lithium ion in the polymer and are given by  $r = [Li]/[EO]$ .

PEO-POSS-PSTFSiLi	$M_{PEO}(Kg\ mol^{-1})$	$M_{POSS}(Kg\ mol^{-1})$	$M_{PSTFSiLi}(Kg\ mol^{-1})$	$r$
5-2-1	5	1.9	1	0.035
5-2-2	5	1.9	2	0.055
5-2-4	5	1.9	4	0.1
5-2-6	5	1.9	6	0.17
5-2-11	5	1.9	11	0.31

## Patents/Publications/Presentations

### Publications

- Frenck, L., G. K. Sethi, J. A. Maslyn, and N. P. Balsara. “Factors That Control the Formation of Dendrites and Other Morphologies on Lithium Metal Anodes.” *Frontiers in Energy Research* (2019): 7–115.
- Maslyn, J. A., L. Frenck, W. S. Loo, D. Y. Parkinson, and N. P. Balsara. “Extended Cycling through Rigid Block Copolymer Electrolytes Enabled by Reducing Impurities in Lithium Metal Electrodes.” *ACS Applied Energy Materials* 2 (2019): 8197–8206.

### Presentations

- 236<sup>th</sup> Electrochemical Society (ECS) Meeting, Atlanta, Georgia: “Predicting the Performance of Lithium Metal Electrodes Stabilized by Polymer Electrolytes”; N. P. Balsara, D. M. Pesko, and J. A. Maslyn. Invited.
- 236<sup>th</sup> ECS Meeting, Atlanta, Georgia: “Experimental Measurement of the Local Current Density in the Vicinity of a Lithium Protrusion: Plating and Stripping”; J. A. Maslyn, K. D. McEntush, K. J. Harry, and N. P. Balsara.
- 2019 AIChE Annual Meeting, Orlando, Florida: “Predicting the Performance of Lithium Metal Electrodes Stabilized by Polymer Electrolytes”; N. P. Balsara and J. A. Maslyn.

## Task 1.7 – Development of Thin, Robust, Lithium-Impenetrable, High-Conductivity, Electrochemically Stable, Scalable, and Low-Cost Glassy Solid Electrolytes for Solid-State Lithium Batteries (Steve Martin, Iowa State University of Science and Technology)

**Project Objective.** The objective of this project is to develop new Li<sup>+</sup>-conducting mixed oxy-sulfide-nitride glassy solid electrolytes (MOSN GSEs) that are impermeable to lithium dendrites, have high conductivities, are scalable through low-cost glass manufacturing, are chemically and electrochemically stable, and will enable low-cost, high-energy-density solid-state lithium batteries (SSLBs). The SSLBs constructed from these new GSEs will meet and exceed all program objectives: useable specific energy @ C/3  $\geq 350$  Wh/kg, calendar life 15 years, cycle life (C/3 deep discharge with < 20% energy fade) 1,000, and cost  $\leq$  \$100/kWh.

**Project Impact.** This project will enable the team to demonstrate that (1) thin MOSN GSE films yield superior performance in a much safer, lower-cost, and Li-dendrite impenetrable form and (2) high rate and long cycle life can be achieved in SSLBs using thin-film MOSN GSEs. The new GSEs in SSLBs are anticipated to increase the energy density (anode basis) from  $\sim 300$  mAh/g to  $\sim 4,000$  mAh/g, enabling replacement of internal combustion engines in both light and heavy duty vehicles. Each 20% reduction in the  $\sim 1.6$  billion liters of gasoline used per day in the United States would reduce CO<sub>2</sub> emissions by  $\sim 4$  billion kg or  $2 \times 10^{12}$  l of CO<sub>2</sub> per day. The team will also increase scientific and engineering knowledge of thin-film GSEs in SSLBs.

**Approach.** The MOSN MGF glasses used for the GSEs in this project have been developed in previous work to have the necessary thermal stability and high ionic conductivity for successful use as a drawn-film electrolyte. In this project, the glass chemistry will be tuned for even more desirable properties, by investigating structure-property relationships and testing variations in glass chemistry.

**Out-Year Goals.** Work will progress toward developing a glass capable of being drawn to 100-micron thickness, while having high conductivity and electrochemical stability and good cycling ability.

**Collaborations.** There are no active collaborations this quarter.

### Milestones

1. Complete hiring and training necessary to begin project. (Completed, January 2, 2020)
2. Preform redraw capability to form 5-m ribbons verified. (Q1, FY 2020; In progress)
3. Accomplish: MOSN MGF GSEs are thermally stable between -20°C and 100°C, have a Li<sup>+</sup> ion conductivity  $> 1$  mS/cm at 25°C, have a Li<sup>+</sup> ion area specific resistance (ASR) of  $\leq 100$  Ohm-cm<sup>2</sup>, have an electronic ASR of  $> 0.1$  M Ohm-cm<sup>2</sup>, are electrochemically stable between 0 and 4.5 V versus Li/Li<sup>+</sup>, and have no more than 1 wt% weight change in 45% RH air. (Q2, FY 2020)
4. Accomplish: MOSN MGF GSE are stable against lithium through 100 cycles. (Q3, FY 2020)
5. *Go/No Go Decision:* MOSN MGF GSE is chemically stable and resistant to crystallization. Analysis indicates technical approach capable of achieving performance targets. (Q4, FY 2020)

## Progress Report

This project began October 1, 2019, and as such, there is limited progress to report.

The team has hired two PhD and two undergraduate researchers as budgeted on the project. They have recruited, but so far have been unsuccessful in hiring, a suitable Post-Doctoral Research Associate (PRDA) for the project. While recruitment efforts continue, the team has hired a temporary full-time Professional and Scientific staff person, Ms. A. Joyce, for the project. Ms. Joyce has a BS in Materials Engineering and has worked in the PI's research group for four years and is exceedingly well trained to carry out most if not all of the required research. The team anticipates hiring the PDRA at the end of the spring 2020 semester.

In previous work, the team has established a baseline MOSN GSE composition (based on  $\text{Li}_2\text{S} + \text{SiS}_2 + \text{LiPO}_3 + \text{LiPON}$ ) that meets most of this quarter's milestone. These are shown in Figure 17. The ISU-4 glass of composition  $0.90 [0.61\text{Li}_2\text{S} + 0.39\text{SiS}_2] + 0.10 [0.74\text{LiPO}_3 + 0.26\text{LiPON}]$  has a  $25^\circ\text{C}$   $\text{Li}^+$  ion conductivity (Figure 17a) of  $7 \times 10^{-4}$  S/cm, gains essentially no weight in contact with air (Figure 17b), shows on nanoamp levels of electronic conductivity in blocking cells against metallic lithium (Figure 17c), shows oxidative voltage stability up to 4 V (Figure 17c), shows no crystallization when scanned in temperature until T is more than  $100^\circ\text{C}$  above the softening point,  $T_g$ , of the glass (Figure 17d), and is stable against metallic Lithium in symmetric  $\text{Li}|\text{GSE}|\text{Li}$  cells (Figure 17e) and can cycle against lithium up to  $1.5 \text{ mA/cm}^2$  for hundreds of cycles, Figure (17f).

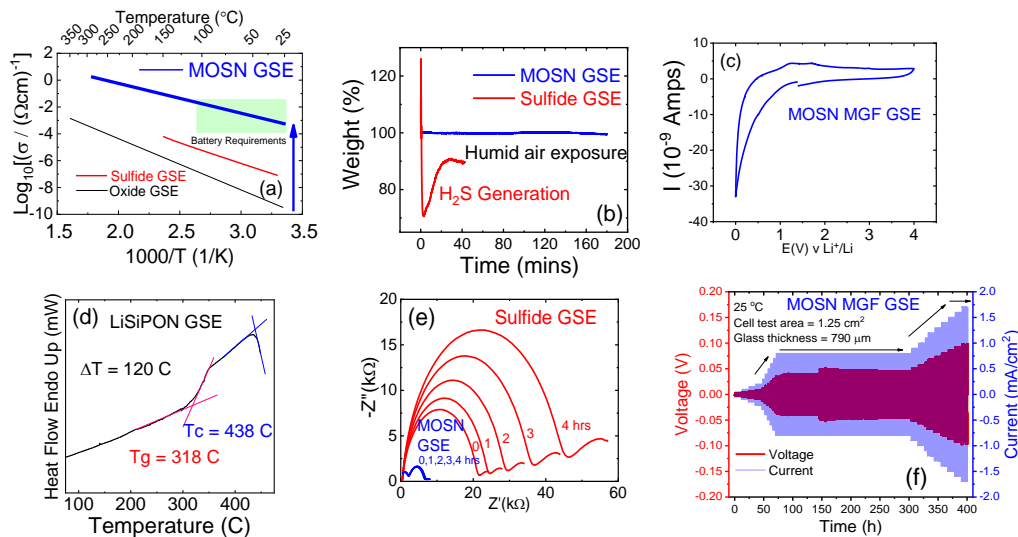


**Figure 17.** The ISU-4 glass of composition  $0.90 [0.61\text{Li}_2\text{S} + 0.39\text{SiS}_2] + 0.10 [0.74\text{LiPO}_3 + 0.26\text{LiPON}]$  has a  $25^\circ\text{C}$   $\text{Li}^+$ -ion conductivity of  $7 \times 10^{-4}$  S/cm (a), gains essentially no weight in contact with air (b), shows only nanoamp levels of electronic conductivity in blocking cells against metallic lithium and shows oxidative voltage stability up to 4 V (c), shows no crystallization when scanned in temperature until T is more than  $100^\circ\text{C}$  above the softening point,  $T_g$ , of the glass (d), and is stable against metallic Lithium in symmetric  $\text{Li}|\text{GSE}|\text{Li}$  cells (e) and can cycle against lithium up to  $1.5 \text{ mA/cm}^2$  for hundreds of cycles (f).

This quarter, the team has focused efforts on the proposed work on two aspects:

- To scale up the gram-level quantities of glass needed for the bench-level property tests described above to hundred and kilogram level quantities of glass needed for this project that form large glass preforms and then draw them into long length glass films.
- To repeatedly make multiple samples of glass to ensure their properties are reproducible so that when the team scales up to kilogram levels of glass, they are confident that the project glasses will be the same.

### Scale-Up Efforts

Regarding the components of the ISU-4 composition described above, all of them are readily available except the  $\text{SiS}_2$ . This material can be bought commercially, but the purity is extremely poor and it is very expensive. Therefore, the team has developed synthesis techniques to produce hundred-gram quantities of  $\text{SiS}_2$ , needed for kilogram quantities of ISU-4 glass, in high purity. The main impurity in  $\text{SiS}_2$ , made by reacting stoichiometric amounts of silicon and sulfur, is unreacted silicon. Figure 18a shows an early batch of  $\text{SiS}_2$ , with the very dark gray color from the unreacted silicon. The team has observed that if they add 20 at% excess sulfur to the batch and then mill the silicon + excess sulfur batch for ~ 20 minutes in a Spex mill, the excess sulfur coats all of the individual silicon particles. When these S-coated silicon particles are then heated in the sealed tube, they are forced to remain apart from one another and cannot do anything else but react with sulfur to form stoichiometric sulfur. The excess sulfur then provides a liquid bath that, with rotation, provides intimate reaction between the silicon and sulfur. After reaction, the excess sulfur is easily removed away from the silicon by simply taking the reaction tube, still sealed, and placing it part way into a vertical tube furnace and heating to above the boiling point of sulfur. The sulfur sublimates/evaporates away from the  $\text{SiS}_2$  and condensates on the cold part of the exposed tube that sticks outside of the furnace.

Figure 18a shows the old impure version of  $\text{SiS}_2$  that is badly contaminated with unreacted silicon. Figure 18b shows the new  $\text{SiS}_2$  produced this quarter that is perfectly white and has no unreacted silicon particles. On close inspection (Figure 18c), the open porosity of the  $\text{SiS}_2$  formed when the sulfur evaporates away from the  $\text{SiS}_2$  is clearly seen.



**Figure 18.** (a) The old impure version of  $\text{SiS}_2$  that is badly contaminated with unreacted silicon. (b) The new  $\text{SiS}_2$  produced this quarter that is perfectly white and has no unreacted silicon particles. (c) Close inspection shows the open porosity of the  $\text{SiS}_2$  that is formed when the sulfur evaporates away from the  $\text{SiS}_2$ .

### Reproducible Glass Properties

One of the most important and first aspects of this project is to scale up the processing of the GSEs from the bench-level, few-grams scale needed for simple electrochemical and physical property tests to the hundred-gram and kilogram-levels needed to make the glass preforms for film drawing. For example, the minimum-size glass the team can use to make the glass films required for this new project is 5-mm thick by 100-mm wide by 300-mm long. At ~ 3 g/mL density, this requires ~ 300 grams of glass. Due to loss on melting and casting, in practice, this requires a 400- or 500-gram glass batch. So, for these reasons, the team has to ensure that the scale-up glass composition is reproducible so that they are confident they will not waste nearly a kilogram of very expensive glass.

Hence, they spent time this quarter remaking the ISU-4 glass multiple times and measuring the properties of the different glasses. Figure 19 shows the differential scanning calorimetry (DSC) scans of four batches of ISU-4 glass that all show the exact same T<sub>g</sub> and T<sub>g</sub> behavior and that confirm reproducible properties. Next quarter, the team will measure the other properties described above to ensure all of the other important properties of glass are equally reproducible.

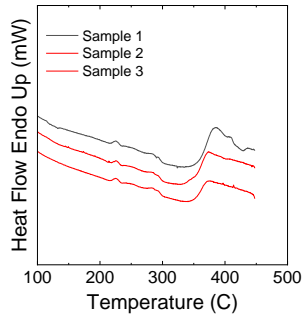


Figure 19. Differential scanning calorimetry (DSC) scans of three different samples of Iowa State University glassy solid electrolytes showing reproducibility of the glass properties. This figure shows the T<sub>g</sub> determined by DSC.

### Patents/Publications/Presentations

The project has no patents, publications, or presentations to report this quarter.

## Task 1.8 – Composite Solid Ion Conductor with Engineered Lithium Interface (Kyler Carroll and Cam Peebles, Wildcat Discovery Technologies)

**Project Objective.** In this project, Wildcat seeks to perform focused, fundamental research and development on composite polymer/ceramic electrolytes and for the protection of Li-metal anodes to develop an all-solid-state Li-metal battery that achieves DOE requirements for performance that enable potential commercialization of this technology. Wildcat will leverage its high throughput battery platform to explore a broad composite electrolyte compositional space. Additionally, the high throughput platform will allow the team to screen hundreds of inorganic and organic coatings for lithium metal protection and translate the best results to all solid cells.

**Project Impact.** Successful widespread commercialization of EVs is contingent on developing safe high-energy-density batteries capable of long cycle life. Lithium metal affords the highest theoretical capacity (3,860 mAh/g) and lowest electrochemical potential (-3.04 V versus SHE), which offers the highest specific energy density of anode materials today. However, significant progress toward the passivation of lithium metal must occur before the energy density benefit can be realized. The intrinsic high reactivity between lithium metal with conventional Li-ion electrolytes (organic carbonate-based solvents) makes it extremely difficult to overcome these problems. The proposed composite polymer/ceramic electrolyte and a protected Li-metal anode will enable an all-solid-state Li-metal battery. It is expected that the outcomes from this effort will deliver a safe all-solid-state Li-metal pouch cell with over 350 Wh/kg and over 1,000 cycles (C/3) with the cost estimate below \$100/kWh.

**Approach.** The project approach involves (1) identifying a suitable combination of solid ion conductor, polymer, and additive that minimizes overall interfacial impedance between the polymer electrolyte and solid ion conductor, and (2) identification of stable Li-metal protection agent or combination of agents that show enhanced cycling performance (relative to a non-protected system) using the down-selected cell architectures.

**Out-Year Goals.** The out-year goals involve screening hundreds of additive, polymer, and solid ion conductor combinations using a high throughput trilayer cell architecture developed during method development phase. Based on the best combinations, Wildcat will develop a composite polymer/ceramic electrolyte where the Li-ion conductivity is occurring at the ceramic phases of the composite. Additionally, the team will screen hundreds of Li-metal protection agents using the designed high-throughput cell architecture with the goal of identifying those that offer highest stability.

**Collaborations.** All project tasks will be performed at Wildcat Discovery Technologies.

### Milestones

1. Establish baseline performance. (Q1, FY 2020; Completed)
2. Complete synthesis of ceramic ion conductors. (Q2, FY 2020; In progress)
3. Perform down-selection of best ceramic ion conductors for further optimization. (Q3, FY 2020; In progress)
4. Perform down-selection of best composite solid electrolyte additives for further optimization. (Q4, FY 2020; In progress)
5. Perform down-selection of best high-voltage polymer formulations for further optimization. (Q4, FY 2020; In process)
6. Demonstrate composite ionic conductivity >> polymer ionic conductivity. (Q4, FY 2020)

## Progress Report

This quarter, the team focused on developing a high-throughput workflow for screening the polymer/ceramic interface and Li-metal protection agents using baseline materials. Wildcat proprietary high-throughput cells can be varied in a number of ways to match other cell formats. To better guarantee that results of high-throughput screening will result in discoveries that can translate across cell formats, Wildcat tested various cell architectures.

### Method Development for Screening Polymer/Ceramic Interface

The proposed composite polymer/ceramic electrolyte will utilize both ceramic surface modifications and innovative coupling agents to ensure low interfacial impedance ( $R_{\text{interface}}$ ) between the ceramic and the polymer. Initial work was aimed at developing an appropriate baseline cell architecture to test the  $R_{\text{interface}}$ . To investigate

the interface of the polymer/ceramic composite, Wildcat developed a trilayer sandwich cell. The baseline trilayer cell (Figure 20a) consisted of a dense LTAP ceramic pellet, previously developed by Wildcat, sandwiched between two polymer electrolytes. The polymer electrolyte consisted of a PEO:LiCF<sub>3</sub>SO<sub>3</sub> blend ([PEO]:[Li]=14:1) cast onto copper foil. The trilayers were placed in a Wildcat high-throughput cell and characterized by AC impedance spectroscopy at various temperatures (30, 40, 50, and 60°C). The LTAP ceramic pellet was measured using a gold blocking electrode, while the polymer electrolyte was measured using a copper blocking electrode. Triplicate samples were allowed to equilibrate for at least 60 minutes at each temperature before impedance characterization. Figure 20b shows representative Nyquist plots of LTAP ceramic pellet, polymer electrolyte, and trilayer cells at 60°C. Temperature dependent conductivity ( $\sigma = \frac{h}{RA}$ ) values were calculated by fitting the data to an equivalent circuit model (Figure 20a).

Ideally, if no interfacial impedance existed, the resistance of the trilayer would equal the sum of the LTAP pellet and polymer electrolyte resistances ( $R_{\text{trilayer}} = R_{\text{LTAP}} + R_{\text{Polymer}}$ ). The ASR plot (Figure 20c) of the trilayer and the LTAP ceramic pellet and polymer electrolyte show that the trilayer deviates from the sum of the ceramic and polymer, indicating a larger interfacial impedance between the LTAP and polymer. The  $R_{\text{interface}}$  was calculated using the following equation:  $R_{\text{interface}} = \left(\frac{1}{2}\right)[R_{\text{trilayer}} - (R_{\text{ceramic}} + R_{\text{polymer}})]$ . For the baseline polymer electrolyte and LTAP, the  $R_{\text{interface}}$  (Figure 20d) shows a large interfacial resistance at room temperature (30°C). To improve the ion transport through a composite polymer/ceramic electrolyte, the interfacial resistance needs to be significantly reduced.

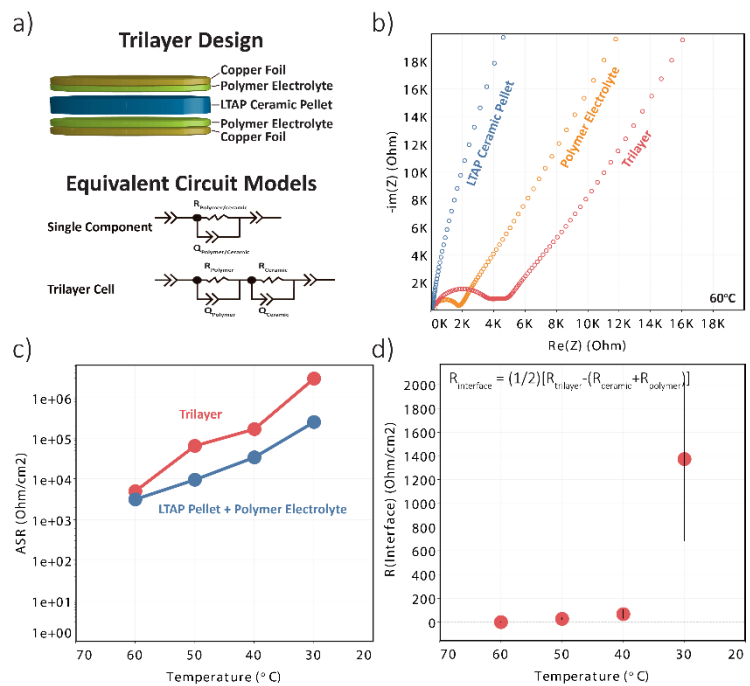


**Figure 20.** (a) The Wildcat high throughput trilayer sandwich cell and equivalent circuit models for AC impedance fitting. (b) Nyquist plots of LTAP ceramic pellet, polymer electrolyte, and trilayer cells. (c) Area-specific resistance of the trilayer cell and the sum of the LTAP pellet and polymer electrolyte. (d) The calculate  $R_{\text{interface}}$  for the trilayer cell.

## Test Vehicle Development for Lithium Metal Screening Strategy

To accurately assess the ability of a protective coating to passivate the surface of lithium metal, a proper test vehicle is required. A brief literature review reveals that several cell formats have been used for testing artificially derived SEIs including both half cells (Li/NMC, Li/LTO, Li/Cu) and symmetric cells (Li/Li). Each cell format (or test vehicle) offers a

different benefit (from relevancy in Li/NMC half cells to more diagnostic in Li/Li symmetric cells). The selected test vehicle should perform several goals: (1) be able to efficiently screen various protective coatings and differentiate electrochemical performance between them, (2) potentially be able to correlate protective coatings formed *in situ* (using an additive in a liquid electrolyte) with protective coatings formed *ex situ* (coatings applied on the lithium metal prior to cell assembly), and (3) illuminate lithium plating/stripping kinetics and mechanisms without cell tear-down and analysis. Figure 21 shows the cycling results of several test vehicles using lithium metal with no protective coating (baseline systems) in combination with a carbonate-based electrolyte (1.0 M LiPF<sub>6</sub> in EC/EMC 4:6 wt/wt). Importantly, all test vehicles are using the same Li-metal anode and the same electrolyte. Additionally, the current densities applied in the Li/Li test vehicle match those of the Li/NMC, Li/LTO, and Li/Cu test vehicles to help shed light on the lithium plating/stripping kinetics during cycling. In this regard, a combination of test vehicles could be beneficial in helping initially screen for useful Li-metal protective agents. More in-depth investigations of the test vehicles and high-throughput studies are being conducted.

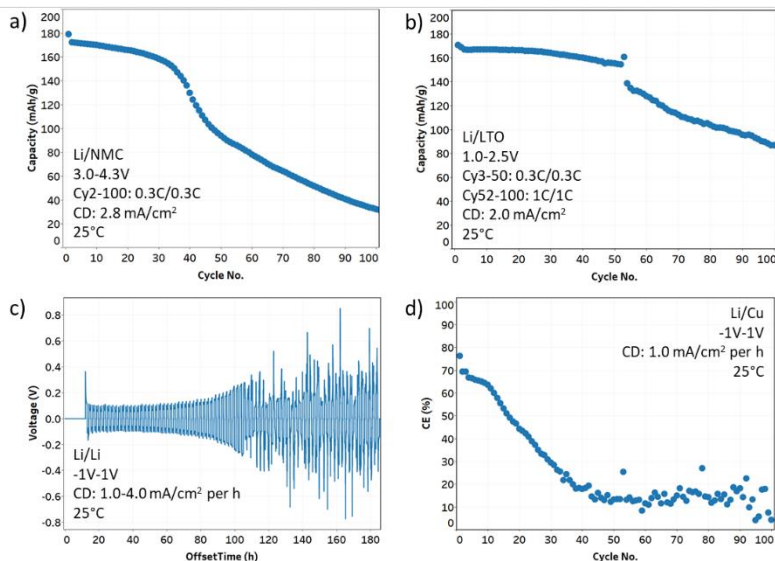


Figure 21. Representative cycling plots for various test vehicles under investigation. Test vehicles include (a) Li/NMC half cells, (b) Li/LTO half cells, (c) Li/Li symmetric cells, and (d) Li/Cu half cells. The cycling rate, current density (CD), and operating temperature for each test vehicle are given. All test vehicles used a standard carbonate-based electrolyte (1.0 M LiPF<sub>6</sub> in EC:EMC 4:6 wt/wt.)

## Patents/Publications/Presentations

The project has no patents, publications, or presentations to report this quarter.

## Task 1.9 – Single-Ion Conducting Electrolyte Extended to Cathode for All-Solid-State Lithium-Ion Batteries (Nianqiang (Nick) Wu, University of Massachusetts Amherst)

**Project Objective.** The objective is to develop single-ion conducting polymer-ceramic electrolyte and to create 3D electrolyte-cathode interface structure for lithium batteries.

**Project Impact.** The coherent electrolyte-cathode bilayer structure will allow for a thick cathode with a high sulfur loading, and result in low interfacial impedance. Furthermore, the solid-state single-ion conducting electrolyte, which has high ionic conductivity and high mechanical strength, will suppress the dendrite formation at the Li-metal anode/electrolyte interface. In short, this proposed work will result in novel all-solid-state lithium batteries, which possess significantly higher energy density, longer cycling life, and better safety than the state-of-the-art Li-ion batteries. Also, it will enable development of flexible Li-metal batteries due to use of flexible nanofiber-polymer structure. Therefore, the project will advance the technology of all-solid-state lithium batteries and promote application of all-solid-state lithium batteries in EVs.

**Approach.** Poly(arylene ether)-based multi-block copolymers with  $\text{Li}^+$  transference number close to unity will be designed as a single-ion conducting polymer. 3D nanofiber network will be incorporated into the polymer matrix to form solid-state single-ion conducting composite electrolyte. In addition, the coherent electrolyte-cathode bilayer structure will generate a 3D electrolyte/cathode interface, enable continuous ionic transport between the electrolyte and cathode, and create abundant triple-phase (ionic/electronic/ $\text{Li}^+$  host) sites throughout the cathode. This will enable a thick cathode with high sulfur loading, showing the reduced interfacial impedance at the electrolyte/cathode interface.

**Out-Year Goals.** Work will progress toward synthesis of the single-ion conducting polymer and 3D electrolyte-cathode architecture. The goal is to find the optimal synthetic route to achieve the desirable conductivity and create 3D electrolyte-cathode interface structure for lithium batteries.

**Collaborations.** This project funds work at University of Massachusetts Amherst (UMass Amherst) and North Carolina State University (NCSU). Dr. N. Wu at UMass Amherst serves as PI. Dr. X. Zhang at NCSU acts as Co-PI. H. Yang (Postdoctoral Fellow at UMass Amherst), X. Zeng (Ph.D. student at UMass Amherst), H. Cheng (Ph.D. student at NCSU), and M. Dirican (Postdoctoral Fellow at NCSU) contributed to the project.

### Milestones

1. Design and synthesize the single-ion conducting multi-block polymers. (Q1, FY 2020; 70% Completed)
2. Characterize the chemical composition, the phase, and microstructure of single ion-conducting polymers. (Q2, FY 2020)
3. Synthesize and test the properties of  $\text{Li}_{6.4}\text{La}_3\text{Al}_{0.2}\text{Zr}_2\text{O}_{12}$  (LLAZO) and LLATO nanofibers. (Q3, FY 2020)
4. Test the ionic conductivity, and Li-ion transference number of polymers of multi-block copolymers,  $\approx 1 \times 10^{-4}$  S/cm; measure the mechanical properties of polymers. (Q4, FY 2020)

## Progress Report

This quarter, the team started synthesis of two types of poly(arylene ether)-based single-ion conducting multi-block copolymer electrolytes. At the same time, a new metal-organic frameworks (MOF) single Li-ion conductor has been synthesized by covalently immobilizing anions to the skeleton of MOF structures. After incorporated EC and propylene carbonate (PC) into the MOF structure, its ionic conductivity reaches a remarkable value of  $7.8 \times 10^{-4}$  S/cm. The team also introduced lithium salt-grafted LLAZO nanofiber into the crosslinked PEGDMA to demonstrate the feasibility of fabricating a single-ion conducting composite solid electrolyte consisting of the lithium salt / silane-co-grafted LLAZO nanofiber/crosslinked multi-block copolymer.

### Develop Single-Ion Conducting Polymer Electrolytes

#### *Poly(arylene Ether)-Based Single-Ion Conducting Multi-Block Copolymers*

Two types of poly(arylene ether)-based single-ion conducting multi-block copolymer electrolytes were synthesized. The first single-ion conducting polymer, (LiPFS-PAE)-FPAES multi-block copolymer, is composed of poly(arylene ether) with pendant lithium perfluoroethyl sulfonate (LiPFS-PAE) and partially fluorinated poly(arylene ether sulfone) (FPAES) blocks. Currently, the team is focusing on synthesis of the precursor LiPFS-PAE. In addition, they devoted extensive effort on establishing a relevant laboratory set-up for realization of the complex polymer synthesis procedures. The second single-ion conducting polymer, (psi-PAES)-FTPAE multi-block copolymer, consists of poly(arylene ether sulfone)-bearing perfluorosulfonimide (psi-PAES) and highly-fluorinated rigid decafluorobiphenyl-terminated poly(arylene ether) (FTPAE) blocks. The team is synthesizing the intermedia product (BrPAES)-FTPAE.

#### *A Functionalized Metal–Organic Framework Single Lithium-Ion Conductor for Lithium Batteries*

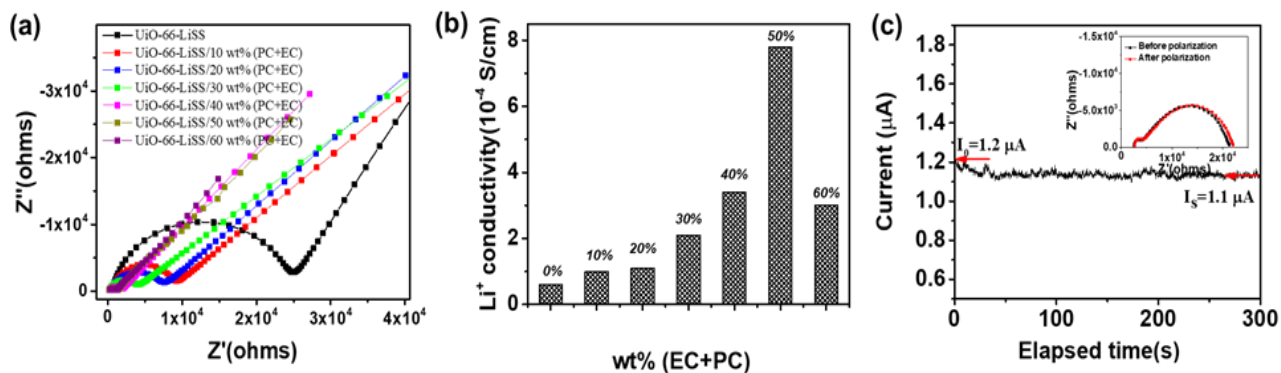


Figure 22. (a) Electrochemical impedance spectroscopy of UiO-66-LiSS with different amount of EC+PC measured at room temperature. (b) Ionic conductivity of UiO-66-LiSS with different amount of EC+PC. (c) DC polarization curve of symmetric  $\text{Li|UiO-66-LiSS-50\% EC/PC|Li}$  cell.

A new MOF single LIC has been synthesized by covalently immobilizing anions to the skeleton of MOF structures. UiO-66-Br was firstly synthesized through slightly modified solvothermal procedure. Sulfonated side chains, sodium p-styrenesulfonate, were then covalently linked to the UiO-66-Br through a post-synthetic modification approach using a Mizoroki-Heck coupling reaction. The subsequent product is named as UiO-66-NaSS. The  $\text{Na}^+$  was then exchanged with  $\text{Li}^+$ , and the final LIC is referred to as UiO-66-LiSS. The functionalized UiO-66 MOF exhibits ionic conductivity of  $6.0 \times 10^{-5}$  S/cm,  $7.9 \times 10^{-5}$  S/cm, and  $1.1 \times 10^{-4}$  S/cm at 25°C, 60°C, and 90°C, respectively. It displayed single-ion conducting behavior with high Li-ion transference number of 0.90 at 25°C. After incorporating EC and PC into the MOF structure, its ionic conductivity reached  $7.8 \times 10^{-4}$  S/cm with 50 wt% EC and PC (Figure 22a-b). The electrochemical window is a very important factor for electrolytes of high-voltage lithium batteries. Linear sweep voltammetry (LSV) of

the UiO-66-LiSS solid electrolyte was tested using stainless steel as the working electrode and lithium foil as the counter and reference electrodes. The LSV profile of UiO-66-LiSS solid electrolyte indicated a stable voltage window up to 5.2 V versus lithium (Figure 22c).

### *Single-Ion Conducting Composite Electrolytes Based on Lithium Salt/Silane-Cografted LLAZO Nanofiber/Crosslinked PEGDMA*

The team successfully synthesized lithium salt (lithium [(4-methylphenyl) sulfonyl] [(trifluoromethyl) sulfonyl] amide salt)-grafted LLAZO nanofibers. Compared to bare LLAZO nanofibers, lithium salt-grafted LLAZO nanofibers demonstrated a different FTIR spectrum (Figure 23). For the lithium salt-grafted LLAZO nanofibers, the absorption peaks at 1127 and 1160  $\text{cm}^{-1}$  could be attributed to siloxane, while the peaks at 1050, 1089, 1344, and 1309  $\text{cm}^{-1}$  represented sulfone. Furthermore, the peaks located at 1665 and 1708 could be attributed to the aryl groups. All of those FTIR peaks confirmed the successful grafting of lithium [(4-methylphenyl) sulfonyl] [(trifluoromethyl)sulfonyl] amide salt on LLAZO nanofibers. These results indicate successful synthesis of a single-ion conducting composite solid electrolyte consisting of lithium salt/silane-co-grafted LLAZO nanofiber/crosslinked multi-block copolymer.

The project's electrochemical testing results demonstrated that the as-prepared lithium salt-grafted LLAZO nanofiber/crosslinked PEGDMA composite electrolyte exhibited ionic conductivity of  $1.5 \times 10^{-5}$  S/cm at room temperature without any structure optimization. The team is preparing the proposed lithium salt / silane-cografted LLAZO nanofibers and fabricating the lithium salt/silane-cografted LLAZO nanofiber / crosslinked PEGDMA based single-ion conducting composite solid electrolytes.

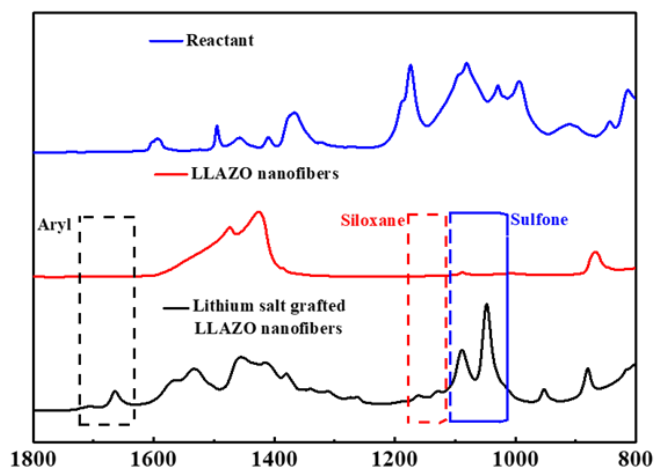


Figure 23. Fourier transform infrared spectra of lithium salt-grafted LLAZO nanofibers, bare LLAZO nanofibers, and reactant (4-[2 (trimethoxysilyl)ethyl]benzene-1-sulfonyl chloride).

## Patents/Publications/Presentations

The project has no patents, publications, or presentations in this quarter.

## Task 1.10 – Physical and Mechano-Electrochemical Phenomena of Thin-Film Lithium-Ceramic Electrolyte Constructs (Jeff Sakamoto, University of Michigan)

**Project Objective.** While a small number of solid electrolytes exhibit high ionic conductivity ( $\sim 1 \text{ mS cm}$  at 298K), few are stable against lithium metal. The garnet-type solid electrolyte, based on the nominal formula  $\text{Li}_7\text{La}_3\text{Zr}_2\text{O}_{12}$  (LLZO), is unique in that it is a fast ion conductor and—as demonstrated in the team’s recent project (DE-EE-00006821)—is stable against lithium. Moreover, the team’s former project successfully demonstrated a decrease in Li-LLZO interface resistance from 12,000 to 2 Ohms  $\text{cm}^2$  and stable cycling at 1 mA  $\text{cm}^2$  for 100 cycles ( $\pm 15 \mu\text{m}$  lithium per cycle). Although the past project demonstrated that LLZO is a viable solid electrolyte for enabling batteries using metallic lithium, the studies used thick pellets (1 mm) and thick anodes ( $\sim 500 \mu\text{m}$ ). The goal of this project is to acquire a deep fundamental understanding of the physical and mechano-electrochemical phenomena that control the performance of cells consisting of thin LLZO ( $\sim 10 \mu\text{m}$ ), thin lithium anodes ( $\sim 20 \mu\text{m}$ ), and thin solid-state composite cathodes.

**Project Impact.** If successful, the project will gain knowledge to guide closely related commercialization efforts to scale the production of LLZO-based SSBs.

**Approach.** The team believes that to achieve a step increase in technology readiness level (TRL), the same performance characteristics previously shown should be demonstrated in technologically relevant cells, for example, thin LLZO and thin lithium.

**Out-Year Goals.** The out-year goals involve the following: custom thin-film construct development, preliminary cycling studies, Vis cell development, lithium cycling, and polymer gel electrolyte screening.

**Collaborations.** This project collaborates with Professors N. Dasgupta and D. Siegel of University of Michigan, Mechanical Engineering.

### Milestones

1. Thin-film LLZO integration.
2. Long-term cycling stability.
3. Mechanics of the Li-LLZO interface.
4. Stability and kinetics of the LLZO-catholyte interface.

## Progress Report

This quarter's milestone to complete custom thin-film construct (TFC) design was successfully completed. Using the reference electrode design criteria for thick-film LLZO, the same approach was used to establish the reference electrode geometry and placement for the TFC to be used throughout the project. The design will guide fabrication and testing of reference electrodes in upcoming milestones that involve cycling TFC with reference electrodes.

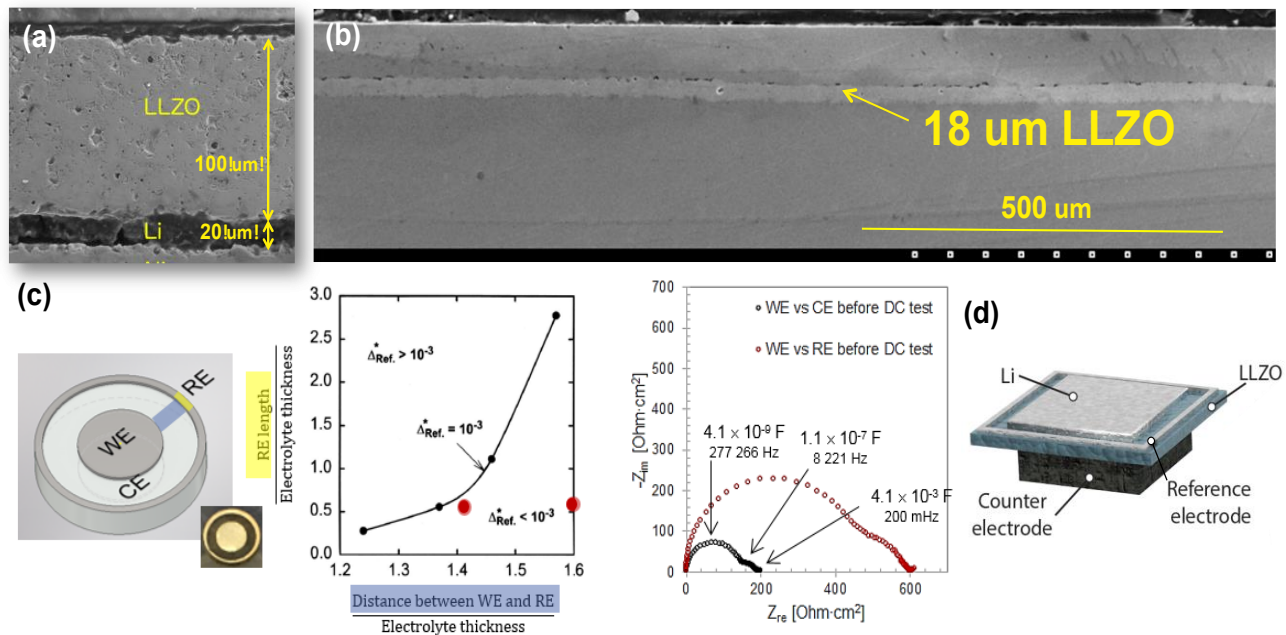


Figure 24. Thin-film construct (TFC) and precision reference electrode experience. (a) TFC consisting of 20- $\mu\text{m}$  thick lithium and 100- $\mu\text{m}$  thick LLZO. (b) 18- $\mu\text{m}$  tape cast and densified LLZO. (c) Demonstrated precision Li-metal reference electrode integration. Normalized potential of the three-electrode cell design;  $< 10^{-3}$ , avoids occurrence of electrochemically driven reactions over the reference electrode (c). (d) The experience with TFC fabrication and reference electrode integration demonstrates feasibility of TFC with reference electrodes.

## Patents/Publications/Presentations

### Presentation

- Materials Research Society (MRS) Fall Meeting, Boston, Massachusetts: “Stabilizing Solid Li and Na Metal Anodes Using Ceramic Membrane Technology”; J. Sakamoto. Invited.

## Task 1.11 – Lithium Dendrite-Free $\text{Li}_7\text{N}_2\text{I-LiOH}$ Solid Electrolytes for High-Energy Lithium Batteries (Chunsheng Wang, University of Maryland)

**Project Objective.** The objective of this project is to research, develop, and test Li-metal-based batteries that implement solid LICs equipped with  $\text{Li}_7\text{N}_2\text{I-LiOH}$  solid electrolyte capable of achieving the cell performance of 350 Wh/Kg energy density for 1000 cycle life with a cost of  $\leq \$100/\text{kWh}$ .

**Project Impact.** Lithium dendrite growth during charge/discharge cycles limits the use of ASSBs. A criterion for lithium dendrite suppression that is developed through systematical investigation on thermodynamics and kinetics of lithium dendrite growth will guide the electrolyte design.  $\text{Li}_7\text{N}_2\text{I-LiOH}$  and  $\text{Li}_3\text{YCl}_6$  solid electrolyte with high ionic conductivity and low electronic conductivity will be used to validate the criterion for lithium dendrite suppression, to achieve the project objective.

**Approach.** Solid-state reaction will be used for synthesis of  $\text{Li}_7\text{N}_2\text{I-LiOH}$  and  $\text{Li}_3\text{YCl}_6$ . The morphology and atomic structure of  $\text{Li}_7\text{N}_2\text{I}$  will be characterized by SEM, transmission electron microscopy (TEM), and XRD. A dendrite suppression model based on the Butler-Volmer model and conductive atomic force microscopy (C-AFM) will be developed.

**Out-Year Goals.** In year one, the project will synthesize, modify, and optimize the  $\text{Li}_7\text{N}_2\text{I-LiOH}$ ,  $\text{Li}_3\text{YCl}_6$  electrolytes, and  $\text{Li}_7\text{N}_2\text{I-LiOH/Li}_3\text{YCl}_6$  bi-layered electrolytes to achieve a high ionic conductivity to  $> 5 \times 10^{-4} \text{ S/cm}$  and to suppress lithium dendrite even at a high current of  $> 3.0 \text{ mA/cm}^2$  and capacity of  $> 3.0 \text{ mAh/cm}^2$ . The team will focus on enhancing the CE for lithium anode to  $> 99\%$ . The CE of the solid electrolyte is a sensitive indicator of stability of the electrolyte against lithium and lithium dendrite, but it has been ignored by the SSB community due to very low CE ( $< 90\%$ ) of the solid electrolytes such as LPS.

**Collaborations.** This project funds work at the University of Maryland College Park.

### Milestones

1. Synthesis of  $\text{Li}_7\text{N}_2\text{I-LiOH}$  and  $\text{Li}_3\text{YCl}_6$  electrolytes with high ionic conductivity. (Q1, FY 2020; Completed, December 31, 2019)
2. Electrochemical property of  $\text{Li}_7\text{N}_2\text{I-LiOH}$  and  $\text{Li}_7\text{N}_2\text{I-LiOH/Li}_3\text{YCl}_6$  bi-layer film. (Q2, FY 2020; In progress)
3. Lithium dendrite suppression capability. (Q3, FY 2020)
4. High CE for lithium plating/stripping. (Q4, FY 2020)

## Progress Report

### Synthesis, Characterization, and Optimization of $\text{Li}_7\text{N}_2\text{I-LiOH}$ , $\text{Li}_3\text{YCl}_6$ , and $\text{Li}_7\text{N}_2\text{I-LiOH/Li}_3\text{YCl}_6$ Bi-Layer Solid Electrolytes

$\text{Li}_7\text{N}_2\text{I-LiOH}$  and  $\text{Li}_3\text{YCl}_6$  were prepared using solid-state reaction. Commercial  $\text{Li}_3\text{N}$  (99.9%, Sigma Aldrich),  $\text{LiI}$  (99.9%, Sigma Aldrich) and dehydrated  $\text{LiOH}$  (99.9%, Sigma Aldrich) were mixed according to the molar ratio. The mixture was ball-milled under an argon atmosphere with zirconia balls in a zirconia vial. The collected powder samples were pressed into pellets under isostatic pressure. The pellet was then sealed and reacted in a silica tube under the argon atmosphere. The  $\text{Li}_3\text{YCl}_6$  powder was prepared by ball-milling of a mixture of  $\text{LiCl}$  (> 99.9%, Sigma-Aldrich) and  $\text{YCl}_3$  (> 99.9%, Sigma-Aldrich) at a molar ratio of  $\text{LiCl/YCl}_3 = 3/1$  for 4.5 h.

As shown in Figure 25a, the  $\text{Li}_7\text{N}_2\text{I-LiOH}$  solid-state electrolyte pellet renders a yellow color. The XRD pattern of the  $\text{Li}_7\text{N}_2\text{I-LiOH}$  powder shows the cubic  $\text{Li}_7\text{N}_2\text{I}$  crystal (Figure 25c). The synthesized  $\text{Li}_3\text{YCl}_6$  also renders crystal peaks in Figure 25d. The morphology of  $\text{Li}_7\text{N}_2\text{I-LiOH}$  pellet was characterized using SEM as the images shown in Figure 26. Hexahedron  $\text{Li}_7\text{N}_2\text{I-LiOH}$  particles are closely connected to each other with a uniform size distribution. Using the suspension casting method, the bi-layer  $\text{Li}_7\text{N}_2\text{I-LiOH/Li}_3\text{YCl}_6$  electrolyte thin film was fabricated. The energy dispersive X-ray spectroscopy (EDS) of the cross-section of the bi-layer electrolyte is shown in Figure 27.

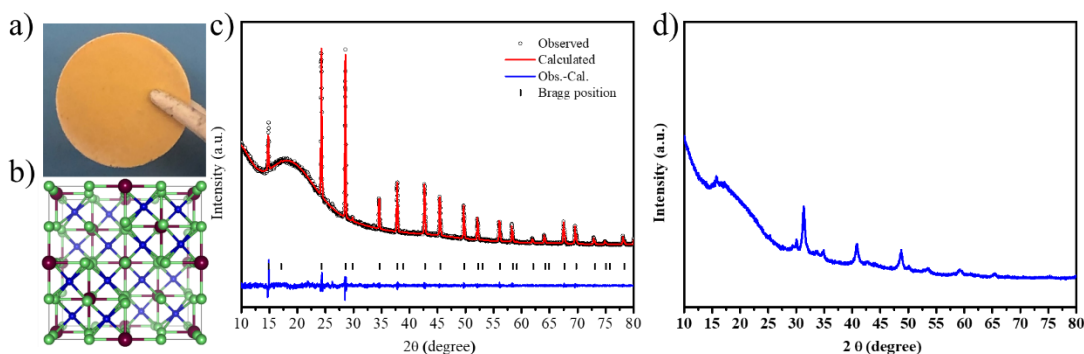


Figure 25. (a) Digital photo of the as-assembled  $\text{Li}_7\text{N}_2\text{I-LiOH}$  pellet and its corresponding (b) crystal structure. X-ray diffraction of the synthesized (c)  $\text{Li}_7\text{N}_2\text{I-LiO}$  and (d)  $\text{Li}_3\text{YCl}_6$  solid-state electrolytes.

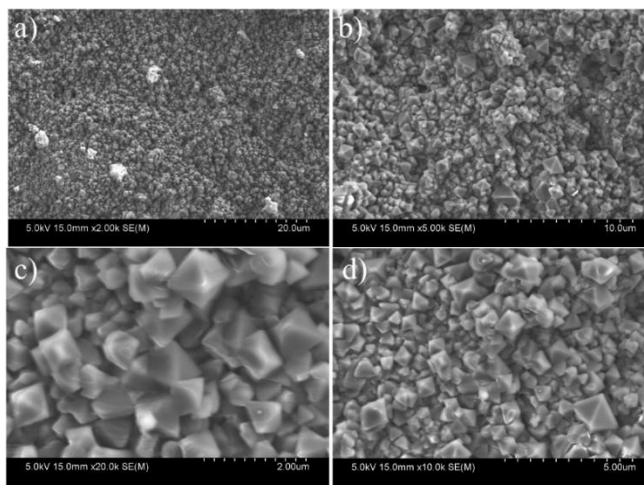


Figure 26. Scanning electron microscopy of the synthesized  $\text{Li}_7\text{N}_2\text{I-LiOH}$  solid-state electrolytes.

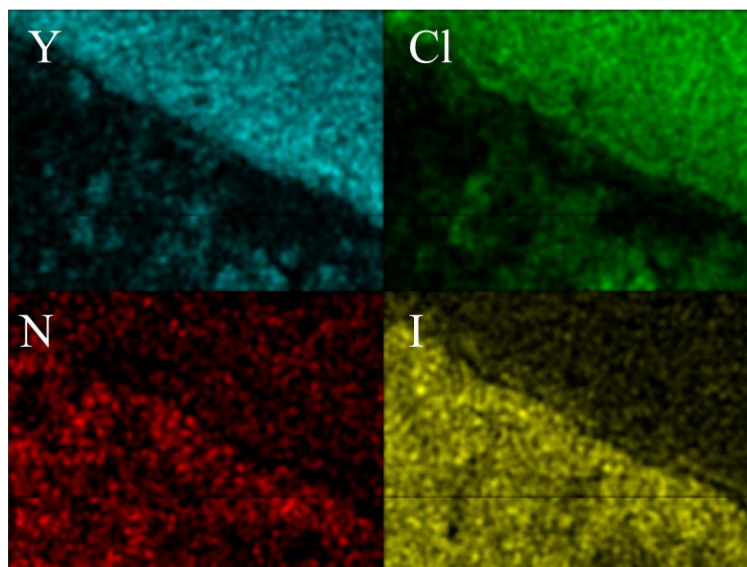


Figure 27. Energy dispersive X-ray spectroscopy of cross-section of the  $\text{Li}_7\text{N}_2\text{I-LiOH/Li}_3\text{YCl}_6$  bi-layered electrolyte fabricated using suspension casting method.

### Fabrication and Electrochemical Characterization of $\text{Li}_7\text{N}_2\text{I-LiOH}$ , $\text{Li}_3\text{YCl}_6$ , and $\text{Li}_7\text{N}_2\text{I-LiOH/Li}_3\text{YCl}_6$ Electrolyte Pellets

The total ionic conductivities of the electrolyte pellets (2 mm in thickness and 1 mm<sup>2</sup> in area) were measured using Au/electrolyte/Au blocking electrodes. As shown in Figure 28a, the total ionic conductivities of  $\text{Li}_7\text{N}_2\text{I-LiOH}$  and  $\text{Li}_3\text{YCl}_6$  at room temperature are 0.14 mS/cm and 0.48 mS/cm, respectively. The ionic conductivity increases with temperature (Figure 28c). Figure 28d shows the Arrhenius plot for the total conductivity of  $\text{Li}_7\text{N}_2\text{I-LiOH}$  pellet. The activation energy calculated based on the Arrhenius Equation is 0.34 eV, thus potentially supporting operation in a wide temperature range. Figure 29 shows the CV curve of  $\text{Li}|\text{Li}_7\text{N}_2\text{I-LiOH-Li}_3\text{YCl}_6|$  solid-state cells at a scan rate of 1 mV/s. The CV indicates that the combination of  $\text{Li}_7\text{N}_2\text{I-LiOH/Li}_3\text{YCl}_6$  bi-layer solid-state electrolyte enables a wide voltage window of 0-5 V.

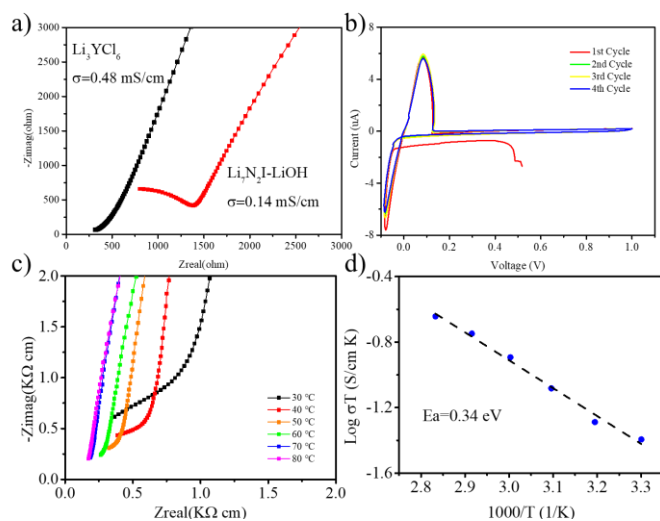


Figure 28. Electrochemical characters of  $\text{Li}_7\text{N}_2\text{I}$  and  $\text{Li}_3\text{YCl}_6$  solid-state electrolytes. (a) Electrochemical impedance spectroscopy (EIS) of  $\text{Li}_7\text{N}_2\text{I-LiOH}$  and  $\text{Li}_3\text{YCl}_6$  solid-state electrolyte. (b) Cyclic voltammetry curve from -0.1 to 1.0 V at the scan rate of 1 mV/s. (c) EIS of  $\text{Li}_7\text{N}_2\text{I-LiOH}$  at different temperatures. (d) Arrhenius plot of  $\text{Li}_7\text{N}_2\text{I-LiOH}$  solid-state electrolyte.

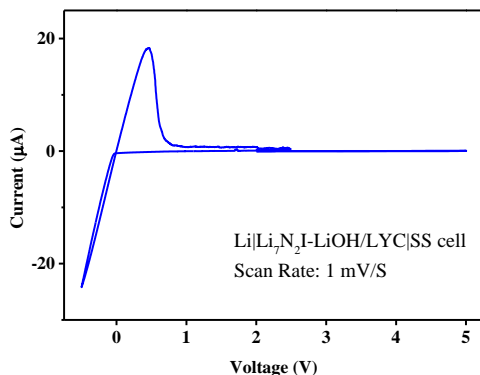


Figure 29. Cycle voltammetry of Li|Li<sub>7</sub>N<sub>2</sub>I-LiOH-Li<sub>3</sub>YCl<sub>6</sub>|SS solid-state cells at a scan rate of 1 mV/s.

### Development of Lithium Dendrite Suppression Criterion for Solid Electrolytes

The investigation of lithium dendrite suppression in SSEs mainly focuses on reaction kinetics of lithium plating/stripping. The grain boundaries (GBs), voids on the interface are considered responsible for the highly effective current density ( $I_{\text{eff}}$ ), which leads to lithium dendrite growth. The high  $I_{\text{eff}}$  will cause a large deviation from the lithium plating/stripping equilibrium at the Li|SSE interface and exacerbate the lithium dendrite formation reaction in the SSE. Interface engineering such as coating and applying stack pressure to the cell enhances the contact area and reduces the  $I_{\text{eff}}$ . However, interface reactions between lithium and SSE will also increase  $I_{\text{eff}}$  during the cycling process. The impact of the interface reaction for the  $I_{\text{eff}}$  has been neglected since most of the interface engineering work using electronic conductivity artificial SEI cannot block the reactions. For example (Figure 30a), when lithium metal was attached to the LPS electrolyte, the LPS would be reduced to form interphases (Li<sub>2</sub>S and Li<sub>3</sub>P). The interface reaction will lead to volume changes, cracks, and losses of physical contact between SSE and lithium metal. Moreover, the main component of the formed interphases, Li<sub>2</sub>S, is an insulator, as discussed above; this leads to invalid contact with lithium metal and increasing of  $I_{\text{eff}}$ . The formed Li<sub>3</sub>P interphase enhances electronic conductivity, further promoting the reduction reaction of LPS. The spatial distribution of the interphases with different ionic and electronic conductivity will generate more voids between lithium and SSE interface for the uneven electric field distribution and lithium deposition.

The  $I_{\text{eff}}$  will serve as a driving force for deviation from the lithium plating/stripping equilibrium at the Li|SSE interface, showing as overpotential in a typical charge/discharge curve. As shown in Figure 30b, the driving force can turn the lithium plating/stripping equilibrium in the Li|SSE system to a meta-stable equilibrium, including the lithium dendrite formation process. As aforementioned, the  $I_{\text{eff}}$  in the unstable interface would be large because the reaction caused losses of physical contact. Hence, lithium plating equilibrium goes to a high-energy meta-equilibrium state, increasing the possibility of lithium dendrite formation reaction. At the same time, cracks will decrease density of SSE and stress during lithium dendrite formation in SSEs, lowering the dendrite formation barrier. The high electronic conductivity of the interphase also promotes lithium deposit into the SSE since electrons can accelerate the lithium dendrite. The larger driving force and lower resistance synergistically make lithium dendrites propagate in SSE easily. To decrease the lithium dendrite formation possibility with a stable or a low  $I_{\text{eff}}$ , SSEs should have high interface energy against lithium metal. When lithium dendrite propagates into SSEs, new Li|SSE interface will form, which introduces more interface energy penalty. Higher interface energy penalty will enhance the lithium dendrite formation barrier, improve the anti-disturbance capability, and reduce the portion of lithium dendrite formation reaction.

A decent Li|SSE interface for lithium dendrite propagation should reduce the disturbance driving force while enhancing anti-disturbance capability. Based on this principle, the SSE should satisfy the following requirements: (1) be stable with lithium metal and have a high interface energy against lithium metal to restrict the lithium penetration into SSEs; (2) have low electronic conductivity to prevent lithium plating inside the SSE; and (3) have low ASR to reduce the lithium plating overpotential (driving force). If the SSEs are not stable against lithium metal, but the formed interphases are dense and satisfy the above requirements, the SSEs could also be able to suppress the lithium dendrite growth in SSEs.

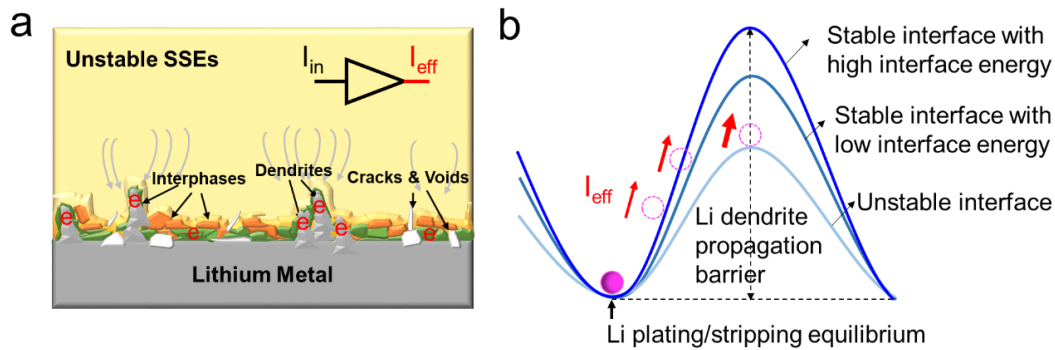


**Figure 30. Schematic of physical and chemical stable interface for dendrite suppression. Schematic illustration of the (a) current amplification effect between lithium and unstable SSEs interface, and (b) lithium dendrite suppression mechanism.**

The phase diagram of  $\text{Li}_7\text{N}_2\text{I}$  shows the phases present in Li-N-I ternary chemical space. The red dashed line shows the thermodynamic equilibrium reaction path for  $\text{Li}_7\text{N}_2\text{I}$  (Figure 31a). According to the grand potential diagram, the  $\text{Li}_7\text{N}_2\text{I}$  is a stable phase against lithium metal. When increasing the potential, the  $\text{Li}_7\text{N}_2\text{I}$  will be oxidized into  $\text{LiN}_3$  and  $\text{LiI}$  at voltage above 0.5 V, and the formed components are further oxidized into  $\text{IN}_4$  and  $\text{I}$  at 2.5 V (Figure 31b). In Figure 31c, the electrochemical window  $\text{Li}_3\text{YCl}_6$  is from 1.0 V to 4.2 V versus  $\text{Li}^+/\text{Li}$ . In comparison to LPS, the electrochemical window of  $\text{Li}_7\text{N}_2\text{I}$ - $\text{LiOH}/\text{Li}_3\text{YCl}_6$  bi-layered electrolyte is significantly extended (Figure 31c).

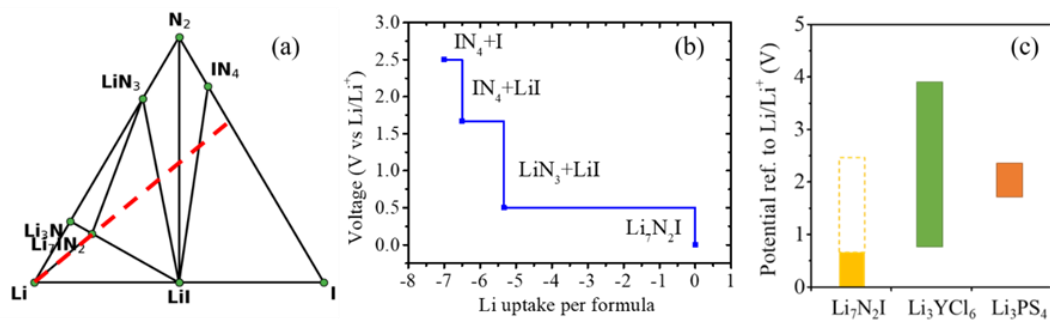


**Figure 31. (a) Density functional theory calculated phase diagram. (b) Grand potential phase diagram. (c) Electrochemical windows; the oxidation potential to fully delithiate  $\text{Li}_7\text{N}_2\text{I}$  is marked by the dashed line.**

C-AFM was set up for both basic topographic information and potential advance function like current response or modulus. Figure 32 shows the current response of a conventional cathode composed of  $\text{LiMn}_2\text{O}_4$ , PVDF binder, and C65 conductive agent measured by C-AFM. As shown in Figure 32c, some scattered high current response areas are observed with a light color, which is attributed to C65 conductive agents. The dark parts that have lower or even no current response, correspondingly, indicate poor conductivity and perhaps the gathered  $\text{LiMn}_2\text{O}_4$  particles. The C-AFM technique will be used to measure electronic conductivity of GB in  $\text{Li}_7\text{N}_2\text{I}$ - $\text{LiOH}$  SSE.

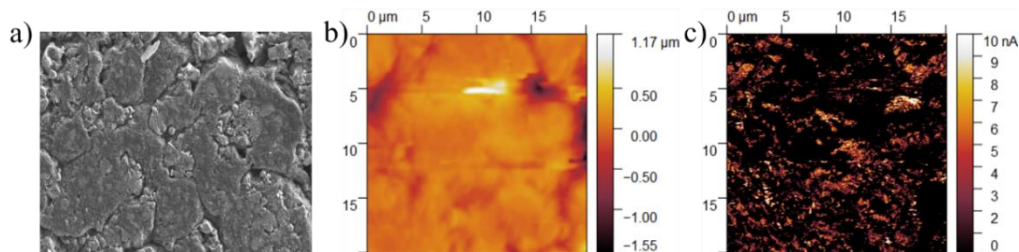


**Figure 32. (a) Scanning electron microscopy image. Atomic force microscopy (AFM) topographic height image (b) and corresponding AFM current image (c) of a conventional cathode composed of  $\text{LiMn}_2\text{O}_4$ , PVDF binder, and C65 conductive agent.**

## Patents/Publications/Presentations

### Publication

- Ji, X., S. Hou, P. F. Wang, X. Z. He, N. Piao, J. Chen, X. L. Fan, and C. S. Wang. “Solid Electrolyte Design for Lithium Dendrite Suppression.” In preparation.

## Task 1.12 – Hot Pressing of Reinforced Lithium-NMC All-Solid-State Batteries with Sulfide Glass Electrolyte (Thomas Yersak, General Motors)

**Project Objective.** The objective of this project is to research, develop, and test Li-NMC ASSBs capable of achieving program performance metrics by implementing sulfide glass SSEs and hot press processing in a dry room environment. The performance of ASSBs with sulfide SSEs is limited because they are essentially green tapes with up to 20% porosity. In composite cathodes, the porosity limits energy density and power, while porosity in the separator acts as a conduit for Li-metal deposits if cycling conditions (that is, C-rate, operating temperature, and pressure) are not strictly controlled. The goal of the project is to demonstrate that the hot pressing method and appropriately formulated sulfide glass SSEs can eliminate porosity to enable Li-NMC ASSBs with energy density of  $\geq 350$  Wh/kg.

**Project Impact.** The hot press processing method and appropriately formulated sulfide glass SSEs may enable Li-NMC ASSBs with improved energy density  $> 350$  Wh/kg. GM's processing technology depends on heating a sulfide glass SSE above its glass transition temperature,  $T_g$ , at which point it can consolidate via viscoplastic flow. In the composite cathode, hot pressing provides liquid-like contact between the NMC cathode and SSE to increase energy density and power by enabling thick composite cathodes with high active material loading. Furthermore, cathode-supported sulfide glass separators can be made dense and thin by hot pressing. A dense separator enables the robust use of a Li-metal anode because lithium deposits may be more effectively blocked, preventing cell shorting.

**Approach.** The sulfide SSE used in the composite cathode, otherwise known as the catholyte, will dictate the processing specifications for ASSB hot pressing. Thermal stability can be achieved by NMC passivation and proper catholyte formulation. This project will systematically evaluate different NMC coatings, catholyte formulations, and hot press processing specifications (that is, temperature, time, and pressure). The performance of hot pressed ASSBs will be compared to green baseline ASSBs and hot pressed control ASSBs consisting of the  $\beta$ -Li<sub>3</sub>PS<sub>4</sub> and Li<sub>6</sub>PS<sub>5</sub>Cl model SSEs. Electron microscopy will be employed to understand interfacial phenomena and track composite cathode microstructure before and after hot pressing.

**Out-Year Goals.** In the second year of this project, a sulfide glass SSE will be formulated specifically for use as the separator. The separator glass SSE formulation will be designed to achieve full densification under the hot press processing specifications determined for the catholyte. Separator glass formulation design will also consider cathodic stability, moisture stability, and ionic conductivity. Once a system of separator glass SSE and catholyte has been determined, the third year of the project will demonstrate hot pressed full cells at the coin-cell and single-layer pouch cell levels, which meet program target performance metrics.

**Collaborations.** GM will lead this project with no subrecipients.

### Milestones

1. Establish protective coating on cathode: select the best coating method and coating chemistry. Confirm conformality of coating using microscopy. (Q2, FY 2020; In progress)
2. Develop a suitable baseline system with a reversible capacity of about 120 mAh/g. (Q3, FY 2020; In progress)
3. Determine the parameters required to prepare cathode samples via focused ion beam (FIB)/SEM lift-out and to analyze samples via high-resolution TEM (HRTEM). (Q4, FY 2020; In progress)
4. Demonstrate a hot pressed cathode with a reversible capacity of 120 mAh/g. Analysis indicates technical approach capable of achieving performance targets. (Q1 FY 2021; In progress)

## Progress Report

The project was finalized and approved this quarter, with the first milestones due in the second quarter. As a result, GM used this quarter to ramp up project activities. Activities included hiring two contract employees to execute project deliverables, setting up laboratory space, acquiring materials, and having personnel undergo training at the University of Michigan's MC<sup>2</sup> user facility in preparation for sample characterization work. The time was also spent conducting work to establish a baseline and to outline a strategy for cell characterization via electron microscopy, as detailed below.

GM began work on developing a suitable baseline ASSB using high-energy LiNi<sub>0.8</sub>Co<sub>0.1</sub>Mn<sub>0.1</sub>O<sub>2</sub> (NMC-811) as the cathode active material. GM's NMC-811 was obtained from BASF without the typical proprietary surface coatings applied for this cathode composition. Proprietary coatings are optimized for conventional Li-ion batteries with liquid electrolyte and not for application in ASSB. Furthermore, it is crucial to fully understand the NMC-811 passivating coating characteristics if GM is to rigorously study interfacial phenomena between NMC-811 and sulfide SSE catholyte during hot pressing. To this end, GM successfully applied a LiNbO<sub>3</sub> coating to NMC-811 via a solution-based method.<sup>1</sup> Work is ongoing to characterize the thickness and conformality of coatings, and these results will be reported next quarter. Another feature of BASF NMC-811 is that it has an average particle diameter of less than 5 μm (Figure 33), which prior work has found to be optimal for ASSB.<sup>2</sup> As the baseline catholyte, GM has chosen the BMR β-Li<sub>3</sub>PS<sub>4</sub> model SSE. This SSE prepared by GM has an ionic conductivity of approximately 2 × 10<sup>-4</sup> S/cm at room temperature and acceptable anodic stability against cathode materials.

In addition to the choice of active material and SSE, GM has also considered the composition of the baseline composite cathode and its preparation method. GM's baseline composite cathode contains an aggressive active material loading of 70 wt% NMC-811@LiNbO<sub>3</sub> and 30 wt% β-Li<sub>3</sub>PS<sub>4</sub>. Furthermore, no carbon black is used in GM's baseline composite cathode for two reasons. First, eliminating carbon black decreases porosity to increase energy density. Second, to effectively study the thermal stability of the NMC-811/β-Li<sub>3</sub>PS<sub>4</sub> interface during hot pressing, it is important to control confounding factors. Carbon black may promote side reactions at the NMC-811/β-Li<sub>3</sub>PS<sub>4</sub> interface, so it is eliminated in the baseline. The preparation method of the baseline composite cathode is also important. As seen in Figure 33, aggregation of SSE particles occurs when the composite cathode is prepared by small-scale hand grinding. Aggregation of SSE particles leads to a degraded percolation network and therefore poor performance. Therefore, GM is evaluating low-energy ball milling as a method to prepare baseline composite cathodes. Ball milling likely promotes uniform particle distribution to increase NMC-811 utilization and results in better electrochemical performance. Cycling data for a preliminary baseline cell (NMC-811@LiNbO<sub>3</sub>/β-Li<sub>3</sub>PS<sub>4</sub>/Li<sub>x</sub>In) with a composite cathode prepared by ball milling is provided in Figure 34. It exhibited a reversible capacity of 138 mAh/g with CE of 73% in the first cycle at 0.05C-rate (Figure 34a) and decent cycling stability after a rate test (Figure 34b).

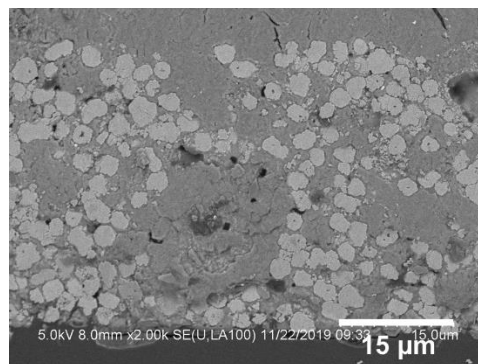


**Figure 33. Cross section of a baseline composite cathode prepared by hand mixing. Severe solid-state electrolyte aggregation is evident. Sample cross section was prepared by Ar-ion milling.**

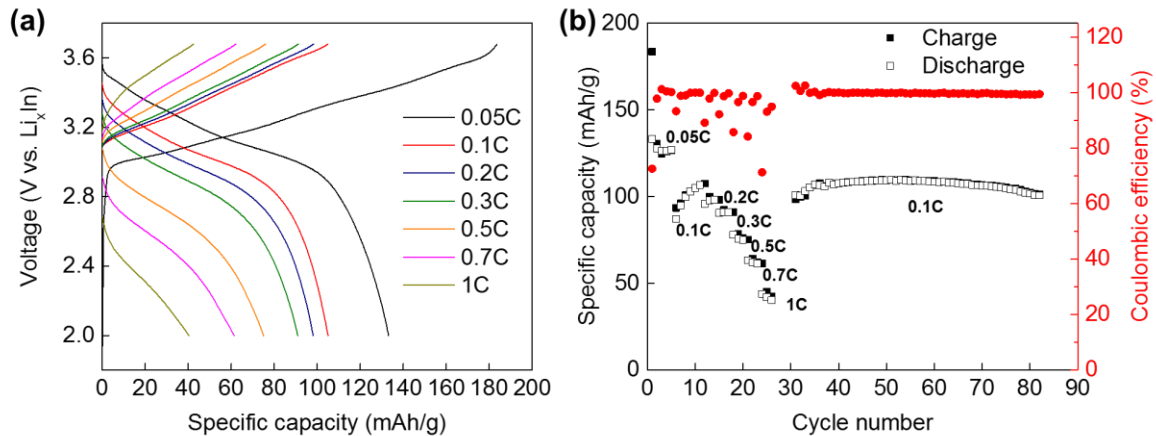


Figure 34. Electrochemical performance of NMC-811@LiNbO<sub>3</sub>/β-Li<sub>3</sub>PS<sub>4</sub>/Li<sub>x</sub>In battery at room temperature: (a) voltage profile and (b) rate capabilities.

In the preceding quarter, GM outlined a strategy to characterize hot-pressed ASSB using electron microscopy. At the GM facility, the team has access to an Ar-ion miller, field emission SEM, a Ga-ion FIB, and Cs-corrected TEM. At the University of Michigan MC<sup>2</sup> user facility, the team has access to another Ga-ion FIB, plasma FIB (PFIB), SEM-Raman spectroscopy, two HRTEMs, a double Cs-corrected TEM, and multiple X-ray detector TEMs. Electron microscopic analysis is carried out for characterization of the NMC-811/SSE interface at multiple length scales. The large-scale (micron) cross-sectional imaging is done with the Ar-ion miller and PFIB. The results obtained by these techniques initially provided microstructural information on NMC particle distribution and SSE aggregation in hand mixed composite cathodes (Figure 33). Future work will investigate degradation of the cathode/anode electrode after cycling, density of the SSE, and micro-scale microstructure evolution of catholyte after hot pressing. Preparation of large-scale sample cross-sections using Ar-ion milling can also be used for future spectroscopic work. The flat surface produced by ion beam is ideal for chemical analysis such as EDS and Raman spectroscopy in SEM. Preparing samples with the Ar-ion mill minimizes artifacts caused by geometric aspect. The SEM-Raman, a Raman spectrometer mounted on a SEM, will provide the team with another chemical analysis technique to complement EDS. High-resolution analysis can be achieved using SEM-Raman because the Raman spectra are collected *in vacuo*.

In addition to providing ideal samples for chemical analysis, cross-sectioned surfaces will also be used to prepare TEM samples by the Ga-ion milling lift-out technique for small-scale (nanometer) analysis. A cross-section prepared by manually fracturing a sample would have a very rough surface and would take longer to prepare TEM samples while also being of poorer quality. The Cs-corrected TEM and double Cs-corrected TEM will be used for the atomic-scale characterization of NMC-811/catholyte interface. GM's aim is to discover the role that the NMC passivating coating and the catholyte formulation have in promoting thermal stability during hot pressing. The MC<sup>2</sup> facility is acquiring and installing an air-sensitive sample transfer system for TEM. The current sample transfer system does not provide full air-protection environment, and it causes samples to be exposed to air briefly. Thus, epoxy resin infiltration is applied to minimize the air and moisture damage. Also, conventional epoxy resin is not suitable for electron microscopic work. Thus, the team uses "Spurr-kit" epoxy resin, which has a low viscosity, long working time, and slow curing rate, and is optimized for electron microscopy. Furthermore, the liquid emersion method can be used for protecting TEM samples in the absence of an appropriate air-sensitive sample transfer system. It is well known that toluene can be used to protect samples from moisture during transfer. However, toluene is a toxic solvent; thus, DEC can be used as an alternative. The protective solvent will be evaporated in the vacuum chamber while the TEM holder is loaded into the TEM.

#### References

- [1] Ohta, N., et al. *Electrochemistry Communications* 9.7 (2007): 1486–1490.
- [2] Bielefeld, A., D. A. Weber, and J. Janek. *The Journal of Physical Chemistry C* 123.3 (2018): 1626–1634.

## Patents/Publications/Presentations

The project has no patents, publications, or presentations to report this quarter.

## Task 1.13 – Low Impedance Cathode/Electrolyte Interfaces for High-Energy-Density Solid-State Batteries (Eric Wachsman and Yifei Mo, University of Maryland)

**Project Objective.** The objective of this project is to research, develop, and test Li-metal-based batteries that implement solid LICs equipped with NMC cathodes integrated into the Li-metal/LLZ ( $\text{Li}_7\text{La}_3\text{Zr}_2\text{O}_{12}$ ) tri-layer architecture capable of achieving the following: (1) identify and demonstrate interfacial layers to achieve low-impedance and stable NMC/LLZ interfaces; (2) develop novel processing techniques to fabricate NMC/LLZ composite cathodes with low interfacial resistance; and (3) high performance ASSBs with an energy density of 450 Wh/kg and 1400 Wh/L and negligible degradation for 500 cycles.

**Project Impact.** Instability and/or high resistance at the interface of high-energy cathode materials with lithium-garnet solid electrolytes limit the high energy density all-solid-state lithium battery. This project will lead to a fundamental understanding of solid-electrolyte/solid-cathode interfaces and a unique and transformative LLZ framework to enable high-energy density, safe Li-metal batteries approaching ~ 400 Wh/kg.

**Approach.** In this new EERE project, the team will build on their demonstrated expertise with garnet electrolytes and ASSB cells to accomplish the following: (1) engineer interfaces to overcome high NMC/LLZ interfacial impedance and interfacial degradation; (2) develop processing and fabrication techniques to achieve high-loading NMC/LLZ composite cathodes with low resistance and high cyclability; and (3) integrate the NMC/LLZ cathodes into all-solid-state Li-metal/LLZ cells to achieve high-energy-density batteries.

**Out-Year Goals.** The project will solve the current challenges of integrating garnet solid electrolyte with a cathode to achieve a high-performance ASSB using a high-energy-density Li-metal anode. The resultant high energy density and stability using both high-energy-density Li-metal anodes and NMC cathodes will open new applications in portable electronics, EVs, and beyond.

**Collaborations.** This project funds work at UMD. Dr. E. Wachsman (PI) will have overall management responsibility for the project and will lead experimental efforts including garnet synthesis, interface processing, cell fabrication, and testing. Dr. Y. Mo (Co-PI) will lead the computational efforts on understanding the stability between garnet and cathode and on identifying promising coating materials.

### Milestones

1. Computationally determine interfacial stability between LLZ solid electrolytes and NMC cathode. (Q2, FY 2020; In progress)
2. Determine thermochemical stability between LLZ and infiltrated NMC. (Q3, FY 2020; In progress)
3. Computationally determine the mechanism of interfacial stabilization between LLZ and NMC through coating layers. (Q3, FY 2020; initiated)
4. Go/No-Go Decision: Computationally determine appropriate compositions to stabilize the LLZ-NMC interface. Achieve design capable of meeting performance requirements. (Q4, FY 2020)

## Progress Report

Computational studies based on first-principles calculations have been initiated to evaluate the thermodynamic interface stability of LLZ solid electrolytes for cathode materials using the thermodynamic analysis demonstrated in previous studies. As a test and benchmark of the project's current model, the team's theoretical calculations found that LLZ garnet has minor reaction with lithiated  $\text{LiCoO}_2$  and decomposes into a phase equilibria of  $\text{La}_2\text{O}_3$ ,  $\text{Li}_6\text{Zr}_2\text{O}_7$ , and  $\text{Li}_5\text{CoO}_4$ , with a small mutual reaction energy of  $-1$  meV/atom. Moreover, LLZ garnet is less stable with delithiated  $\text{Li}_{0.5}\text{CoO}_2$ , decomposing into  $\text{La}_2\text{O}_3$ ,  $\text{La}_2\text{Zr}_2\text{O}_7$ ,  $\text{Li}_7\text{Co}_5\text{O}_{12}$ , with a reaction energy of  $-39$  meV/atom. These formed products are consistent with previous computation studies and previous experimental studies, confirming the validity of the project's current computation models.

The computational analyses based on the same method have been initiated to identify the interface stability of LLZ solid electrolytes with NMC cathode in comparison to  $\text{LiCoO}_2$  (Figure 35). The computation study found that Ni-rich cathode materials such as NMC in general exhibit more reaction than  $\text{LiCoO}_2$ , and thus a poor interface stability of garnet-NMC is expected. In particular, the delithiated NMC shows much lower stability than lithiated NMC. The team further identified the thermodynamic equilibria of the reaction products, which will

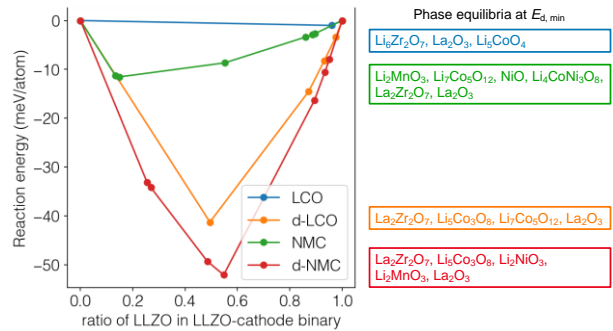


**Figure 35. Decomposition of LLZ with lithiated and delithiated (prefix "d-") LCO and NMC-111. Phase equilibria of each reaction at the minimum decomposition energy for the pseudobinary of LLZO and cathode are written at right.**

be compared to experimental results in the future stage of the project. In addition, the team also studied the stability of LLZ solid electrolytes for a variety of compositions with dopants such as niobium, tantalum, and tin on the zirconium site, and found similar stability trends as LLZ.

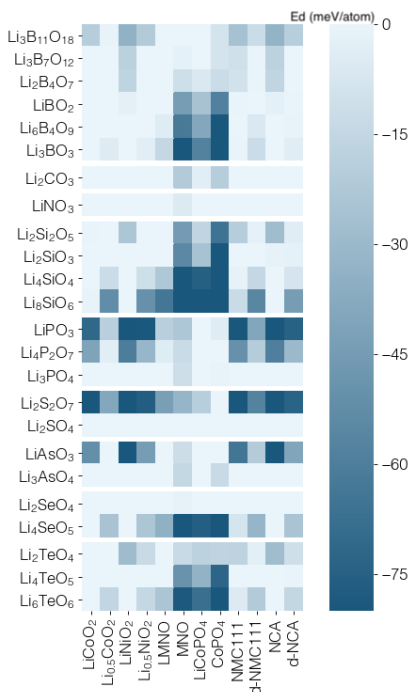


**Figure 36. Stability heatmap of lithiated and delithiated (prefix "d-") NMC-111 ( $\text{LiMn}_{0.3}\text{Co}_{0.3}\text{Ni}_{0.3}\text{O}_2$ ) and NCA ( $\text{LiAl}_{0.05}\text{Co}_{0.15}\text{Ni}_{0.8}\text{O}_2$ ) cathodes compared to  $\text{LiNiO}_2$ ,  $\text{LiCoO}_2$ , and other high-voltage cathodes.**

They also studied the coating layer on cathode materials as the first step to identify the promising coating layers between LLZ-NMC interfaces. Using the project's thermodynamic scheme, the team studied the interface stability of a wide range of lithium ternary oxides with commonly used cathode materials. Their analyses identified a wide range of coating materials that have been demonstrated in previous experimental studies, suggesting the validity of their approach and the promises in predicting new materials. In addition, the team compared the materials stability with different cathodes, such as  $\text{LiCoO}_2$ ,  $\text{LiNiO}_2$ , NMC-111 ( $\text{LiMn}_{0.3}\text{Co}_{0.3}\text{Ni}_{0.3}\text{O}_2$ ) and NCA ( $\text{LiAl}_{0.05}\text{Co}_{0.15}\text{Ni}_{0.8}\text{O}_2$ ). The variation of materials stability was identified among these cathodes (Figure 36). It was found that in all these cathodes, the delithiated states are generally less stable, and higher nickel content generally leads to poor stability with these coating materials. These results will be used for further detailed analyses to identify promising coating for LLZ-NMC interfaces.

## Patents/Publications/Presentations

### Publication

- Nolan, A. M., Y. Liu, and Y. Mo.\* “Solid-State Chemistries Stable with High-Energy Cathodes for Lithium-Ion Batteries.” *ACS Energy Letters* 4 (2019): 2444–2451.

**Task 1.14 – Developing an *In Situ* Formed Dynamic Protection Layer to Mitigate Lithium Interface Shifting: Preventing Dendrite Formation on Metallic Lithium Surface to Facilitate Long Cycle Life of Lithium Solid-State Batteries**  
(Deyang Qu, University of Wisconsin Milwaukee)

**Project Objective.** The objective of this project is to research, develop, and test lithium metal-based batteries that implement solid LICs equipped with a formed dynamic protection layer. The proposed project aims to enable safe, long-cycle lithium anodes to achieve cell performance targets of 400 Wh/Kg, over 100 cycles, with 15-year shelf life and < \$100/KWh cost.

**Project Impact.** Project efforts are to contribute an in-depth understanding of the lithium interface and dendrite growth prevention to the field of Li-metal batteries, which will pave the way for eventual development of high-energy-density, low-cost, and long-lasting lithium batteries. This advancement could be a crucial selling point for the greater adoption of EVs. This project will make possible the translation of fundamental research into practical implementation of high-energy lithium anodes, enabling eventual achievement of cell performance targets.

**Approach.** The novelty of this approach is that the team intends to mitigate the dendrite problem by creating a dynamic protection layer during the interface shift to prevent dendrite formation throughout battery operation.

**Out-Year Goals.** The project has three out-year goals: (1) *in situ* diagnostic tools are fully functional; (2) potential candidates for Li-anode modifications are identified; and (3) synthesis routes are designed.

**Collaborations.** The PI is the Johnson Control Endowed Chair Professor, who has close and frequent collaboration with Johnson Controls' scientists and engineers. The collaboration enables the team to validate the outcomes of fundamental research in pilot-scale cells. The PI also has been working closely with top scientists at Argonne National Laboratory (ANL), Brookhaven National Laboratory (BNL), LBNL, and PNNL and with U. S. industrial collaborators, for example, General Motors, Millipore Sigma, and Clarios. In addition, the team works with international collaborators in China, Japan, and South Korea. These collaborations will be strengthened and expanded to give this project a vision with both today's state-of-the-art technology and tomorrow's technology in development, while incorporating feed-back from the material designers and synthesizers upstream, as well as from the industrial end users downstream.

### Milestones

1. *Baseline.* Conduct literature review and establish baseline for proposed technologies. (Q1, FY 2020; Completed)
2. *Fully functional fixtures and setups.* *In situ* electrochemical-optical and *in situ* electrochemical-MS cells are capable of observing dendrite growth and detecting gas generation real-time. (Q1, FY 2020; Completed)
3. *Coating methods.* Physical requirements of each coating technique and adaption of different coating methods for various coating materials based on their properties are identified. (Q2, FY 2020; In progress)
4. *N-type polymer compounds.* N-doped polymer compounds are synthesized. (Q3, FY 2020; In progress)
5. *In situ* diagnostic tools capable of investigating a coated lithium electrode / projected cell performance. Various selected materials can be coated on a lithium surface forming an artificial layer before cell assembly. The dendrite growth and gassing of the coated electrode can be investigated real-time during cell operation with *in situ* diagnostic tools. Analysis indicates technical approach capable of achieving performance targets. (Q4, FY 2020; In progress)

## Progress Report

This quarter, the team has reviewed and will continue reviewing the literature on dendrite growth protection and Li/solid state interface. In addition, they have modified and validated the apparatus for the *in situ* electrochemical MS analysis (Figure 37) and the *in situ* electrochemical optical analysis (Figure 38). The

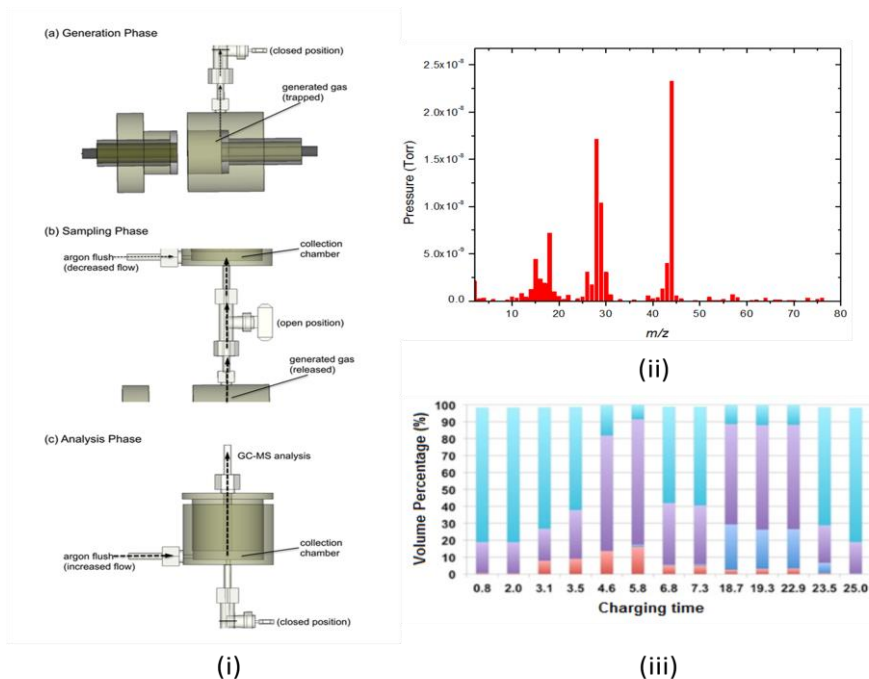


Figure 37. Electrochemical cell for *in situ* mass spectroscopic (MS) experiments (i). The gas generated during the cycling can be monitored in real-time with a gas analyzer (MS). The design of the *in situ* cell eliminates the influence of the carry-over residual gases, so the gas amount and composition can be determined either at various voltage or various charging time (iii). An example of analysis data is shown in (ii).

former one is used to detect gas generation real-time during the cycling of a lithium anode, and the latter one is for observation of dendrite growth/dissolution in real-time during cycling. Examples of results and observations are shown in Figures 37 and 38. Figure 37 shows that the gases generated can be well identified (ii) and the change of gas composition can be monitored in real time (iii). Figure 38 shows that the change of lithium morphology can be viewed in a 3D photo.

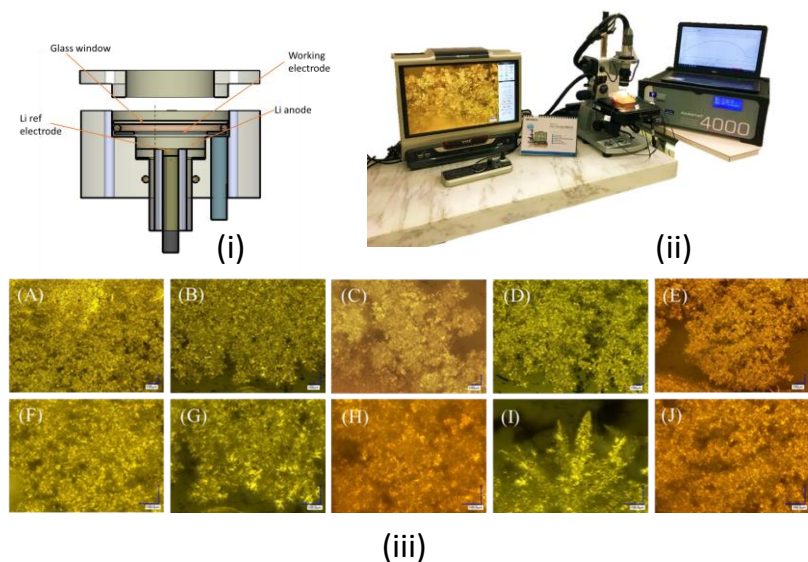


Figure 38. (i) Optical electrochemical cell for *in situ* electrochemical observations during the discharge and recharge of a lithium anode. (ii) Photo of the set-up for the *in situ* electrochemical optical experiments, including laser confocal microscope, optical cell, and electrochemical workstation. Surface morphology and dendrite growth can be observed in real-time. Examples are shown in (iii).

## Patents/Publications/Presentations

The project has no patents, publications, or presentations to report this quarter.

## Task 1.15 – Molecular Ionic Composites: A New Class of Polymer Electrolytes to Enable All-Solid-State and High-Voltage Lithium Batteries (Louis Madsen, Virginia Polytechnic Institute and State University)

**Project Objective.** Based on a newly discovered class of solid polymer electrolyte materials, that is, molecular ionic composites (MICs), the overall objective is to develop solid-state lithium conductors targeted for use in transportation applications. MICs form a mechanically stiff, electrochemically stable, and thermally stable matrix. Specific objectives include the following: (1) development of robust MIC electrolyte thin films ( $\sim 20 \mu\text{m}$ ) to serve as simultaneous nonflammable separators and dendrite-blocking  $\text{Li}^+$  conductors, (2) electrochemical quantification of key performance metrics including electrolyte stability, interfacial reactions, and suitability/compatibility with a range of electrode materials, and (3) comprehensive investigation of ion transport mechanisms and electrode-electrolyte interfacial reactivity under practical operating conditions using NMR and synchrotron X-ray analyses.

**Project Impact.** Commercialization of Li-metal SSBs is hampered by lack of a functional nonflammable solid electrolyte that can provide high ionic conductivity, wide electrochemical window, favorable mechanical properties to inhibit lithium dendritic growth, and low interfacial resistance. The tunable MIC materials platform has potential to fulfill these requirements with relatively simple fabrication techniques, and thus shows promise for enabling SSBs that can be optimized for low cost and high energy density and are nonflammable.

**Approach.** MICs rely on a unique polymer that is similar to Kevlar® in its strength, stiffness, and thermal stability, but with densely spaced ionic groups that serve to form an electrostatic network that permeates mobile ions in the MIC. The team can tailor the ion concentrations and types to yield MIC electrolyte films that are electrochemically compatible with Li-metal anode as well as a range of high-voltage layered cathodes. They are searching the composition space of lithium salts, electrochemically compatible ionic liquids, and polymer (PBDDT) molecular weight to determine best composition windows for MIC electrolytes. The team is also investigating best methods for casting thin films in terms of temperature, solvent/evaporation conditions, and control over the initial liquid crystalline gel formation point. Concurrently, they are testing MIC films in various electrochemical cells, quantifying transport and structural/morphology parameters with NMR and X-ray techniques, and measuring key mechanical (DMTA, stress-strain) and thermal (DSC, TGA) properties.

**Out-Year Goals.** This year, the team is focused on understanding evolution of structure and morphology during the film casting process to optimize this process and obtain thin MIC electrolyte films. As part of the team's electrolyte optimization, they are determining the composition windows that yield fast  $\text{Li}^+$  conduction, mechanical stability, and electrochemical compatibility with lithium metal and selected cathode materials. They will develop robust electrolyte films and an array of testing schemes (that is, electrochemical, thermal, mechanical, NMR, and X-ray) to sensibly feedback on film composition and fabrication.

**Collaborations.** The team is beginning a collaboration with T. J. Dingemans' group at University of North Carolina (UNC) Chapel Hill in which they will supply various charged rigid-rod polymers. The team is also starting a collaboration with D. Nordlund at SLAC National Accelerator Laboratory (SLAC) to conduct synchrotron X-ray studies on MIC films.

### Milestones

1. Determine synthetic conditions for 100- $\mu\text{m}$  thick electrolyte. (Q1, FY 2020; Completed)
2. Determine optimal Li-ion loading and chemical composition of solid composite electrolyte. (Q2, FY 2020; In progress)
3. Develop electrochemical, thermal, and mechanical testing protocols for solid electrolytes and battery cells. (Q3, FY 2020; In progress)

## Progress Report

The team has so far generated solid MIC electrolyte films with uniform thickness and with areas up to  $10 \times 10$  cm. These films contain the charged rigid-rod PBDDT polymer along with mobile and non-volatile ions (lithium salt and ionic liquid). These films are nonflammable and flexible, and can conduct  $\text{Li}^+$  over a wide range of temperature. Figure 39 shows the chemical components of the team's prototype films, a transparent and flexible large area film and an SEM image showing a smooth film surface after Li-Li electrochemical cell cycling. Table 3 shows composition by weight of the three main components (PBDDT, LiTFSI salt, and Pyr<sub>14</sub>TFSI) as well as the final film thickness and the ionic conductivity. The team has completed the first milestone in that they have generated robust and uniform films that are  $< 100 \mu\text{m}$  thick and that show relatively high room temperature ionic conductivity (up to  $2.7 \times 10^{-3} \text{ S/cm}$ ). Madsen (PI) and Lin (co-PI) are dividing the project: Madsen will address film fabrication, thermal/mechanical/NMR transport, and morphology analyses, while Lin will address electrochemical, interfacial, and X-ray morphology and surface analyses.

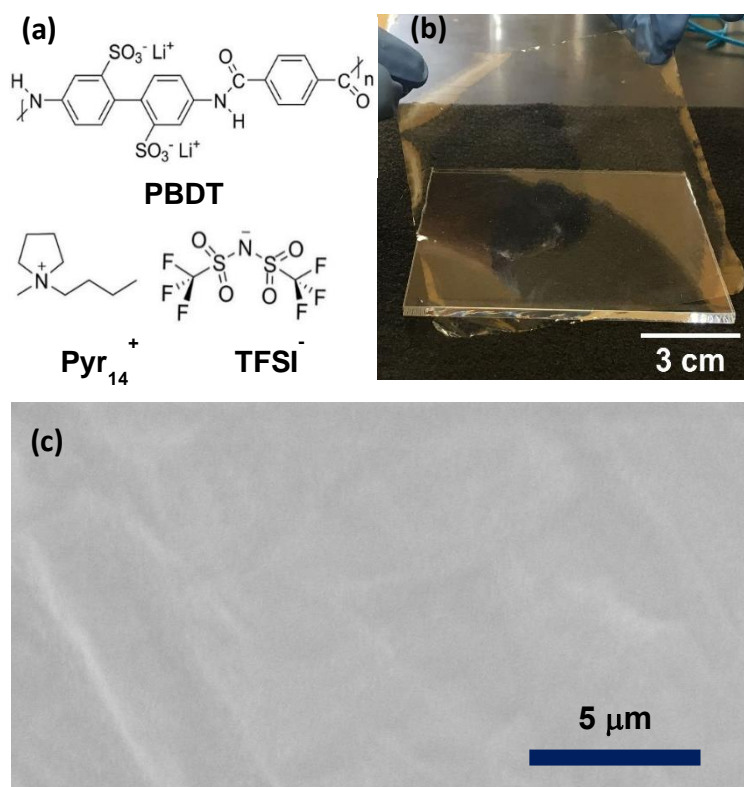


**Figure 39.** Initial molecular ionic composite (MIC) electrolyte films. (a) Chemical structures of PBDDT polymer and ionic liquid Pyr<sub>14</sub>TFSI. (b) Large area as-cast 80-mm thick MIC film. (c) Scanning electron microscopy image of MIC film after Li-Li electrochemical cell cycling (pinhole free).

The team is continuing to scan composition space and casting conditions to optimize various film properties: conductivity, elastic modulus, and electrochemical stability with several electrode materials. They have discovered that a liquid crystalline gel forms during the casting process, as solvent evaporates. They are investigating details of this phase formation with NMR and X-ray, which should lead to more rational control over the casting process. The team is also beginning to measure conductivity over at least the range  $-30^\circ\text{C}$  to  $+100^\circ\text{C}$ , as well as DSC, TGA, and DMTA over a similar or wider temperature range.

**Table 3.** Prototype molecular ionic composite electrolyte film compositions, thicknesses, and room-temperature conductivities.

Composition (PBDDT-LiTFSI-Pyr <sub>14</sub> TFSI, wt%)	Thickness ( $\mu\text{m}$ )	Conductivity (mS/cm) @ $25^\circ\text{C}$
10-10-80	<b>86</b>	<b>0.22</b>
10-15-75	<b>82</b>	<b>0.27</b>
15-10-75	<b>69</b>	<b>0.23</b>
15-15-70	<b>75</b>	<b>0.080</b>

Figure 40 shows preliminary DMTA on MIC films made using the current casting process. These films do not have lithium salt included, and those tests are upcoming. The high modulus and thermal stability are evident in the initial tests.

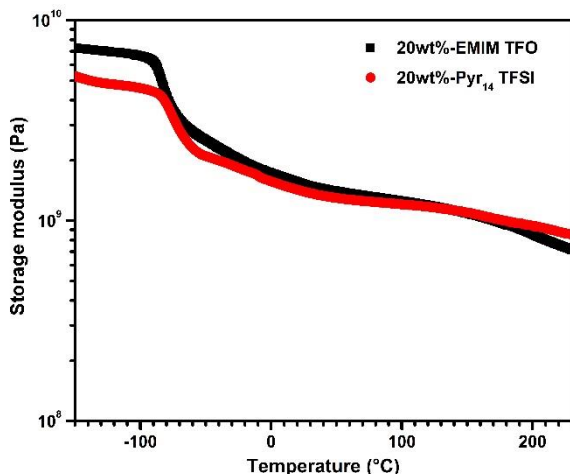


Figure 40. Dynamic mechanical analysis of molecular ionic composite electrolyte films. The red curve shows storage modulus for 20 wt% PBDT / 80% Pyr<sub>14</sub>TfSI electrolyte film, and the black curve shows the same for 20 wt% PBDT / 80% EMIM TfO (an initial pilot material). Similar analysis of Li-loaded films is under way. These films have tensile storage modulus > 1 GPa over a wide temperature range and show no evidence of decomposition (also with TGA – not shown) to well above 200°C.

## Patents/Publications/Presentations

### Presentations

- PNNL, Materials Sciences Group, Richland, Washington (October 23, 2019): “Confinement Effects on Diffusion in Nanostructured Polymers”; L. A. Madsen.
- Macromolecules Innovation Institute Technical Conference and Review, Blacksburg, Virginia (November 4–6, 2019): “Molecular Ionic Composites: Tunable, Stiff, Safe, and Conductive Electrolytes for Advanced Batteries”; C. J. Zanelotti, D. Yu, N. F. Pietra, Y. Wang, and L. A. Madsen. Poster.

## Task 1.16 – All-Solid-State Batteries Enabled by Multifunctional Electrolyte Materials (Pu Zhang, Solid Power Inc)

**Project Objective.** The project objective is to develop Li-metal SSBs enabled by multifunctional SSEs for EV application. The ultimate goal is scalable production of large-format ASSBs able to deliver  $\geq 350$  Wh/kg specific energy,  $\geq 1000$  cycle life, and  $\leq \$100/\text{kWh}$  cost.

**Project Impact.** The project impact is enabling scalable production of large format all-solid batteries required by the vehicle market and building domestic battery manufacturers as leaders in the global vehicle ASSB production. The proposed technology will address key limitations of state-of-the-art lithium batteries to meet DOE EV battery targets and accelerate their adoption as large format EV batteries for sustainable transportation technology.

**Approach.** The project will develop a high performance Li-metal solid-state cell enabled by a multifunctional SSE. The new SSE will (1) have high conductivity (up to 10 mS/cm), (2) be stable against lithium metal and high-voltage cathode (0-4.5 V), (3) promote uniform lithium plating (enabling  $> 2\text{C}$  charge rate), and (4) be compatible with large-scale manufacturing processes. The specific cell chemistry to be demonstrated will be the SSE with Li-metal anode and high-nickel-content Li-metal oxide cathode. The solid-state cell will be assembled by scalable roll-to-roll processes developed by Solid Power.

**Out-Year Goals.** In Year 1, multifunctional SSE will be developed with lithium ionic conductivity of  $\geq 3 \times 10^{-3}$  S/cm. Critical current density (CCD) of  $\geq 6$  mA/cm<sup>2</sup> will be achieved in a symmetric lithium cell. The design concept of the SSE will be proven by demonstrating cycle life of  $\geq 200$  in a full cell. In Year 2, the SSE material will be optimized with lithium ionic conductivity of  $\geq 5 \times 10^{-3}$  S/cm. Scalable cell assembly processes will be developed. Cycle life of  $\geq 500$  will be demonstrated in a full cell. In Year 3, large-format solid-state cells ( $> 2\text{Ah}$ ) will be assembled and tested to meet the final goal:  $\geq 350$  Wh/kg,  $\geq 1000$  cycles, and  $\leq \$100/\text{kWh}$  cost.

**Collaborations.** The proposed team consists of Solid Power and subcontractor University of California San Diego (UCSD). Solid Power (PI: Dr. P. Zhang) will develop the multifunctional SSE and other cell components, assemble cells, and conduct cell tests. UCSD (PI: Prof. S. Meng) will carry out material characterization by using advanced techniques such as XPS, Cryo-STEM imaging, Cryo-STEM EDX, electron energy loss spectroscopy (EELS), and cryo-FIB milling. The UCSD team seeks to quantify the kinetics and evolution of each contributing factor and its impact on battery performance.

### Milestones

1. Secure precursors and equipment. (Q1, FY 2020; Completed, December 31, 2019)
2. Down-select cathode materials. (Q2, FY 2020; Completed, December 31, 2019)
3. Cathode loading  $\geq 3.5$  mAh/cm<sup>2</sup>. (Q3, FY 2020; In progress)
4. SSE ionic conductivity  $\geq 3$  mS/cm; cell cycle life  $\geq 200$ . (Q4, FY 2020; In progress)

## Progress Report

### SSE Development

Precursors for electrolyte synthesis have been identified and ordered. Both Solid Power and UCSD have secured necessary equipment (facility) for electrolyte synthesis, characterization, cell fabrication, and cell testing, which includes gloveboxes, ball mills, presses, XRD, SEM, Cryo STEM-EDX and EELS, nano computed tomography, cell assembly facility, and cell test stations. Figure 41 shows key capabilities deployed for this project.

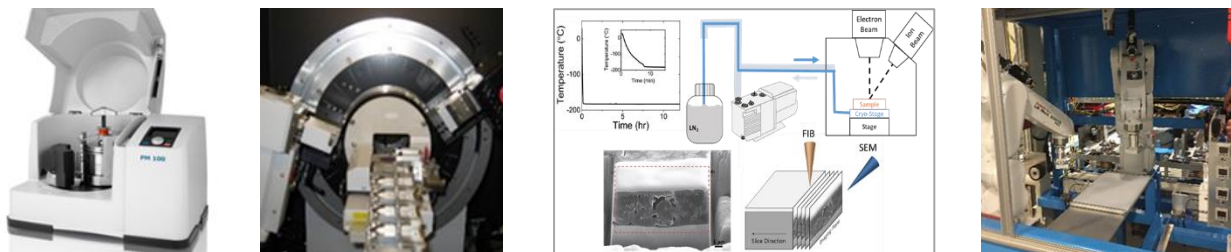


**Figure 41. (left to right) Ball mill for powder synthesis; X-ray diffraction for powder structure analysis; cryo focused ion beam and scanning transmission electron microscopy energy dispersive X-ray facility for material characterization; and cell assembly station.**

Solid Power’s halogenated LPS material was used as a starting point.  $\text{Li}_2\text{S}$ ,  $\text{P}_2\text{S}_5$ , a halogen, and other selected dopants were ball-milled to form glassy sulfide electrolytes by using a planetary ball mill. A subsequent heat-treatment was conducted to obtain glass-ceramic solid electrolytes.

Achieving comparable performance to liquid electrolyte requires lithium ionic conductivity on the order of  $10^{-3}$  S/cm from the SSE, or even higher to accommodate potentially higher interfacial resistance in the ASSB than that in the liquid system. A promising multifunctional SSE has demonstrated a conductivity of  $5 \times 10^{-3}$  S/cm at  $25^\circ\text{C}$ , 10 times higher than a baseline LPS electrolyte (Figure 42).

Several other SSE materials showed even higher conductivity of up to  $1 \times 10^{-2}$  S/cm; however, these materials lack the same anode or cathode stability of the lower conductivity materials. Starting next quarter, the composition and process of the electrolyte materials will be investigated extensively by using a “Design of Experiments” principle. An L18 orthogonal matrix will be initially applied, which consists of 18 experiments and 8 control factors. The control factors will include dopant parameters, milling parameters, and heat-treatment parameters, as shown in Table 4. The power pre-treatment factor will have two levels, and all other seven factors will have three levels. Li-ion conductivity, CCD with lithium, and long-term cyclability of the electrolyte will be used as the key criteria to qualify the electrolyte materials.

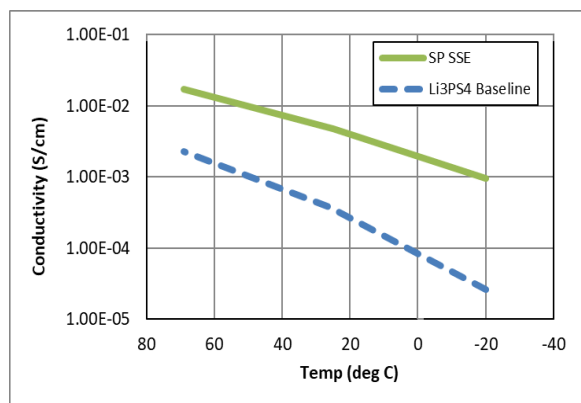


**Figure 42. Lithium ionic conductivity of solid-state electrolyte (SSE) at various temperatures. A promising multifunctional SSE shows  $5 \times 10^{-3}$  S/cm at  $25^\circ\text{C}$ , 10 times higher than the LPS baseline.**

Table 4. Process parameter design control factors (■ indicates baseline conditions developed in Q1).

Control Factors		Level 1	Level 2	Level 3
1	Dopant type	A	B	C
2	Doping level	d <sub>1</sub>	d <sub>2</sub>	d <sub>3</sub>
3	Powder pre-treatment	Yes	No	
4	Milling speed	M <sub>1</sub>	M <sub>2</sub>	M <sub>3</sub>
5	Milling time	t <sub>1</sub>	t <sub>2</sub>	t <sub>3</sub>
6	Media-to-powder ratio	R <sub>1</sub>	R <sub>2</sub>	R <sub>3</sub>
7	Process temperature	T <sub>1</sub>	T <sub>2</sub>	T <sub>3</sub>
8	Process atmosphere	A <sub>1</sub>	A <sub>2</sub>	A <sub>3</sub>

### Lithium Metal Development

Solid Power has access to thin lithium foils ( $\leq 35 \mu\text{m}$ ) and Li-coated current collectors from seven different lithium production companies, including one ongoing JDA. Several lithium surface treatments are also being evaluated to improve Li-metal stability, ranging from binary lithium compounds to polymers. CCD measurement is used as an effective tool to screen lithium anode and Li/SSE interphase for long-term stability and fast charge capability. The measurement of CCD on lithium metal was initiated this quarter by using a Li/SSE/Li symmetric cell. The symmetric cell is subjected to step-wise current increase, and cell failure is noted by discontinuity or noise in voltage profile. The CCD data will be reported next quarter.

### Cathode Development

NMC cathodes were developed and screened based on the balanced performance of energy, power, and cycle life under an internal commercialization project. The cathode parameter variables include material composition, particle size, surface area, surface morphology, and tap density. The performance factors include capacity, efficiency, rate capability, and cyclability. Based on the initial capacity and efficiency screening, three Ni-rich NMC (60%, 70%, and 85% nickel, respectively) cathode materials were selected for long-term cycling evaluation. The cycle-life data of the three cathodes are shown in Figure 43. The 85% nickel material showed the highest initial capacity but faded faster than the other two. The 60% nickel material showed slightly lower initial capacity, but higher cycling stability, than the 70% nickel material. The NMC-622 material has been down-selected for concept-proven demonstration in Year 1, based on its balanced advantages of high capacity and high cyclability. A pathway to higher nickel cathode ( $> 80\%$ ) will be continuously developed under the internal commercialization project in Solid Power.

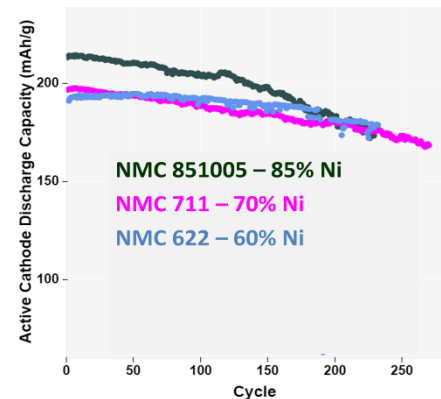


Figure 43. Cycle life of Li-metal solid-state cells with NMC cathode materials containing 60%, 70%, and 85% nickel, respectively. The cells were cycled at 2.5-4.3 V, C/10 rate, and 70°C.

### Patents/Publications/Presentations

The project has no patents, publications, or presentations to report this quarter.

## Task 1.17 – Developing Materials for High-Energy-Density Solid-State Lithium-Sulfur Batteries (Donghai Wang, Pennsylvania State University)

**Project Objective.** The project objectives are to develop materials involving advanced S-C composite materials, solid additives, and sulfide-based SSEs, and to acquire knowledge for Li-S ASSBs. Li-S ASSBs with large areal sulfur loading ( $\geq 5 \text{ mg cm}^{-2}$ ) and high sulfur content ( $\geq 50 \text{ wt\%}$  in cathode), pairing with lithium or lithium alloy anode, shall deliver a high initial specific capacity of over  $1200 \text{ mAh g}^{-1}$  at high charge/discharge rate ( $> 0.3 \text{ C}$ ) for 500 cycles with over 80% capacity retention.

**Project Impact.** This project aims to develop new materials to enable Li-S ASSBs with high energy density, excellent cycling stability, and good rate performance, and thus to build knowledge for fabrication of prototype Li-S ASSBs batteries. Specifically, the developed new materials will greatly increase the specific capacity of sulfur and sulfur utilization at high areal sulfur loading, alleviate the interfacial problem between sulfur-carbon composite and SSE within sulfur cathode, boost Li-ion conductivity, and improve moisture stability of glass and glass-ceramic sulfide-based SSE. Meeting the technical targets will potentially promote development of high-energy-density Li-S ASSBs and their practical application in EVs and plug-in hybrid EVs (PHEVs), and reduce petroleum consumption in the transportation sector by helping battery-powered vehicles become more accepted by consumers as a reliable source of transportation.

**Approach.** The project goal will be accomplished through developing new materials, together with in-depth characterization of sulfur cathode. Specifically, approaches to realize the project objectives include: (1) development of new carbon material with unique structure, high surface area, and large pore volume; (2) development of new sulfur-carbon materials to facilitate electron/ion transport; (3) development of novel additives to tune interfacial behavior among components in the cathode; (4) development and optimization of new SSE through cation and anion doping with superior properties such as high ionic conductivity, good moisture, and stability; and (5) diagnostics, characterization, and cell tests on the developed new material or advanced sulfur cathode.

**Out-Year Goals.** The out-year goals are as follows: (1) develop new S-C materials, new cathode additives, and cation-doped solid electrolytes (ionic conductivity above  $2 \text{ mS cm}^{-1}$  at room temperature), (2) conduct characterization and performance tests on both material and electrode levels. The *Go/No-Go Decision* will be demonstration of all-solid-state sulfur cathode with over  $1000 \text{ mAh g}^{-1}$  discharge capacity at  $0.3 \text{ C}$  discharge rate and  $50 \text{ wt\%}$  sulfur content for 50 cycles at  $60^\circ\text{C}$ .

**Collaborations.** There are no active collaborations.

### Milestones

1. Demonstrate sulfur cathode with above  $800 \text{ mAh g}^{-1}$  capacity at  $0.1 \text{ C}$  at  $60^\circ\text{C}$ . (Q1, FY 2020; Completed December 31, 2019)
2. Demonstrate sulfur cathode  $> 1000 \text{ mAh g}^{-1}$  using new solid additives or developed new electrolyte ( $> 1 \text{ mS cm}^{-1}$ , at  $25^\circ\text{C}$ ). (Q2, FY 2020; In progress)
3. Demonstrate sulfur cathode with  $> 1000 \text{ mAh g}^{-1}$  using optimized carbon materials. (Q3, FY 2020)
4. Demonstrate sulfur cathode with  $> 1000 \text{ mAh g}^{-1}$  at  $0.3 \text{ C}$  for 50 cycles at  $60^\circ\text{C}$ . (Q4, FY 2020)

## Progress Report

As solid electrolyte is a key component that will affect sulfur cathode performance, the team first synthesized the most representative sulfide-based solid electrolyte,  $75\text{Li}_2\text{S}\cdot 25\text{P}_2\text{S}_5$  (LPS) glass, and investigated the influences of different electrolyte preparation processes on solid electrolytes, namely, dry and wet ball milling processes. In the dry ball milling process, only dry powders of  $\text{Li}_2\text{S}$  and  $\text{P}_2\text{S}_5$  are used and milled for 20 hours. In the wet ball milling process, heptane is added. Both of the LPS synthesized showed an amorphous structure, as verified by XRD spectra shown in Figure 44a-b. The ionic conductivity of LPS synthesized through wet ball milling process ( $3.8 \times 10^{-4} \text{ S cm}^{-1}$ ) is slightly higher than the LPS synthesized through dry ball milling process ( $3.2 \times 10^{-4} \text{ S cm}^{-1}$ ). The ionic conductivity of LPS synthesized by wet ball milling process at different temperatures was plotted and shown in Figure 45. The activation energy was measured to be 0.331 eV. It was also found that with the use of heptane, the agglomeration of solid electrolyte is reduced and the particle size of LPS synthesized by wet ball milling process is reduced to  $1 \sim 10 \mu\text{m}$  compared with LPS synthesized by dry ball milling process (Figure 46a-b). Moreover, the decrease of synthesized particle size through the wet ball milling process is also valid for other sulfide-based solid electrolytes. Glass-type  $\text{Li}_6\text{PS}_5\text{Cl}$  has been synthesized using dry and wet ball milling approaches. The reduction of particle size and different particle morphology were clearly observed in SEM images, as illustrated in Figure 46c-d. It is believed that solid electrolyte with smaller particle size is more favorable for cathode performance.

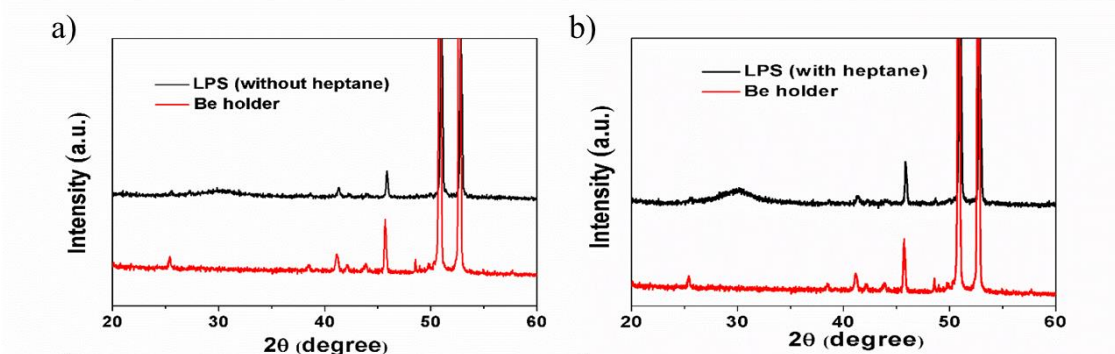


Figure 44. X-ray diffraction patterns of  $75\text{Li}_2\text{S}\cdot 25\text{P}_2\text{S}_5$  glass solid electrolyte prepared by (a) dry ball milling process and (b) wet ball milling process.

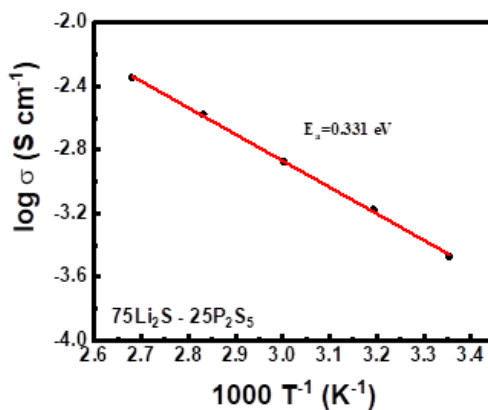
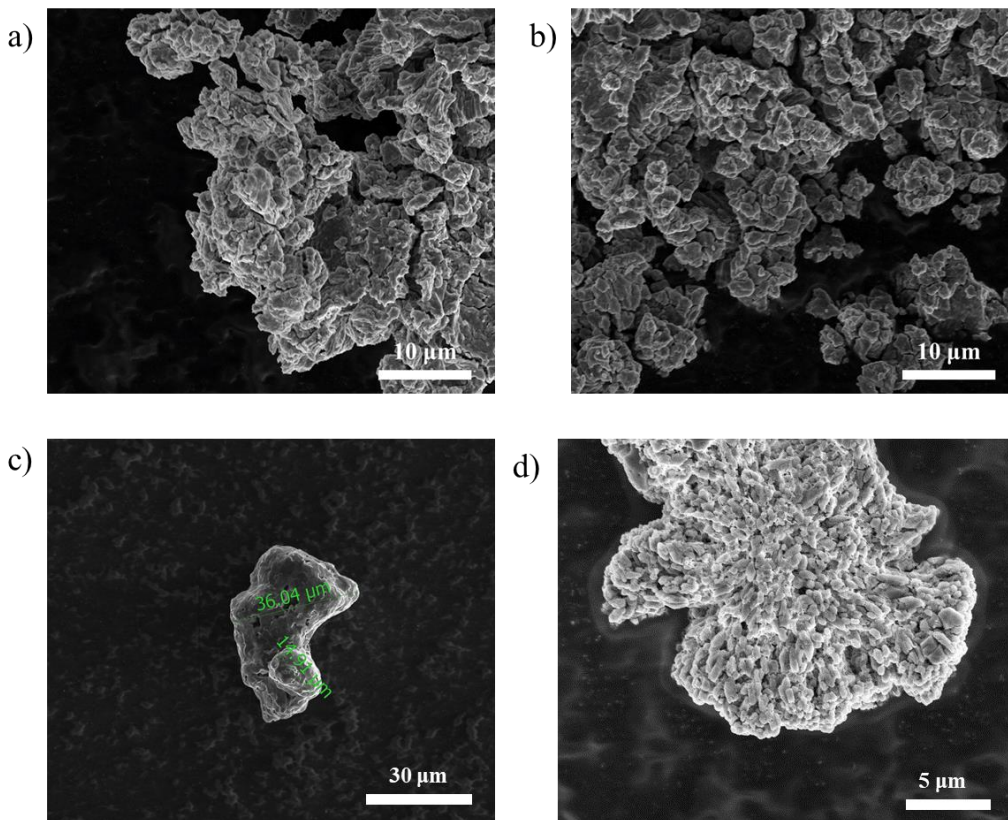


Figure 45. Arrhenius plot for measured ionic conductivity of LPS glass synthesized by wet ball milling process.



**Figure 46.** Scanning electron microscopy images of dry-ball-milling synthesized (a)  $75\text{Li}_2\text{S}\cdot 25\text{P}_2\text{S}_5$  and (c)  $\text{Li}_6\text{PS}_5\text{Cl}$  glass solid electrolytes and of wet-ball-milling synthesized (b)  $75\text{Li}_2\text{S}\cdot 25\text{P}_2\text{S}_5$  and (d)  $\text{Li}_6\text{PS}_5\text{Cl}$  glass solid electrolytes.

Since LPS prepared by the wet ball milling process showed reduced particle size, it was further used for fabrication of sulfur cathode. Ketjenblack EC600 JD, as one of the most common commercial conductive carbon materials with high surface area and large pore volume, was employed as a conductive additive for sulfur cathode. To prepare sulfur cathode, sulfur and conductive carbon were first mixed together under weight ratio of 50:20 using ball milling. Afterward, the obtained S-C composite and synthesized LPS powders were ball milled together following the weight ratio of 70:60. As a result, in final sulfur cathode, the weight ratio of Ketjenblack carbon, sulfur, and LPS solid electrolyte is 20:50:60. Rate performance of the as-fabricated sulfur cathode was tested using LPS as solid electrolyte membrane and Li-In alloy as anode at  $60^\circ\text{C}$  (Figure 47a). The voltage profiles at different rate are shown in Figure 47b. Sulfur loading was controlled at  $1.5\text{ mg cm}^{-2}$ .  $60^\circ\text{C}$  was chosen because at such temperature, LPS solid electrolyte delivered an ionic conductivity of around  $1.2 \times 10^{-3}\text{ S cm}^{-1}$ , which meets the ionic conductivity requirement for practical all-solid-state Li-S batteries. According to the testing result, the as-fabricated sulfur cathode delivered a high specific discharge capacity of around  $1200\text{ mAh g}^{-1}$  at 0.1 C, although improvement of the rate performance and sulfur content of the sulfur cathode is still needed. In addition, from the result, the milestone of demonstrating sulfur cathode with above  $800\text{ mAh g}^{-1}$  capacity at 0.1 C at  $60^\circ\text{C}$  has been achieved.

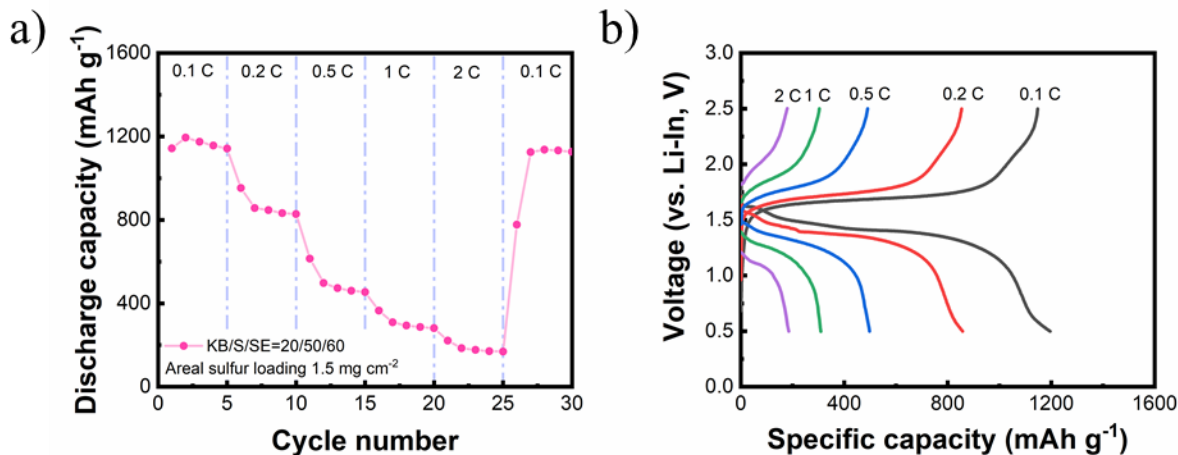


Figure 47. (a) Rate performance of sulfur cathode at 60°C. (b) Corresponding charge/discharge voltage profiles.

This quarter, the team also investigated impacts of adding titanium disulfide ( $\text{TiS}_2$ ) as solid additive in sulfur cathode on battery performance. Following a similar ball milling preparation procedure, sulfur cathode with  $\text{TiS}_2$  additive was synthesized (sulfur:ketjenblack: $\text{TiS}_2$ :LPS = 50:20:5:60). The rate performance and detailed charge/discharge profile are shown in Figure 48. The sulfur cathode was tested at 60°C. The specific capacity based on the total weight of sulfur and  $\text{TiS}_2$  at around 0.2 mA  $\text{cm}^{-2}$  is very high at around 1600 mAh  $\text{g}^{-1}$ . Even at 2 mA  $\text{cm}^{-2}$  (2.86 C), the specific capacity of sulfur cathode still retains at over 800 mAh  $\text{g}^{-1}$ . The slope shown in Figure 47b at first cycle below 0.7 V should be attributed to the decomposition of solid electrolyte.

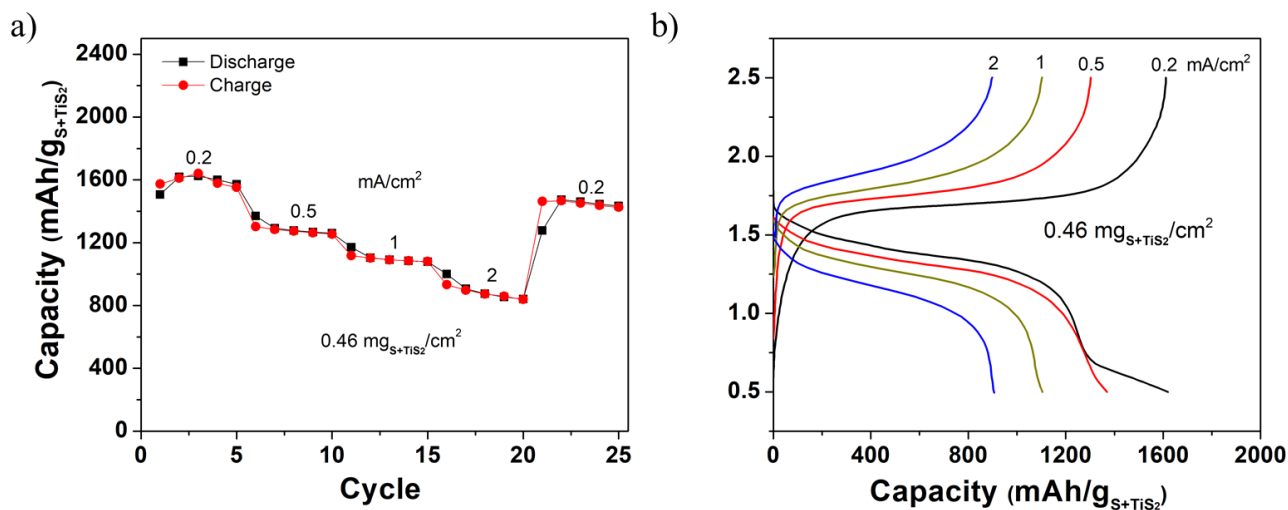


Figure 48. (a) Rate performance of sulfur cathode using  $\text{TiS}_2$  as solid additive at 60°C. (b) Corresponding charge/discharge voltage profiles.

### Patents/Publications/Presentations

The project has no patents, publications, or presentations to report this quarter.

## TASK 2 – DIAGNOSTICS

### Summary and Highlights

To meet the goals of the VTO Multi-Year Program Plan and develop low-cost, abuse-tolerant batteries with higher energy density, higher power, better safety, and longer lifetimes suitable for the next-generation EVs, there is a strong need to identify and understand structure-property-electrochemical performance relationships in materials, life-limiting and performance-limiting processes, and various failure modes to guide battery development activities and scale-up efforts. In pursuit of batteries with high energy density, both high cell operating voltages and demanding cycling conditions are used, which leads to unprecedented chemical and mechanical instabilities in cell components. Successful implementation of promising materials (such as silicon anode and high-voltage cathodes) and new cell chemistry (such as high-energy Li-metal cells) also requires better understanding of fundamental processes, especially those at the interface/interphase of both anode and cathode.

Task 2 takes on these challenges by combining model systems, *ex situ*, *in situ*, and *operando* approaches, with an array of state-of-the-art analytical and computational tools. A number of subtasks are tackling the chemical processes and reactions at the electrode/electrolyte interfaces in Li-metal batteries. Researchers at LBNL use surface- and bulk-sensitive techniques, including FTIR, attenuated total reflectance (ATR)-FTIR, near-field infrared (IR) and Raman spectroscopy/microscopy, and scanning probe microscopy (SPM) to characterize changes in materials and the physio-chemical phenomena occurring at the interface of Li-metal electrode. GM is developing *in situ* diagnostic techniques, including AFM, nano-indentor, dilatometer, and stress-sensor, to be combined with atomic/continuum modeling schemes to investigate the coupled mechanical/chemical degradation of the SEI layer as well as the microstructural evolution at the interface/interphase of Li-metal anode. ANL aims to develop high-conductivity ceramic electrolytes through cation doping and identify mechanistic barriers that limit the chemical/mechanical/electrochemical durability of the solid/solid interfaces. University of Houston is developing multidimensional diagnostic tools, including FIB-SEM, TOF-SIMS, and in-SEM nanoindentation, to probe structural, chemical, and mechanical evolution at the interfaces of solid-state lithium batteries. At LBNL, model systems of electrode, SSE, and their interfaces with well-defined physical attributes are being developed and used for advanced diagnostic and mechanistic studies at both bulk and single-particle levels. These controlled studies remove the ambiguity in correlating a material's physical properties and reaction mechanisms to its performance and stability, which is critical for further optimization. Subtasks at BNL and PNNL focus on the understanding of fading mechanisms in electrode materials, with the help of synchrotron-based X-ray techniques (diffraction and hard/soft X-ray absorption) at BNL and HRTEM / scanning transmission electron microscopy (STEM) and related spectroscopy techniques at PNNL. The final subtask at Stanford University/SLAC develops and utilizes a correlative X-ray microscopy platform to investigate lithiation dynamics and understand factors that determine rate capability and degradation mechanisms in cathode materials. The diagnostics team not only produces a wealth of knowledge that is key to developing next-generation batteries, it also advances analytical techniques and instrumentation that have a far-reaching effect on material and device development in many fields.

**Highlight.** PNNL (Wang's group) developed a new capability to measure the growth force of lithium whisker by integrating an AFM cantilever into a solid open-cell setup in environmental TEM, which enables direct observation of the nucleation and growth behavior of lithium whiskers under an elastic constraint that mimics the effect of a separator.

## Task 2.1 – Characterization and Modeling of Li-Metal Batteries: Model-System Synthesis and Advanced Characterization (Guoying Chen, Lawrence Berkeley National Laboratory)

**Project Objective.** This project will use a rational, non-empirical approach to design and develop SSE materials and interfaces for the next-generation Li-metal batteries. Combining a suite of advanced diagnostic techniques with carefully prepared model-system samples, the project will perform systematic studies to achieve the following goals: (1) obtain understanding on the role of SSE grain and GBs on ion conduction and dendrite formation, (2) obtain fundamental knowledge on rate- and stability-limiting properties and processes in SSEs when used in Li-metal batteries, (3) investigate the reactivities between SSE and electrodes and gain insights on the dynamic evolution of the interfaces, and (4) design and synthesize improved SSE materials and interfaces for safer and more stable high-energy Li-metal batteries.

**Impact.** The project will focus on fundamental understanding of SSE and relevant interfaces to enable its use in Li-metal batteries. Knowledge gathered from model-system based studies will guide the design and engineering of advanced materials and interfaces. The use of the non-empirical, rational-design approach will develop high-energy battery systems with improved commercial viability.

**Approach.** The project will combine model-system synthesis and advanced diagnostic studies to investigate ion conduction and interfacial chemistry of SSE in Li-metal batteries. Single crystalline, polycrystalline, and amorphous model SSE samples with various grain and GB properties will be synthesized. Model interfaces between the SSE and electrodes with controlled properties will also be developed. Both bulk-level and single-grain level characterization will be performed. Global properties and performance of the samples will be established from the bulk analyses, while the single-grain-based studies will utilize time- and spatially-resolved analytical techniques to probe the intrinsic redox transformation processes and failure mechanisms under battery operating conditions.

**Out-Year Goals.** In the out-years, the project will deliver fundamental knowledge on the role of SSE microstructure in Li<sup>+</sup> conduction and lithium dendrite formation/propagation. Insights on performance-limiting physical properties and phase transition mechanisms as well as the dynamic evolution of the SSE/electrode interfaces will be obtained. Mitigating approaches, such as use of surface coating or “buffer layer” in stabilizing SSE/electrode interfaces, will be evaluated. Further, advanced SSE materials and interfaces for improved high-energy Li-metal batteries will be designed and synthesized.

**Collaborations.** This project collaborates with the following PIs: G. Ceder, K. Persson, M. Doeff, B. McCloskey, R. Kostecki, and R. Prasher (LBNL); W. Yang (Advanced Light Source, ALS); D. Nordlund and Y. Liu (Stanford Synchrotron Radiation Lightsource, SSRL); C. Wang (PNNL); and J. Nanda (Oak Ridge National Laboratory, ORNL).

### Milestones

1. Develop model systems suitable for studying the impact of SSE grain and GBs in Li-metal based batteries. (Q1, FY 2020; Completed)
2. Synthesize model SSE samples with various grain and GB characteristics. (Q2, FY 2020; On schedule)
3. Advanced diagnostic studies of SSE model samples at both particle-level and bulk-sample level (Q3, FY 2020; On schedule)
4. Obtain understanding on SSE grain and GB chemistry, properties, and their effect on ion conduction and dendrite formation. (Q4, FY 2020; On schedule)

## Progress Report

To understand the role of SSE grains, GB chemistry, and properties in ion conduction and interfacial behavior, it is important that SSE particles with well-controlled physical characteristics, particularly grain morphology and surface properties, are used for the studies. This quarter, the feasibility of preparing high-quality grains of model SSEs was evaluated. Because LLZO has been well studied, it was selected as the initial SSE system. In previous studies, molten-salt methods were used in the project's lab to produce single crystals of oxide cathode materials with well-defined properties. Here, a similar approach was adopted to synthesize LLZO single-grain samples. After heat treatment of the pre-mixed  $\text{La}(\text{OH})_3$ ,  $\text{Li}_2\text{CO}_3$ ,  $\text{ZrO}_2$ , and  $\text{Al}_2\text{O}_3$  precursors in a  $\text{LiNO}_3$  flux at  $1000^\circ\text{C}$  for 6 h, Al-substituted LLZO ( $\text{Li}_{6.75}\text{Al}_{0.25}\text{La}_3\text{Zr}_2\text{O}_{12}$ , Al-LLZO) primary particles with an average grain size of  $\sim 40\ \mu\text{m}$  were obtained (Figure 49a-b). Various experimental conditions were explored, and uniform size distribution was achieved by maintaining the mole ratio between the flux and total metal precursors (defined as R) at 20. Due to the presence of a large excess of lithium from the flux, the as-synthesized Al-LLZO sample adopted a tetragonal phase, as shown in the XRD pattern in Figure 49c. A simple proton exchange process was found to effectively convert the tetragonal phase to the cubic phase, which is more desirable due to its higher ionic conductivity. To facilitate the  $\text{Li}^+/\text{H}^+$  exchange process in the garnet lattice, the tetragonal Al-LLZO powder was mixed with deionized water in a hydrothermal autoclave and heated at  $150^\circ\text{C}$  for 12 h, followed by annealing in air at  $300^\circ\text{C}$  for 12 h to remove the protons. The final product was found to have the garnet cubic structure without any impurities (Figure 49d), with the same particle morphology fully retained.

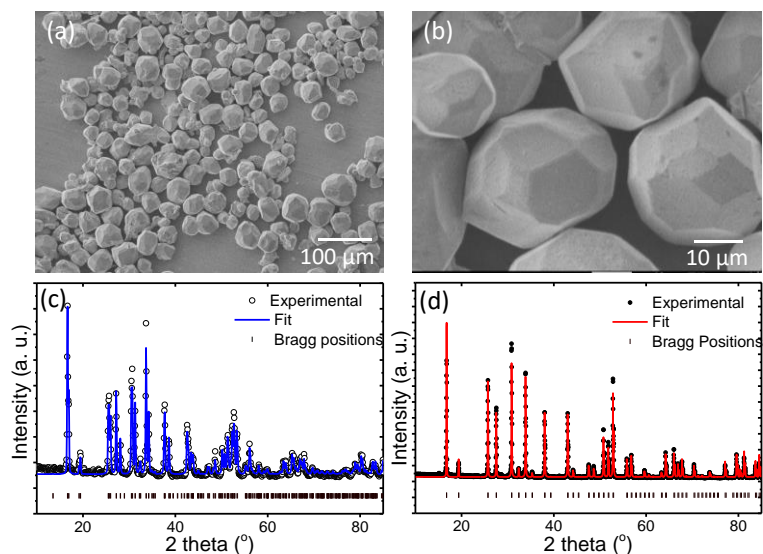


**Figure 49.** (a-b) Scanning electron microscopy images of Al-LLZO particles prepared using the molten-salt method and (c-d) refinement of X-ray diffraction patterns collected on as-synthesized (garnet tetragonal phase) and proton exchanged Al-LLZO particle after annealing (garnet cubic phase).

Single-grained cubic Al-LLZO was also obtained by annealing pre-formed garnet phase in a  $\text{LiNO}_3$  flux, a process similar to recrystallization. Figure 50a shows the SEM image obtained on an Al-LLZO sample prepared by heating a commercially available cubic Al-LLZO in a  $\text{LiNO}_3$  flux at  $1100^\circ\text{C}$  for 12 h, with the mole ratio between the oxide and flux maintained at 1:1. The as-synthesized sample showed a well-defined single particle morphology with an average particle size of  $\sim 4\ \mu\text{m}$ , which is ten times smaller than that of the sample made by the molten-salt method. This suggests feasibility in varying grain sizes through synthesis. The cubic crystal

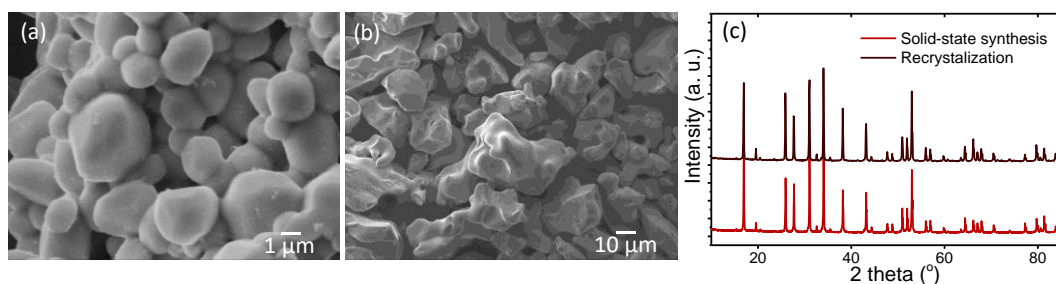


**Figure 50.** (a-b) Scanning electron microscopy images and (c) X-ray diffraction patterns of Al-LLZO samples obtained from the recrystallization process and solid-state synthesis method.

structure remained even after the thermal treatment (Figure 50c), as lithium loss during the high-temperature process, which typically promotes the formation of tetragonal phase, was prevented by the presence of a  $\text{LiNO}_3$  flux in this case. In the absence of the flux, on the other hand, large aggregated LLZO secondary particles were obtained. As shown in Figure 50b, the sample obtained after heating  $\text{La}(\text{OH})_3$ ,  $\text{Li}_2\text{CO}_3$ ,  $\text{ZrO}_2$ , and  $\text{Al}_2\text{O}_3$  precursors alone under the same conditions adopted a secondary particle morphology with an average size of  $\sim 20\text{-}40\ \mu\text{m}$ . Obtaining the garnet cubic crystal structure was possible when an excess amount of  $\text{Li}_2\text{CO}_3$  was used during the solid-state synthesis (Figure 50c).

## Patents/Publications/Presentations

### Publications

- Yi, E., H. Shen, S. Heywood, J. Alvarado, D. Y. Parkinson, G. Chen, S. W. Sofie, and M. M. Doeff. “All-Solid-State Batteries Using Rationally Designed Garnet Electrolyte Frameworks.” *ACS Applied Energy Materials*. Accepted (2020).
- Shen, H., E. Yi, S. Heywood, D. Y. Parkinson, G. Chen, N. Tamura, S. Sofie, K. Chen, and M. M. Doeff. “Scalable Freeze Tape Casting Fabrication and Pore Structure Analysis of 3D LLZO Solid-State Electrolytes.” *ACS Applied Materials & Interfaces* (2019). doi: 10.1021/acsami.9b11780.

### Presentation

- 236<sup>th</sup> ECS Meeting, Atlanta, Georgia (October 2019): “Understanding Surface Reactivities on Layered Oxide Cathodes”; J. Zhu, M. Kim, and G. Chen.

## Task 2.2 – Interfacial Processes – Diagnostics (Robert Kostecki, Lawrence Berkeley National Laboratory)

**Project Objective.** The objective of the proposed research is to establish specific design rules toward the next generation of low impedance Li-metal rechargeable batteries that are capable of performing 1000 deep discharge cycles at CE > 99.9% and suppress lithium dendrites formation at high current densities (> 2 mA/cm<sup>2</sup>). This project aims at the following: (1) establishing general rules between Li<sup>+</sup> transport properties in novel liquid/solid electrolytes, and (2) determining the mechanism of the SEI layer (re)formation. The other goal is development and application of far- and near-field optical probes and synchrotron-based advanced X-ray techniques to obtain insight into the mechanism of Li<sup>+</sup> transport and interfacial reactions in lithium/liquid model systems. Through an integrated synthesis, characterization, and electrochemistry effort, this project aims to develop a better understanding of Li/liquid electrolyte interface so that rational decisions can be made as to their further development into commercially viable Li-metal cells.

**Project Impact.** Chemical instability and high impedance at the interface of Li-metal electrodes limits electrochemical performance of high-energy-density batteries. A better understanding of the underlying principles that govern these phenomena is inextricably linked with successful implementation of high-energy-density materials in Li-metal-based cells for PHEVs and EVs. New state-of-the-art techniques to identify, characterize, and monitor changes in materials structure and composition that take place during battery operation and/or storage will be developed and made available to the Program participants. The proposed work constitutes an integral part of the concerted effort within the BMR Program, and it supports development of new electrode materials for high-energy, Li-metal-based rechargeable cells.

**Approach.** The pristine and cycled composite electrode and model thin-film electrodes will be probed using various surface- and bulk-sensitive techniques, including FTIR, ATR-FTIR, near-field IR and Raman spectroscopy/microscopy, and SPM to identify and characterize changes in materials structure and composition. Novel *in situ* / *ex situ* far- and near-field optical multi-functional probes in combination with standard electrochemical and analytical techniques are developed to unveil the structure and reactivity at interfaces and interphases that determine materials electrochemical performance and failure modes.

**Out-Year Goals.** In the out-years, the project aims to achieve the following: (1) understand factors that control performance and degradation processes, (2) unveil structure and reactivity at hidden or buried interfaces and interphases that determine electrochemical performance and failure modes, and (3) propose effective remedies to address inadequate Li-metal-based battery calendar/cycle lifetimes for PHEV and EV applications.

**Collaborations.** The diagnostic studies will be carried out in sync with other diagnosticians (G. Chen, B. McCloskey, R. Prasher, and L-W. Wang) and theory and computational scientists (G. Ceder and K. Persson).

### Milestones

1. Develop novel experimental approach(es) suitable for studying Li/electrolyte interfaces. (Q1, FY 2020; Completed)
2. Manufacture model thin-film lithium model electrodes for *ex situ* and *in situ* fundamental studies of Li/electrolyte interfaces. (Q2, FY 2020; In progress)
3. Characterize chemistry of Li/electrolyte with *ex situ* near-field IR, X-ray absorption spectroscopy (XAS), and XPS. (Q3, FY 2020; In progress)
4. Gain preliminary insights into SEI composition and reaction pathways for baseline electrolytes. Propose first approximative reaction scheme. (Q4, FY 2020; In progress)

## Progress Report

This quarter, the team carried out a series of preliminary measurements of the molecular structure of a model graphene-SSE interface at nano-scale spatial resolution. Measurements were performed with a unique combination of SPM and FTIR spectroscopy (nano-FTIR). The IR laser irradiation of the AFM tip generates a strong dipole at the tip apex, which extends a strong local evanescent wave that couples with the phonons in the sample. The single layer graphene (SLG) acts as an optical window and the electrode in direct contact with the SSE. The probing field extends from the tip through the graphene window and interacts with specimens at the surface of the SLG electrode. This novel and unique experimental setup enables IR nano-probing of the interface C/electrolyte, which could enable *in situ* characterization of the C/electrolyte and Li/electrolyte interface in close vicinity of the electrode.

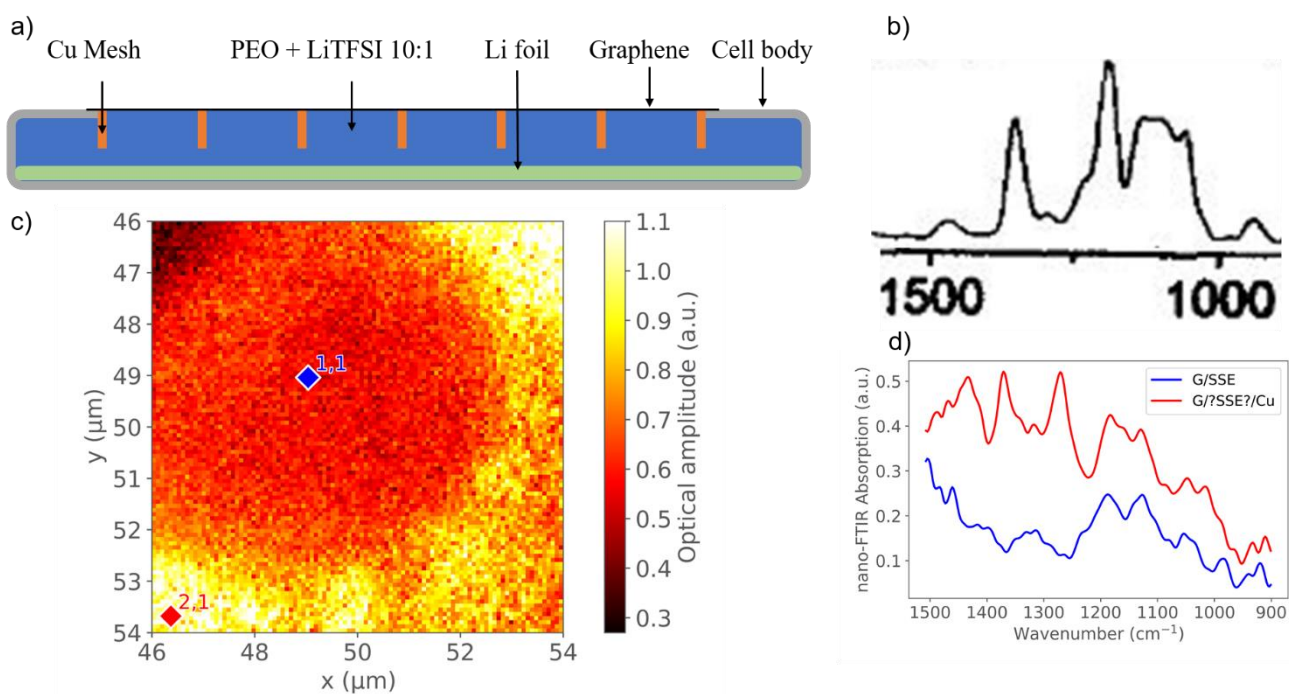


**Figure 51.** (a) Schematic illustration of the fabrication of the *in situ* cell with graphene window to study electrode/electrolyte interfaces. (b) Fourier transform infrared (FTIR) absorption spectrum of PEO+ LiTFSI mixtures at EO/Li ratios of 10:1. (c) Scattered near-field infrared amplitude image in a region where graphene window is in contact with the solid-state electrolyte in the cell. (d) Nano-FTIR spectra collected at locations marked by blue and red dots mark points.

Figure 51 shows the experimental cell set-up for *in situ* nano-FTIR measurements. The mixture of PEO and LiTFSI was first filled in the cell and then sealed with copper mesh and single-layer graphene window. Two representative points from the scattered near-field IR amplitude image are selected for nano-FTIR measurements. Even with slight shifts, characteristic peaks in the red area can fully match with peaks shown in a standard FTIR spectrum of EO/Li (10:1). In fact, two sharp peaks at 1360 and 1215  $\text{cm}^{-1}$  and one broad peak at 1160  $\text{cm}^{-1}$  are typically observed in the FTIR spectrum of EO/Li (10:1) composite. However, the blue area shows quite weak signal intensity, and the peaks at 1360  $\text{cm}^{-1}$  and 1215  $\text{cm}^{-1}$  disappeared completely. This may be caused by inhomogeneous pressure and poor contact between copper mesh and graphene window, which could lead to the formation of a gap between SSE and graphene.

Future work will focus on modifying and improving the current cell set-up and studies of Li/electrolyte interfaces. This work concludes efforts toward Milestone 1.

## Patents/Publications/Presentations

The project has no patents, publications, or presentations to report this quarter.

## Task 2.3 – Advanced *In Situ* Diagnostic Techniques for Battery Materials (Xiao-Qing Yang and Seong-Min Bak, Brookhaven National Laboratory)

**Project Objective.** The primary objective of this project is to develop new advanced *in situ* material characterization techniques and to apply these techniques to support development of new cathode and anode materials with high energy and power density, low cost, good abuse tolerance, and long calendar and cycle life for beyond Li-ion battery systems to power PHEVs and battery electric vehicles (BEVs). The diagnostic studies will focus on issues relating to capacity retention, thermal stability, cycle life, and rate capability of beyond Li-ion battery systems.

**Project Impact.** The VTO Multi-Year Program Plan describes the goals for battery: “Specifically, lower-cost, abuse-tolerant batteries with higher energy density, higher power, better low-temperature operation, and longer lifetimes are needed for development of the next-generation of HEVs, PHEVs, and EVs.” The knowledge gained from diagnostic studies through this project will help U. S. industries develop new materials and processes for next-generation Li-ion batteries in the effort to reach these VTO goals.

**Approach.** This project will use the combined synchrotron-based *in situ* X-ray techniques (XRD; and hard and soft XAS) with other imaging and spectroscopic tools such as HRTEM and MS to study the mechanisms governing performance of electrode materials.

**Out-Year Goals.** In the out years, the project will complete development of diagnostic techniques using X-ray pair distribution function (*x*-PDF), XRD, and XAS combined with neutron diffraction and neutron PDF (*n*-PDF), as well as STEM imaging and transmission X-ray microscopy (TXM) for cathode materials studies. It will then apply these techniques to study the structural changes of various new cathode and anode materials.

**Collaborations.** The BNL team will work closely with material synthesis groups at ANL (Drs. Shin and Amine) for the high-energy composite, at PNNL for the S-based cathode and Li-metal anode materials, and with ORNL on neutron scatterings. This project will also collaborate with industrial partners at GM and Johnson Controls, as well as with international collaborators.

### Milestones

1. Complete the first-stage development of diagnostic techniques to study and improve performance of high-energy-density Li-ion batteries and Li/S batteries. (Q1, FY 2020; Completed)
2. Complete hard X-ray fluorescence (XRF) imaging on the concentration gradient Ni-rich NCM cathode particles in a noninvasive manner with 3D reconstructed images through tomography scans to study the 3D nickel, cobalt, and manganese elemental distribution from surface to the bulk. (Q2, FY 2020; In progress)
3. Complete hard X-ray absorption spectroscopy (hXAS) and soft XAS (sXAS) on the concentration gradient Ni-rich NCM cathode particles to study the valence state changes of nickel, cobalt, and manganese at the surface and bulk. (Q3, FY 2020; In progress)
4. Complete spatially resolved XAS at sulfur K-edge and imaging of sulfur-based chemical species using XRF on the Li-metal anode in a cycled high-energy Li/S pouch cell. (Q4, FY 2020; In progress)

## Progress Report

This quarter, the first milestone was completed and work on other milestones began. BNL has been focused on developing new diagnostic techniques to study and improve performance of high-energy-density Li-ion batteries and Li/S batteries. The team has developed new synchrotron-based XPS with depth-profiling functionality. Compared with the lab-based XPS, the synchrotron-based XPS offers the following advantages:

- Capability to do experiments under ambient pressure (elevated gas pressure up to 10 torr) rather than the need for Lab-based XPS to be done in ultra-high vacuum (UHV) chamber.
- Quick data acquisition time.
- Tunable energy (probing different depth).
- Good signal-to-noise ratio.
- Special sample transfer holder.

This new technique was used to study surface chemistry and surface stability of high-nickel-content  $\text{LiNi}_{0.92}\text{Co}_{0.06}\text{Al}_{0.02}\text{O}_2$  (NCA) cathode materials during storage with reaction with  $\text{CO}_2$  and moisture. Li 1s, O 1s, and Ni 2p XPS spectra of NCA were measured in the  $\text{CO}_2$  environment. As shown in Figure 52, compared with the data measured in UHV,  $\text{Ni}^{3+}$  peak in Ni 2p XPS collected at 1200 eV is still observed, but with slightly decreasing intensity after reacting with  $\text{CO}_2$ . After increasing the energy to 1500 and 1800 eV to probe deeper and deeper from the outer surface, the  $\text{Ni}^{3+}$  peak increased significantly. Moreover, the characteristic peaks of bulk lithium and oxygen still can be clearly observed even after reacting with  $\text{CO}_2$ . This result suggests that aluminum doping may improve stability of NCA by stabilizing the active oxygen on the surface.

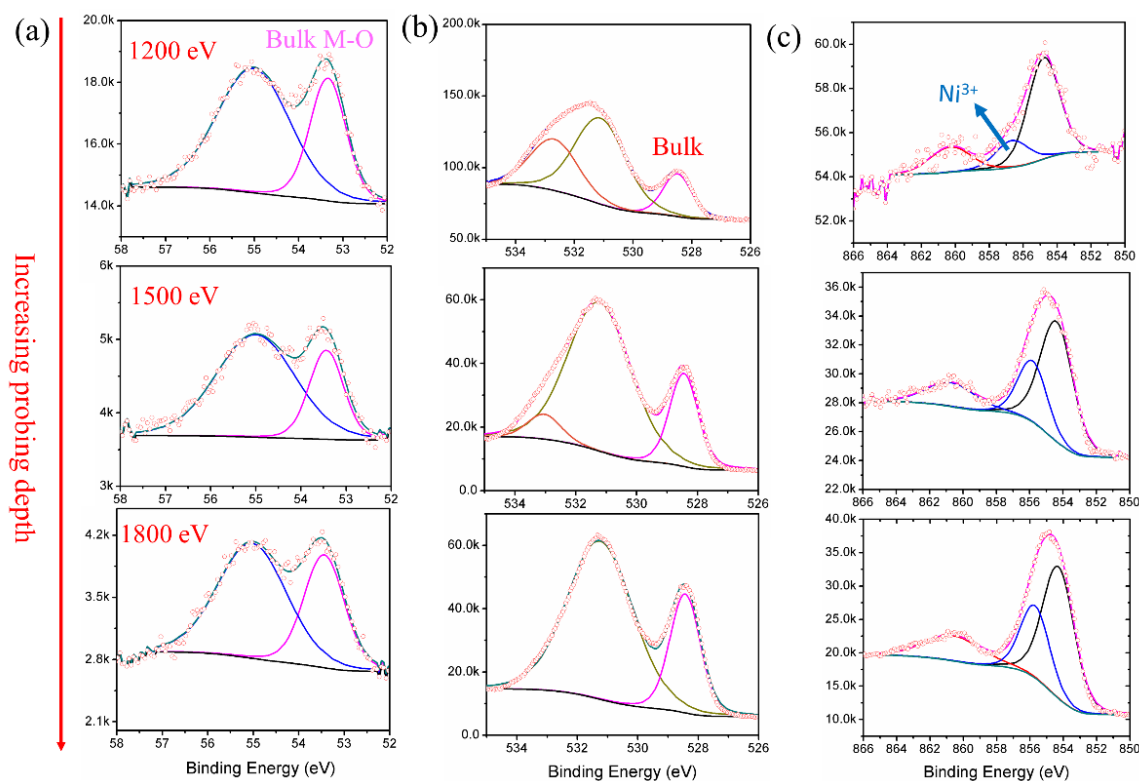


**Figure 52.** Depth profile X-ray photoelectron spectroscopy (XPS) spectra of as-synthesized NCA collected in the  $\text{CO}_2$  environment (1.6 Torr). (a) Li 1s, (b) O 1s, and (c) Ni 2p XPS spectra of NCA measured at 1200, 1500, and 1800 eV in the  $\text{CO}_2$  environment.

## Patents/Publications/Presentations

### Publication

- Wang, X., S. Tan, X-Q. Yang, and E. Hu.\* “Pair Distribution Function Analysis: Fundamentals and Application to Battery Materials.” *Chinese Physics B*. Publication date (Web): December 31, 2019.

### Presentation

- Münster Electrochemical Energy Technology (MEET), Münster, Germany (October 10, 2019): “Using X-Ray and Neutron Multi-Probe Spectroscopy Combined with TEM and TXM Imaging Techniques to Study the New Cathode Materials for Batteries”; E. Hu, Z. Shadike, R. Lin, X. Yu, S-M. Bak, H. S. Lee, Y. Liu, K. Page, J. Liu, H. Xin, X. Wang, Y. Zhou, and X-Q. Yang.\* Invited.

**Task 2.4 – *In Situ* Diagnostics of Coupled Electrochemical-Mechanical Properties of Solid Electrolyte Interphases on Lithium-Metal Rechargeable Batteries**  
(Xingcheng Xiao, General Motors; Brian W. Sheldon, Brown University; Yue Qi, Michigan State University; and Y. T. Cheng, University of Kentucky)

**Project Objective.** The project objective is to develop a comprehensive set of *in situ* diagnostic techniques combined with atomic/continuum modeling schemes to investigate and understand the coupled mechanical/chemical degradation of the SEI layer / lithium system during lithium cycling. The goal of this understanding is to develop a new coating design strategy to achieve dendrite-free, high-cycle efficiency and extend the cycle life of high-energy-density batteries with lithium as the anode for EV application.

**Project Impact.** The fundamental understanding of the coupled mechanical/chemical degradation of the SEI layer during lithium cycling will enable the project to identify the desirable mechanical properties on SEI/lithium as a system and also the specific transport properties that enable the homogenous lithium stripping/plating while avoiding the mossy structure. Furthermore, it will allow the project to develop a highly impactful strategy to protect lithium metal and achieve dendrite-free high cycle efficiency, which can dramatically increase the energy density of lithium batteries for EV applications.

**Approach.** Different *in situ* techniques, including AFM, nano-indentor, dilatometer, and stress-sensor, will be developed to investigate the mechanical compatibility between SEI and soft lithium and the relationship between surface morphology and CCD that results in an inhomogeneous lithium plating/stripping process. Multiple strategies will be developed to tailor the mechanical and transport properties of SEI and to properly engineer the protective coating / lithium interface.

**Out-Year Goals.** The out-year goals involve using *in situ* electrochemical tools to reveal failure mechanisms of SEI/lithium as a whole electrode system, including correlating mechanical failure mechanisms of SEI/lithium, morphology evolution, cycle efficiency, and transport properties of SEI. Then, the project will develop continuum framework to establish the failure modes of SEI layer on lithium metal and provide the governing mechanical/material properties of SEI responsible for the critical failure mode based on experimental results and atomic-scale simulation.

**Collaborations.** Prof. H. Gao (Brown University) and Dr. Q. Zhang (GM) will be the key researchers involved in continuum simulation and postmortem analysis. Dr. C. Wang (PNNL), Dr. W. Yang (LBNL), and Dr. J. Xiao (PNNL) will be collaborators on advanced *in situ* analysis and electrolyte additives.

### Milestones

1. Determine coating design window required to achieve mechanically stable coating on lithium metal. (Q1, FY 2019; Completed)
2. Determine impact of stress on morphological evolution of coated Li-metal surface, and identify failure modes of protective coatings on lithium. (Q2, FY 2019; Completed)
3. Vary coating modulus and investigate its impact on interfacial strength and cycle efficiency, and develop coating with desirable mechanical and transport properties. (Q3, FY 2019; Completed)
4. Establish a design strategy of protective coatings as artificial SEI on Li-metal electrode to achieve high cycle efficiency (> 99.8%). (Q4, FY 2019; Completed)

## Progress Report

**Density Functional Theory (DFT) Calculations to Understand Lithium Diffusion Tendency, and Kinetic Monte Carlo (KMC) Simulation to Study Void Evolution during Delithiation.** These simulations allow the team to see if voids formed at the interface can be filled due to different interfacial chemistry. Li-atom diffusion barriers normal to the Li/SEI interface are shown in Figure 53a, considering bonded lithium and non-bonded lithium atoms separately at the interface. Two kinds of diffusion barriers were studied, as illustrated in Figure 53a: lithium atom diffusion “toward the bulk” (for example, from L1 to L2) and “toward the interface” (for example, from L4 to L3.) The bonded and non-bonded lithium atoms showed no energy barriers when diffusing toward the bulk for Li/LiF, while bonded and non-bonded lithium atoms showed barriers of 0.37 eV and 0 eV, respectively, toward the bulk for Li/Li<sub>2</sub>O.

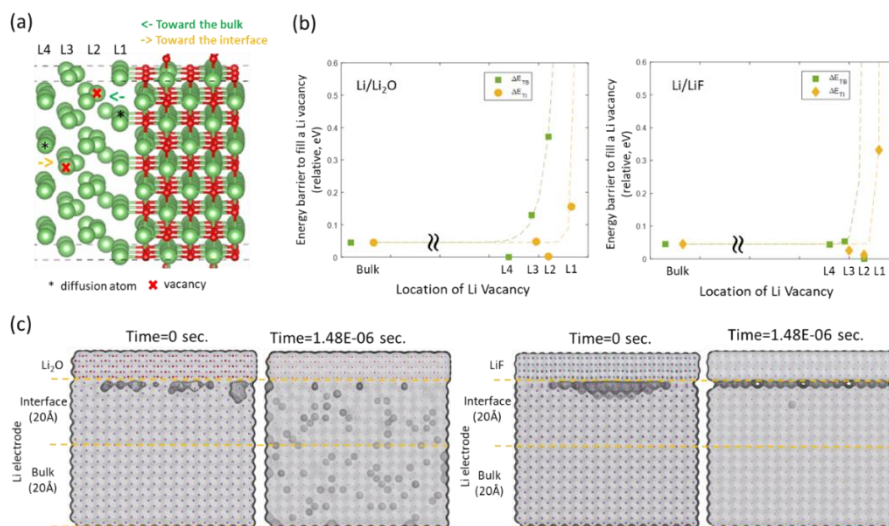


**Figure 53. (a) Illustration of Li-atom diffusion mechanism among layer 1 (L1) to layer 4 (L4) of Li/Li<sub>2</sub>O interface. Red: oxygen atom; Green: lithium atom. (b) Energy barriers to fill lithium vacancy at L1 to L4, respectively, for left (Li/Li<sub>2</sub>O) and right (Li/LiF) interfaces. (c) Kinetic Monte Carlo simulation of void evolution from time = 0 sec to time = 1.48E-06 sec (100 K steps). Left panel: Li/Li<sub>2</sub>O; right panel: Li/LiF.**

The vacancy filling tendency toward the interface and toward the bulk regarding L1, L2, L3, and L4 are plotted in Figure 53b. It is indicated that when a vacancy is present at L1 (interface) due to stripping, the fairly low lithium diffusion barrier toward the interface from lithium atom at L2 reveals it will be filled quickly. Concerning the vacancy in L2, it is very likely the vacancy would be filled by a lithium atom at L3 by comparing the diffusion energy toward the bulk and toward the interface. The same trend can be seen in L3. This indicates that Li/Li<sub>2</sub>O may have smaller voids at the interface, while Li/LiF is likely to trap the voids at the interface due to the fairly high barrier toward the interface regarding L1 and comparable barriers toward the bulk and toward the interfaces at L2, L3, and L4, as shown in right graph of Figure 53b.

The KMC simulation was then used to study the evolution of voids at different Li/SEI interfaces. An interfacial model for KMC is considered consisted of SEI layers (5 Li<sub>2</sub>O layers and 4 LiF layers) and a lithium metal comprised of a lithium layer 2-nm long (attaching to the SEI layers), followed by another lithium layer of the same size; the former lithium layer is denoted as interface region, and the latter as bulk region. The Arrhenius equation is used with prefactor of  $10^{13} \text{ s}^{-1}$  to obtain rate constants, as input for KMC simulation. In the left graph of Figure 53c, the team assumed void initially formed at the Li/Li<sub>2</sub>O interface due to the stripping (at time = 0 sec). It can be seen that at time = 1.48E-06 sec, the voids at the interface are filled by diffusion of lithium atoms from the bulk; in other words, the voids are digested by the bulk lithium. In the right graph of

Figure 53c, KMC simulation shows the Li/LiF interface does not migrate to the bulk portion of the lithium metal. The fundamental concept behind the difference in these two interfaces will be investigated and in-depth analysis of KMC results will be performed.

## Patents/Publications/Presentations

### Publications

- Wang, Y., D. Dang, X. Xiao, and Y-T. Cheng. “Structure and Mechanical Properties of Electroplated Mossy Lithium: Effects of Current Density and Electrolyte.” *Energy Storage Materials*. <https://doi.org/10.1016/j.ensm.2020.01.004>.
- Wang, Y., D. Dang, D. Li, J. Hu, X. Zhan, and Y-T. Cheng. “Effects of Polymeric Binders on the Cracking Behavior of Silicon Composite Electrodes during Electrochemical Cycling.” *Journal of Power Sources* 438 (2019): 226938.

### Presentations

- MRS Fall Meeting, Boston, Massachusetts (December 1–6, 2019): “Mechanical Property Measurements of Electroplated Mossy Lithium at Room Temperature” (EN05.01.07); D. Dang, Y. Wang, M. Wang, X. Xiao, and Y-T. Cheng.
- International Conference on Plasticity, Damage, and Fracture, Riviera Maya, Mexico (January 3–9, 2020): “Understanding the Coupled Electrochemical-Mechanical Behavior of Materials for Improving the Performance and Durability of Lithium Ion Batteries”; Y-T. Cheng. Keynote.

## Task 2.5 – Probing Interfacial Processes Controlled Electrode Stability in Rechargeable Batteries (Chongmin Wang, Pacific Northwest National Laboratory)

**Project Objective.** The main objective of the proposed research is to explore interfacial phenomena in rechargeable Li-ion batteries of both solid state and liquid electrolyte configuration, to identify the critical parameters that control the stability of interface and electrodes as well as solid electrolyte. The outcome will be establishing correlations between structural-chemical evolution of active components of batteries and their properties. These correlations will provide insight and guidance to battery materials development groups for developing high-performance battery materials.

**Project Impact.** The proposed characterization work focuses on atomic-level structural and chemical analysis and direct correlation with battery fading properties. The work can be directly used to guide design of electrode materials with tailored microstructure and chemistry for enhanced properties of increasing the energy density of Li-ion batteries and to accelerate market acceptance of EVs, especially for PHEVs as required by the EV Everywhere Grand Challenge.

**Approach.** The project will use integrated advanced microscopic and spectroscopic techniques, including *in situ* S/TEM and *ex situ* S/TEM, environmental S/TEM, cryo-electron microscopy, and *in situ* liquid secondary-ion mass spectrometry (SIMS) to directly probe the structural and chemical information during lithium deposition and stripping. Cryo-S/TEM with analytical tools, such as EDS and EELS, will be used to gain chemical and electronic structural information at the interface between lithium metal and electrolyte of both solid state and liquid, which will allow direct correlation between the morphology and chemistry. STEM – high-angle annular dark-field (HAADF) atomic-level imaging and EDS/EELS will be used to probe the interface and bulk lattice stability. The work will be in close collaboration with the battery development group within the BMR and U. S.–Germany Collaboration on Energy Storage.

**Out-Year-Goals.** This project has the following out-year goals:

- Atomic-level multi-scale *ex situ* / *in situ* and *operando* TEM and cryo-TEM investigation of failure mechanisms of energy-storage materials and devices; develop fundamental understanding of electrochemical energy-storage processes and kinetics of electrodes.
- Develop new *in situ* TEM capability for probing challenging questions related to energy storage technology.

**Collaborations.** This project collaborates with G. Chen (LBNL); J. Nanda (ORNL); K. Amine (ANL); D. Wang (PSU); A. Manthiram (UT Austin); W. Tong (LBNL); Y. Cui (Stanford University); J. Zhang (PNNL); J. Liu (PNNL); W. Xu (PNNL); X. Jie (PNNL); D. Lu (PNNL); X. Xiao (GM); S. Meng (UCSD); and S. Whittingham (State University of New York at Binghamton).

### Milestones

1. Integration of AFM cantilever into TEM column to *in situ* measure lithium dendrite growth force. (Q1, FY 2020; Completed)
2. Identify correlation of SEI structure and chemistry with electrolyte composition and electrochemical operating condition. (Q2, FY 2020)
3. Establish molecular signature of SEI formation process. (Q3, FY 2020)
4. Establish cathode stability in solid-state configuration. (Q4, FY 2020)

## Progress Report

It is generally believed that lithium dendrite (whisker) formation in batteries is essentially a non-regulated lithium plating process, where localized current concentrations give rise to localized lithium deposition. Yet, the fundamental reason for lithium whisker formation and its interaction with the separator remain far from clear, which may hold crucial insights for mitigating the lithium dendrite problem and hence the safe operation of Li-metal anode in batteries.

In this work, the team developed a new capability to measure growth force of lithium whisker. They integrate an AFM cantilever into a solid open-cell setup in environmental transmission electron microscopy, which enables them to directly *in situ* grow lithium whiskers, observe the growth characteristics, and, at the same time, measure the force that a growing lithium whisker will exert on a separator (Figure 54).

The team directly captured the nucleation and growth behavior of lithium whiskers under elastic constraint that mimics the effect of a separator (Figure 55). To mimic interactions between a growing lithium whisker and the separator in a battery, AFM cantilever with appropriate spring constant ( $0.1 \sim 2.0 \text{ nN}\cdot\text{nm}^{-1}$ ) was used for the test. The experiment was conducted in  $\sim 10^{-2}$  mbar  $\text{CO}_2$  to form the SEI layer dominated by  $\text{Li}_2\text{O}$  and  $\text{Li}_2\text{CO}_3$  on the deposited Li-metal surface. They experienced a typical process of lithium whisker formation, starting from nucleation (onset of lithium deposition), to whisker growth, to final “failure” by increasing compression. On applying a constant electric potential, lithium deposition started with the formation of a lithium nucleus at the interface between the solid electrolyte and the working-electrode. The lithium nucleus is featured, morphologically, as a faceted particle. Diffraction analysis of the lithium nucleus in a similar nucleation process demonstrates that the lithium nucleus is single crystalline body-centered cubic lithium metal and terminated preferentially by  $\{110\}$  surfaces. Three types of interaction scenarios were revealed: buckling of the lithium whisker; the ceasing of the lithium deposition at the interface between the lithium whisker and the solid electrolyte; and yielding of the lithium whisker. Based on the force measurement, the engineering stress at the point of yielding is  $\sim 100 \text{ MPa}$ , which is comparable to the yield strength of submicron-sized lithium metal.

Therefore, the team directly captured the lithium whisker nucleation and growth processes under elastic constraint that mimics the effect of a separator. It is found that the growth mode and morphology of deposited lithium can be critically related to the ionic conductivity of the initial SEI that is introduced by the basic reactions of freshly deposited lithium metal with the surrounding gas molecules.

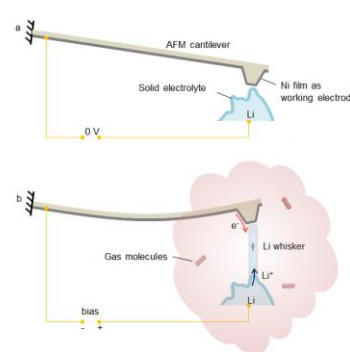


**Figure 54.** The atomic force microscope – environmental transmission electron microscope (AFM-ETEM) solid open-cell setup for the study. (a) Schematic of experimental setup prior to lithium deposition. (b) Schematics illustrating that a growing lithium whisker will push the AFM cantilever, which leads to measurement of the force that the growing whisker can potentially exert on an obstacle.

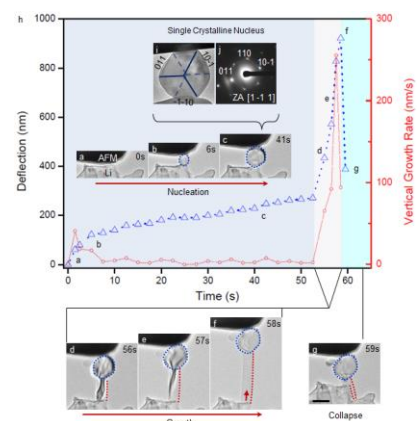


**Figure 55.** The lithium whisker formation during the electrochemical deposition of lithium in  $\text{CO}_2$  environment. (a-c) Sequential transmission electron microscopy snapshots of lithium particle nucleation. (d-f) Whisker growth process. (g) Whisker collapse. Red arrow in (f) indicates that the lithium whisker sprouts up from the whisker-electrolyte interface. Blue dotted lines indicate the nucleus. Red dotted lines highlight the side surface and shape of the lithium whisker. (h) Deflection of atomic force microscopy (AFM) tip and vertical growth rate of whisker during the process. (i-j) Lithium particle in another nucleation case and corresponding electron diffraction pattern. Spring constant of the AFM cantilever is  $\sim 0.4 \text{ N}\cdot\text{m}^{-1}$ . The scale bar is  $200 \text{ nm}$ .

## Patents/Publications/Presentations

### Patent

- Zhu, Z., and C. Wang. “Battery Cell and *In Situ* Battery Electrode Analysis Method.” Granted Patent Number: US 10505234B2; Date of Patent: December 10, 2019.

### Publication

- He, Y., X. Ren, Y. Xu, M. H. Engelhard, X. Li, J. Xiao, J. Liu, J-G. Zhang, W. Xu, and C. Wang. “Origin of Lithium Whisker Formation and Growth under Stress.” *Nature Nanotechnology* 14 (2019): 1042–1047.

### Presentation

- MRS Fall Meeting, Boston, Massachusetts (November 30 – December 4, 2019): “The Multiscale and Multi-Modality *In Situ* and *Ex Situ* Microscopy and Spectroscopy Diagnosis on the Fading Mechanism of Rechargeable Batteries”; C. Wang. Invited.

## Task 2.6 – Integrated Atomic-, Meso-, and Micro-Scale Diagnostics of Solid-State Batteries (Yi Cui, William Chueh, and Michael Toney; Stanford University / SLAC National Accelerator Laboratory)

**Project Objective.** This project aims to develop and utilize a correlative microscopy platform to investigate the lithiation dynamics of lithium- and manganese-rich (LMR) NMC and NCA, with the specific goal of understanding factors that determine the rate capability and degradation mechanisms at the single primary particle length scale. By developing a nanoscale and single-particle understanding of lithiation, the project addresses specific engineering problems including electrochemical hotspot, electrode utilization, safety, and capacity/voltage fade.

**Project Impact.** Fundamental insights from this new diagnostic capability are expected to increase the power density and cycle life of oxide electrodes by improving electrode utilization, reducing electrochemical hotspots, decreasing capacity and voltage fade, and enhancing safety, which all improve the viability of Li-ion batteries for vehicle transportation. By understanding lithiation at the single-particle level, this project's success will contribute to improving on-vehicle battery management, such as charging/discharging protocol, and SOC and state-of-health monitoring.

**Approach.** As stated, the project aims to develop a correlative microscopy platform to investigate the lithiation dynamics of LMR-NMC and NCA, with the goal of understanding factors that determine the rate capability and degradation mechanisms at the single primary particle length scale. On recharging time, the specific phenomena to be addressed include nonuniform current distribution and the correlation between surface property and the local lithiation rate. On degradation, phenomena to be addressed include correlating local chemistry and phases to capacity and voltage fading.

**Out-Year Goals.** Develop X-ray microscopy to investigate NMC and LMR-NMC cathodes at the single primary particle and single secondary particle level.

**Collaborations.** Commercial battery electrode particles are being supplied by Samsung.

### Milestones

1. Design, build, and test *operando* SSB cell for depth-resolved XAS. (Q1, FY 2020; Completed)
2. Record micro-tomograms of Li/SE/Li half cells for 10 cycling conditions. (Q2, FY 2020; In progress)
3. Record DC conducting AFM map of pristine solid electrolytes. (Q3, FY 2020)
4. Prepare X-ray transparent cathode/SE by cryo-sectioning. (Q4, FY 2020)

## Progress Report

This quarter, the team initiated an effort to develop X-ray characterization methods for ASSBs based on sulfide and oxide solid electrolytes. The focus is on the following:

- *Operando* XRT for characterizing microstructure evolution of Li/SE interface.
- Spectro-microscopy for characterizing cathode/SE composites (bulk and interfaces).

The high X-ray absorption of sulfide and oxide solid electrolytes necessitates a thin specimen for XRT. The team has designed and fabricated a 2-mm diameter solid-state cell that can be cycled *operando* and without air exposure inside a micro XRT microscope. Pressure can also be controlled, which is important for lithium plating and stripping. Initial experiments were carried out on LPS and LLZO while performing standard cycling and CCD measurements. Micron-scale fractures could be observed in LPS under active lithium plating, whereas none could be observed in LLZO, presumably due to the higher absorption. Stripping does not generate significant microstructure change. Fracture during cycling is very sensitive to the initial morphology and microstructure of the SE, which is being optimized. The team has also successfully carried out imaging of cathode/SE composition using micro tomography and determined the porosity and active material loading.

To provide local chemical information in the cathode/SE composite, the team is developing soft X-ray spectro-microscopy. They are mapping the TM absorption edges of the cathode, such as nickel, manganese, and cobalt, as well as the relevant edges for the solid electrolytes, such as sulfur, phosphor, and oxygen. Specimen preparation was carried out by cryogenic ultramicrotomy to prevent reactivity of H<sub>2</sub>O and CO<sub>2</sub> in air. Air-free transfer was enabled by a vacuum-transfer holder, which transferred microtomed sample from the glovebox to the microscope. Preliminary experiments show that sulfur, phosphor, and oxygen spectroscopy could be carried out. Beam damage studies are under way.

## Patents/Publications/Presentations

### Presentations

- Cell Symposium: Next-Generation Materials for Energy Applications, Xiamen, China (November 18, 2019): W. C. Chueh.
- Annual Meeting of the American Physical Society Far West Section, Stanford, California (November 1, 2019): W. C. Chueh. Plenary.
- Canadian Light Source (CLS) Energy Materials Workshop, Saskatoon, Canada (October 25, 2019): W. C. Chueh. Plenary.

## Task 2.7 – Investigating the Stability of Solid/Solid Interface (Zonghai Chen, Argonne National Laboratory)

**Project Objective.** The project objective is to fundamentally understand the critical issues that limit the mechanical, chemical, and electrochemical stability of solid/solid interfaces at the cathode and the anode.

**Project Impact.** The project will lead to several areas of impact: (1) improve the cycle life of ASSBs, (2) improve the mass transport properties across solid/solid interfaces, and (3) mitigate the formation of lithium dendrite.

**Approach.** The project approach is multi-fold: (1) understanding the physics behind the transformation between the low conductivity phase and the high conductivity phase; (2) investigating the bonding strength of the cathode/electrolyte interface using model systems; and (3) developing electrolytes with high ionic conductivity and good bonding to cathodes through cation doping.

**Out-Year Goals.** The project has the following out-year goals:

- Developing synchrotron-based diagnosis tools to investigate physical/chemical properties of solid/solid interface.
- Identifying mechanistic barriers that limit the chemical/mechanical/electrochemical durability of solid/solid interface.
- Developing model systems to validate the failure mechanism of solid/solid interface.

**Collaborations.** The project collaborates with Dr. A. Ngo (ANL), Dr. L. Curtiss (ANL), Dr. V. Srinivasan (ANL), Dr. Y. Ren (ANL), Dr. J. Libera (ANL), Dr. T. Li (Northern Illinois University), Dr. F. Wang (BNL), Dr. X. H. Xiao (BNL), and Dr. D. Chen (University of Houston).

### Milestones

1. Formation of Ta-LLZO/NMC-622 interface through co-sintering. (Q1, FY 2020; Completed)
2. Investigation of stability of Ta-LLZO/NMC-622 interface on cycling. (Q2, FY 2020; In Progress)
3. Investigating the electrochemical stability of Li/Ta-LLZO interface. (Q3, FY 2020; In Progress)
4. Investigating the chemical/mechanical stability of Li/Ta-LLZO. (Q4, FY 2020; In Progress)

## Progress Report

This co-sintering exercise uses  $\text{LiNi}_{0.6}\text{Mn}_{0.2}\text{Co}_{0.2}\text{O}_2$  (NMC-622) as the model cathode material and  $\text{Li}_{1.6}\text{La}_3\text{Zr}_{1.6}\text{Ta}_{0.4}\text{O}_{12}$  (LLZTO) as the model electrolyte material. The model materials were mixed with a mass ratio of 9:1 (NMC-622:LLZTO); the sample was sintered at  $1050^\circ\text{C}$ . Figure 56a shows a typical XRD pattern collected during whole course of the co-sintering. In principle, the sample can be fully indexed with three phases throughout the process: a layered structure for NMC-622, a cubic structure for LLZTO, and a second cubic structure for a residual  $\text{La}_2\text{Zr}_2\text{O}_7$  impurity. Figure 56b-c shows the evolution of lattice parameters (both  $a$  and  $c$ ) of NMC-622 during both the heating (see solid symbol) and cooling processes (see open symbols). It is clear that the co-sintering process did not alternate either the structure or the chemistry of NMC-622; both  $a$  and  $c$  reversibly return to their original values after the sample cooled to room temperature. However, the crystal structure evolution of LLZTO during the thermal processing revealed a completely different process (see Figure 56d). During the initial heating process, the XRD pattern can be successfully fitted using a cubic structure, and the lattice parameter  $a$  increases at a low-temperature region, primarily due to thermal expansion. When the temperature goes beyond  $400^\circ\text{C}$ , the material maintains a cubic structure while the lattice parameter shrinks. After sintering at  $1050^\circ\text{C}$ , the lattice parameter  $a$  decrease almost linearly during the cooling process, displaying a huge hysteresis between room temperature and  $600^\circ\text{C}$ . This hysteresis suggests that the starting material is not a real LLZTO, but proton-doped LLZTO, which is generated during the storage period from the reaction between LLZTO and moisture. The reaction at about  $400^\circ\text{C}$  is associated with the deprotonation reaction to form  $\text{La}_2\text{Zr}_2\text{O}_7$ . Therefore, the co-sintering process is also beneficial to mitigate the impact of the proton-lithium exchange reaction during the storage period.

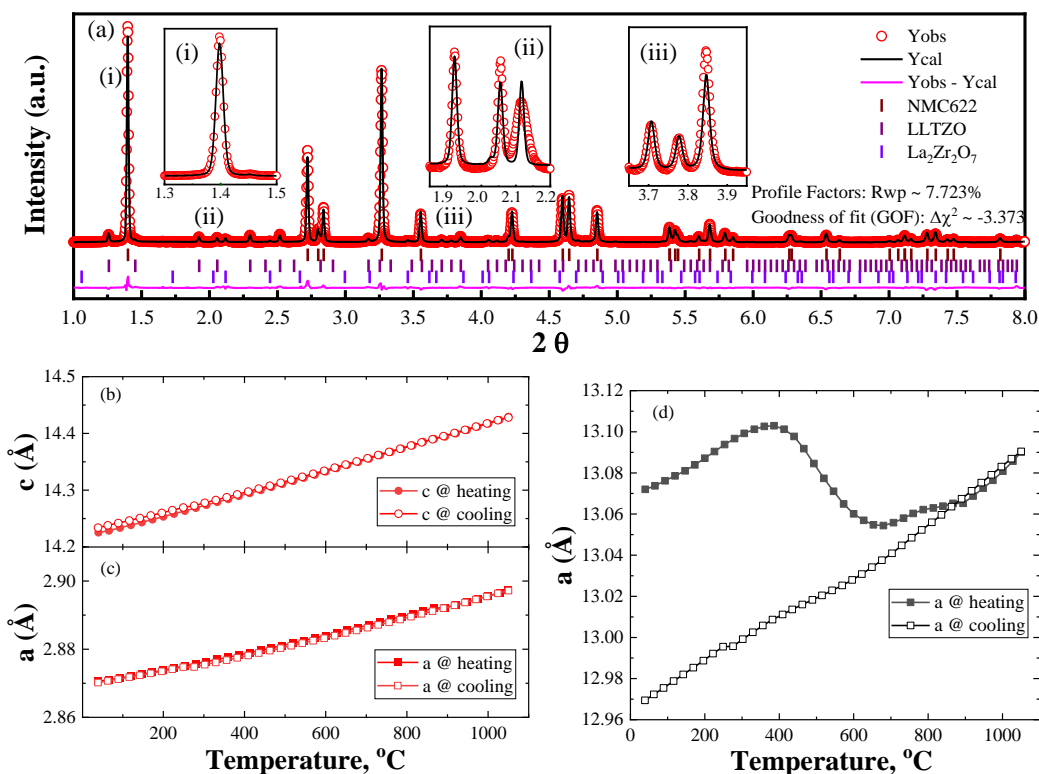


**Figure 56.** (a) A typical Rietveld refinement result showing that the materials can well be described using a three-phase model; evolution of lattice parameter  $c$  (b) and  $a$  (c) of NMC-622 during the co-sintering process; and (d) the evolution of lattice parameter of LLZTO during the co-sintering process.

## Patents/Publications/Presentations

### Publication

- Gim, J., H. Nguyen, T. Li, F. Wang, L. Wang, X. He, Y. Ren, and Z. Chen. “Phase Transformation of  $\text{Li}_7\text{La}_3\text{Zr}_2\text{O}_{12}$ : A Perspective from Thermodynamics and Kinetics.” *Journal of Physical Chemistry Letters* (2020). Submitted.

## Task 2.8 – Fundamental Understanding of Interfacial Phenomena in Solid-State Batteries (Xingcheng Xiao, General Motors)

**Project Objective.** The project objective is to develop a comprehensive set of *in situ* diagnostic techniques combined with atomic/continuum modeling schemes to investigate and understand the coupled mechanical/chemical degradation associated with dynamic interfacial phenomena in SSBs. Specifically, *in situ* observations and characterizations of lithium plating-stripping processes, lithium dendrite formation, interphase formation, and the induced interfacial stresses, as well as the mechanical and electrochemical properties of interfaces and interphases, are paramount. The study will provide useful guidelines for optimizing cell structure design and engineering interfaces and interphases to enable SSBs.

**Project Impact.** The project will provide fundamental understanding of the dynamic interfacial phenomena and the coupled mechanical and chemical degradation. In addition, it will establish a critical guideline to design safe and durable SSBs with energy density > 500 wh/kg for EV applications.

**Approach.** The multiscale *in situ* diagnostic tools, including AFM, nanoindentation, dilatometer, stress sensors, and pressure cells, will be used to investigate mechanical behavior and microstructure evolution at interface/interphase during the lithium plating and stripping. The information (along with Li-ion transport properties and microstructure evolution obtained using the advanced spectroscopic ellipsometry, and *in situ* TEM) will be correlated with electrochemical performance toward high cycle efficiency and dendrite-free SSBs. The goal of this understanding is to develop strategies for surface and interface engineering, apply them to commercially available solid electrolytes (including powder, pellets, and foils), and assemble SSBs for further validation and optimization, eventually extending cycle life for EV application.

**Out-Year Goals.** The project seeks to develop SSB model systems to capture critical mechanical properties and probe the coupled mechanical-chemical degradation by further developing comprehensive *in situ* diagnostic tools. All results obtained from these *in situ* studies, combined with advanced postmortem analysis and modeling, will be correlated with the cycling stability of SSBs. The *in situ* tools developed will be applied to the following two periods to deeply understand the couple mechanical and chemical degradation of interface/interphase.

**Collaborations.** The co-PIs involved in experiments and simulation will be as follows: Profs. B. W. Sheldon (Brown University), Y-T. Cheng and Ambrose Seo (University of Kentucky), Yue Qi (Michigan State), and Dr. Q. Zhang (GM).

### Milestones

1. Thin-film electrode system for different *in situ* electrochemical tests developed. (Q1, FY 2020; Ongoing)
2. Thin-film solid electrolyte system established with the comparable ionic conductivity reported in literature. (Q2, FY 2020)
3. *In situ* electrochemical-mechanical tools established. (Q3, FY 2020)
4. A rank of the interfacial adhesion between solid electrolyte and electrodes determined. (Q4, FY 2020)

## Progress Report

**Synthesized Epitaxial Thin Films of  $\text{Li}(\text{Ni}_x\text{Mn}_y\text{Co}_{1-x-y})\text{O}_2$  Electrode by Pulsed Laser Deposition.** This study provides invaluable information in device applications of these materials, as transport and optical properties may change in the ultrathin limit (for example, a few nanometers). For the first time, the team has successfully synthesized the electrode epitaxial thin film of NMC on substrates such as  $\text{Al}_2\text{O}_3$  and on Au on  $\text{Al}_2\text{O}_3$  ( $\text{Au}/\text{Al}_2\text{O}_3$ ). The samples are grown under the growth conditions of  $1.2 \text{ J}/\text{cm}^2$  laser fluence (KrF excimer,  $\lambda = 248 \text{ nm}$ ), and  $700^\circ\text{C}$  substrate temperature and oxygen partial pressure of 10 mTorr. These samples were cooled at 1 Torr oxygen partial pressure. All the thin films are structurally characterized by XRD and AFM. The successful epitaxial growth of NMC thin films as electrolyte and electrodes opens a way to understand interfacial properties of these SSB materials, giving insight into the next generation of Li-ion batteries. As shown in Figure 57a-b, the team has successfully synthesized the electrode epitaxial thin film of NMC on substrates such as  $\text{Al}_2\text{O}_3$  and on Au on  $\text{Al}_2\text{O}_3$  ( $\text{Au}/\text{Al}_2\text{O}_3$ ).

The next step is to measure the conductivity and electrochemical performance of NMC and to synthesize LLZO solid electrolyte. The capability built here offers a new route to understanding the physics of these materials in the field of SSBs.

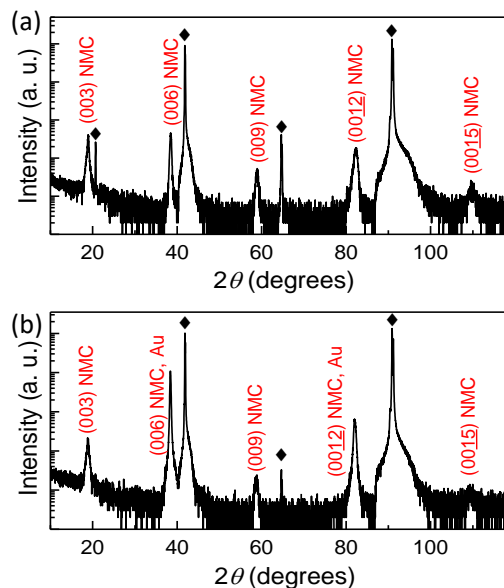


Figure 57. (a-b) X-ray diffraction scan of NMC on  $\text{Al}_2\text{O}_3$  and on  $\text{Au}/\text{Al}_2\text{O}_3$  substrates, respectively.

## Patents/Publications/Presentations

The project is new and has no patents, publications, or presentations to report this quarter.

## Task 2.9 – Multidimensional Diagnostics of the Interface Evolutions in Solid-State Lithium Batteries (Yan Yao, University of Houston)

**Project Objective.** The objective of this project is to develop structural, chemical, and mechanical characterization tools for multidimensional diagnostics of the interface evolutions in solid-state lithium batteries. Such characterization tools will allow assessment of varying testing conditions (such as external pressure and current density) on the evolutions of interfaces.

**Project Impact.** Development of the planned characterization tools will allow assessment of varying testing conditions (such as external pressure and current density) on the evolutions of interfaces.

**Approach.** Space- and time-resolved structural, chemical, and mechanical characterizations of the cathode–electrolyte and anode–electrolyte interfaces will be performed on all-solid-state lithium batteries using FIB-SEM, TOF-SIMS, and in-SEM nanoindentation. Tasks include the following: (1) development of solid-state cell thin stacks and test-cell configurations that are suitable for *in situ* characterizations, (2) quantitative characterization and *in situ* tracking of interfacial voids formation within composite cathode and electrolyte layer; (3) identification and *in situ* tracking of the chemical composition, spatial distribution, and mechanical properties of electrolyte decomposition products at the lithium- and cathode-electrolyte interfaces; and (4) visualization, chemo-mechanical properties detection, and *in situ* tracking of lithium dendrites grown within the solid electrolyte layer.

**Out-Year Goals.** The project has the following out-year goals:

- The FY 2020 goals are to develop complementary tools including thin solid-state cell stacks, in-SEM nanoindentation, micro- ( $\sim\mu\text{m}$ ) scale miniature cells, and accompanying cell configurations and testing protocols. The correlation between structural evolution, electrolyte decomposition, interfacial resistance increase, and lithium dendrite growth will be investigated.

**Collaborations.** The co-PIs of this project are Prof. J. Lou and Prof. H. Guo at Rice University focusing on microstructure and mechanical property characterization, and Prof. Z. Fan and Prof. Y. Liang at University of Houston focusing on *in situ* cell development.

### Milestones

1. Thin-cell stack development. (Q2, FY 2020; In progress)
2. In-SEM nanoindentation. (Q3, FY 2020)
3. Micro-cell for TOF-SIMS development. (Q3, FY 2020)
4. Cell optimization and electrochemical benchmarking. (Q4, FY 2020)

## Progress Report

Thin-stack solid-state cells for structural-chemical-mechanical analysis are being developed. The cell consists of a solid-state composite cathode, a solid electrolyte layer, and a Li-metal anode. Here, the composite cathode was prepared by coating a slurry consisting of  $\text{LiCoO}_2$  as the active material (AM),  $\text{Li}_6\text{PS}_5\text{Cl}$  (LPSCL) solid electrolyte, and poly(styrene-butene/ethylene-styrene) (SEBS) binder on aluminum foil. The solid electrolyte layer was prepared by coating a slurry of LPSCL and SEBS on the cathode sheet. Finally, a lithium foil was stacked and pressed on the solid electrolyte sheet for the full cell integration (Figure 58a). Figure 58b shows the representative voltage profile for one such cell. The cell delivered a specific capacity  $\sim 150$  mAh/g based on the mass of cathode active material, which is stable after 50 cycles (Figure 58b, inset). Efforts are being made to improve the reproducibility and stability of the thin-stack cells.

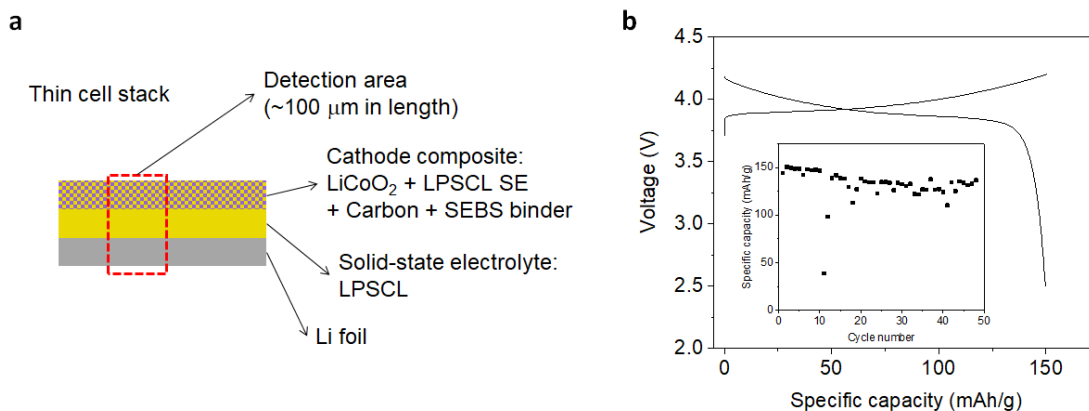


**Figure 58. The thin-stack solid-state cell. (a) The schematic illustration of the thin cell stack. (b) Charge–discharge curve of the thin-stack all-solid-state full cell. The specific capacity reaches 150 mAh/g (based on the mass of  $\text{LiCoO}_2$ ). Inset: capacity stays stable after about 50 cycles.**

After cell fabrication, the thin-stack cell was delivered for cross-section polishing to expose a flat cross section. Conventionally, ion polisher is suitable for milling a specimen composed of homogeneous materials. For a composite specimen, the ion milling-induced heating could result in voids due to heat capacity differences. Measures have been taken to overcome this issue by using a cryogenic condition to reduce heat damage, as shown in Figure 59a. To alleviate the heating-induced damage to the AM/SE interfaces in the cathode, the team has also developed a “step-protrude polishing” method, where the protrusion of a specimen was broken down into small steps. Figure 59b shows the polished AM/SE interfaces with suppressed void formation. The team is still optimizing parameters to minimize polishing time and heat damage. The capability to produce a clean cross-section lays the foundation to carry out studies monitoring interface evolutions. The next step is to develop an air-free transfer box to enable external pressure, current density, temperature, etc. to be applied to the thin-stack cell, which will be reported in next quarter.

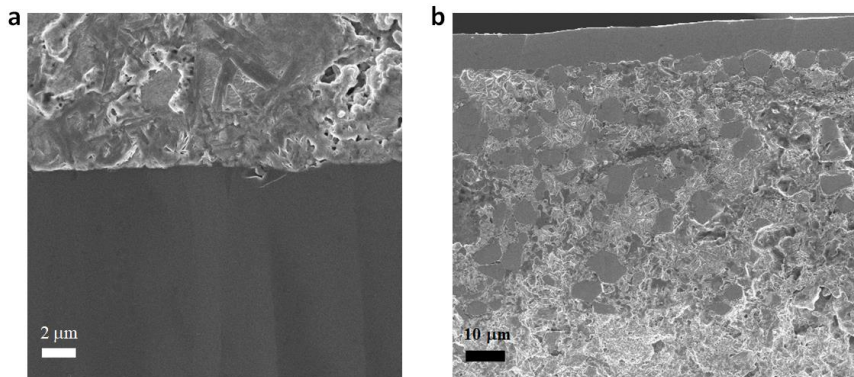


**Figure 59. Cross-section polishing result of the cell. (a) Cryogenic polishing of a Li-metal anode. (b) The cathode composite fabricated as shown in Figure 58a.**

## Patents/Publications/Presentations

### Presentations

- MRS Fall Meeting, Boston, Massachusetts (December 4, 2019). “Developing Materials and Diagnostics Tools for Understanding Interface Evolutions in Solid-State Batteries”; Y. Yao. Contributed.
- MRS Fall Meeting, Boston, Massachusetts (December 4, 2019). “Electrolyte Dictated Organic Electrode Materials Design for Energy Storage”; Y. Yao. Invited.

## TASK 3 – MODELING

### Summary and Highlights

Achieving the performance, life, and cost targets outlined by VTO will require moving to next-generation chemistries, such as higher capacity Li-ion intercalation cathodes, silicon and other alloy-based anodes, Li-metal anode, and sulfur cathodes. However, numerous problems plague development of these systems, from material-level challenges in ensuring reversibility to electrode-level issues in accommodating volume changes, to cell-level challenges in preventing cross talk between the electrodes. In this task, a mathematical perspective is applied to these challenges to provide an understanding of the underlying phenomenon and to suggest solutions that can be implemented by the material synthesis and electrode architecture groups.

The effort spans multiple length scales, from *ab initio* methods to continuum-scale techniques. Models are combined with experiments, and extensive collaborations are established with experimental groups to ensure that the predictions match reality. Efforts also focus on obtaining parameters needed for the models, either from lower-length scale methods or from experiments. Projects also emphasize pushing the boundaries of the modeling techniques used to ensure that the task stays at the cutting edge.

In the area of intercalation cathodes, effort is focused on understanding working principles of high nickel layered materials with an aim of understanding structural changes and associated changes in transport properties. Coatings, an effective strategy for high-voltage operation, are being explored with the aim of providing a rational design approach for new coating materials. In parallel, design of liquid electrolytes and gaining understanding of their behavior are used to determine their usability at high voltages. In addition, focus is paid to assembling of porous electrodes with particles to predict conduction behavior and impact of heterogeneities on electrode behavior.

In the area of Li-metal anodes, the focus is on understanding how materials can be designed to prevent dendrite growth using continuum modeling approaches, combined with calculations on mobility in solid conductors. The results are used to guide materials development by providing the properties needed to prevent dendrites while also achieving energy and power goals. Models are also starting to examine the role of the SEI on morphology of the dendrite and to describe mechanical-electrochemical coupled effects that are critical for dendrite formation. Finally, models are being developed to examine the solid-cathode interface in Li-metal based systems, where interface debonding issues are known to limit cycling.

Models are also being developed for solid electrolytes against intercalation cathodes and for developing methods to predict delamination at the interface during cycling in different cathode materials. These models are being used to understand how to prevent chemo-mechanical failure at the interface.

**Highlights.** The Srinivasan group has examined cathode-SEI to understand the impact of the cathode molar volume change on delamination and capacity fade of solid-state cells. Results show the importance of minimizing the cycling range and importance of smaller grain sizes in minimizing delamination.

## Task 3.1 – Characterization and Modeling of Li-Metal Batteries: First-Principles Modeling and Machine Learning (Kristin Persson, Lawrence Berkeley National Laboratory)

**Project Objective.** This project supports VTO programmatic goals by developing next-generation, high-energy cathode materials and enabling stable cathode operation at high voltages through target particle morphology design, functional coatings, and rational design of electrolytes. The end-of-project goals include the following: (1) understanding of the factors that govern charge transport in nonaqueous, superconcentrated liquid electrolytes, (2) critical surface and coating design and optimization strategies that will improve cycling of Li-ion battery cathodes by reducing cathode degradation from oxygen loss, and (3) simulation and machine learning of the early formation of the SEI on Li-metal electrodes.

**Project Impact.** This project is aimed to provide fundamental insights into the atomistic mechanisms underlying surface reactivity and performance of Li-ion cathode materials and electrolytes with the ultimate goal to suggest improvement strategies, such as coatings, surface protection, novel electrolyte formulations, and particle morphology design. Transport modes as a function of solvent and salt concentrations will be clarified, and a data-driven reaction network framework will be designed and implemented to predict early SEI formation on lithium metal.

**Approach.** First-principles calculations, both static and dynamic approaches, are used to model solid-state electrode material thermodynamics and kinetics. Liquid electrolytes are modeled through coupled classical MD and first-principles methods to accurately capture solvation structure as well as reactivity of the liquid system. The reaction network is built on large-scale first-principles data, using graph theory and machine learning models.

**Out-Year Goals.** Electrolyte work will be aimed toward understanding the atomistic interactions underlying the performance of lithium electrolytes specifically elucidating conductivity (as a function of salt concentration) and impact on the charge transport mechanisms at play. Amorphous coatings will be evaluated based on ionic transport metrics and thermodynamic stability. The reaction network will be tested against known interfacial species forming on lithium metal in LiPF<sub>6</sub>/EC electrolytes.

**Collaborations.** This project is highly collaborative between BMR PIs G. Chen (LBNL), G. Ceder (LBNL), and R. Kostecki (ANL). Improved coating formulations will be examined by Chen and Ceder, and interfacial reactivity insights corroborated by Kostecki.

### Milestones

1. Obtain desirable chemical and structural traits of amorphous cathode coatings. (Q1, FY 2020; Completed, December 2019)
2. Identify the lithium diffusion bottlenecks in two known coating materials. (Q2, FY 2020; In progress)
3. Quantify the conduction mechanisms in superconcentrated LiPF<sub>6</sub>/PC. (Q3, FY 2020; In progress)
4. Preliminary insights into the SEI composition and reaction pathways for baseline electrolytes. First approximative reaction scheme proposed. (Q4, FY 2020; In progress)

## Progress Report

The current BMR project is aimed toward understanding transport in superconcentrated electrolytes for Li-ion batteries. Due to the high level of correlation between the ionic species dissolved in solution, the use of dilute-limit descriptions for transport are precluded. Using classical MD simulations to model the electrolytes  $\text{LiBF}_4$  in propylene carbonate (PC) and  $\text{LiPF}_6$  in PC, transport properties were investigated via residence time analysis.

In Figure 60 (top), the residence time is plotted as function of concentration. The residence time increases as a function of salt concentration, which is generally expected due to the large increase in solution viscosity. In Figure 60 (middle), the characteristic diffusion length  $L^c = \sqrt{6D\tau^{res}}$  is shown as a function of concentration. For  $\text{Li}^+$ -PC, with both anions ( $\text{PF}_6^-$  and  $\text{BF}_4^-$ ),  $L^c$  slightly decreases with concentration, implying a slight shift toward a more structural diffusion.

However, here, the transport mode remains a mix of vehicular and structural diffusion, since  $L^c$  is comparable to the size of the solvation shell. For the transport mode of  $\text{Li}^+$  with respect to  $\text{PF}_6^-$ : the vehicular quality increases with concentration, but is at all concentrations more structural than  $\text{BF}_4^-$ . This may be due to the stronger binding energy of  $\text{Li}^+$  to  $\text{BF}_4^-$ .  $\text{Li}^+$  with respect to  $\text{BF}_4^-$ , in contrast, although more vehicular at all concentrations, shows a shift toward more structural diffusion at higher concentrations. Figure 60 (bottom) shows the ratio of the average time a  $\text{Li}^+$  spends around at least one anion to the residence time (one specific anion),  $\frac{\tau^{bound}}{\tau^{res}}$ . A higher

value of  $\frac{\tau^{bound}}{\tau^{res}}$  can be argued as a higher amount of ion hopping. Interestingly, although the ion hopping quality increases with concentration above 1.5 M, it is similar for both  $\text{Li}^+$ - $\text{PF}_6^-$  and  $\text{Li}^+$ - $\text{BF}_4^-$ .

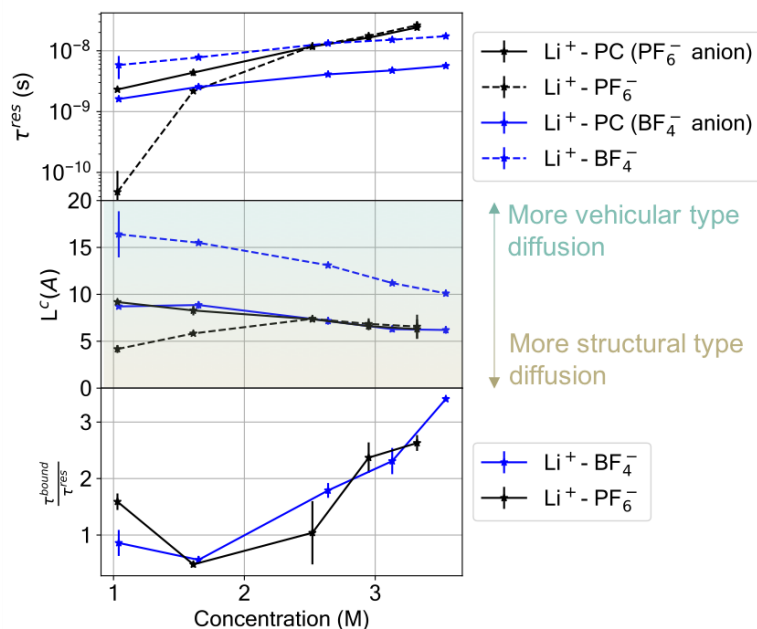


Figure 60. (top) Residence time plotted as function of concentration. (middle) Characteristic diffusion length  $L^c = \sqrt{6D\tau^{res}}$  is shown as function of concentration. (bottom) Ratio of the average time a  $\text{Li}^+$  spends around at least one anion to the residence time (one specific anion),  $\frac{\tau^{bound}}{\tau^{res}}$ .

## Patents/Publications/Presentations

### Publication

- Self, J., K. D. Fong, and K. A. Persson. “Transport in Superconcentrated  $\text{LiPF}_6$  and  $\text{LiBF}_4$ /Propylene Carbonate Electrolytes.” *ACS Energy Letters* 4, no. 12 (2019): 2843–2849.

## Task 3.2 – Understanding and Strategies for Controlled Interfacial Phenomena in Lithium-Ion Batteries and Beyond (Perla Balbuena and Jorge Seminario, Texas A&M University; Partha Mukherjee, Purdue University)

**Project Objective.** The project objective is to evaluate and characterize interfacial phenomena in lithiated silicon and Li-metal anodes and to develop guidelines for potential solutions leading to controlled reactivity at electrode/electrolyte interfaces of rechargeable batteries using advanced modeling techniques based on first principles.

**Project Impact.** Understanding SEI growth on constantly evolving silicon surfaces and on highly reactive Li-metal surfaces is expected to allow definition of the electrolyte properties required in high-performance cells. Strategies to control the silicon anode instability and pulverization issues and the well-known safety and short effective lifetimes of Li-metal anodes will be developed by tuning the electrolyte composition, structure, dynamic, and stability, as well as that of the electrode morphology and interactions with the electrolyte, based on multiple characterizations of interfacial phenomena.

**Approach.** A comprehensive multi-scale modeling approach, including first-principles *ab initio* static and dynamics, classical MD, and coarse-grained mesoscopic models, will focus on the roles of the electrolyte's chemical, structural, and dynamical properties and of the electrode micro- and nano- structure on the formation and evolution of the SEI layer and the associated electrochemical performance on silicon and on Li-metal anodes.

**Out-Year Goals.** Work will progress toward characterizing lithiation and SEI formation at silicon surfaces as well as the subsequent cracking and reforming events under the most realistic modeling conditions. Similarly, the project will investigate electrolyte effects on reactivity and dendrite formation in Li-metal surfaces. The project aims to capture how the chemistry of the various electrolyte components (mainly liquids, but also solid polymers and gels) affects the main issues that influence the electrode performance.

**Collaborations.** This project funds work at Texas A&M University (TAMU) and Purdue University. The team has collaborated with Prof. G. Somorjai (UC Berkeley), Prof. S. Yassar (University of Illinois at Chicago, or UIC), and Dr. V. Murugesan (PNNL).

### Milestones

1. Complete thermal and chemical/electrochemical analysis of dendrite growth. (Q1, FY 2020; Completed)
2. Complete analysis regarding SEI formation and electrodeposition processes. (Q2, FY 2020)
3. Complete studies on cationic additive effect on electrodeposition. (Q3, FY 2020)
4. Complete mesoscale investigation on external field effects on electrodeposition. (Q4, FY 2020)

## Progress Report

**Thermally Driven Operational Strategies to Heal Lithium Dendrites.** The morphological evolution during lithium electrodeposition is governed by competing phenomena occurring at the metal-electrolyte interface: ionic transport in the electrolyte, electrochemical reaction, and surface diffusion of deposited atoms. All of these phenomena exhibit T dependence. Reduced lithium atoms vibrate about their lattice sites at a frequency of  $10^{12}$ - $10^{13}$  s<sup>-1</sup>, and a higher T would provide the thermal energy required for enhanced migration of these atoms. Analogously, transport of ions in the electrolyte is also significantly improved.

Based on the coarse-grained mesoscale model, the team explores the synergistic effect of electrolyte transport and surface diffusion at elevated cell Ts. It is concluded that operating at Ts of ~350K would result in significant smoothing of the metal morphology, even compensating for increased reaction rates. The electrochemical performance of the cell additionally benefits from the reduced porosity of the metal deposit, which alleviates electrolyte seepage and starvation over prolonged cycling. The phenomenon of reduced dendrite height at ~350K (compared to morphologies at 300K and 325K) is depicted in Figure 61a. Subsequently, the team reduces the scope of the thermal field up to the electrode surface. Any healing of dendrite morphology at such an event is solely due to enhanced surface diffusion of lithium atoms, with no contribution from electrolyte transport. Such an operational technique would only require heating the metal anode, rather than the application of a uniform field across the entire cell. This is also to some extent, similar to the operational strategy of an externally applied thermal gradient. The project results indicate that even increasing the cell temperature as high as ~400K does not lead to the desired relaxation of the metal morphology. Further, this elucidates the crucial role played by electrolyte transport in the suppression of dendrites. Obtained metal

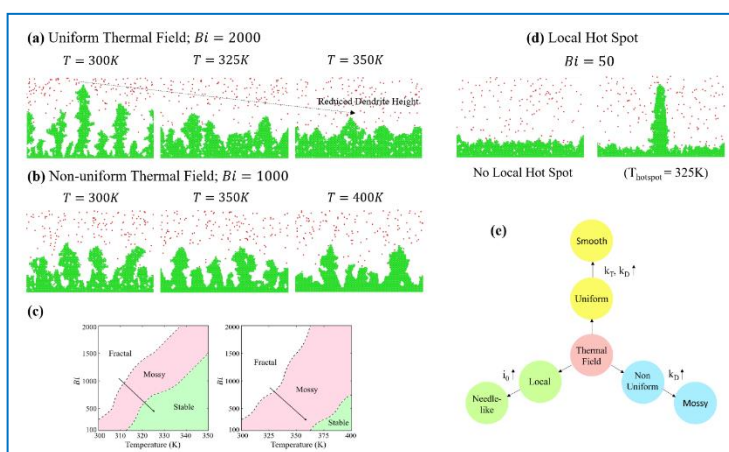


**Figure 61.** (a) Phenomenon of reduced dendrite height at ~350K (compared to morphologies at 300K and 325K). (b) Obtained metal morphologies at 300K, 350K, and 400K. (c) Phase maps summarizing electrodeposition morphologies obtained at various operating temperatures. (d) Contrasting morphologies: simulations predict that for operating temperature of 300K, a local hot spot temperature of 325K is sufficient to trigger aggravated dendrite growth. (e) Homogenizing internal thermal field (~350K) helps effective dendrite suppression.

morphologies at 300K, 350K, and 400K have been shown in Figure 61b. The electrodeposition morphologies formed in the uniform and non-uniform thermal field fall into three regimes: stable, mossy, and fractal. The electrodeposition morphologies obtained at various operating temperatures have been summarized in the phase maps shown in Figure 61c. A transition in the metal morphology from fractal to stable is depicted by the black arrows. As illustrated in Figure 61c, a general trend in morphology transition is observed from fractal to stable with an increase in temperature and a decrease in the electrochemical Biot number (Bi), which is directly correlated to the reaction rate and hence to the current density of the system. High Bi numbers represent high reaction rate, resulting in ion depletion and dendrite growth initiation at moderate Ts. Finally, the team further shrinks the domain of high T to a confined local spot at the electrode surface. Here, they observe the formation of a needle-like morphology. The governing mechanism is enhancement of local exchange current density, which is due to the elevated temperature of the hot spot. This increases the intrinsic rate of reaction in this region to a substantially higher value compared to other portions of the electrode. The team's simulations predict that for an operating temperature of 300K, a local hot spot temperature of 325K is sufficient to trigger aggravated dendrite growth. The contrasting morphologies are shown in Figure 61d.

In conclusion, homogenizing the internal thermal field (~ 350K) helps effective dendrite suppression. The team infers that application of a uniform thermal field would outperform other strategies such as an external thermal gradient. In contrast, localization of the thermal field substantially increases the exchange current density of the confined region, leading to needle-like dendrites. Even at 25K, a thermal hotspot could instigate needle-like dendrite growth and internal short-circuit. See summary in Figure 61e.

**Development of a Simple Model to Describe Dendrite Formation.** A simple *ab initio*-based model was implemented to characterize the SEI reactions and cation electrodeposition. The model is based on characterization of the electrostatic potential changes in lithium clusters models (Kamphaus and Balbuena, *Physical Chemistry Chemical Physics*, 2020).

## Patents/Publications/Presentations

### Publications

- Kamphaus, E. P., K. Hight, M. Dermott, and P. B. Balbuena. “Model Systems for Screening and Investigation of Lithium Metal Electrode Chemistry and Dendrite Formation.” *Physical Chemistry Chemical Physics* 22 (2020): 575–588.
- Ponce, V. H., and J. M. Seminario. “Sulfur–Graphene Cathode Model Using Reactive Force Field Molecular Dynamics Simulations.” Submitted.
- Galvez-Aranda, D. E., and J. M. Seminario. “Formation of a Solid Electrolyte Interphase between the Solid State Electrolyte  $\text{Li}_{0.29}\text{La}_{0.57}\text{TiO}_3$  and a Li-Metal Anode: An *Ab Initio* Molecular Dynamics Study.” *RSC Advances*. Submitted.

### Presentations

- 236<sup>th</sup> ECS Meeting, Atlanta, Georgia (October 14, 2019): “Solid-Electrolyte Interphase on Li Metal Surfaces”; P. B. Balbuena. Invited.
- 236<sup>th</sup> ECS Meeting, Atlanta, Georgia (October 14, 2019): “Analysis of the Formation, Evolution, and Alternatives of the Solid-Electrolyte Interface in Li-Metal Batteries” [MA2019-02 (4), 198]; J. M. Seminario, D. E. Galvez-Aranda, M. Gamero T., L. Selis, V. H. Ponce, and F. Franco-Gallo.
- 236<sup>th</sup> ECS Meeting, Atlanta, Georgia (October 13–17, 2019): “Lithium Electrodeposition at the Solid Electrolyte and Lithium Metal Interface”; D. Tewari and P. P. Mukherjee.
- AIChE National Meeting, Orlando, Florida (November 14, 2019): “Solubility of the Solid Electrolyte Interphase Layer Components”; E. P. Kamphaus and P. B. Balbuena.

### Task 3.3 – Electrode Materials Design and Failure Prediction (Venkat Srinivasan, Argonne National Laboratory)

**Project Objective.** The main project objective is to develop computational models for understanding the various degradation mechanisms for next-generation Li-ion batteries. This year's goal is to use the continuum-based mathematical model to (1) investigate interfacial stability between electrodes and ceramic-based SSEs, and (2) experimentally measure and understand the impedance observed at the cathode/SSE interface. Ceramic-based SSEs are expected to enable high-energy-density and liquid-free, safe, next-generation Li-ion batteries. Li-metal anodes should be incorporated due to their substantially larger specific capacity, as compared to present day graphite-based anodes. During deposition, lithium dendrite growth through the SSEs, and subsequent short circuit, has been a major issue, limiting successful implementation of SSEs. Similarly, on the cathode side, diffusion of TMs into the SSEs, along with delamination between cathode and SSE, leads to increased interfacial resistance. The developed computational model will be used to investigate the impact of microstructural (grain size), physical (mechanical stiffness), and transport (conductivity) properties of the SSE on the overall interfacial degradation observed at both the cathode and anode sides. Due to the SOC-dependent electrochemical and mechanical properties of the cathode, an attempt will be made to experimentally measure the SOC-dependent impedance at the cathode/SSE interface. The main focus will be to elucidate interfacial issues, observed at both anode and cathode sides, and to devise strategies to enable successful implementation of SSE in next-generation Li-ion batteries.

**Project Impact.** Findings from this research will give a better understanding of the factors, at the cathode/SSE interface, limiting the cycle life of solid-electrolyte-based Li-ion batteries. These results will help to enable incorporation of cathode particles within SSEs.

**Project Approach.** The approach used here is to develop mesoscale models, based on continuum modeling, to describe the critical processes in the materials, and combining them with electrochemical, microscopic, and spectroscopic data to ensure parameter estimation and model validation. The model is then used to provide insights on impact of material properties on performance and life and as guidance for design of new materials.

**Out-Year Goals.** At the end of this project, a computational framework will be presented that is capable of estimating delamination and impedance at cathode/SSE interface.

**Collaborations.** This project collaborates with L. A. Curtiss, A. T. Ngo, and C. M. Phatak at ANL.

#### Milestones

1. Elucidate the difference in delamination mechanisms for NMC/LLZO- and LCO/LLZO- type cathode/SEIs. (Q1, FY 2019; Completed)
2. *Go/No-Go Decision:* Investigate impact of exchange current density on delamination-induced capacity fade. If effect is minor, use experimentally observed exchange current values. Otherwise, use value obtained from DFT calculations. (Q2, FY 2020; In progress)
3. Develop continuum model for charge transport and mechanical degradation incorporating an interphase layer between LLZO electrolyte and NMC cathode. (Q3, FY 2020, In progress)
4. Gain understanding of growth rate of electrodepositing lithium nuclei. (Q4, FY 2020, In progress)

## Progress Report

**Elucidate the Difference in Delamination Mechanisms for NMC/LLZO- and LCO/LLZO- Type Cathode/SEIs.** Due to the high elastic modulus and non-conformability of SSEs, the interface between cathodes and SSEs are prone to rupture and detachment. During lithiation and delithiation processes, the cathode particles expand or contract, which depends on the partial molar volume of lithium within the cathode material. As the cathode shrinks, tensile stresses evolve at the cathode/SSE interface because the solid electrolytes cannot change shape easily to accommodate the volume change within the cathodes. If the magnitude of tensile stress exceeds its fracture threshold, delamination would occur at the interface of cathode and SSEs. Figure 62a-b demonstrates the partial molar volume of lithium within NMC and LCO cathodes, respectively. In NMC, the partial molar volume of lithium is positive, meaning that during charge as lithium goes out, the cathode material shrinks and induces tensile stress at the interface. This eventually leads to delamination at the NMC/LLZO interface at the time of charge process. In contrast, the partial molar volume of lithium within LCO is negative for the voltage range of battery operation. Hence, the cathode expands as lithium goes out during charge, and shrinks at the time of discharge process when lithium ions move into the LCO lattice. As a result, tensile stress at the LCO/LLZO interface is observed at time of discharge, and the majority of delamination occurs then.

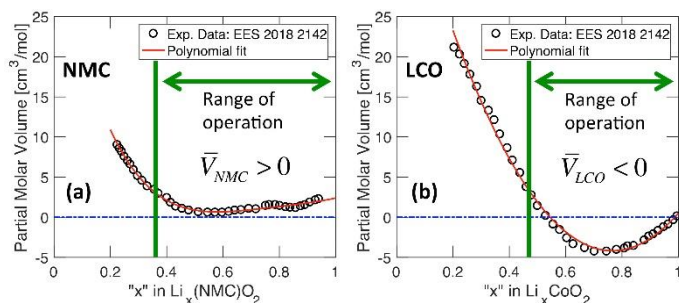


**Figure 62.** (a) Concentration-dependent partial molar volume of lithium within NMC cathodes. (b) Partial molar volume of lithium within LCO cathodes. It is evident that within the range of operation, NMC and LCO demonstrate positive and negative partial molar volumes with respect to lithium, which impacts their performance.

The charge and discharge curves as observed in NMC and LCO cathodes with LLZO SSE are shown in Figure 63a-b, respectively. As mentioned earlier, major interfacial delamination occurs for NMC during charge, and for LCO during the discharge process. This interfacial delamination leads to increase in charge transfer resistance, and eventually, discharge capacity fade. Both the NMC and LCO cathodes have been operated under constant current and constant voltage (CC-CV) charge and CC discharge protocol under an applied current density of  $1\text{A/m}^2$ . It has been argued that decreasing LLZO grain size can help to minimize delamination-induced capacity fade. Accordingly, capacity fade experienced by LCO and NMC cathodes with various LLZO grain sizes is demonstrated in Figure 63c. For both NMC and LCO, adoption of smaller LLZO grains can minimize capacity fade. This analysis shows the correlation between delamination-induced capacity fade experienced by LCO and NMC cathodes, and completes the first-quarter milestone.

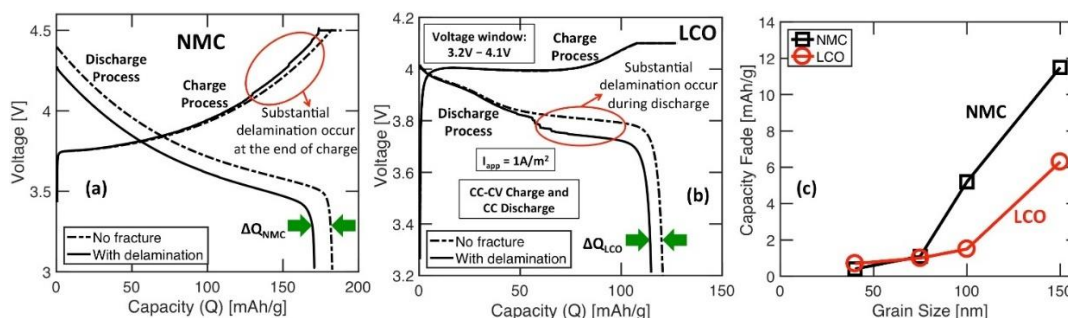


**Figure 63.** (a) Performance curves demonstrated by NMC cathodes with LLZO electrolytes. Substantial delamination-induced impedance rise observed during charge, which leads to capacity fade during discharge. (b) Charge/discharge performance curves experienced by the LCO cathodes with LLZO electrolytes. Major delamination-induced impedance rise, and subsequent capacity fade, occurs during the discharge process. (c) LLZO grain size dependent discharge capacity fade experienced by NMC and LCO cathodes. Smaller grains help to minimize the delamination-induced capacity fade in both the cathode materials.

## Patents/Publications/Presentations

### Presentation

- 236<sup>th</sup> ECS Meeting, Atlanta, Georgia (October 2019): “Investigation of Volume Change Induced Delamination and Subsequent Capacity Fade at Cathode/Solid-State-Electrolyte Interface”; A. P. Barai, A. T. Ngo, L. A. Curtiss, and V. Srinivasan.

## Task 3.4 – Dendrite Growth Morphology Modeling in Liquid and Solid Electrolytes (Yue Qi, Michigan State University)

**Project Objective.** The project goal is to develop a validated model to predict lithium dendrite morphology evolution in both liquid and solid electrolytes during electrodeposition and stripping to accelerate the adoption of Li-metal electrodes in current and emerging battery technologies. To achieve this goal, the project has four objectives: (1) formulate a general framework that captures the electrochemical-mechanical driving forces for lithium morphology evolution; (2) consider the role of the nm-thin SEI in liquid electrolytes as well as the microstructures of  $\mu\text{m}$ -thick solid electrolytes for lithium morphology evolution; (3) connect micron-scale phase-field models and atomic-scale DFT-based simulations via parameter- and relationship-passing to predict lithium dendrite nucleation and growth kinetics and morphology; and (4) validate the key input parameters and main conclusions of the multi-scale model as new capabilities are being developed step-by-step.

**Project Impact.** This atomically informed, fully coupled, electrochemical-mechanical dendrite morphology evolution model will allow the project to design the desired properties of artificial SEI coatings, the microstructure of solid electrolyte materials, and the corresponding battery operating conditions, so as to avoid dendrite growth during cycling. It will accelerate design of durable and safe lithium anodes for Li-S, Li-air, and all-solid Li-ion batteries. Thus, it directly impacts such emerging technologies that aim to meet the DOE target of the high-energy-density battery cells ( $> 350 \text{ Wh/kg}$ ) for EV applications and to push the cost below  $\$100/\text{kWh}_{\text{use}}$ .

**Approach.** A multi-scale model approach is taken to connect micron-scale phase-field models and atomic-scale DFT-based simulations via parameter- and relationship-passing.

**Out-Year Goals.** The second-year goal is to establish the model to simulate metallic lithium precipitation in solid electrolytes while further developing understanding of lithium dendrite growth in liquid electrolytes. To reach this goal, mechanical and electrochemical driving forces for lithium dendrite growth in solid electrolytes will be coupled in phase-field model, while DFT is used to address the lithium plating tendency in various solid electrolyte and coating materials. Validation of the model will come from experiments to correlate the distinctive transport properties of artificial SEI layers with their impact on lithium dendrite morphology.

**Collaborations.** This project collaborates with UMD, Sandia National Laboratories (SNL), PNNL, University of Arkansas, and University of Houston.

### Milestones

1. Identify an ideal microstructure of LLZO to avoid lithium dendrite growth. (Q1, FY 2019. It was predicted that a coating layer, such as LiPON, between the Li/LLZO would be more efficient in resisting lithium dendrite. A *Go* decision was made to experimentally vary this prediction.)
2. Develop a fully coupled Li/SEI/liquid electrolyte dendrite morphology model. (Q2, FY 2019; Completed)
3. Illustrate the relationship between Li/SEI interface roughness, adhesion, and dendrite morphology in a liquid electrolyte. (Q3, FY 2019; Completed)
4. Determine the effect of multi-component SEI layer on dendrite morphology in a liquid electrolyte. (Q4, FY 2019; In progress)

## Progress Report

### Phase Field Model to Reveal Impact of Crack in SEI on Dendrite Morphology in Liquid Electrolyte

The influence of cracks in SEI layer on lithium electrodeposition kinetics and plating morphology was investigated using the as-developed “implicit SEI” phase-field model. In this model, no additional order parameter was included to resolve SEI layer as an independent phase. Instead, the SEI layer properties, such as Li-ion diffusion coefficient, were described via interpolated parameters at the diffuse anode/electrolyte interface. The crack in SEI layer was described by a narrow region in the SEI layer, which takes the Li-ion diffusion coefficient in the liquid electrolyte. Figure 64 shows the lithium plating morphologies in the presence of cracked SEI with different properties. By controlling the crack width at 0.2  $\mu\text{m}$  with no space charge, the team observes an increasing trend of dendrite growth length in Y direction, as the ratio of the Li-ion diffusion coefficients in the electrolyte and in SEI ( $D_{\text{sol}}/D_{\text{sei}}$ ) becomes larger, as shown in Figure 64a-c. Furthermore, the team varied the crack width from 0.2  $\mu\text{m}$  to 1  $\mu\text{m}$  with no space charge, while keeping the Li-ion diffusion coefficient in SEI to be  $10^{-13} \mu^2/\text{s}$ . They also found that the dendrite morphologies are not prominently affected by the change in crack scale if crack width is under 0.5  $\mu\text{m}$ , as demonstrated in Figure 64d-f. As crack width becomes larger than 0.5  $\mu\text{m}$ , the dendrite tip splits into two. Considering the local charge non-neutrality at the crack, the team also studied the crack-induced space charge impact on Li-plating morphology. By increasing the space electron density from  $0.8 \times 10^{-10}$  to  $1.6 \times 10^{-9} \text{ C} \cdot \text{m}^3$  while keeping the other two properties invariant, that is, crack width of 0.2  $\mu\text{m}$  and Li-ion diffusion coefficient in SEI to be  $10^{-12} \mu^2/\text{s}$ , the team sees an increasing trend of dendrite growth along the Y direction with even faster growth rates (Figure 64g-i) than those shown in Figure 64a-c. Based on these phase-field simulation results, conclusions can be drawn that:

- Lithium dendrite tends to initiate at the cracked SEI region, and dendrite growth morphology does not depend much on crack width if the crack width is less than 0.5  $\mu\text{m}$ .
- A larger lithium diffusivity difference between SEI and electrolyte and a higher local electron density on the crack surface both lead to more inhomogeneous lithium deposition and faster dendrite growth at cracks.

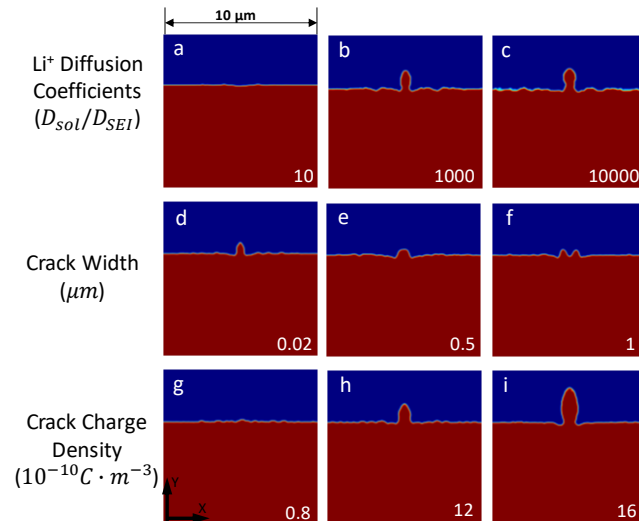


Figure 64. Morphologies of lithium plating under different conditions.

### DFT Prediction of Space Charges in Inhomogeneous SEI

A key inhomogeneity in the SEI is the GBs. A systematic study of the electronic properties of GBs was conducted via DFT calculations. All the GBs reduced the bandgaps, and the tilt GBs reduced the bandgaps to a larger extent than the twist GBs. More detailed electronic structure and bond coordination numbers analysis was performed to understand what determines the bandgap drop at GBs. It was found that the more that GB atoms are less coordinated, the larger the band gap drop at the GBs. For example, for LiF Twist  $\Sigma 3$  (111) GB, no atoms at the GB are under coordinated, and its bandgap is 8.19 eV, which is a 0.64 eV drop from the bulk band gap value. For LiF Tilt  $\Sigma 3$  ( $\bar{1}2\bar{1}$ ), the GB width is about 6.32  $\text{\AA}$ , and all atoms in this region are under coordinated. The corresponding GB bandgap drops to 7.26 eV (a 1.92 eV decrease). This trend holds for all the LiF and Li<sub>2</sub>O tilt and twist GBs that the team has investigated. This is because when the anions ( $\text{F}^-$  or  $\text{O}^{2-}$ ) are under coordinated, they can serve as traps for excess electrons. In the next step, the team will evaluate the space charge at heterogeneous interfaces in multicomponent SEI, such as LiF/Li<sub>2</sub>CO<sub>3</sub> interfaces.

## Patents/Publications/Presentations

### Publications

- Xu, B., Z. Liu, J. Li, X. Huang, B. Qie, T. Gong, L. Tan, X. Yang, D. Paley, M. Dontigny, K. Zaghbi, X. Liao, Q. Cheng, H. Zhai, X. Chen, L-Q. Chen, C-W. Nan, Y-H. Lin, and Y. Yang. “Engineering Interfacial Adhesion for High-Performance Lithium Metal Anode.” *Nano Energy* 67 (2020): 104242.
- Liu, Z., Y. Li, Y. Ji, Q. Zhang, X. Xiao, Y. Yao, L-Q. Chen, and Y. Qi. “Dendrite Free Li – Lesson Learned from the Li and Mg Electrodeposition Morphology Simulations.” Pending submission (2020).
- Xu, J. G., B. S. Li, M. Wang, Q. L. Zhang, Y. Qi, and X. C. Xiao. “Impact of Solid Electrolyte Interphases on Lithium Metal Plating and Stripping at Early Stages.” Pending submission (2020).

### Presentations

- Materials Science and Technology (MS&T), Portland, Oregon (October 1, 2019): “Modeling the Origin of the Interface Resistance in Solid-State Batteries”; Y. Qi, M. Swift, and H. K. Tian.
- MRS Fall Meeting, Boston, Massachusetts (December 2019): “The Electronic Reasons for Li Dendrite Growth in Solid Electrolytes”; Y. Qi, H. K. Tian, Z. Liu, Y. Z. Liu, and L. Q. Chen.

### Task 3.5 – Modeling of Amorphous Solid-State Conductors (Gerbrand Ceder, Lawrence Berkeley National Laboratory)

**Project Objective.** SSEs are promising to achieve high energy density. The project objective is to determine the design principles needed to create SSEs with high Li-ion conductivity while also achieving stability against common Li-ion cathodes and Li-metal anodes.

**Project Impact.** The project will lead to understanding the factors that control Li-ion motion in crystalline and amorphous solids and will develop strategies to create stable interfaces against lithium metal and high-voltage cathode materials. The understanding of such processes is necessary to determine design principles to develop reliable ASSBs.

**Approach.** High-throughput computation method is used to screen suitable solid electrolyte with high electrochemical stability and high ionic conductivity, by incorporating Nudged Elastic Band (NEB) and an *ab initio* molecular dynamics (AIMD) method. Meanwhile, DFT is used to calculate bulk elastic constants of materials, surface energies, and interface decohesion energies of GBs. Thermodynamic interface stability is assessed from *ab initio* computed grand potential phase diagrams in which the lithium voltage can be controlled. Kinetic limits for solid electrolyte decomposition are assessed by topotactic lithium insertion and removal from the solid electrolyte.

**Out-Year Goals.** Future goals include the following: (1) gain insight into what creates high Li-ion conduction in sulfide and oxide solids, and (2) develop stable, processable solid-state conductors that can be applied in ASSBs.

**Collaborations.** There are no collaborative activities this quarter.

#### Milestones

1. Modeling of the  $\text{Li}_2\text{S-P}_2\text{S}_5$  ground state phase diagram for SSEs: solid phases correctly modeled. (Q1, FY 2020; Completed)
2. Modeling of LPS lithium mobility in amorphous state with variations of  $\text{PS}_4$  structural units. (Q2, FY 2020)
3. Develop model for the lithium conductivity in amorphous sulfide solids. (Q3, FY 2020)
4. Modeling of the full finite temperature L-S-P phase diagram to understand metastability of the highly conducting solids. (Q4, FY 2020)

## Progress Report

### Modeling of LPS Lithium Mobility for at Least Three Distinct Compositional Modifications

The stoichiometric composition of amorphous Li-P-S phase is a key descriptor for ionic conductivity.<sup>[1]</sup> Recent experimental work shows that amorphous Li-P-S consists of anion blocks such as  $\text{PS}_4^{3-}$ ,  $\text{P}_2\text{S}_6^{4-}$ , and  $\text{P}_2\text{S}_7^{4-}$  and that their ratio is determined by the atomic composition.<sup>[2]</sup>

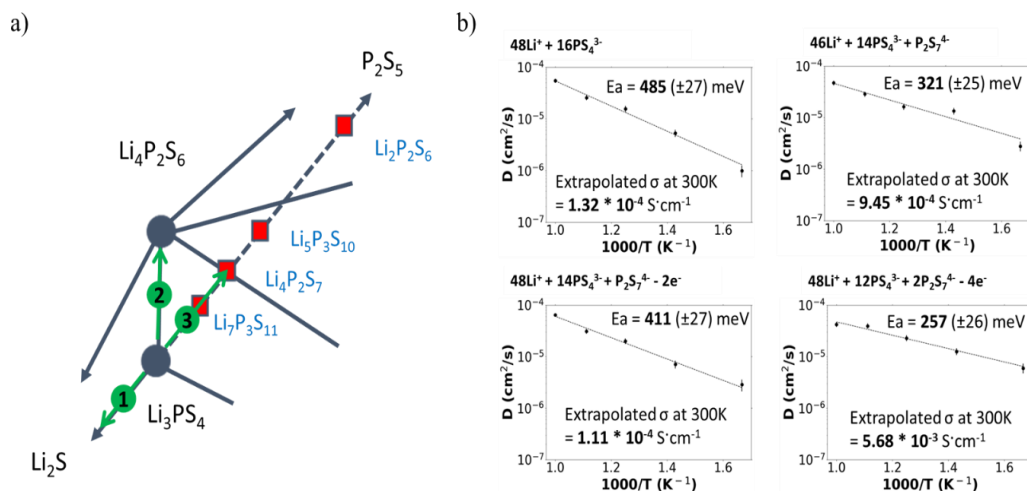


Figure 65. (a) Part of Li-P-S phase diagram. Stable and unstable phases are written in black and blue font, respectively. Each arrow depicts substitution from  $\text{PS}_4^{3-}$  to a different anion block. (b) Arrhenius plots of *ab initio* molecular dynamic simulation on the Li-P-S systems with different compositions, that is, substitution from  $\text{PS}_4^{3-}$  to  $\text{P}_2\text{S}_7^{4-}$  (the third arrow).

The relationship between the ratio of anion blocks and the atomic composition can be understood in terms of crystalline phase diagram (Figure 65a). Starting from the  $\text{Li}_3\text{PS}_4$  phase that contains only  $\text{PS}_4^{3-}$  anion, the first, second, and third arrows in Figure 65a represent substitution of  $\text{PS}_4^{3-}$  to  $\text{S}^{2-}$ ,  $\text{P}_2\text{S}_6^{4-}$ , and  $\text{P}_2\text{S}_7^{4-}$ , respectively. Among these substitutions, direction 3 on the Figure (that is,  $\text{PS}_4^{3-}$  to  $\text{P}_2\text{S}_7^{4-}$ ) is studied in this report because  $\text{Li}_7\text{P}_3\text{S}_{11}$  phase, which consists of 50% of  $\text{PS}_4^{3-}$  and 50% of  $\text{P}_2\text{S}_7^{4-}$  anion blocks, is a well-known lithium super ionic conductor.<sup>[3]</sup> To verify the role of substitution in amorphous LPS system, the structures consisting of different composition (and corresponding ratio of building blocks) are prepared by a high-temperature anneal and quench AIMD method. The reference structure, which only contains  $\text{PS}_4^{3-}$  anions, is modeled by annealing the  $\beta$ - $\text{Li}_3\text{PS}_4$  phase at 1000K. The density is kept constant at  $2 \text{ g cm}^{-3}$  for all structures. From the reference structure, two  $\text{PS}_4^{3-}$  anions are substituted to  $\text{P}_2\text{S}_7^{4-}$ , while charges are balanced by removing  $2\text{Li}^+$  and  $\text{S}^{2-}$  ions. From diffusion simulations more than 250 ps at 600, 700, 800, 900, and 1000 K on these materials, the activation barriers of diffusion are determined to be 485 (Figure 65b, upper left) and 321 (Figure 65b, upper right) meV. The decrease of diffusion barrier is apparent, which can be attributed to the increased concentration of lithium vacancies. To remove the effect of lithium vacancy concentration, an alternate model structure is generated. Instead of balancing charges by removing  $2\text{Li}^+$  and  $\text{S}^{2-}$  ions,  $\text{S}^{2-}$  ion and two electrons are subtracted in the structure, to keep the number of lithium ions constant. Diffusion simulation of this structure results in a migration barrier of 411 meV (Figure 65b, lower left), showing a slight decrease of the barrier as compared to reference case. Interestingly, simulation of the structure with further substitution of  $\text{PS}_4^{3-}$  to  $\text{P}_2\text{S}_7^{4-}$  shows a dramatic decrease of the migration barrier to 257 meV (Figure 65b, lower right), which corresponds to 15 times faster Li-ion conductivity. This improvement can be explained by the frustration of the Li-ion energy landscape by substitution, which requires further study. From this series of simulations, it is revealed that both the lithium vacancy concentration and presence of  $\text{P}_2\text{S}_7^{4-}$  anion significantly affect the ionic conductivity of amorphous LPS.

#### References

- [1] Zheng, F., et al. *Journal of Power Sources* 389 (2018): 198–213.
- [2] Dietrich, C., et al. *Journal of Materials Chemistry A* 5, no. 34 (2017): 18111–18119.
- [3] Yamane, H., et al. *Solid State Ionics* 178 (2007): 1163–1167.

## Patents/Publications/Presentations

The project has no patents, publications, or presentations to report this quarter.

## Task 3.6 – Characterization and Modeling of Li-Metal Batteries: Force Field Theory and Lithium-Sulfur Battery Simulations (Lin-Wang Wang, Lawrence Berkeley National Laboratory)

**Project Objective.** The project objective is to develop force field based on *ab initio* calculations to study Li-S cathode and lithium liquid electrolyte. It also includes designs for Li-S cathode systems for high gravimetric and volumetric capacities. Lithium diffusion in both liquid electrolyte in a confined space, and in Li-S cathode systems, is a main focus of this subtask. To enable calculation of large systems, machine learning force field (ML-FF) trained on *ab initio* calculation data will also be developed. The success of this new approach will greatly expand the capability of theoretical simulation for battery systems. Such ML-FF can also be used in combination with traditional classical force field to deal with the nonreactive parts of the system.

**Project Impact.** Making the Li-S battery a commercial reality will have a major impact on society and also help to realize the VTO goal of 500 km per charge for EV. However, the nature of chemical reaction makes it different from the traditional intercalation-based Li-ion battery. The molecular nature of  $\text{Li}_2\text{S}_n$  also allows solvation in the electrolyte. To address these problems, it is essential to have fundamental studies and understandings of the underlying mechanisms. Theoretical simulations can play an important role in discovering and designing new cathode materials. However, traditional *ab initio* calculations are limited by their computational size, while the classical force field simulations are limited by their accuracy and the lack of adequate force field. The development of ML-FF can overcome these problems by bridging the size gap between the *ab initio* simulation and the real systems that need to be studied.

**Approach.** ML-FF will be developed by first running *ab initio* simulations, which can generate hundreds of thousands of data sets. The project has a unique capability of decomposing the total energy of a DFT calculation into the energy of each atom. Compared to conventional DFT calculations, this increases the number of data by hundreds of times, an important requirement for ML model training. The dependence of the atomic energy to the local atomic bonding environment will be captured using ML methods. Three ML approaches will be: linear fitting, neural network model, and Gaussian process regression (GPR) model. The team will compare the efficacies of these models. In the meanwhile, they will also deal with the long-range Coulomb interactions existing in the electrolyte system and the ionic species in liquid electrolyte. The idea is to first fit the charge density of the system, and remove the long-range electrostatic energy before the fitting of the local energy on each atom. The team will also design new Li-S and Na-S cathode materials. In particular, they will design amorphous Li-S mixture, with some other materials (for example, carbon nanotube, black carbon, or electric conductive 2D materials).

**Out-Year Goals.** In outgoing years, the project will further develop computational methods for more accurate entropy and interaction energy calculations for the electrolyte, as well as for Li-S cathode systems.

**Collaborations.** The project will collaborate with G. Liu and Y. Cui for cathode design. It has also collaborated with Prof. F. Pan of Beijing University for lithium battery research in general.

### Milestones

1. New Li-S design, mixing Li-S with carbon nanotube for an ultrafine mixture. (Q1, FY 2020; Partly completed)
2. Lithium charge density fitting in electrolyte, to fit the long-range Coulomb interaction. (Q2, FY 2020; Initiated)
3. Incorporation of Coulomb interaction in the local energy calculation; ML-FF fitting. (Q3, FY 2020)
4. Further study of Li-S cathode with polymer, to study electric conductivity in such a system. (Q4, FY 2020)

## Progress Report

Carbon nanotube is widely used as an additive in the cathode of Li-S battery due to its good electronic conductivity. How the carbon nanotube interacts with sulfur and Li-S systems is unknown. The team has tried to explore other roles beyond electric conductivity that carbon nanotube plays in Li-S battery via AIMD. In particular, the team seeks to know in what case the system is stable on repeated charging and discharging. In Figure 66, they show that there is no obvious chemical interaction between an empty carbon nanotube and sulfur. In that case, when lithium is added in the system, the Li-S can crash the empty carbon nanotube, making it form additional bonds. Thus, the team proposes that such a system can become unstable on repeated charging and discharging. On the other hand, if the carbon nanotube can be filled with lithium atom from the beginning, then the carbon nanotube maintains good bonding topology during the discharging (lithiation) process, except the shape changes from circle into oval. After the charging process (removing the lithium from Li-S), the carbon nanotube returns to its initial condition. Therefore, only when the carbon atom is filled with lithium is the system stable for charge/discharge process. This is a case for extremely fine grain mixing between the carbon nanotube and the Li-S system.

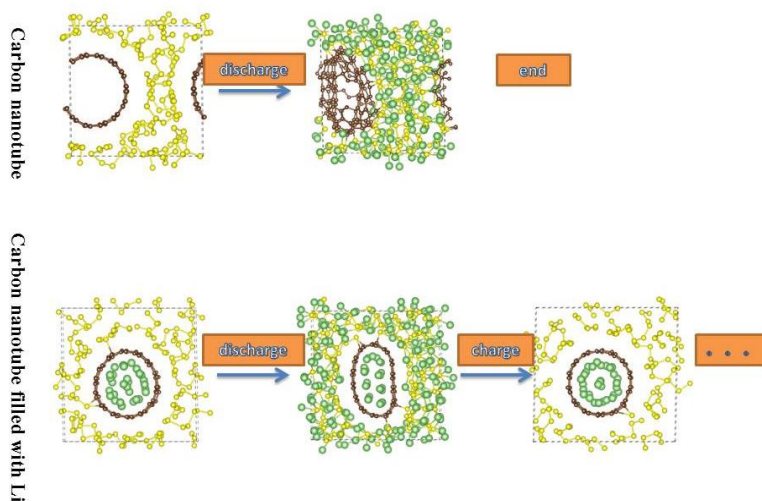


Figure 66. The interaction of sulfur and Li-S with carbon nanotube with and without internal filling with lithium.

The team has also initiated study of electrostatic potential calculation in lithium electrolyte. This is for the ML-FF development. As the current ML-FF model only describes the atomic energy dependence on local atomic binding environment, it is incapable of describing any long-range interaction. One major long-range interaction is the Coulomb interaction. This will be a concern for the lithium electrolyte, where the  $\text{Li}^+$  ion and the counter anion (for example,  $\text{PF}_6^-$ ) can cause long-range interaction. The team has developed a way to fit the charge density around each atom. Using such charge density, the long-range electrostatic interaction can be precalculated. Furthermore, this part of the energy can be taken out of the total energy expression of the DFT formalism. The hope is that the remaining energy will be absent in such long-range interaction. On the other hand, the fitted density part of the long-range interaction can be presented by an analytical pair potential expression, which can be included in the force field simulation.

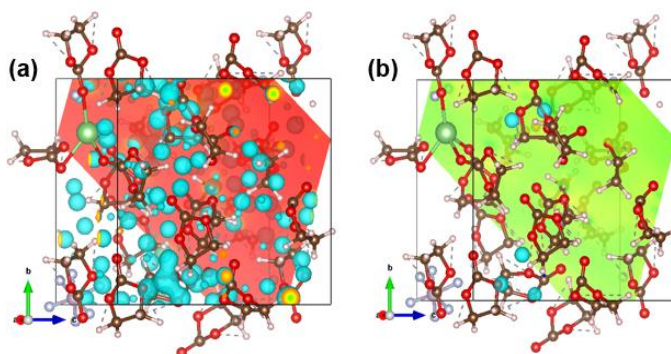


Figure 67. The electrostatic potential in ethylene carbonate electrolyte with  $\text{LiPF}_6$  salt. The  $\text{Li}^+$  and  $\text{PF}_6^-$  can induce long-range electric field. (a) Full electrostatic potential. (b) Electrostatic potential after removing the fitting charge density electrostatic potential.

## Patents/Publications/Presentations

### Publications

- Zhou, G., A. Yang, Y. Wang, G. Gao, A. Pei, X. Yu, Y. Zhu, L. Zong, B. Liu, J. Xu, N. Liu, J. Zhang, Y. Li, L. W. Wang, H. Hwang, M. Brongersma, S. Chu, and Y. Cui. “Electrotunable Liquid Sulphur Microdroplets.” *Nature Communications* (2019). Accepted.
- Zhang, B., Z. Lin, H. Dong, L. W. Wang, and F. Pan. “Revealing Cooperative Li-Ion Migration in  $\text{Li}_{1+x}\text{Al}_x\text{Ti}_{2-x}(\text{PO}_4)_3$  Solid State Electrolyte with High Al Doping.” *Journal of Materials Chemistry A* (2019): Accepted.

## Task 3.7 – *In Situ* and *Operando* Thermal Diagnostics of Buried Interfaces in Beyond Lithium-Ion Cells (Ravi Prasher, Lawrence Berkeley National Laboratory)

**Project Objective.** Transport at various interfaces in *beyond lithium ion* cells will play a major role in electrochemical performance and reliability. It has not yet been possible to thermally profile a Li-metal cell during operation to provide a spatially resolved map of thermal transport properties throughout the cell. The objective of this research is to create a metrology capable of spatially resolved *in operando* thermal property profiling, and then relate those thermal properties to the quality of electrodes and interfaces, and use the developed thermal metrology to understand electrochemical processes in Li-metal batteries such as dendrite growth and lithium plating characteristics under different situations.

**Project Impact.** Characterizing electrochemical processes in Li-metal cells such as lithium deposition and dendrite growth at interfaces is of great significance for understanding and enhancing their electrochemical performance and reliability. *In situ* and *operando* 3-omega micro thermal sensors can provide significant information regarding the impact of buried interfaces as a function of time, material, voltage, current, and temperature *etc.* Therefore, it is important to develop *operando* 3-omega micro thermal sensors and develop models relating those signals to electrochemical performance for *beyond lithium ion* cells. The physics-based model relating thermal and electrochemical properties based on these measurements can facilitate future design of Li-metal batteries.

**Approach.** To accomplish project goals, the team will utilize an in-house adapted 3-omega technique to probe thermal properties of a Li-metal cell while it is in operation, without affecting the operation of the cell. 3-omega sensors will be deposited and fabricated on Li-metal cells based on previous learning on 3-omega sensor fabrication. The characteristic depth of the thermally probed region is defined by the wave's "thermal penetration depth,"  $\delta_p = \sqrt{D/2\omega}$ , where D is the sample's thermal diffusivity, and  $2\omega$  is the heating frequency of the thermal wave. By depositing the project's  $3\omega$  sensors on the battery's outer surface and adjusting  $\omega$ , the team controls  $\delta_p$  to span the full range from the top to the bottom layer, thereby noninvasively probing the thermal transport in subsurface layers and interfaces within the bulk of the battery. Thermal transport can be related to quality of the interface. By doing concurrent thermal transport and electrochemical performance measurements, the team plans to relate thermal transport to electrochemical performance.

**Out-Year Goals.** In outgoing years, the project will design, build, and implement the adapted 3-omega metrology. This will involve developing and testing the metrology itself along with accompanying theory, designing compatible battery samples, and applying the technique to live cells. The team will measure thermal transport properties of battery materials provided by collaborators. Combined with the electrochemical performance measurement, this will provide significant information relating the thermal signal to the electrochemical process.

**Collaborations.** This project collaborates with two LBNL groups: V. Battaglia's for cell assembly for 3-omega studies, and R. Kostecki's for pristine battery active material growths for studies of thermal signals related to electrochemical process.

### Milestones

1. Design pristine samples to be compatible with 3-omega and ambient environments. (Q1, FY 2020; Completed)
2. Perform sensitivity analysis and pristine sample design optimization to maximize measurement sensitivity to thermal interfaces. (Q2, FY 2020; In progress)

- Fabrication of bi-layer pristine samples to experimentally isolate different kinds of interfaces. (Q3, FY 2020)
- Thermal measurements of battery composites made from various materials. (Q4, FY 2020)

## Progress Report

The Prasher group is building *operando*  $3\omega$  micro thermal sensors and developing models relating thermal signals to electrochemical performance for *beyond lithium ion* cells. The anode-side  $3\omega$  sensor will be used to probe thermal properties of Li-metal anode and related interfaces (see Figures 68a and 69a).

The team performed sensitivity analyses for the anode-side  $3\omega$  measurement of thermal properties of Li-metal anode and interfaces, which will be used for characterizing morphology of lithium. For lithium symmetric cells using solid electrolyte LLZO, Figure 68b-c shows that the  $3\omega$  signal is sensitive to the thermal boundary resistance between lithium metal and LLZO, and the peak sensitivity around 1-10 Hz is  $\sim 0.1$ . In combination with *ex situ* thermal measurement of lithium anode, it is possible to measure the thermal boundary resistance and characterize the contact between lithium metal and LLZO by thermal measurements. Further, this can be potentially applied to understand how contact varies with temperature and pressure, which are two factors broadly used to modulate lithium dendrite growth in Li-metal batteries. As a proof, the team calculated the peak sensitivity to  $R_{b_{Li-LLZO}}$  as a function of  $R_{b_{Li-LLZO}}$ , and showed good sensitivity across a wide range of the thermal boundary resistance.

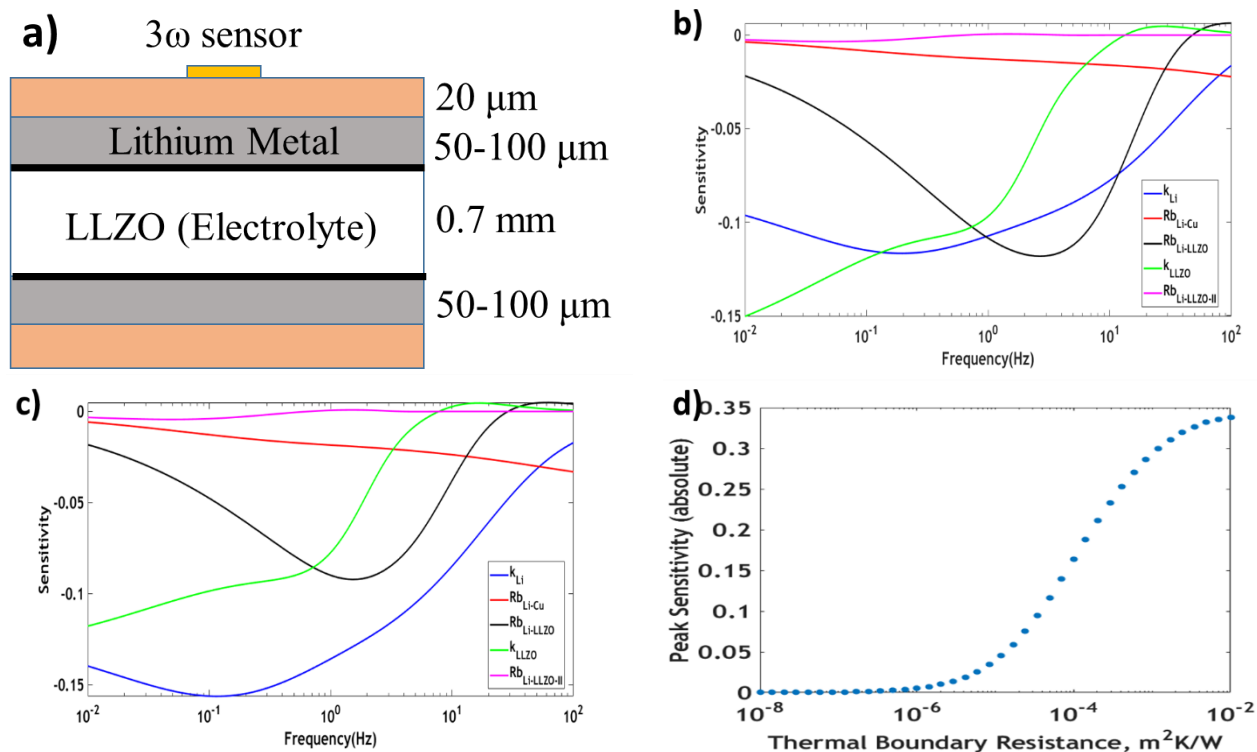


Figure 68. (a)  $3\omega$  sensor for analysis of lithium symmetric cell based on thermal signal. Sensitivity analysis of symmetric cells with (b) 50- $\mu\text{m}$  and (c) 100- $\mu\text{m}$  Li-metal anode, assuming  $R_{b_{Li-LLZO}} = 3 \times 10^{-5} \text{ m}^2\text{K/W}$ . (d) Peak sensitivity to  $R_{b_{Li-LLZO}}$  as a function of  $R_{b_{Li-LLZO}}$ .

Similarly, the  $3\omega$  sensor can be developed for characterizing lithium morphology in Li-metal batteries based on wet electrolyte. Figure 69b-d shows a sufficiently high sensitivity to the thermal boundary resistance between lithium metal and separator for cells with Li-metal anode across a range of thicknesses (20  $\mu\text{m}$ , 50  $\mu\text{m}$ , and 100  $\mu\text{m}$ ). In addition, the  $3\omega$  signal is sensitive to thermal boundary resistance  $> 5 \times 10^{-5} \text{ m}^2\text{K/W}$ , as shown in Figure 69e, which demonstrates promise for future study of cells in various conditions such as different temperatures and pressures. Next quarter, the team will perform pristine sample design optimization to maximize measurement sensitivity to thermal interfaces and prepare for fabrication of  $3\omega$  sensors on symmetric cells.

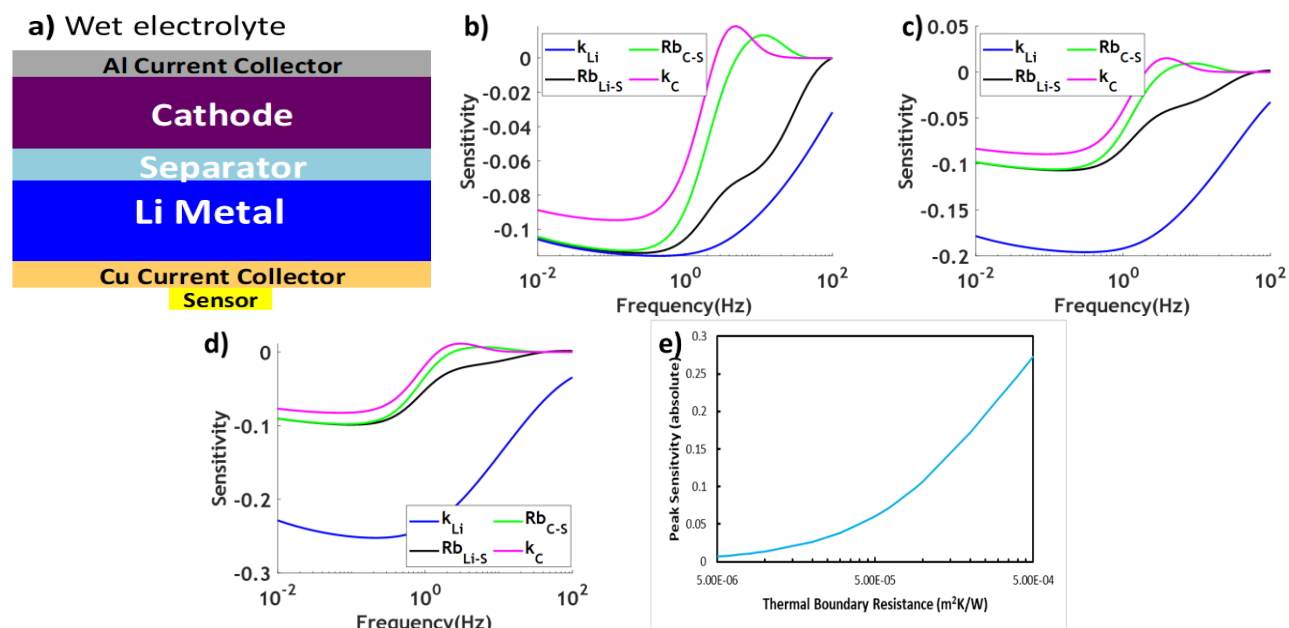


Figure 69. (a)  $3\omega$  sensor for analysis of Li-metal cells using wet electrolyte based on thermal signal. Sensitivity analysis of cells with (b) 20- $\mu\text{m}$ , (c) 50- $\mu\text{m}$ , and (d) 100- $\mu\text{m}$  Li-metal anode. Peak sensitivity to  $R_{\text{b}_{\text{Li-S}}}$  as a function of  $R_{\text{b}_{\text{Li-S}}}$  for cells with 50- $\mu\text{m}$  Li-metal anode.

## Patents/Publications/Presentations

The project has no patents, publications, or presentations to report this quarter.

## Task 3.8 – Multi-Scale Modeling of Solid-State Electrolytes for Next-Generation Lithium Batteries (Anh Ngo, Larry A. Curtiss, and Venkat Srinivasan, Argonne National Laboratory)

**Project Objective.** This project is part of a multi-scale modeling effort to obtain an in-depth understanding of the interaction of the electrode and the solid electrolyte aimed at developing highly efficient SSE batteries for vehicle applications. Input parameters needed for mesoscale (continuum) level calculations are being obtained from atomistic calculations including DFT and classical MD simulations. This atomistic input will enable a multi-scale computational procedure for SSEs that is capable of successfully capturing the physicochemical aspects during charge and discharge process including lithium transport mechanisms, interfacial phenomena during the insertion and extraction of lithium ions, and mechanical deformation of SSE.

**Project Impact.** A major safety concern experienced with commercially available Li-ion batteries under some scenarios is leakage of the liquid electrolyte, which can potentially catch fire. Replacement of the liquid electrolyte is necessary to decrease the fire hazard and improve safety associated with present-day Li-ion batteries. In addition, use of solid electrolytes provides a path to prevent dendrites in Li-metal anodes, thereby leading to batteries with significantly higher energy density. The impact of this project will be to help in development of good SSEs as a replacement for the commercially used organic liquid electrolytes to improve safety and energy density in Li-ion batteries.

**Approach.** Parameters needed for mesoscale modeling of grain interior (GI), GB, and electrode-electrolyte interface will be calculated by DFT-based calculations along with Monte Carlo (MC) and MD simulations. The calculations will be used to determine properties of the electrode with the solid electrolyte as well as in GB regions of the solid electrolyte. This will include calculations of structure, stability, ionic conductivity, Young's modulus, fracture toughness, exchange current density, and other properties.

**Out-Year Goals.** The out-year goals of this work are to calculate other properties such as fracture toughness and include other SSEs and coatings in the multi-scale modeling.

**Collaborations.** This project collaborates with Y. Cui at Stanford.

### Milestones

1. Determine the most stable interface between LLZO solid electrolyte and lithium borate carbonate (LBCO) coating material. Calculate the activation energy barrier between LLZO and LBCO coating materials (Q1, FY 2020; Completed)
2. Determine the most stable interface between NMC cathode and LBCO coating material, and calculate the activation energy barrier. (Q2, FY 2020; Initiated)
3. Estimate the exchange current density associated with charge transfer from LBCO coating to NMC cathode and LLZO solid electrolyte. (Q3, FY 2020; Initiated)
4. Incorporate the information obtained from the atomistic calculations into the mesoscale model, and predict the impact of coating on performance. (Q4, FY 2020; Initiated)

## Progress Report

The use of ceramic solid electrolytes to create ASSBs can enable the use of lithium metal by preventing propagation of lithium dendrites, therefore enhancing safety and decreasing capacity fade. The interfaces between the cathode and solid electrolyte must be stable to enable the use of these materials in batteries. Multi-scale modeling can provide insight into the mechanism for dendrite growth and other instabilities for guidance into how to prevent them. Mesoscale (continuum) modeling requires atomistic level input from theory or experiment to accurately capture physicochemical aspects during charge and discharge processes.

LBCO is an interesting compound that can be used as a coating material for stabilizing the cathode/solid-electrolyte interface. The chemical composition of LBCO is given as  $\text{Li}_{2.3}\text{B}_{0.3}\text{C}_{0.7}\text{O}_3$ , and it is manufactured either by a solid-state reaction between  $\text{Li}_3\text{BO}_3$  and  $\text{Li}_2\text{CO}_3$  or by atomic layer deposition (ALD) techniques, leading to formation of amorphous LBCO. In general, LBCO demonstrates decent ionic conductivity, around  $10^{-5}$  S/cm, single-ion-conducting behavior, very high electrochemical stability with lithium ( $\sim 0.1$ -6 V), and extremely low interfacial impedance against lithium, around  $5 \text{ } \Omega\text{-cm}^2$ . All these properties indicate that incorporation of a thin layer of LBCO between the cathode and LLZO solid electrolyte may not hamper the electrochemical performance substantially. LBCO is a better choice as a cathode coating material than LBO because LBCO demonstrates higher ionic conductivity. Lithium carbonate can form on top of LLZO and cathode particles due to reaction with moisture and carbon dioxide from air. It is well known that  $\text{Li}_2\text{CO}_3$  demonstrates very high resistance to transport of lithium. LBCO can easily form a solid solution with  $\text{Li}_2\text{CO}_3$  due to their iso-structural lattice configuration, and can remove the resistive lithium-carbonate layer from the surface of the cathode and electrolyte particles, effectively reducing the interfacial impedance. However, the Li-ion transport mechanism between LLZO/LBCO and LBCO/cathode is not well understood. Delamination between the cathode and solid-electrolyte, along with subsequent capacity fade, has been reported with LBCO as the coating material. Hence, further study is required to better understand the interfacial properties of LBCO with the cathode and solid-electrolyte materials.

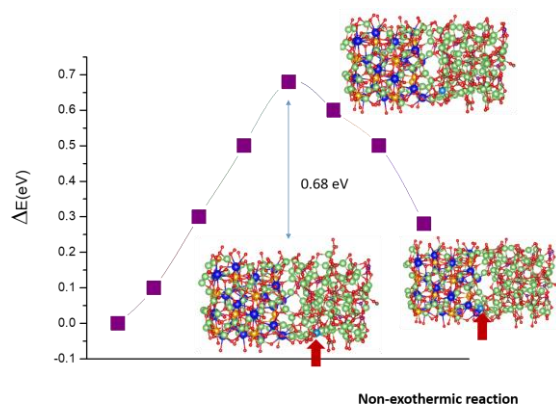


**Figure 70.** Energy barrier obtained from the DFT analysis as a lithium atom travels from an LBCO coating material to a LLZO electrolyte. The magnitude of  $\Delta G$  obtained from the PBE-GGA calculation is 0.68 eV.

formation energy can be calculated as  $E_f = (E_{AB} - N_A E_A - N_B E_B) / 2S$ , where  $E_{AB}$  is the total energy of the fully relaxed interfacial supercell, containing  $N_A$  units of A and  $N_B$  units of B.  $E_A$  and  $E_B$  are the energy per unit of the stress-free pure A and B bulk structure, respectively. The calculations were carried out with the Perdew-Burke-Ernzerhof (PBE) functional with a plane wave basis, and generalized gradient approximation (GGA) with spin-polarized calculations was performed. These results will be used as input for use in continuum mechanism calculations.

From the team's previous study, the LLZO lowest energy surface was found to be the (100) surface with lithium termination, which had a surface energy of  $0.8 \text{ J/m}^2$ . The stability of the interface between amorphous LBCO and the lowest energy LLZO surface [(100) lithium terminated] was investigated with AIMD simulations. All production runs of AIMD trajectories were obtained after 5 ps of thermal equilibration. The team then carried out calculations for the barrier of the Li-ion migration from LBCO layer into LLZO electrolyte to determine the Li-ion transport using DFT. The energy barrier obtained from DFT is shown in Figure 70, which indicates that the magnitude of  $\Delta G$  is around 0.68 eV.

The team also carried out calculations for the interfacial formation binding energy of the interfaces between LLZO and LBCO ( $\sim 3 \text{ J/m}^2$ ). The interfacial

## Patents/Publications/Presentations

### Publications

- Barai, P., K. Higa, A. T. Ngo, L. A. Curtiss, and V. Srinivasan. “Mechanical Stress Induced Current Focusing and Fracture in Grain Boundaries.” *Journal of the Electrochemical Society* 166, no. 10 (2019): A1752–A1762.
- Barai, P., A. T. Ngo, B. Narayanan, K. Higa, L. A. Curtiss, and V. Srinivasan. “Multiscale Modeling of Current Focusing and Dendrite Growth at Lithium/LLZO Interface.” Submitted.

## Task 3.9 – Integrated Multi-Scale Modeling for Design of Robust 3D Solid-State Lithium Batteries (Brandon Wood, Lawrence Livermore National Laboratory)

**Project Objective.** This project will develop a multi-scale, multi-physics modeling framework for probing the effects of materials microstructure and device architecture on ion transport within 3D ceramic SSB materials, with the goal of enhancing performance and reliability. The project has three primary objectives: (1) integrate multi-physics and multi-scale model components; (2) understand interface- and microstructure-derived limitations on ion transport; and (3) derive key structure-performance relations for enabling future optimization.

**Project Impact.** This project will lead to understanding interfacial losses and instabilities that impede performance and promote failure of SSBs. The multi-scale and multi-physics modeling framework developed in this work will address shortcomings of existing modeling strategies that either lack coupling of the multi-physics nature of various processes active in 3D batteries or fail to incorporate processes at different length scales to understand function. Ultimately, the tools and understanding generated by this project can be utilized to realize optimization of interface-dominated 3D batteries.

**Approach.** The project approach integrates simulations at three scales to predict ion transport limitations within the ceramic SSE LLZO, as well as across the interface between LLZO and  $\text{LiCoO}_2$  (LCO) cathodes. A particular focus is on understanding the effects of microstructures and architectures resulting from processing of 3D SSBs, as well as their mechanical and chemical evolution at different stages of cycling. First-principles and classical MD simulations are used to compute fundamental Li-ion diffusion within bulk solid electrolyte and cathode materials, along/across GBs of the electrolyte, and along/across electrolyte/cathode interfaces. Next, phase-field simulations are used to generate digital representation of realistic microstructures of the materials, which are combined with the atomistic simulation results to parameterize mesoscale effective property calculations and to establish microstructure-property relationships for ion transport. Finally, these relationships inform a cell-level macroscopic electro-chemo-mechanical modeling framework, which can be used to optimize the performance of ceramic 3D solid-state lithium batteries based on LLZO solid electrolytes.

**Out-Year Goals.** Future activities will focus on refining the project's atomistic interface models for improved fidelity of ion transport simulations through crystalline and amorphous LLZO and across interfaces. The team will also work with collaboration partners to reconstruct microstructures of 3D-printed materials and apply them to determine effective stresses and ion transport through the polycrystalline materials.

**Collaborations.** This project collaborates with Dr. N. Adelstein from San Francisco State University (SFSU, atomistic diffusion modeling) and Dr. Ye from LLNL (3D printing of SSB materials). They also partner with Dr. E. Ivers-Tiffée from Karlsruhe Institute of Technology (KIT, impedance spectroscopy of SSEs), Dr. P. Zapol from ANL (modeling of solute segregation in LLZO), and Prof. D. Fattakhova-Rohlfing from Forschungszentrum Jülich (FZJ, controlled synthesis of LLZO with varying densities and microstructures) as part of the U. S.–Germany partnership on SSB research.

### Milestones

1. Construct models of solid-solid LCO/LLZO interface. (Q1, FY 2020; Completed)
2. Perform phase-field simulation to reproduce 3D-printed microstructure of LLZO and LCO. (Q2, FY 2020; In progress)
3. Perform AIMD of LCO/LLZO interface model to determine interdiffusion. (Q3, FY 2020; In progress)
4. Quantify threshold grain/pore size that eliminates Griffith-criterion hotspots based on computed internal stress in polycrystalline LLZO. (Q4, FY 2020; On schedule)

## Progress Report

**Mesoscale Modeling of Lithium Transport through Complex Microstructures.** Last quarter, the team parameterized their mesoscale model for computing effective ionic conductivity of a polycrystalline LLZO microstructure. To characterize the temperature-sensitive ionic conductivity behavior, they defined a critical temperature ( $T_{crit}$ ) where a transition from bulk-dominant to GB-dominant diffusive behavior occurs. This quarter, the team conducted comprehensive parametric computations of effective  $\text{Li}^+$  conductivities for the varying GB diffusion property, which is characterized by a prefactor ( $D_0^{GB}$ ) and activation energy ( $E_a^{GB}$ ). Following the analysis procedure reported last quarter, the team identified  $T_{crit}$  as functions of  $D_0^{GB}$  and  $E_a^{GB}$  with varying grain size and GB width. Figure 71 shows computational analysis results. The plots represent designability of ionic transport properties by controlling mesoscopic and atomistic features of LLZO microstructures. In all cases, it is shown that  $T_{crit}$  is highly sensitive to the GB diffusion property, which is usually determined by its atomistic structure and/or chemistry. Interestingly, the sensitivity of  $T_{crit}$  variation to GB diffusion property depends on the mesoscopic microstructural features (that is, grain size and GB width) of LLZO. As grain size increases or GB becomes thinner, the  $T_{crit}$  varies more sensitively with the GB diffusion property.

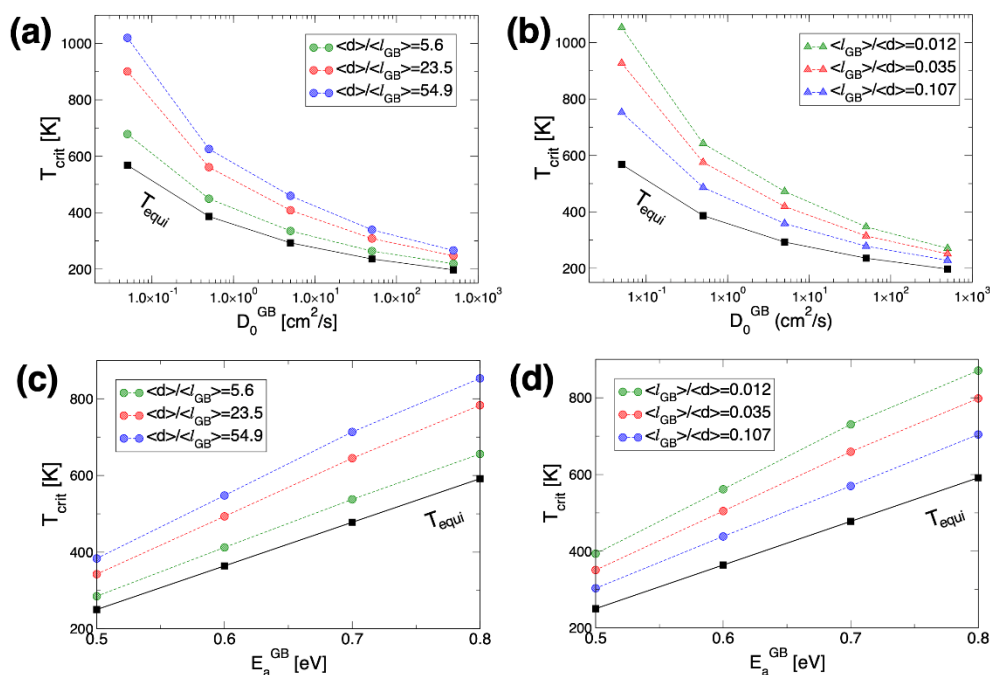


**Figure 71.** Analyzed critical temperatures ( $T_{crit}$ ) as a function of the grain boundary (GB) diffusion property for simulated effective ionic conductivities of systematically varied LLZO microstructures.  $T_{crit}$  variation (a) with  $D_0^{GB}$  for different grain sizes; (b) with  $D_0^{GB}$  for different GB width; (c) with  $E_a^{GB}$  for different grain sizes; and (d) with  $E_a^{GB}$  for different GB width.

**Atomistic Simulations of LCO/LLZO Interfaces.** As a first step of going beyond GBs to also consider transport at electrolyte/cathode interfaces in SSBs, the team constructed three interface models of LCO/LLZO generated from different crystallographic orientations of LCO. The initial interface models of LCO(100)|LLZO(001), LCO(104)|LLZO(001), and LCO(110)|LLZO(001) were first fully relaxed (Figure 72a-c) using DFT. To search for potential lower energy structures at the interfaces, the team explored two methods. The first is to use AIMD with a melt-and-quench technique, in which the interfacial structures are heated at high temperature for a short period of time and then quickly cooled to a local-minimum

configuration (Figure 72d-f). In all three interfacial models tested, cobalt is found highly mobile so that it either diffuses into the LLZO surfaces or starts to occupy the lithium sites at the interlayer positions of LCO. The team is performing extensive AIMD runs to examine potential interdiffusion of cobalt, lanthanum, and zirconium across the interface and is investigating how this interdiffusion affects the structure of the interface and Li-ion mobility. As a second avenue, the team has also been exploring a method to search for lower potential energy surfaces at the interfaces based on a basin-hopping algorithm. They are now comparing the numerical efficiency of these two methods.

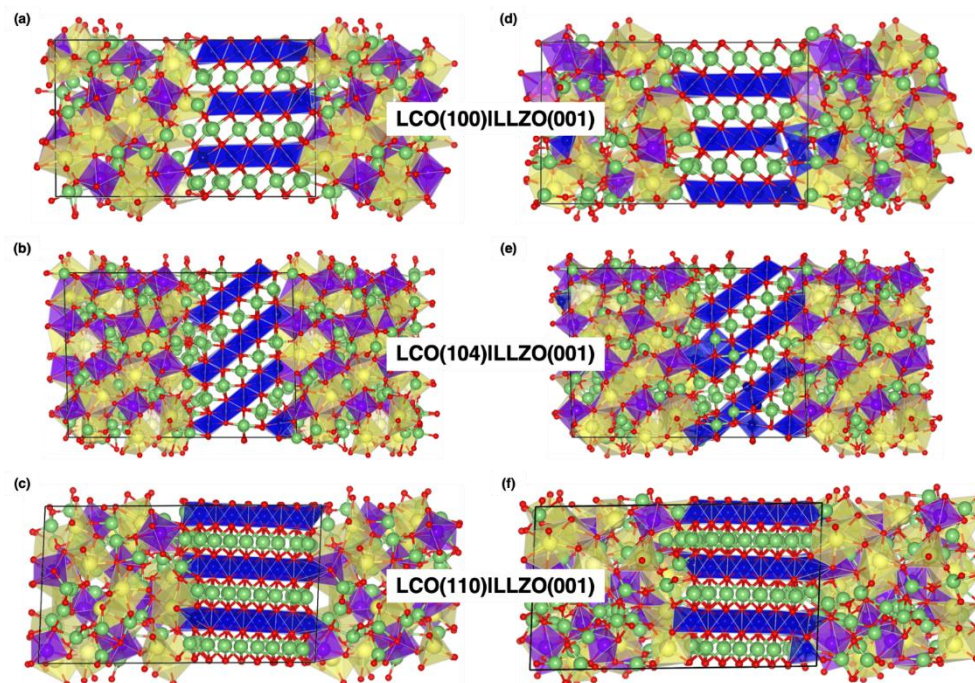


Figure 72. Interfacial structures of LCO/LLZO from three LCO orientations. (a-c) Density functional theory relaxed structures followed by initial construction of the interfaces. (d-f) Quenched structures from *ab initio* molecular dynamics trajectories that are equilibrated at 2000K for 2 ps. The green, blue, yellow, purple, and red spheres represent lithium, cobalt, lanthanum, zirconium, and oxygen in the LCO/LLZO structures, respectively.

### Modeling of Microstructural Effects on Electrochemical Impedance Spectroscopy.

Collaboration with the team's German partners involves direct comparison of microstructure-dependent EIS measurements with the project's models. As a step in this direction, the team reports preliminary activity to build a physics-based EIS modeling framework that can be parameterized using the atomistic and mesoscale simulation results. Traditionally, equivalent circuits have been optimally fit with lumped resistors, capacitors, or a combination thereof, to the complex impedance measured through EIS. Such equivalent circuit models, though computationally efficient and deployed in battery management systems, neglect heterogeneous microstructural information and local impedance contributions, and hence do not provide insight into microstructural impacts on battery performance and long-term degradation mechanisms. To this end, based on fundamental measurable properties of the electrode and the electrolyte, the team has initiated development of a physical mesoscale model that aims to address microstructure-impedance correlation for SSBs. Figure 73 shows an example of preliminary results for a simplified microstructure system, which is designed for validating the model. The model will incorporate complex and realistic solid electrolyte microstructures during upcoming quarters.

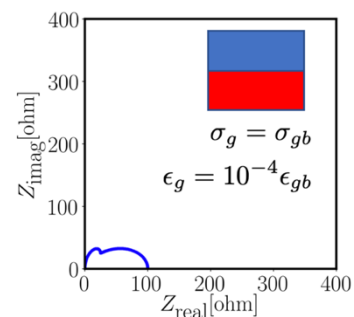


Figure 73. Demonstration of a physical model for electrochemical impedance spectroscopy for a simple two-phase microstructure.

## Patents/Publications/Presentations

### Presentations

- 236<sup>th</sup> ECS Meeting, Atlanta, Georgia (October 2019): “Impacts of Microstructures on the Ionic Diffusivity of Solid Electrolytes: Mesoscale Modeling”; T. W. Heo, A. Grieder, L. F. Wan, N. Adelstein, and B. C. Wood.
- PNNL Solid-State Electrolytes Workshop, Richland, Washington (October 2019): “Integrated Multiscale Model for Design of Robust 3-D Solid-State Lithium Batteries”; L. F. Wan, T. W. Heo, A. Jana, and B. C. Wood.
- 236<sup>th</sup> ECS Meeting, Atlanta, Georgia (October 2019): “Comparison of Correlated Li<sup>+</sup> Diffusion from Molecular Dynamics of Promising Solid Electrolytes”; V. Wei, Z. Mehmedovic, A. Grieder, A. Hall, N. Leclerc, A. Musaelian, L. Kahle, N. Marzari, B. Kozinsky, T. J. Udovic, P. Mehta, V. Stavila, O. Borodin, S. Akhade, P. Shea, K. Kweon, J. Varley, B. C. Wood, and N. Adelstein.
- 236<sup>th</sup> ECS Meeting, Atlanta, Georgia (October 2019): “Effects of Cell Size and Structure on Li<sup>+</sup> Diffusion in LLZO”; A. Grieder, T. W. Heo, S. Akhade, B. C. Wood, and N. Adelstein.

## Task 3.10 – First-Principles Modeling of Cluster-Based Solid Electrolytes (Puru Jena, Virginia Commonwealth University)

**Project Objective.** The objective of the project is to use cluster-ions, which are stable atomic clusters that mimic the chemistry of individual atoms, as the building blocks of new solid electrolytes and the corresponding battery system. The advantages of using the cluster-ions to replace elemental ions is that the size, shape, and composition of the former can be tailored to achieve higher superionic conductivity, electrochemical stability, and charge transfer across the solid-solid interfaces than the conventional materials. More specifically, the goal is to develop superior solid electrolytes based on the cluster-ions and to model these solid electrolytes and their interfaces with electrodes, especially with the Li-metal anode, for their successful integration into high-performance SSBs for EVs. Compared to the conventional solid electrolytes, the team will model and screen cluster-based solid electrolytes that have low activation energies, practical room-temperature ionic conductivities, wide electrochemical stability windows, and desired mechanical properties that, for example, can inhibit the Li-metal anode dendrite growth. They will provide a fundamental understanding of the ionic conduction mechanism in the newly developed, cluster-based solid electrolytes and identify means to further improve their property metrics via chemical and defect engineering. The team will model the interfacial properties, such as the structural, chemical, electrochemical, and ion/charge transfer properties, between the cluster-based solid electrolytes and electrodes at the atomic level, as well as find the interfacial coating materials with desired properties. Based on accumulated data from the modeling, they will establish links between the basic parameters of the cluster-ions and the bulk/interface properties, which can directly guide experiments. Meanwhile, the team will work closely with experimentalists in the BMR Program to complement the project's theoretical efforts and to guide them in the focused development of the predicted cluster-based solid electrolytes and the interfaces.

**Project Impact.** The proposed project will open a new avenue for guiding experiments in the synthesis of SSBs equipped with cluster-based solid electrolytes and capable of operating over a wide temperature range. Modeling and understanding of the ionic conduction of the cluster-based electrolytes and their interfacial properties with electrodes, especially with Li-metal anode, will enrich the current battery science, as well as train the future work force in SSB development for next-generation EVs by supporting postdoctoral fellows.

**Approach.** This project will employ multi-scale theoretical methods and computational techniques.

**Out-Year Goals.** The out-year goals involve modeling development of new cluster-based solid electrolyte materials and database.

**Collaborations.** The team is working with Dr. J. Nanda of ORNL on antiperovskite-based SSEs.

### Milestones

1. Structural studies of the designed cluster-based solid electrolyte materials with selected cluster-ions. (Q1, FY 2020; Completed, December 31, 2019)
2. Property characterizations of the stable cluster-based solid electrolyte materials. (Q2, FY 2020; In progress)
3. Ionic conductivity characterization for the cluster-based solid electrolyte materials and the ionic conduction mechanism. (Q3, FY 2020)
4. Complete development of new cluster-based solid electrolyte materials with a database. (Q4, FY 2020)

## Progress Report

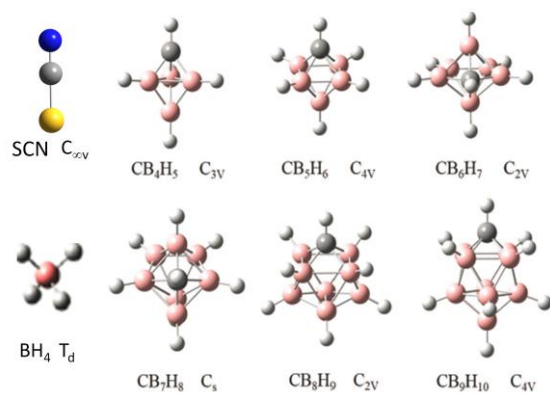


**Figure 74. Demonstration of some of the cluster-ions used in the study. They exhibit different shapes, sizes, and compositions.**

Through extensive structure search and characterization, the team has developed 45 new structures of cluster-based solid electrolytes for Li-ion batteries using selected cluster-ions (as partially shown in Figure 74). The major findings are as follows: (1) the cluster-ion will retain its original composition and structure in the most identified lowest-energy bulk structures; (2) in a few cases, the cluster-ion will react with phosphorus and sulfur in the lowest-energy bulk structure, which would slightly change the original composition of the cluster-ion without changing its geometry; (3) new multiple cluster-ions may form in the bulk structure when there is a reaction, which may result in new chemical and physical properties of the material as a solid electrolyte; and (4) in rare cases, the cluster-ions are either highly distorted or disintegrated in the lowest-energy bulk structures, suggesting instability of

the corresponding cluster-ions under the presence of certain other elements in the material. The cluster-based structures are searched using a first-principles structure search program with Particle Swarm Optimization (PSO) algorithm. In a normal search, a population of 30-40 initial crystal structures that contain certain cluster-ions will be generated according to different symmetries and number of atoms in the unit cell. These structures will then be subject to full optimization (in both lattice parameters and atomic positions) until certain convergence criteria are met. Sixty percent of the optimized structures showing the lowest energies will form the next generation with newly generated structures according to symmetries. After 10- to 20-generation optimization, structures with the lowest energies will be picked as the preferred candidates.

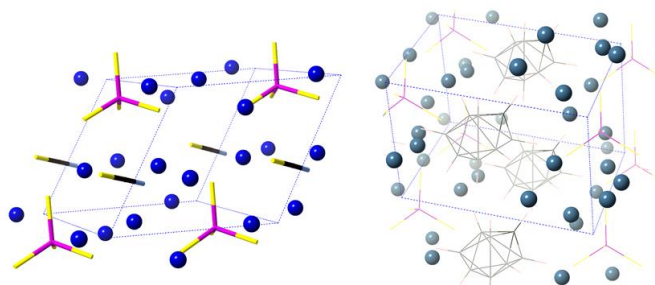


**Figure 75. Two typical cluster-based solid electrolyte structures identified from the extensive structure search. Cluster-ions are shown in tetrahedron, rod and cage configurations. Li-ions are shown in blue.**

In most cases, the resulting cluster-based structure retains the original composition and geometry of the original cluster-ion. In several special cases, the original composition of the cluster-ion is slightly changed due to reaction with phosphorus and sulfur existing in the corresponding material family. However, the geometry of the original cluster-ion remains. One case is with the cluster-ion  $\text{OH}^-$ , where new cluster-ions, including  $\text{P}(\text{S}_3\text{O})^{3-}$  and  $\text{HS}^-$ , are formed in the final structure. All other cases involve the boranes  $\text{B}_x\text{H}_x^-$  ( $x = 6-8$ ), where new cluster-ions  $\text{B}_x(\text{H}_{x-1}\text{S})^{2-}$  and  $\text{HS}^-$  are formed in

the structure. These new cluster-ions, formed in the bulk structures, may result in interesting chemical and physical properties, which will be further studied at later stages of the project. According to the calculated tolerance factors (based on the ionic radii of the adopted cluster-ions) of the developed materials in the antiperovskite family, almost half of the materials show tolerance factors in the range of 0.8 to 1.2, suggesting that these materials are likely to be stabilized in a (pseudo-)cubic phase. It is also found that, with larger ionic radius of the cluster-ion, the dispersion of lithium adopts a more layered configuration in the bulk structure, which may result in interesting diffusion behavior. Figure 75 demonstrates some of the cluster-based solid electrolyte structures found from the search.

## Patents/Publications/Presentations

### Patent

- Jena, P., and H. Fang. Cluster-Ion Based Superionic Conductors. U. S. Patent Application, US20180241080A1, Status: pending starting January 9, 2020.

### Publication

- Fang, H., and P. Jena. “Sodium Superionic Conductors Based on Clusters.” *ACS Applied Materials & Interfaces* 11, no. 1 (2019): 963–972.

### Presentation

- International Symposium on Clusters and Nanomaterials, Richmond, Virginia (November 3–6, 2019): “Cluster-Inspired Anti-Perovskites as Solid State Electrolytes in Li and Na-Ion Batteries”; H. Fang.

## Task 3.11 – Predictive Engineering of Interfaces and Cathodes for High-Performance All-Solid-State Lithium-Sulfur Batteries (Badri Narayan, University of Louisville)

**Project Objective.** The primary goal of this project is to leverage data-driven methods and machine learning strategies to develop accurate multi-physics models for all-solid-state Li-S battery (ASLSB) materials that can capture electrochemical and transport phenomena over atomic to mesoscopic length/timescales; these models will be rigorously validated by synthesis and advanced characterization experiments. The team will leverage the predictive power of these models, alongside synthesis/characterization experiments and battery fabrication to address longstanding issues at the electrode/electrolyte interfaces in ASLSBs. The project’s proposed technology involves the following: (a) halide-doped solid sulfide electrolytes that can concurrently provide high  $\text{Li}^+$  ion conductivity and suppress dendrite growth; (b) novel mesoporous cathode composed of interconnected carbon nano-cages co-infiltrated with sulfur and sulfide electrolyte, which hold potential to allow high sulfur loading and optimal ion/electron pathways; and (c) functionalization of sulfide electrolyte with ionic liquids to improve physical contact and minimize impedance at the cathode/electrolyte interface.

**Project Impact.** ASLSBs remain far from commercialization due to poor understanding of the fundamental electrochemical/chemical and transport processes that occur at the interfaces, especially at atomic to mesoscopic scales. Successful development of the proposed predictive models (at multiple scales) will bridge this knowledge gap and will advance fundamental understanding of reaction chemistry, kinetics, charge transfer, and dendrite growth at electrified solid-solid interfaces. This, in turn, would enable predictive design of effective strategies to mitigate interfacial problems in ASLSBs, including poor interfacial contact, interfacial impedance to  $\text{Li}^+$  ion transport and poor electron/ion conduction within cathodes. Ultimately, the fundamental knowledge gained by this work will lead to development of high-performance ASLSBs that meet DOE targets of specific energy (350 Wh/kg @C/3), sulfur loading ( $> 6 \text{ mg/cm}^2$ ), and high cycle life (1000).

**Approach.** The project brings together innovative solutions in multi-scale materials modeling, electrolyte synthesis, fabrication of cathode architecture, and electrolyte functionalization to overcome the issues at electrode/electrolyte interfaces in ASLSBs. The central idea is to employ a data-driven and machine-learning based approach to develop accurate multi-physics battery models at atomic-to-mesoscopic scales. This approach overcomes critical problems with existing model development methods, by foregoing need for pre-defined functional forms; introducing deep-learning technique to describe reactivity; and employing optimization methods that do not require human intuition. Multi-scale simulations based on the newly developed models will provide insights into electrochemical phenomena at electrode/electrolyte interfaces.

**Out-Year Goals.** In Year 1, the goal is to optimize electrolyte composition and to develop accurate reactive atomic-scale interaction models of representative SSE system and ionic liquids.

**Collaborations.** The team collaborates with the groups under Dr. A. Ngo, and Dr. L. Curtiss at ANL for quantum simulations of battery systems; they plan to collaborate with Dr. J. Nanda at ORNL for advanced spectroscopic *in situ* characterization of interfaces.

### Milestones

1. Demonstrate scalable electrolyte synthesis with precise composition control. (Q1, FY 2020; Completed)
2. Computationally optimize electrolyte composition for high  $\text{Li}^+$  conductivity ( $10^{-3} \text{ S/cm}$ ) and good electrochemical stability. (Q2, FY 2020; In progress)
3. Synthesize cathode architectures based on interconnected carbon nano-cages with co-infiltrated sulfur and SSE; obtain baseline for battery performance. (Q3, FY 2020; In progress)
4. Develop reactive models for electrolyte, and ionic liquid. (Q4, FY 2020; In progress)

## Progress Report

This quarter, the team made significant progress in the following areas: electrolyte synthesis using liquid phase methods; AIMD of  $\text{Li}^+$  ion transport in halide-doped sulfide electrolytes (SSE), as well as evolution of Li-anode/SSE interface; extension of automated model development frameworks for deep neural network based force fields; and synthesis of carbon nanocages (CNCs) with impregnated sulfur for cathode design.

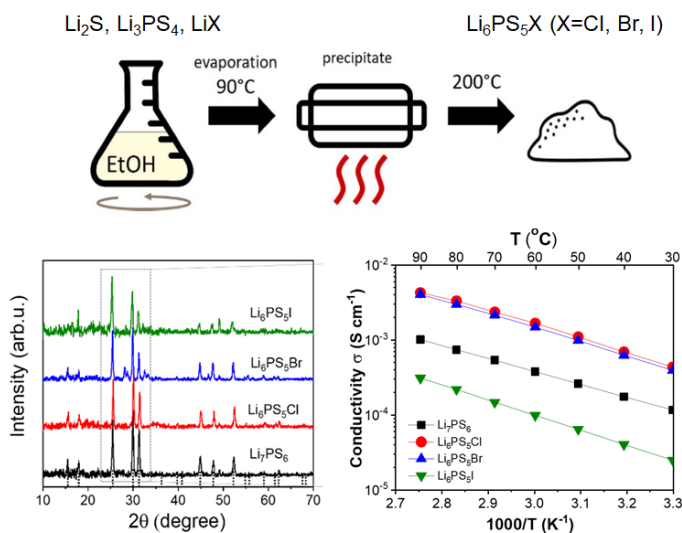


**Figure 76. Liquid phase synthesis of lithium argyrodites solid electrolytes. (top) Scheme of solution-based synthesis method. (lower left) X-ray diffraction shows as-produced electrolytes are high-purity and possess high crystallinity. (lower right) Measured ionic conductivity of various halide-doped sulfide electrolytes produced by liquid phase method.**

synthesized using a similar technique with  $\text{Li}_2\text{S}$  and  $\text{P}_2\text{S}_5$  precursors using acetonitrile as solvent. Using this technique, the team has successfully synthesized  $\text{LiPSX}$  compounds with a wide-range of compositions (each with excellent control over the final composition). Figure 76 shows a small subset of halide-doped SSEs that was produced using this technique [namely,  $\text{Li}_7\text{PS}_6$ ,  $\text{Li}_6\text{PS}_5\text{X}$  ( $\text{X} = \text{Cl}, \text{Br}, \text{I}$ )]. The as-produced electrolytes are of high-purity and exhibit good crystallinity, as shown by XRD patterns (Figure 76, lower left). The produced  $\text{Li}_6\text{PS}_5\text{Cl}$  showed the best ionic conductivity of  $0.34 \text{ mS cm}^{-1}$  at room temperature, followed by  $\text{Li}_6\text{PS}_5\text{Br}$  and  $\text{Li}_6\text{PS}_5\text{I}$ . More importantly, the chlorine- and bromine-doped SSEs show three times higher Li-ion conductivity than pristine  $\text{Li}_7\text{PS}_6$ , similar to the work using solid-state synthesis techniques. Interestingly, excess chlorine content further pushed the ionic conductivity of  $\text{Li}_6\text{PS}_5\text{Cl} \cdot \text{LiCl}$  up to  $0.53 \text{ mS cm}^{-1}$  at room temperature and  $5 \text{ mS cm}^{-1}$  at  $90^\circ\text{C}$ . CV on assembled  $\text{Li}/\text{Li}_6\text{PS}_5\text{X}/\text{stainless-steel}$  cells show that all  $\text{Li}_6\text{PS}_5\text{X}$  electrolytes (synthesized by the project's liquid phase method) possess good electrochemical stability against lithium metal in a voltage window of 0.5-5.0 versus  $\text{Li}/\text{Li}^+$ . For all  $\text{Li}_6\text{PS}_5\text{X}$  ( $\text{X} = \text{Br}, \text{Cl}, \text{I}$ ) materials, only one pair of oxidation and reduction peaks is observed near 0 V versus  $\text{Li}/\text{Li}^+$ , attributed to lithium dissolution ( $\text{Li} \rightarrow \text{Li}^+ + e^-$ ) and lithium deposition ( $\text{Li}^+ + e^- \rightarrow \text{Li}$ ), respectively. This clearly illustrates the team's ability to synthesize SSEs in a scalable, economic manner while having precise control over the composition. Next, the team will prepare fluorine-doped sulfide electrolytes; this provides an excellent opportunity to achieve high electrochemical stability (via possible formation of  $\text{LiF}$  at the Li-electrolyte interface) and high ion conductivity.

### Demonstration of Precise Composition Control over Synthesis of Halide-Doped Sulfide Electrolytes using Scalable Liquid-Phase Methods (Completed)

Most SSEs are synthesized using solid-state methods that require high-temperature chemical reactions. These methods are typically not scalable, are expensive, and offer poor composition control. The team recently developed a scalable, efficient, and economic solvent-based method to produce SSEs. This quarter, they extended this technique to introduce halogen dopants in SSEs with excellent composition control (see Figure 76, top). Using this solvent-based synthetic approach, they employed a stoichiometric mixture of  $\text{Li}_2\text{S}$ ,  $\text{Li}_3\text{PS}_4$ , and  $\text{LiX}$  ( $\text{X} = \text{Cl}, \text{Br}, \text{I}$ ) and dissolved in anhydrous ethanol solvent; this was followed by evaporation and heat-treatment to achieve the desired halide-doped SSE with prescribed composition. The required  $\text{Li}_3\text{PS}_4$  is

## AIMD Simulations to Understand Li<sup>+</sup> Ion Transport and Evolution of Anode/Electrolyte Interface

Halide doping of SSE provides an excellent route to enhance conductivity of Li<sup>+</sup> ions through the electrolyte. Additionally, fluorination of SSE yields stable SEI layer made up of LiF, which inhibits dendrite formation. Halide doping of SSE provides a unique opportunity to concomitantly achieve enhanced Li<sup>+</sup> ion conduction, and a stable SEI (containing LiX) during battery operation. At optimized doping levels, halide ions could either segregate to the Li-anode or the SSE could phase separate to form a SEI layer containing LiX, while providing fast Li<sup>+</sup> transport. In particular, doping with fluorine holds great potential to achieve SEI containing LiF. Additionally, co-doping with fluorine and Cl/Br/I ions could provide enhancement in ion-transport. To

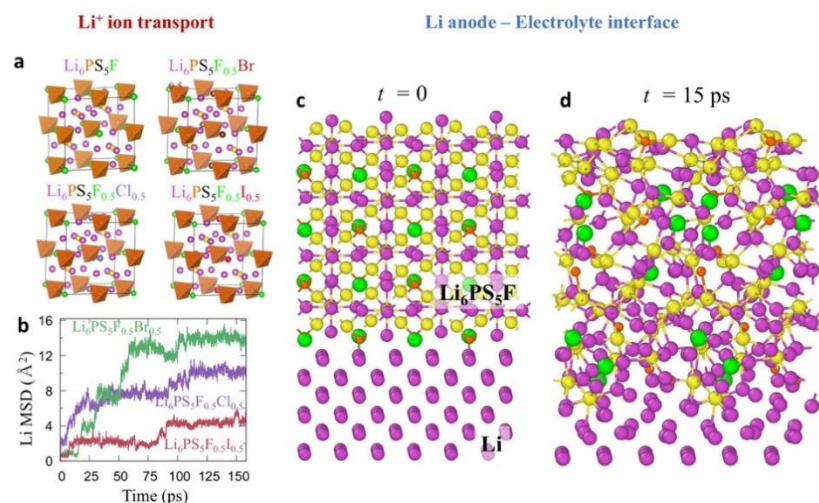


Figure 77. *Ab initio* molecular dynamics (AIMD) simulations to understand Li<sup>+</sup> ion transport and structural evolution at anode/sulfide-electrolyte interfaces. (a) Unit cells of various  $\text{Li}_6\text{PS}_5\text{FaX}_{1-a}$  (X = Cl, Br, I) compounds. (b) Mean-squared displacement of lithium atoms over 150 ps of AIMD simulations at 450K. (c-d) AIMD snapshots showing evolution of lithium (001) ||  $\text{Li}_6\text{PS}_5\text{F}$ (001) interface at 450K.

understand the effect of co-doping, the team performed AIMD simulations on three F-containing SSEs, namely,  $\text{Li}_6\text{PS}_5\text{F}_{0.5}\text{X}_{0.5}$  (X = Cl, Br, I). For all simulations, they adopted a unit cell wherein fluorine atoms form a face-centered cubic lattice (Figure 77a), similar to the one observed for  $\text{Li}_6\text{PS}_5\text{Cl}$  (Materials Project). For all the co-doped cases, half the fluorine atoms were replaced by another halogen atom (Cl/Br/I); the configurations shown in Figure 77a were selected based on a limited search of the potential energy landscape with different possible halogen ordering configurations. A more thorough search (based on genetic algorithms) is in progress. Nevertheless, AIMD simulations on chosen well-ordered  $\text{Li}_6\text{PS}_5\text{F}_{0.5}\text{X}_{0.5}$  can provide insights into trends in Li<sup>+</sup> diffusion. Interestingly, the team found that all the  $\text{Li}_6\text{PS}_5\text{F}_{0.5}\text{X}_{0.5}$  (X = Cl, Br, I) have similar crystal volumes (within ~ 1% of each other). However, they show vastly different Li<sup>+</sup> diffusion behavior (Figure 76b). At a representative temperature of 450K, the  $\text{Li}_6\text{PS}_5\text{F}_{0.5}\text{Br}_{0.5}$  shows much higher Li<sup>+</sup> ion diffusivity ( $\sim 10^{-6}$  cm<sup>2</sup>/s) than the other halogen dopants ( $\sim 2.5$  times greater than that for  $\text{Li}_6\text{PS}_5\text{F}_{0.5}\text{I}_{0.5}$ ). Such differences in diffusivity are largely linked with effect of the bromine atom on the activation energy of Li<sup>+</sup> hops; the team is investigating the activation barriers using NEB calculations.

In addition to Li<sup>+</sup> ion mobility, it is also crucial to investigate the interfacial stability of the  $\text{Li}_6\text{PS}_5\text{F}$  electrolytes with respect to lithium anode; a key hypothesis based on previous literature is that  $\text{Li}_6\text{PS}_5\text{F}$  electrolyte could form a SEI layer containing LiF. The team performed AIMD simulations at 450K to monitor the structural evolution of Li(001)// $\text{Li}_6\text{PS}_5\text{F}$ (001) interface (see Figure 77c-d) over a period of 15 ps; note this interface was chosen since the as-formed hetero-structure was nearly epitaxial (< 0.5% strain). The team finds that ~ 50% of the fluorine atoms indeed leave the electrolyte to form Li-F bonds with the lithium atoms in the anode; additionally, few new Li-P and Li-S bonds also form at the interface. The movement of fluorine out of the SSE lattice results in high local strains, which propagate to cause a complete amorphization of the electrolyte. Interestingly, in the glassy state, a few  $\text{PS}_4^{3-}$  tetrahedra break up, resulting in  $\text{PS}_3^-$  ions. AIMD simulations with larger supercells are in progress. These would provide insights into the extent of amorphization of F-doped SSE.

The team is leveraging their expertise with AIMD and DFT calculations to accomplish the following: (a) understanding of impact of halogen ordering on the  $\text{Li}^+$  transport properties with ordering of different types of halogen atoms; (b) evolution of the Li/electrolyte interface, and (c) continual building of a large DFT training set of energies, structures, and charges in a wide variety of configurations (for developing ML-FFs) in F-containing SSEs co-doped with other halogens.

### Framework for Developing Neural-Network Based Interatomic Potentials

A major thrust of this proposal relies on the ability to develop accurate materials models using neural networks (and are agnostic of functional forms). Recently, the team extended automated FF learning framework to develop deep-neural network (DNN) based interaction potentials (Figure 78) whose input layers consist of rotational and translational invariant functions of atomic position vectors (also called symmetry functions). Using this framework, the team successfully trained a DNN model for water by fitting exclusively against energies of 30,000 bulk water configurations (Patra, et al. *Applied Physics Letters* 115 (2019): 193101). This DNN potential accurately predicts both the energies and the molecular forces of water, within 0.9 meV/molecule and 54 meV/Å of a reference (coarse-grained bond-order potential) model. The DNN water model also provides the following: (a) good prediction of several structural, thermodynamic, and temperature dependent properties of liquid water, with values close to those obtained from the reference model, and (b) capturing of the well-known density anomaly of liquid water observed in experiments (a challenging feat for most available water models). The project work lays the groundwork for a scheme to develop a fully flexible neural network based potential for ASLSB materials by training against sparse data from high-fidelity DFT calculations. The team will employ this framework to develop DNN potentials for Li-S system; they will leverage the existing database of DFT-calculated energies/structures/charges in the PI's group to train these models.

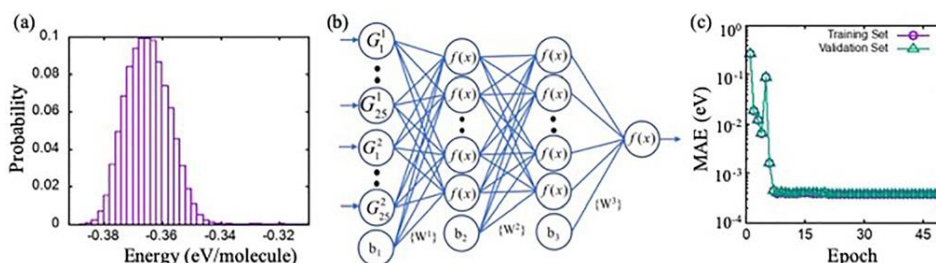


Figure 78. Development of the deep neural network (DNN) model. (a) Data: Distribution of data used in training the neural network (NN). (b) Model: Schematic representation of the NN that takes 50 translationally/rotationally invariant features of a configuration and outputs its energy. The input layer of the network holds these coordinates, which are represented by  $G_1$  and  $G_2$ .  $G_1$  and  $G_2$  are radial and angular symmetry functions, respectively. The network contains two hidden layers in each of the 10 compute nodes. All the compute nodes in the network are labeled as  $f(x)$ .  $b_1, b_2$ , and  $b_3$  are biased nodes, which hold a constant value of one.  $\{W_i\}$  represents the weights between nodes of the  $i$ th and  $(i+1)$ th layers. (c) Optimization-mean absolute energy during the training of the NN is plotted as a function of the training cycle for training and validation datasets.

### Fabrication of Cathodes using Interconnected Carbon Nano-Cages with Impregnated Sulfur

A cathode architecture containing interconnected CNCs encapsulating SSE and sulfur shows large surface area  $\sim 1000 \text{ m}^2/\text{g}$ , which offers promise to achieve high sulfur loading ( $> 6 \text{ mg}/\text{cm}^2$ ). At the same time, the porous architecture can accommodate large strains without detachment. The team has successfully demonstrated impregnation of sulfur into CNC structures for a wide range of diameters, including (a) very small ( $\sim 3 \text{ nm}$ ) and (b) large (20-100 nm) nanocages. The CNC materials were synthesized using the recently patented process *via* templating on the surface of nickel nanoparticles formed *in situ* during thermolysis of sol-gel precursor consisting of nickel salt and carbon precursor. Citric acid and caffeine were used as carbon precursors for the synthesis of small ( $\sim 3 \text{ nm}$ ) and large (20-100 nm) CNCs, respectively. The CNC powders were obtained by subsequent acid treatment and the dissolution of most of nickel. In this preliminary study, some residual nickel,

mostly for the larger CNCs, remained un-etched; however, this will be addressed during actual electrode/electrolyte fabrication. Sulfur was impregnated by melt injection. CNC powder was placed on a hot plate, heated to about 120°C, and sulfur was simply melted on the powder. Due to the capillary effects, sulfur is believed to penetrate into the CNC pores through defects of the graphitic shells. Figure 79 shows representative TEM images of S-impregnated CNCs; the energy dispersive spectrum provides an elemental map, which clearly shows that the sulfur are impregnated in the CNCs. For these initial, proof-of-concept experiments, a rough sulfur to carbon loading, as obtained from automatic EDS quantification, is 2-4 wt%. However, these values are significantly underestimated, and further analysis is in progress to directly measure the S-loading. Next, the team will plan to demonstrate the impregnation of SSE and the co-impregnation of sulfur and SSE.

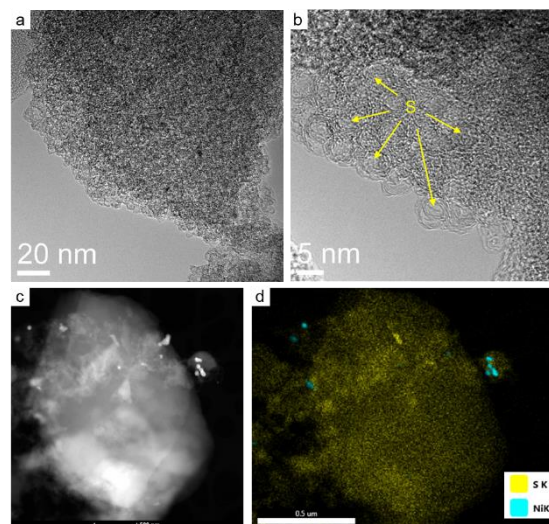


Figure 79. (a) Low- and (b) high-magnification transmission electron microscopy images of small (~ 3 nm) carbon nanocages impregnated with sulfur. (c) high-angle annular dark field – scanning transmission electron microscopy image and (d) corresponding elemental map of this sample.

## Patents/Publications/Presentations

### Presentation

- 236<sup>th</sup> ECS Meeting, Atlanta, Georgia (October 13–17, 2019): “Atomistic Insights into Cathode Dissolution and Ion Transport in Li-Ion Batteries.” B. Narayanan. Invited.

## TASK 4 – METALLIC LITHIUM

### Summary and Highlights

The use of a metallic lithium anode is required for advanced battery chemistries like Li-ion, Li-air, and Li-S to realize dramatic improvements in energy density, vehicle range, cost requirements, and safety. However, use of metallic lithium with liquid and solid polymer or ceramic electrolytes has so far been limited due to parasitic SEI reactions and dendrite formation that eventually short circuit the battery. Adding excess lithium to compensate for such losses negates the high-energy-density advantage of a Li-metal anode and leads to further concern for battery safety. For a long lifetime and safe anode, it is essential that no lithium capacity is lost either (1) to physical isolation by roughening, dendrites, or delamination processes, or (2) to chemical isolation from side reactions. The key risk, and current limitation, for this technology is the gradual loss of lithium over the cycle life of the battery.

BMR, Battery500, and other DOE programs are addressing this challenge with many innovative and diverse approaches. Key to all is the need for a much deeper analysis of the degradation processes and new strategies to maintain a dense, fully connected lithium and a dendrite-free electrolyte so that materials can be engineered to fulfill the target performance metrics for EV application, namely 1000 cycles and a 15-year lifetime, with adequate pulse power. Projecting the performance required in terms of just the lithium anode, this requires a high rate of lithium deposition and stripping reactions, specifically about 30  $\mu\text{m}$  of lithium per cycle, with pulse rates up to 10 and 20 nm/s (15 mA/cm<sup>2</sup>) charge and discharge, respectively, with little or no excess lithium inventory. This is daunting in the total mass and rate of material transport that must be achieved without failures.

The efficient and safe use of metallic lithium for rechargeable batteries is then a great challenge, and one that has eluded R&D efforts for years. This project takes a broad look at this challenge for both SSBs and batteries continuing to use liquid electrolytes. Electrolytes reported here include: nonflammable liquid solutions, gel type polymer-in-a-salt, composites of ceramic polymer phases, common and novel polymer electrolytes, and both oxide and sulfide ceramic electrolytes. In most studies, the electrolyte phases were modified by addition of plasticizers or interface coatings to improve transport, stability, and ease of manufacturing. Researchers are typically working toward cycling of full cells with relevant and balanced capacities for the lithium anode and cathode using measures of CE, interface resistance, and post-cycling observation of the disassembled cell components to assess stability of the Li-metal anode and chosen electrolyte.

**Highlights.** The highlights for this quarter are described below.

The PNNL group (Xu and Zhang) reports on several compositions of highly concentrated salt electrolytes, so-called solvent-in-a-salt and polymer-in-a-salt electrolytes. Their work is distinguished by an emphasis on using and testing non-flammable components and evaluating stability with lithium metal by measures of the CE and TEM observations of the SEI and lithium morphology on cycling. This quarter, a 1:1 PEO:LiFSI electrolyte was plasticized with an ionic liquid. The addition of the ionic liquid gave a gel-like electrolyte that, when contained in a porous polyimide separator membrane, was difficult to ignite and had good conductivity, near 1 mS/cm, above 50°C.

Work from ORNL (Chen and Dudney) highlights ceramic polymer composite electrolytes, most recently using a cross-linked polymer within a sintered ceramic skeleton, a structure designed to maximize the mechanical strength and lithium ionic transport conductivity. To date, the LATP-based ceramic is protected from reaction with the lithium by a thin excess polymer film at the interface. The added resistance of this polymer layer is reduced by adding a small amount of plasticizer. The work also reports an anomalous behavior that may be seen as an unexplained overcharge that is believed to result from assembling full cells with a polymer electrolyte in coin-cell hardware.

From ANL (Markovic and Curtis), the report showed the interface reaction of lithium with PEO as determined by X-ray photoelectron analysis before and after lithium deposition and heating to 100°C under vacuum. New features in the O 1s, C 1s, and Li 1s spectra reveal evidence for lithium dissolution in the PEO and reaction forming organolithium (LiCR) and lithium alkoxide (LiOR) species.

Ye's group (LLNL) reports work to fabricate sintered garnet LLZO membranes, where various coatings have been applied to large batches of Ta-doped LLZO powder. The purpose of the coating is two-fold: to control decomposition of  $\text{Li}_2\text{CO}_3$  at surface during sintering and to improve interface of sintered membrane with the Li-metal anode. This report highlights  $\text{Al}_2\text{O}_3$  coatings applied by ALD onto LLTZO powder, using up to five cycles of the ALD process. Pellets of coated LLTZO sintered at 1100°C were up to 96% dense. The interface of LLZTO-Al with lithium metal was  $\sim 100 \text{ ohm cm}^2$ , but there was evidence of reaction with the lithium.

Nanda's group (ORNL) is investigating synthesis and processing of lithium thiophosphate solid electrolyte membranes. In this report, results of solvent mediated synthesis were compared using five solvents. For each solvent, Raman spectroscopy reveals the  $\text{P}_2\text{S}_6^{2-}$  anion; this was supported by XRD and XPS results for the dried materials. Variations of final stoichiometry and conductivity depend largely on the thermal treatment and amount of excess  $\text{Li}_2\text{S}$  incorporated thiophosphate.

From Stanford, Cui's group reports on a simple, one-step process to lithiate a standard silicon slurry cathode cast onto copper foil. By adding a thin lithium foil between the silicon anode and porous separator, on assembly of the full cell with a liquid electrolyte, the silicon becomes lithiated when allowed to rest for up to 4 h before initial cycles. Disassembly of the cell reveals the larger silicon particles and SEI formed from the solvent decomposition.

## Task 4.1 – Lithium Dendrite Prevention for Lithium Batteries (Wu Xu and Ji-Guang Zhang, Pacific Northwest National Laboratory)

**Project Objective.** The objective of this project is to enable lithium metal to be used as an effective anode in rechargeable Li-metal batteries with good stability and high safety. The investigation this fiscal year will focus on two aspects. First, develop nonflammable polymer electrolytes and investigate effects of various flame-retardant solvents and polymers on ionic conductivity, lithium CE, Li-anode morphology, flammability, and battery performances in terms of long-term cycling stability and rate capability at various temperatures. Second, establish correlation of morphologies of SEI layer and deposited lithium with electrolyte formulation, current density, and lithium deposition/stripping cycling.

**Project Impact.** Lithium metal is an ideal anode material for rechargeable batteries, but the application of Li-metal anode is hindered by lithium dendrites and low CE. Although much progress has been achieved in suppressing lithium dendrites and increasing lithium CE in liquid electrolytes, most of the liquid electrolytes are flammable and may pose a safety hazard in case of extreme conditions. Therefore, development of electrolytes with improved safety for advanced battery chemistry is imperative. An ideal electrolyte for Li-metal anode should not only suppress lithium dendrite growth and have high CE, but also be intrinsically nonflammable. This fiscal year, the team will develop low flammable or nonflammable hybrid polymeric composite electrolytes (NHPCEs) that have high lithium CE, suppress lithium dendrites, and are stable with high-voltage cathodes. The success of this project will increase safety of Li-metal and Li-ion batteries and accelerate market acceptance of EVs, especially for PEVs as required by the EV Everywhere Grand Challenge.

**Approach.** The approach will encompass several areas: (1) develop appropriate high-concentration phosphate liquid electrolytes (HCEs) that have high lithium CE over 98% and can suppress lithium dendrites, (2) add flame-retardant phosphate monomers into the HCEs and utilize radical polymerization to form crosslinked polymer gel electrolyte, and (3) investigate ionic conductivity, electrochemical window, flammability, lithium CE and morphology; battery performance of HCEs and NHPCEs will also be investigated.

**Out-Year Goals.** The long-term goal of the proposed work is to enable Li-metal and Li-ion batteries with a specific energy of > 350 Wh/kg (in cell level), 1000 deep-discharge cycles, 15-year calendar life, and less than 20% capacity fade over a 10-year span to meet the goal of EV everywhere.

**Collaborations.** This project collaborates with C. Wang of PNNL on characterization by TEM/SEM; Dr. K. Xu and Dr. M. Ding of U. S. Army Research Laboratory (ARL) on solvent purification and DSC measurements; and Dr. B. Polzin at ANL on coated electrode sampling.

### Milestones

1. Develop polymerization method to get nonflammable polymer electrolytes with lithium CE > 98%. (Q1, FY 2020; Delayed to February 28, 2020)
2. Characterize morphologies of SEI layers and deposited lithium films at different current densities and deposition capacities. (Q2, FY 2020; Ongoing)
3. Investigate lithium CE, deposited lithium morphology, and flammability of hybrid polymer composite electrolytes. (Q3, FY 2020)
4. Achieve over 100 cycles for Li||NMC-622 batteries with nonflammable hybrid polymer composite electrolytes. Characterize compositions of SEI layers and deposited lithium films at different current densities and deposition capacities. (Q4, FY 2020)

## Progress Report

This quarter, the team used two strategies to develop NHPCEs. One was crosslinking nonflammable monomer in nonflammable liquid electrolyte to form nonflammable gel polymer electrolyte (which is named NGPE). Another was plasticizing polymer-in-salt electrolyte (PISE) with ionic liquid to get polymer-in-salt composite electrolyte (PISCE).

Trimethyl phosphate (TMPa) is a typical nonflammable solvent. High concentration LiFSI-nTMPa electrolyte is not only nonflammable, but also has high lithium CE. LiFSI-1.1TMPa has a CE of 98.5%, and LiFSI-1.3TMPa has a slightly higher CE of 98.7% (both at 25°C). Increasing the temperature reduces the lithium CE; for instance, LiFSI-1.3TMPa has a lithium CE of 96.4% at 60°C, because the side reactions of the electrolyte and lithium metal are amplified. A flame-retardant phosphate monomer was added into LiFSI-1.3TMPa HCE to conduct radical polymerization and form NGPE. The obtained NGPE is transparent, self-standing, and nonflammable. However, it has a low lithium CE of 88.0% at 60°C. NGPEs will be further improved by modifying the polymerization process and the monomer structures.

PISE with reduced ratio of polymer can largely reduce the flammability of the electrolyte. PISE was prepared using a solvent-free process. With the decrease of O/Li ratio, the conductivity decreases to lowest in P(EO)<sub>4</sub>LiFSI, then increases to highest in P(EO)<sub>1</sub>LiFSI, and finally decreases to a lower value again in P(EO)<sub>0.5</sub>LiFSI (Figure 80a). However, the conductivity is still not high enough for battery testing. After the PISE is plasticized with ionic liquid Pyr14FSI, the conductivity of PISCE increases with the increase of Pyr14FSI ratio (Figure 80b). P(EO)<sub>1</sub>LiFSI-0.4Pyr14FSI has an ionic conductivity of  $1.1 \times 10^{-3} \text{ S cm}^{-1}$  at 60°C, which is suitable to test in batteries. Polyimide nonwoven membrane was chosen as a framework to soak P(EO)<sub>1</sub>LiFSI-0.4Pyr14FSI to get the composite electrolyte (PISCE). The flammability test shows that the PISCE is difficult to ignite. More testing will be conducted, and results will be reported next quarter.

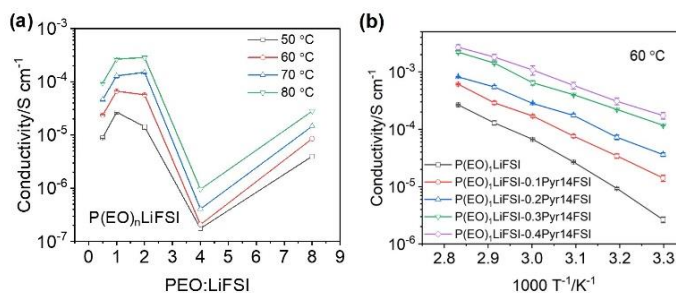


**Figure 80.** (a) Ionic conductivity of P(EO)<sub>n</sub>LiFSI polymer-in-salt electrolytes with different [EO]/[Li<sup>+</sup>] molar ratio. (b) Temperature dependence of ionic conductivity of P(EO)<sub>1</sub>LiFSI-xPyr14FSI polymer-in-salt composite electrolytes at 60°C.

In a separate effort, HCEs of LiFSI<sub>x</sub>-AN-VC<sub>y</sub> system (LAVs) were also investigated with  $x = 0.2 \sim 1.1$  and  $y = 0.02 \sim 0.15$  in molar ratio, where AN is acetonitrile and VC is vinylene carbonate. Addition of VC in LiFSI-AN HCEs can significantly stabilize the compatibility of Li-metal anode and the electrolyte, thus increasing lithium CE to 99.2% for the optimal electrolyte of LiFSI<sub>0.52</sub>-AN-VC<sub>0.09</sub> with large granular lithium deposition. The optimal LAV is also stable at 4.5 V versus Li/Li<sup>+</sup> and allows Li||NMC-333 cells to stably cycle for more than 400 cycles in 2.7-4.3 V at 1.8 mA cm<sup>-2</sup> or 250 cycles in 2.7-4.5 V at 3.6 mA cm<sup>-2</sup>.

In addition, the team also collaborated with Dr. C. Wang's team and studied the origin of VC on lithium CE, morphology, and SEI components of electrochemically deposited lithium (EDLi) by using cryo-TEM and EELS. The VC-containing electrolyte results in a slightly oxidized lithium, with SEI being nanoscale mosaic-like structure comprised of organic species, Li<sub>2</sub>O and Li<sub>2</sub>CO<sub>3</sub>, while the VC-free electrolyte leads to a combination of fully oxidized lithium with Li<sub>2</sub>O SEI layer and pure lithium metal with multilayer nanostructured SEI.

## Patents/Publications/Presentations

### Publication

- Xu, Y., H. Wu, Y. He, Q. Chen, J-G. Zhang, W. Xu, and C. Wang. “Atomic to Nanoscale Origin of Vinylene Carbonate Enhanced Cycling Stability of Lithium Metal Anode Revealed by Cryo-Transmission Electron Microscopy.” *Nano Letters* (2019). doi:10.1021/acs.nanolett.9b04111.

### Presentation

- MRS Fall Meeting, Boston, Massachusetts (December 3, 2019): “Polymer in Quasi-Ionic Liquid Electrolytes for High-Voltage Lithium Metal Batteries”; H. Wu,\* Y. Xu, X. Ren, B. Liu, M. H. Engelhard, M. S. Ding, P. Z. El-Khoury, L. Zhang, Q. Li, K. Xu, C. Wang, J-G. Zhang, and W. Xu.

## Task 4.2 – Composite Electrolytes to Stabilize Metallic Lithium Anodes (Nancy Dudney and X. Chelsea Chen, Oak Ridge National Laboratory)

**Project Objective.** The project has several objectives: (1) prepare novel polymer and ceramic electrolyte materials that can work together to achieve thin membranes that have the unique combination of electrochemical and mechanical properties required for practical manufacturing and to stabilize the metallic lithium anode for good power performance and long cycle life, (2) identify key features of the composite composition, architecture, and fabrication that optimize performance, and (3) fabricate thin electrolyte membranes to use with a thin metallic lithium anode that provides good power performance and long cycle life.

**Project Impact.** A stable lithium anode is critical to achieve high energy density with excellent safety, lifetime, and cycling efficiency. This study will identify key design strategies that should be used to prepare composite electrolytes to meet the challenging combination of physical, chemical, and manufacturing requirements to protect and stabilize the Li-metal anode for advanced batteries. By utilizing well characterized and controlled component phases, design rules developed for composite structures will be generally applicable toward substitution of alternative and improved solid electrolyte component phases as they become available. Success will enable DOE technical targets: 500-700 Wh/kg, 3000-5000 deep discharge cycles, and robust operation.

**Approach.** This project seeks to develop practical solid electrolytes to provide stable, long-lived protection for Li-metal anode. Current electrolytes have serious challenges when used alone; oxide ceramics are brittle, sulfide ceramics are air sensitive, polymers are too resistive and soft, and many electrolytes react with lithium. Composites provide a clear route to address these issues. While work continues to emphasize study of ceramic electrolyte / polymer electrolyte interfaces, this effort has expanded to address the following: (1) practical processing routes to fabricate full batteries using better composite electrolytes with a composite cathode and thin Li-metal anode, and (2) introduction of alternative polymer and ceramic phases to replace well-known model materials and develop improved composite electrolytes. In addition to solid-state devices, hybrid batteries are investigated using a fluid or gel catholyte within the porous cathode. Coatings have also been employed to stabilize electrode interfaces. These directions increase complexity of the studies, but are needed to improve cycling stability and rate performance and to advance practical implementation of the solid electrolyte and Li-anode technology.

**Out-Year Goal.** The goal is to use advanced manufacturing processes where the architecture of the composite membrane can be developed and tailored to maximize performance and cost-effective manufacturing.

**Collaborations.** Work is conducted by Dr. Y. Zhang and Dr. X. Chen. Ceramic electrolyte powders (LICGC™) are obtained from Ohara Corporation. ORNL internal collaborators include Dr. B. Armstrong and Dr. S. Kalnaus. The team will work with partners from the U. S.–German Cooperation on Energy Storage.

### Milestones

1. Develop methods to minimize interconnected composite electrolytes' interfacial resistance with lithium by varying polymer chemistry. (Q1, FY 2020; Completed – Ongoing for further improvement.)
2. Fabricate interconnected ceramic network with different ceramic chemistry and particle size to increase strength of the composite. (Q2, FY 2020)
3. Investigate the trade-off between  $\text{Li}^+$  transference number and ionic conductivity of the gel composite electrolytes, and optimize it. (Q3, FY 2020)

- Fabricate full batteries using NMC cathode, composite electrolyte, and Li-metal anode. Identify cell failure mode. (Q4, FY 2020)
- Create chemical/physical bonding between polymer and interconnected ceramic network that leads to optimized interface to improve mechanical modulus and ionic conductivity. (Annual stretch milestone).

## Progress Report

This quarter, the team fabricated a free-standing interconnected composite film consisting of LICGC<sup>TM</sup> ceramic and crosslinked PEO-based polymer electrolyte to assess and minimize interface resistance with Li-metal electrodes. The free-standing film was made using tape-casting method instead of spray-coating to provide access to both faces. The rest of the film preparation procedure was the same as described in Reference 1. The physical appearance and a cross-sectional SEM image of the film are shown in Figure 81a-b. The film was ~80- $\mu\text{m}$  thick, with some flexibility. With the free-standing film, the team achieved the same uniform interconnected ceramic morphology (Figure 81b). They intentionally overfilled the ceramic so that there are two thin layers of polymer (~5  $\mu\text{m}$ ) protecting the surface of the ceramic. After being in contact with lithium metal, the part of the composite with no surface polymer layer turned black (Figure 81c), indicating that LICGC<sup>TM</sup> reacted with lithium. With the surface polymer layer, reactions between LICGC<sup>TM</sup> and lithium were prevented (Figure 81d).

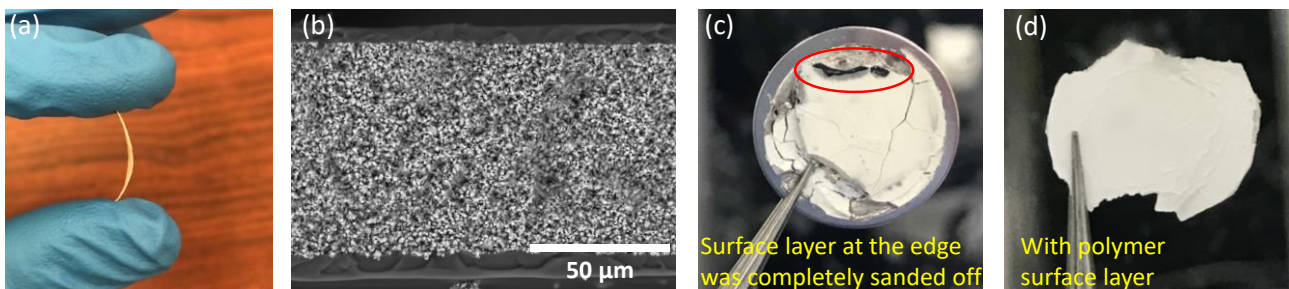


**Figure 81.** (a) A free-standing interconnected composite film made of LICGC<sup>TM</sup> ceramic and crosslinked polymer electrolyte (TC composite). (b) A cross-sectional scanning electron microscopy image of the film. Note the presence of thin layers of polymer protecting both surfaces of the ceramic. (c-d) Pictures of the composite electrolyte film after being in contact with lithium. (c) The part where there was no surface polymer layer turned black. (d) With the surface polymer layer, no sign of ceramic reacting with lithium was observed.

The team performed lithium symmetrical cell testing using the tape-cast composite film. With no or very little (a few microliters) TEGDME plasticizer, the cell could not cycle well. This is due to very large interfacial resistance between the polymer surface layer and lithium. At room temperature, the interfacial resistance was approximately 13  $\text{K}\Omega\cdot\text{cm}^2$ . At 80°C, lithium symmetrical cell cycling was possible, but very large overpotential

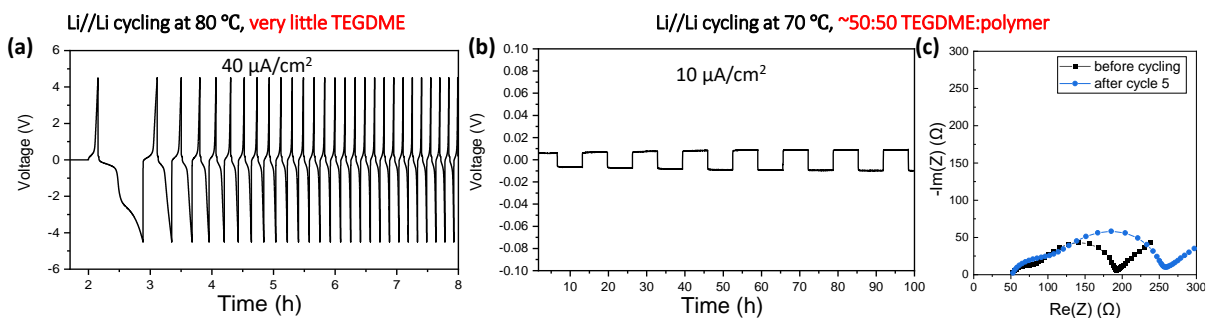


**Figure 82.** Lithium symmetrical cell cycling using interconnected composite film. (a) Cycling at 80°C with very little plasticizer in the film. (b) Cycling at 70°C with the polymer phase containing 50:50 TEGDME plasticizer/polymer by weight. (c) Impedance spectra of the cell in (b) before cycling and after 5 cycles.

was observed (Figure 82a). The team then filled the ceramic with 50:50 TEGDME:polymer (by weight) and repeated the lithium symmetrical cell testing. This cell showed relatively good cycling performance at 70°C, with overpotential < 0.01 V (Figure 82b). The interfacial resistance with lithium, however, increased with further cycling (Figure 82c). This indicates that the polymer electrolyte and/or the plasticizer is not stable with lithium. The polymer phase composition needs to be optimized toward better stability with lithium. At room temperature, with 50% TEGDME, the interfacial resistance with lithium decreased greatly, but is still very significant at approximately 5 K $\Omega$ ·cm<sup>2</sup>. Without the ceramic, the plasticized polymer electrolyte exhibited an interfacial resistance of 500  $\Omega$ ·cm<sup>2</sup> with lithium at room temperature. Understanding the interfacial resistance is important; ongoing investigations will incorporate alternative ceramic and polymer phases.

The team also tested their dry, unplasticized polymer electrolyte and ceramic-polymer composite electrolytes as full and packaged coin cells. The cathodes, supplied by an industrial collaborator, were high-quality and composed of LiFePO<sub>4</sub> in a dry polymer composite with a nominal 1.1 mAh/cm<sup>2</sup> capacity. (They are also investigating in-house cathodes.) It became necessary to step-back and study the coin-cell assembly because of unexpected cycling behavior. While the discharge behavior was stable with the expected voltage and capacities, for some cells there were periods where the charge capacity was two or three times larger than that provided by the cathode. This “overcharge” did not appear to impact cell discharge, but it cannot be ignored.

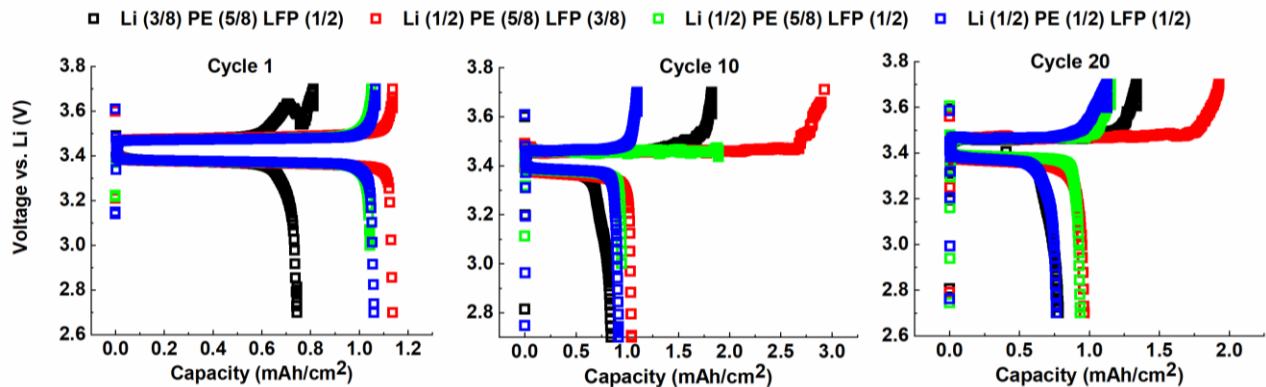


Figure 83. Charge and discharge curves of the cells at cycle 1, 10, and 20. Dimensions of cell components are: Li (3/8) PE (5/8) LFP (1/2), Li (1/2) PE (5/8) LFP (3/8), Li (1/2) PE (5/8) LFP (1/2), and Li (1/2) PE (1/2) LFP (1/2).

To understand the charge behaviors, coin cells were assembled with four geometries providing different overlap and contact areas. It appears that this might provide the key to understand the observation and mechanism. Examples of the results are shown in Figure 83. The relative sizes of the cathode, polymer electrolyte, and lithium foil anode were varied, with punch diameters of 3/8, 1/2, and 5/8 inch. The polymer electrolyte spreads with compression and heating to surround the cathode and lithium, and likely contacts the 5/8-inch stainless spacer. All cells have completed 30 cycles; analysis of harvested components is under way. As illustrated in Figure 83, the cell with the smallest LFP (3/8 inch) always shows the most overcharge capacity, while the cell with smallest PE (1/2 inch) shows the least overcharge capacity. Further analysis is needed to confirm the contact areas, confinement of the lithium, reproducibility, and consistency with other cathodes. Additionally, measures of chemical composition and deformation of the PE and of spreading of lithium during cycling are in progress. Through these evaluations, the team intends to identify the mechanism responsible for the excess charge capacity and best-practice for assembly of small coin cells.

#### Reference

- [1] Palmer, M. J., et al. “A Three-Dimensional Interconnected Polymer/Ceramic Composite as a Thin-Film Solid Electrolyte.” *Energy Storage Materials* (2020).

## Patents/Publications/Presentations

### Publications

- Palmer, M. J., S. Kalnaus, M. Dixit, A. Westover, K. Hatzell, N. Dudney, and X. C. Chen. “A Three-Dimensional Interconnected Polymer/Ceramic Composite as a Thin Film Solid Electrolyte.” *Energy Storage Materials* 26 (2020): 242–249.
- Merrill, L. C., X. C. Chen, Y. Zhang, H. O. Ford, J. L. Schaefer, and N. Dudney. “Polymer-Ceramic Composite Electrolytes for Lithium Batteries: A Comparison Between Single Ion Conducting Polymer Matrix and Its Counterpart.” In preparation.
- Zhang, Y., et al. “Poly(ethylene) Oxide Solid Polymer Electrolyte in Coin Cell Configuration: Insights on the Cell Assembling.” In preparation.

### Presentations

- MRS Fall Meeting, Boston, Massachusetts (December 1–6, 2019): “Gel Composite Electrolyte Membrane for Lithium Metal Batteries.” X. C. Chen, Y. Zhang, L. C. Merrill, M. Lehmann, T. Saito, J. L. Schaefer, F. M. Delnick, and N. J. Dudney.
- MRS Fall Meeting, Boston, Massachusetts (December 1–6, 2019): “Thin Solid Composite Electrolyte with Three-Dimensional Interconnected Structure”; X. C. Chen, M. J. Palmer, M. B. Dixit, S. Kalnaus, A. S. Westover, K. B. Hatzell, and N. J. Dudney. Poster.

## Task 4.3 – Enabling Solid-State Batteries through Characterization and Modeling (Nenad M. Markovic and Larry A. Curtiss, Argonne National Laboratory)

**Project Objective.** The project objectives are multi-faceted, including development of a new mechanically and chemically stable and Li-ion conductive ( $\geq 2 \times 10^{-4}$  S/cm at 298 K) solid electrolyte for a SSB encompassing a Li-metal anode, Li-oxide-based cathode, and nonflammable crystalline and amorphous solid electrolytes that can operate at cathode potentials  $> 5$  V (denoted as a  $S_{Li}$ - $S_{EL}$ - $S_C$  system).

**Project Impact.** Protective organic and inorganic compounds can enhance stability of the interface, improve Li-ion interfacial transport, minimize dendrite formation, and increase safety in Li-ion batteries.

**Approach.** The project proposes to develop and use interdisciplinary, atomic-/molecular-level insight obtained from integrating both experimental- and computational- based methodologies to define the landscape of parameters that control interfacial properties for a new generation of the Li-ion solid-solid battery systems. The strategy will involve transferring knowledge gained from well-characterized thin-film materials to real-world materials. This strategy forms a closed loop wherein the knowledge gained from model systems is used to design more complex, real-world materials, and vice versa. The work will focus on utilizing existing in-house synthesis and characterization methods to enable rapid transition from fundamental science to realistic cells.

**Out-Year Goals.** The out-year goals are to use and develop the physical and chemical synthesis methods for design of solid-solid interfaces with unique chemical/mechanical/conductivity properties. The proposed work will develop and exploit a variety of *ex situ* and *in situ* experimental optical and surface sensitive techniques and electrochemical methods to explore and explain bulk and interfacial properties of the selected materials. The results will serve to unravel many puzzling bulk and interfacial properties of  $S_{Li}$ - $S_{EL}$ - $S_C$  systems, including various types of ceramic and glass materials.

**Collaborations.** This project funds work at ANL and collaboration with J. Sakamoto at University of Michigan.

### Milestones

1. Chemical stability, evaluation, and correlation with interfacial and bulk chemical reactivity for Li/PEO interfaces. (Q1, FY 2020; Completed)
2. Characterization of Li/LLTO interfaces: effect of crystallinity on surface and bulk reactivity and electrochemical stability. (Q2, FY 2020)
3. Characterization of LCO/electrolyte interfaces: effect of crystallinity and orientation on surface and bulk reactivity. (Q3, FY 2020)
4. Characterization of lithium interfaces with doped and undoped LLZO, with experimental and modeling study. (Q4, FY 2020)

## Progress Report

PEO has been widely studied as a possible electrolyte for Li-ion batteries. One challenge of realizing this application is to understand its stability with lithium metal, which is theoretically the best candidate for advanced anode materials in batteries. During the first quarter, the team used both XPS and EIS to study stability of the PEO/Li interface and its potential contribution to ionic conductivity of PEO.

In the first part of this work, the team utilized XPS to investigate the chemical interaction between PEO and lithium metal. A thin film of neat PEO was spin coated on a clean SiO<sub>2</sub> substrate, and another piece of clean SiO<sub>2</sub> substrate was used as a control sample. XPS data were acquired from both samples before lithium E-beam deposition (Figure 84a/d), after lithium deposition (Figure 84b/e), and after another three hours of heating at 100°C (Figure 84c/f). All experiments were done in UHV to minimize contamination. After lithium deposition, a clear organolithium (LiCR) peak at ~ 282 eV was found (Figure 84e) in the PEO sample. The same peak was not found on the control sample (Figure 84b). This evidence strongly suggests that PEO reacted with lithium metal on contact. Lithium alkoxide (LiOR), another main product of the reaction, was found in Figure 84f where the Li-metal peak dropped after three hours of heating. Based on the XPS data, the team has proposed the reactions between lithium and PEO involving breaking of C-C and C-O bonds with addition of lithium from the surface that can be responsible for the observed LiCR and LiOR peaks. They also carried out density functional calculations of various Li-PEO fragments using glymes of various lengths as models for PEO. The calculations of the free energies of the reactions indicated that these reactions are thermodynamically favorable, confirming the results deduced from the XPS data.

In the second part of this work, the team used *in situ* EIS measurement to study the PEO/Li interface electrochemically with the help of the unique interdigitated electrodes (IDE) devices. The results not only confirmed the reaction between PEO and lithium, but also revealed an interesting phenomenon that the reaction product LiOR may act as “lithium salt,” that is, with the OR having a negative charge. This “salt” resulting from the reaction of lithium and PEO can contribute to the ionic conductivity of the PEO.

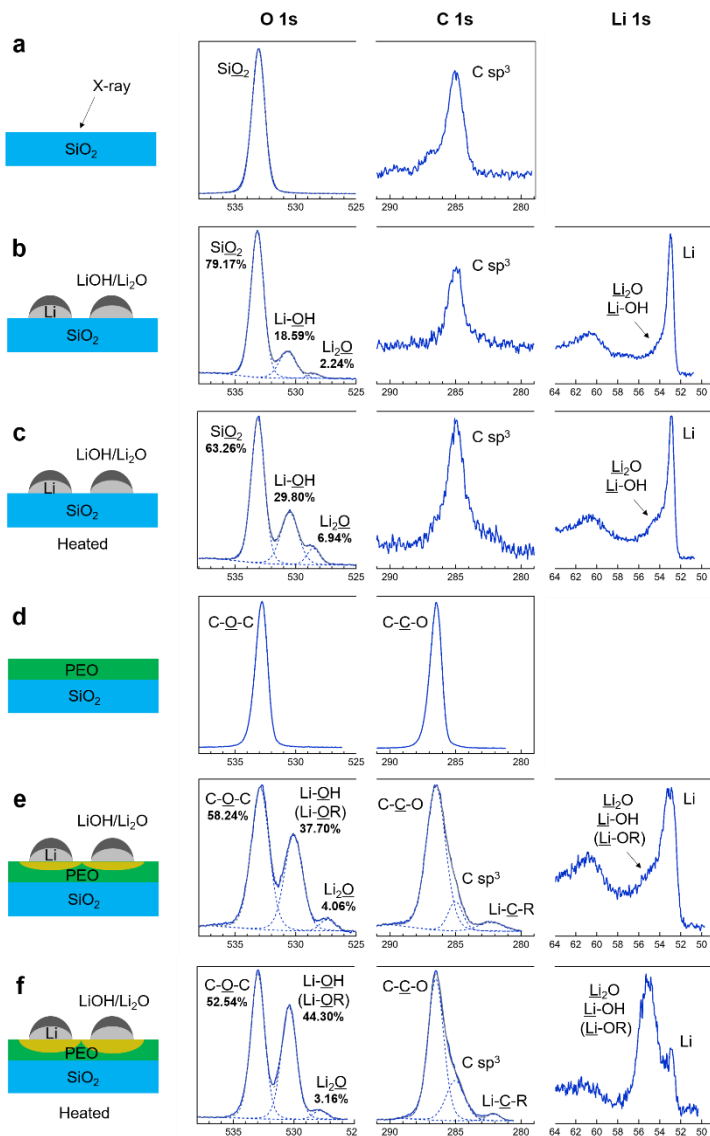


Figure 84. X-ray photoelectron spectroscopy (XPS) data of SiO<sub>2</sub> control sample (a), after lithium deposition (b), and after heating (c). XPS data of neat PEO (d), after lithium deposition (e), and after heating (f).

## Patents/Publications/Presentations

### Patent

- IN-19-084: Interface Design for High Current Density Cycling of Solid-State Battery.

### Publications

- Tepavcevic, S., Y. Zhu, J. G. Connell, P. Zapol, P. Liu, J. W. Freeland, D. D. Fong, V. R. Stamenkovic, R. Garcia-Mendez, J. Sakamoto, L. A. Curtiss, and N. M. Markovic. “Interface Design for High Current Density Cycling of Solid State Batteries.” *Energy & Environmental Science*. Under review.
- “Improved Ion Conductivity of Polyethylene Oxide by *In Situ* Lithium Salt Formation.” In preparation.

### Presentation

- PNNL Solid-State Electrolytes Meeting, Richland, Washington (October 24, 2019): “Advancing Solid State Interfaces in Li-ion Batteries”; S. Tepavcevic.

## Task 4.4 – 3D Printing of All-Solid-State Lithium Batteries (Jianchao Ye, Lawrence Livermore National Laboratory)

**Project Objective.** This project has three objectives: (1) tuning microstructures of 3D-printed SSE separators, (2) determining material and processing compatibilities with cathode printing, and (3) 3D printing of sintering-free SSE separators.

**Project Impact.** All-solid-state lithium batteries are difficult to process due to the brittleness of ceramic materials, poor solid-solid contact, and the electrolyte-electrode stability issues. As a result, the energy and power density and also cycling stability are far from satisfying. This project will address fabrication difficulties by using state-of-the-art 3D-printing techniques, which can introduce 3D interfaces and architectures to enhance the solid-solid contact and reduce charge transfer resistance. Success of the project will benefit the DOE by establishing the best manufacturing methods for ASSBs to achieve VTO goals on the performance of beyond Li-ion batteries.

**Approach.** The project employs 3D-printing techniques to manufacture SSEs and related components for ASSBs. The team starts with direct ink writing (DIW) to develop ink recipes with desired rheological properties and explore post-sintering approaches to achieve high densification. In parallel with DIW 3D printing, the team also explores other 3D printing options, such as projection microstereolithography (PuSL), electrophoretic deposition (EPD), and projection-based two-photon polymerization. Both sintering and sintering-free approaches can gain benefit from 3D printing and therefore will be investigated in this project.

**Out-Year Goals.** The team will determine particle sizes and morphologies as well as post-processing conditions that deliver good ionic conductivity and charge transfer properties of LLZTO separators. They will examine co-sintering of LLZTO/cathode and determine the effects of material, particle size, surface coating, and sintering conditions.

**Collaborations.** Microstructures, ionic conductivities, and mechanical properties will be provided to the LLNL simulation team, led by PI B. Wood, for establishing and validating phase-field modeling methods.

### Milestones

1. ALD coating on LLZTO/electrode powders. (Q1, FY 2020; In progress)
2. Thermochemical stabilities of electrolyte-electrode-conductive additive mixtures. (Q2, FY 2020; Initiated)
3. Down selection of electrolyte-electrode-conductive additive mixtures with good electronic and ionic conductivities. (Q3, FY 2020)
4. Evaluation of half-cell stability and failure mechanisms. (Q4, FY 2020)

## Progress Report

Last quarter, the team obtained dense LLZTO films by using high energy ball milled powders and  $\text{Li}_3\text{BO}_3$  as a sintering agent in the ink formula. To evaluate the ionic conductivity and reduce charge transfer resistance against metallic lithium, the sintered surface has to be treated to remove nonconducting  $\text{Li}_2\text{CO}_3$ . The acid treatment method was examined and found to be fairly effective at improving the LLZTO/Li interfacial properties. Another reported surface treatment method is ALD of  $\text{Al}_2\text{O}_3$  or ZnO on sintered pellets/films. However, it is time consuming to run ALD every time after preparation of new films.

This quarter, the team developed a powder ALD coating approach to modify large batches of LLZTO powders with an ultrathin  $\text{Al}_2\text{O}_3$  coating. These modified powders are used for pellet/film sintering. Potential effects include: (1) aluminum enters into the LLZTO lattice and results in dual doping that could further enhance ionic conductivity; (2)  $\text{Al}_2\text{O}_3$  coating regulates the decomposition of  $\text{Li}_2\text{CO}_3$ , allowing lithium to reenter the LLZTO lattice during sintering; (3)  $\text{Al}_2\text{O}_3$  aggregates on the surface of the LLZTO pellets and enhances contact between LLZTO and lithium. There are several advantages to this approach. The first advantage is simplified processing. A large amount of powders can be treated using a simplified ALD facility. At lab scale, 1 kg of powders can be coated each time. The coated powders can be pressed into pellets, sintered at relatively low temperatures, and used directly for electrochemical testing with no need for further surface treatment to enhance wettability. The pellets form good contact with melted lithium immediately after sintering. A second advantage is that only one cycle of  $\text{Al}_2\text{O}_3$  ALD is needed to observe dramatic improvement of conductivity and charge transfer resistance. Finally, sintering temperature can be reduced to less than  $900^\circ\text{C}$  without much sacrifice in conductivity and charge transfer.

An example of Ta-doped LLZO (LLZTO) powders with one to five cycles of  $\text{Al}_2\text{O}_3$  coating is shown below. After sintering at temperatures of  $900^\circ\text{C}$ ,  $1000^\circ\text{C}$ , and  $1100^\circ\text{C}$ , the relative density of the pellet ranges from 76.4% up to 96.5%. Even though the density of LLZTO-1Al (LLZTO powders with one cycle of  $\text{Al}_2\text{O}_3$  coating) sintered at  $900^\circ\text{C}$  is only 76.4%, the EIS reveals an ionic conductivity of over  $10^{-4}$  S/cm and charge transfer resistance of less than  $100 \text{ ohm cm}^2$ . In contrast, without the  $\text{Al}_2\text{O}_3$  coating, the sintered pellets have to be surface treated to reduce charge transfer resistance. For example, using  $\text{H}_3\text{PO}_4$ /ethanol solution to remove residual  $\text{Li}_2\text{CO}_3$  on the surface of the  $900^\circ\text{C}$  sintered LLZTO pellets, the measured interfacial impedance is still  $> 10^4 \text{ ohm cm}^2$ , which is two orders of magnitude higher than the ALD  $\text{Al}_2\text{O}_3$  coated case without acid treatment. After cell disassembly, the team found a black interfacial layer was formed between lithium and the LLZTO electrolyte, which could be the origin of improved wetting with lithium and low interfacial impedance.

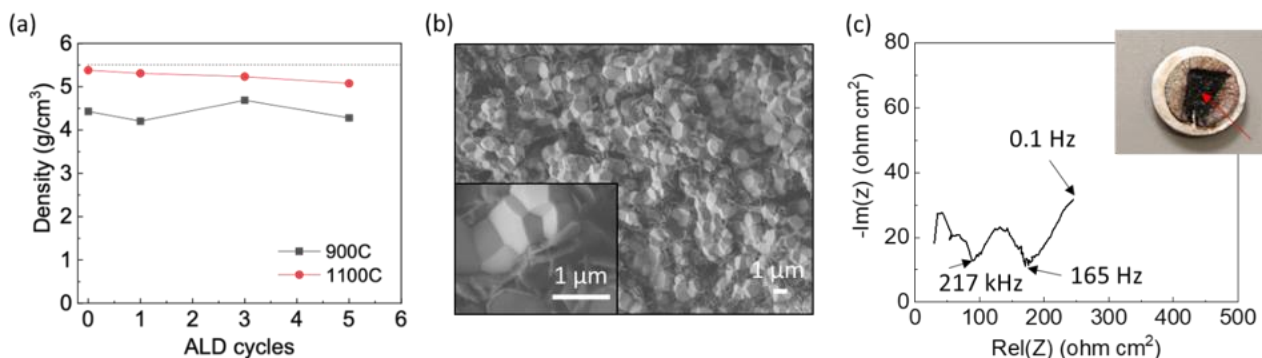


**Figure 85.** (a) Density of LLZTO-Al pellets with different atomic layer deposition (ALD) cycles of  $\text{Al}_2\text{O}_3$  coating after sintering at  $900^\circ\text{C}$  (black) and  $1100^\circ\text{C}$  (red). (b) Scanning electron microscopy image of LLZTO-1Al with 1 cycle of  $\text{Al}_2\text{O}_3$  sintered at  $900^\circ\text{C}$ . Inset is a zoom-in image showing the existence of a low-z phase between LLZTO grains. (c) Electrochemical impedance spectroscopy of LLZTO-1Al sintered at  $900^\circ\text{C}$ . Inset is an optical image of a disassembled Li/LLZTO-1Al/Li cell with the interface exposed. Arrow indicates the black color formed after contact between lithium and LLZTO-1Al above the lithium melting point.

In the coming quarter, the team will use these Al<sub>2</sub>O<sub>3</sub>-modified LLZTO powders to prepare inks for 3D printing. They expect the obtained solid-state electrolyte films can be directly tested after sintering, even with low densities. These powders may also help to lower the co-sintering temperature for cathode printing.

### Patents/Publications/Presentations

#### Presentation

- 236<sup>th</sup> ECS Meeting, Atlanta, Georgia (October 13–17, 2019): “3D Printing of Solid-State Electrolytes for Li-Ion Batteries: Processing and Morphology Optimization”; M. Wood.

## Task 4.5 – Interfacial Studies on Lithium Thiophosphate Based Solid Electrolytes and Cathodes (Jagjit Nanda, Oak Ridge National Laboratory)

**Project Objective.** Capacity fading and the underlying interfacial side reactions between thiophosphate solid electrolytes and cathode active materials are not well understood. One of this project's key deliverables is to combine EIS measurements with complementary *in situ* and *ex situ* spectroscopy and microscopy to quantify the buried interfacial decomposition reaction product. Ultimately, this work will enable a mechanistic understanding of factors that limit the rate performance and capacity loss of SSBs. The goal here is to combine the information from these techniques to provide a unified overview of the interfacial layer's composition, structure, and morphology. In this multi-year work, the team will investigate a number of solid electrolytes [ $\text{Li}_3\text{PS}_4$  (LPS),  $\text{Li}_{10}\text{GeP}_2\text{S}_{12}$  (LGPS), and  $\text{Li}_{9.54}\text{Si}_{1.74}\text{P}_{1.44}\text{S}_{11.7}\text{Cl}_{0.3}$  (LSiPCl)] and cathode compositions belonging to different structural families [ $\text{LiFePO}_4$  (olivine),  $\text{FeS}_2$  (sulfide-based conversion cathode), and  $\text{LiNi}_{0.6}\text{Mn}_{0.2}\text{Co}_{0.2}\text{O}_2$  (NMC-622, layered oxide)].

**Project Impact.** SSBs are poised to be the next-generation battery technology for meeting EV goals in terms of energy density, cycle life, and safety. Among other technical barriers, the success of this technology relies on design of stable electrode/electrolyte interfaces. Sulfide-based solid electrolytes have high ionic conductivity ( $> 10^{-4}$  S/cm) and are mechanically soft, which simplifies processing compared to their oxide counterparts. Furthermore, sulfide solid electrolytes are comprised of earth abundant materials (for example, sulfur and phosphorus) and can be easily synthesized using scalable, low-temperature solution-based routes.

**Approach.** Low-temperature ( $< 350^\circ\text{C}$ ) solution-based synthesis method will be used to synthesize LPS family of solid electrolytes. The structure of these materials is characterized using XRD, Raman spectroscopy, and neutron scattering. Standard AC/DC electrochemical methods are used to characterize ionic conductivity, electrochemical stability, and CCD. The scope of the work includes using various *in situ* and *ex situ* electrochemical, microscopic, and spectroscopic tools for characterizing the structure, morphology, and kinetics of the interfacial reaction layer formed between thiophosphate solid electrolytes and cathodes.

**Out-Year Goals.** Develop low ASR thiophosphate SE-sulfide cathode interfaces for ASSBs.

**Collaborations.** This project will collaborate with Profs. G. Ceder (LBNL) and P. Jena (Virginia Commonwealth University) on modeling and synthesis guideline, as well as with Prof. S. Greenbaum on solid-state NMR to measure ion-diffusivity and local bonding.

### Milestones

1. Identify synthesis, doping, and processing conditions to prepare  $\text{Li}_3\text{PS}_4$ -based solid electrolytes with a  $\text{Li}^+$  conductivity exceeding  $10^{-4}$  S/cm. (Q1, FY 2020; Completed December 31, 2019)
2. Develop binder systems for  $\text{Li}_3\text{PS}_4$  family of solid electrolytes for improving processability and stability at the Li-metal and cathode interfaces. (Q2, FY 2020; In progress)
3. Measure and compare the  $\text{Li}^+$  diffusion coefficient for pristine  $\text{Li}_3\text{PS}_4$  and substituted  $\text{Li}_3\text{PS}_4$  solid electrolytes using solid-state NMR. (Q3, FY 2020)
4. Undertake *in situ* Raman and electron microscopy including cryo-TEM for characterizing  $\text{Li}_3\text{PS}_4$  and cathode- $\text{Li}_3\text{PS}_4$  interfaces as part of determining the ASR. (Q4, FY 2020)

## Progress Report

Solvent mediated synthesis (also known as solvent suspension synthesis) of  $\text{Li}_2\text{S}$ - $\text{P}_2\text{S}_5$  glass and glass-ceramic superionic thiophosphates offers a means for high-volume, low-cost production of SSB electrolytes. Typically, this synthetic approach utilizes organic solvents in which the reactants  $\text{Li}_2\text{S}$  and  $\text{P}_2\text{S}_5$  are virtually insoluble. Nevertheless, milled/mixed slurries containing  $\text{Li}_2\text{S}$  and  $\text{P}_2\text{S}_5$  yield solvent complexes of  $\text{Li}_3\text{PS}_4$  and  $\text{Li}_7\text{P}_3\text{S}_{11}$  superionic conductors through the precipitation of  $(\text{PS}_4^{3-})$  anionic/polyanionic salts. The coupling, coordination, orientation, and lattice disposition of these  $(\text{PS}_4^{3-})$  tetrahedra are highly dependent on the ratio of the reactants ( $\text{Li}_2\text{S}$  and  $\text{P}_2\text{S}_5$ ), the organic solvent, the mixing/milling protocol, and the subsequent thermal processing. The resulting wide variation in microstructure has led to a broad range (typically several orders of magnitude) of reported ionic conductivities for thiophosphate solid electrolytes prepared by solvent mediation. It has been reported that  $\text{Li}_2\text{S}:\text{P}_2\text{S}_5$  mixtures (molar ratio 1:1) form soluble solvate complexes in AN and EP solvents, and these complexes react with excess  $\text{Li}_2\text{S}$  to precipitate the above  $(\text{PS}_4^{3-})$  anionic/polyanionic salts.

To reproducibly control the synthesis of highly conducting lithium thiophosphate solid electrolytes, the team is evaluating the role of the solvent and corresponding soluble intermediate solvate complexes during synthesis. They utilized various materials characterization methods including the following: (1) Raman spectroscopy to identify the soluble anionic/polyanionic solvate complexes and resulting insoluble anionic/polyanionic products after precipitation and thermal processing, (2) XPS to establish changes in oxidation state and Li-P-S bonding environments, and (3) XRD to evaluate the materials' crystallinity.

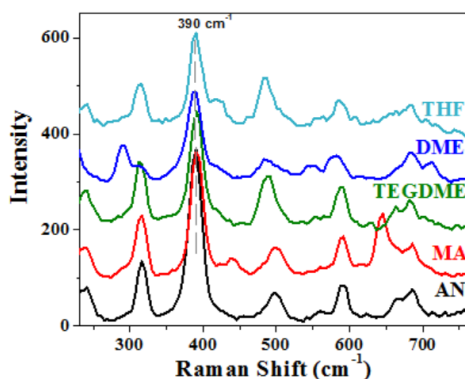


Figure 86. Raman spectra of solution phase  $\text{Li}_2\text{S} : \text{P}_2\text{S}_5$  (molar ratio 1:1) solvate complexes in AN, MA, TEGDME, DME, and THF.

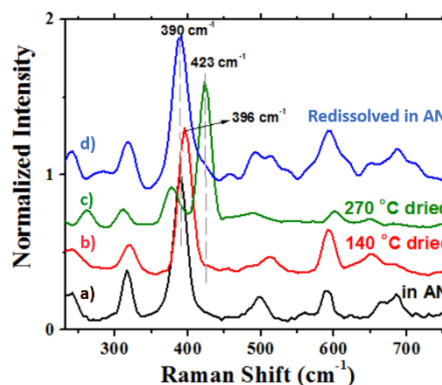


Figure 87. (a) Raman spectra for solution phase solvate complex in AN. (b) The same complex vacuum dried at  $140^\circ\text{C}$  for 24 h (still containing  $\sim 3$  wt% strongly coordinated AN). (c) The same complex heated to  $270^\circ\text{C}$  to remove the remaining AN. (d) Raman spectra of sample (c) re-dissolved in AN.

Figure 86 shows the Raman spectra of solution phase  $\text{Li}_2\text{S}:\text{P}_2\text{S}_5$  (molar ratio 1:1) solvate complexes in AN, MA, TEGDME, DME, and THF. The solvate complex has the same structure in all solvents with the most distinguished Raman band centered at  $390 \pm 1 \text{ cm}^{-1}$  ( $395 \text{ cm}^{-1}$  for TEGDME).

Figure 87 shows the following: (a) Raman spectra for the solution phase solvate complex in AN, (b) the same complex vacuum dried at  $140^\circ\text{C}$  for 24 h (this complex still contained about 3 wt% strongly coordinated AN), (c) the same complex heated to  $270^\circ\text{C}$  to remove the remaining AN, and (d) the Raman spectra of sample (c) re-dissolved in AN. The Raman shift at  $423 \text{ cm}^{-1}$  is assigned to the symmetric stretch of the P-S-P-S ring for crystalline  $\text{Li}_2\text{P}_2\text{S}_6$  (reported in the literature at  $421 \text{ cm}^{-1}$ ). However, this band is also very close to the  $422 \text{ cm}^{-1}$  characteristic shift for  $\text{PS}_4^{3-}$ . Furthermore, the  $390 \text{ cm}^{-1}$  band shown in all solution phases complexes is very close to the  $385 \text{ cm}^{-1}$  characteristic shift for  $\text{P}_2\text{S}_6^{4-}$  in  $\text{Li}_4\text{P}_2\text{S}_4$ . To ensure accurate assignment of the Raman bands, additional XRD and XPS measurements were performed.

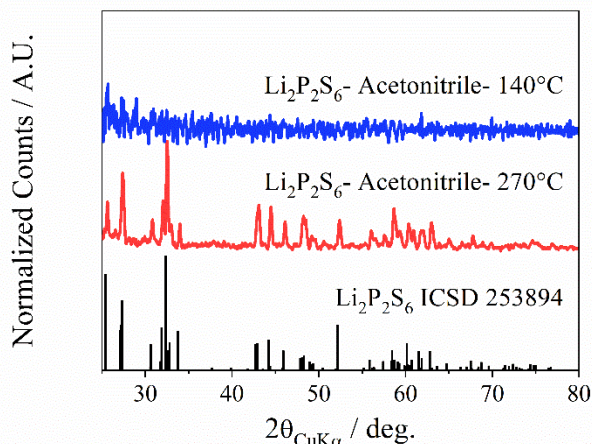


Figure 88. X-ray diffraction patterns of the same solvate complexes described in Figure 87.

Figure 88 shows XRD of the same solvate complexes described in Figure 87. These results indicate that  $\text{Li}_2\text{P}_2\text{S}_6$  dried at  $140^\circ\text{C}$  was completely amorphous, but heating this powder at  $270^\circ\text{C}$  induced crystallization of the desired phase. When the crystalline  $\text{Li}_2\text{P}_2\text{S}_6$  (dried at  $270^\circ\text{C}$ ) sample was re-dissolved in AN, the resulting solvated complex exhibited a Raman shift at  $390\text{ cm}^{-1}$ , which is attributed to the solvated  $\text{P}_2\text{S}_6^{2-}$  anion.

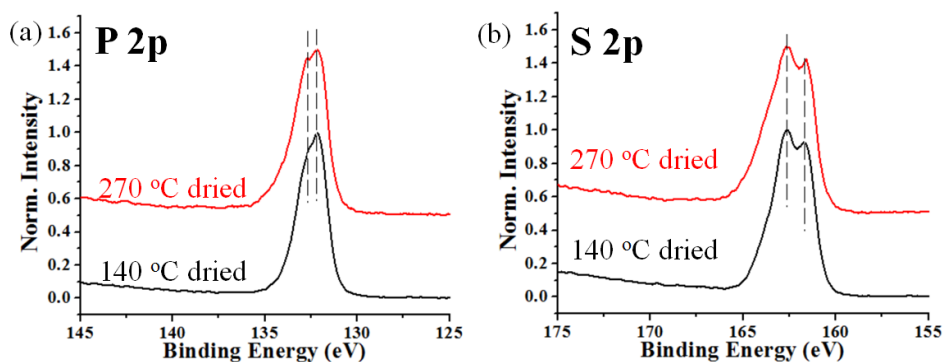


Figure 89. X-ray photoelectron spectra for the same solvate complexes analyzed in Figures 87-88.

Figure 89 shows XPS spectra for the same solvate complexes analyzed in Figures 87-88. The P 2p and S 2p spectra were normalized with respect to the maximum intensity of each core level for ease of comparison. The P 2p and S 2p spectra were almost identical for the samples processed at  $140^\circ\text{C}$  and  $270^\circ\text{C}$ . This result indicates that the sulfur and phosphorus in the amorphous sample ( $140^\circ\text{C}$ ) had similar local bonding environments compared to that of the crystalline  $\text{Li}_2\text{P}_2\text{S}_6$  sample ( $270^\circ\text{C}$ ), thus eliminating consideration of  $\text{Li}_4\text{P}_2\text{S}_6$  as a reaction product.

The team concludes that the solution mediated synthesis of lithium thiophosphates proceeds through the same  $\text{P}_2\text{S}_6^{2-}$  anion (independent of the solvent) and also that variations in final stoichiometry and conductivity depend on thermal treatment and the amount of excess  $\text{Li}_2\text{S}$ .

## Patents/Publications/Presentations

### Presentation

- MRS Fall Meeting, Boston, Massachusetts (December 1–6, 2019): “Lithium Thiophosphate-Based Solid Electrolytes and Cathodes”; J. Nanda. Invited.

## Task 4.6 – Prelithiation of Silicon Anode for High-Energy Lithium-Ion Batteries (Yi Cui, Stanford University)

**Project Objective.** Prelithiation of high-capacity electrode materials is an important means to enable those materials in high-energy batteries. This study pursues three main directions: (1) developing facile and practical methods to increase first-cycle CE of anodes, (2) synthesizing fully lithiated anode to pair with high-capacity Li-free cathode materials, and (3) prelithiation from the cathode side.

**Project Impact.** Prelithiation of high-capacity electrode materials will enable those materials in next-generation high-energy-density Li-ion batteries. This project's success will make high-energy-density Li-ion batteries for EVs.

**Approach.** Silicon electrode film will be prepared by coating the slurry of silicon nanoparticles, carbon black, and binder mixture on copper foil through a doctor-blading method. The silicon electrode film will be prelithiated by pressing a Li-metal foil on top of it and heating it in an argon glovebox for a certain time. Then,  $\text{Li}_x\text{Si}$  electrode film can be obtained by removing the redundant lithium foil through a peeling-off approach. The redundant lithium foil is reusable for the next prelithiation. The structure, morphology, and other properties can be analyzed by SEM, TEM, XPS, Raman spectroscopy, XRD, etc. In the first year, the team aims to fabricate  $\text{Li}_x\text{Si}$  freestanding electrode film and improve its air stability. In the second year, the team aims to improve the electrochemical stability in full cells.

**Out-Year Goals.** Materials containing a large quantity of lithium will be synthesized for pre-storing lithium ions inside batteries. Materials and process will be developed to be compatible with battery electrode and cell fabrication. First-cycle CE of anodes will be improved and optimized by prelithiation materials. Develop materials for prelithiation from the cathode side.

**Collaborations.** This project engages in collaboration with the following: BMR PIs; SLAC: Dr. M. Toney (*In situ* X-ray); and Stanford: Prof. Nix (mechanics) and Prof. Bao (materials).

### Milestones

1. Demonstrate a new solvent-free dry method for anode prelithiation. (Q1, FY 2020; Completed)
2. Demonstrate control of prelithiation amount by adjusting contact duration between thick lithium foil and anode materials. (Q2, FY 2020; In progress)
3. Demonstrate synthesis of thin lithium foil with different thickness (5-20  $\mu$ ) for use in dry prelithiation method. (Q3, FY 2020)
4. Demonstrate thin lithium foil with different thicknesses as dry prelithiation reagents for anode materials to pair with different-capacities cathode materials. (Q4, FY 2020)

## Progress Report

Substantial improvements on energy density of Li-ion batteries require development of high-capacity electrodes. Alloy anodes with much higher capacity have been recognized as promising alternatives to graphites. Without pre-stored lithium in anodes, the energy density is limited by the low capacity of Li-metal oxide cathodes. Recently, lithium metal has been revived as a high-capacity anode, but faces many challenges resulting from its high reactivity and uncontrolled dendrite growth.

In previous reports, the team shows that silicon electrode film can be prelithiated by pressing a Li-metal foil on top of it for a certain time, and then  $\text{Li}_x\text{Si}$  electrode film is obtained after removing the redundant lithium foil. Here, the team shows that prelithiation can be achieved through a one-step, heat-free, solvent-free, and pressing-free approach, which is even much more facile and compatible for industry application.

The one-step prelithiation process is shown in Figure 90. Silicon electrode film was prepared by coating the slurry of silicon nanoparticles, carbon black, and binder mixture (the mass ratio is 8:1:1) on copper foil through a doctor-blading method. Then, 2032 coin cell was assembled using silicon electrode as the anode paired with cathode material (such as  $\text{LiFePO}_4$ ,  $\text{LiCoO}_2$ , etc.) film. For prelithiation treatment on silicon anode, a piece of thin lithium foil was put on the top of silicon electrode during the coin cell assembly. After assembly of the Si/cathode cell, the cell rested for 10 min to 4 h before charge/discharge cycles. During the rest, silicon reacted with the top thin lithium foil and completed the prelithiation (Figure 90a). To confirm that, the cell was disassembled after rest, and silicon electrode film was taken out, washed, and dried for SEM characterization. As shown in Figure 90b, before prelithiation, silicon nanoparticles are well dispersed, showing a size  $\sim 100$  nm. After prelithiation, the size of silicon nanoparticles increased noticeably, while the integrity of the structure is well maintained, which is due to the initial size of silicon nanoparticle being below the critical crack size of 150 nm (Figure 90c). It is worth noting that SEI film can also be observed at the top of the prelithiated silicon film, which is due to decomposition of electrolyte solvent along with the prelithiation. In the future, efforts will be devoted to optimizing surface area and porosity of the thin lithium foil to optimize prelithiation capacity, as well as improving the air stability of the prelithiated electrode film.

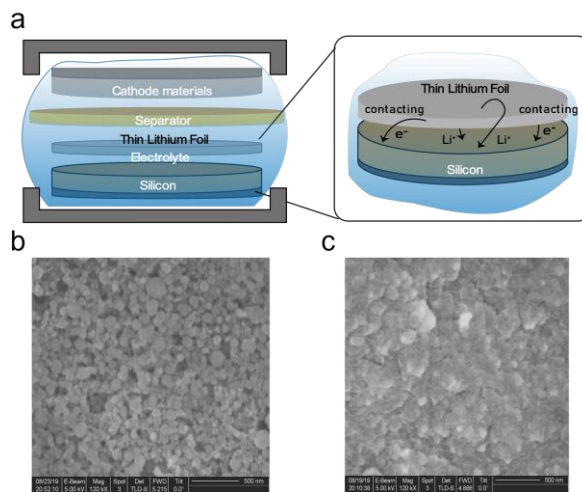


**Figure 90. (a) Schematic illustration of one-step solvent-free prelithiation method for silicon anodes. (b-c) Scanning electron microscopy images of silicon anode before prelithiation (b) and after (c) prelithiation.**

## Patents/Publications/Presentations

The project has no patents, publications, or presentations to report this quarter.

## TASK 5 – SULFUR ELECTRODES

### Summary

The collected work in this Task focuses on the following areas:

- Conducting focused fundamental research on the mechanism of “shuttle effect” inhibition for rechargeable Li-S batteries.
- Developing electrode and electrolyte systems that can mitigate the “shuttle effect” so low self-discharge and long cycle life can be achieved.
- Synthesizing sulfur composite materials with an emphasis on polymer sulfur composite materials.
- Developing creative electrode-making processes to improve processability and aerial capacity; for example, polymeric sulfur composites may not be suitable for the traditional slurry casting process.
- Developing a novel  $S_xSe_y$  cathode material for rechargeable lithium batteries with high energy density and long life, as well as low cost and high safety.
- Delivering an electrochemically responsive self-formed hybrid LIC as a protective layer for Li-metal anodes, enabling Li-metal anodes to cycle with a high efficiency.
- Developing high-energy, low-cost Li-S batteries with long lifespan.

**Highlights.** The highlights for this quarter are reported here.

Dr. Amine’s group at ANL has designed a new carbon host (hollow carbon) and investigated the effect of selenium doping on sulfur utilization and cycling performance of Li-S batteries. They also compared electrochemical performance in previously developed fluorinated ether electrolytes with conventional dioxolane/ dimethoxyethane (DOL/DME) electrolytes. The new carbon host prepared by a facile strategy can accommodate up to 80 wt% of the active sulfur material doped with selenium to the extent of 20%. With 10% selenium doping, the composite at a loading of  $2.5 \text{ mg cm}^{-2}$  exhibits a reversible capacity of  $\sim 1000 \text{ mAh g}^{-1}$ , while pure sulfur containing composite exhibits a reversible capacity of  $400 \text{ mAh g}^{-1}$ . Furthermore, the  $SeS_x$ -HC composite can maintain a capacity of  $\sim 900 \text{ mAh g}^{-1}$  with CE of  $\sim 100\%$  for 100 cycles showing a suppression of the shuttle effect.

Dr. Liu’s group at PNNL has designed the integrated Ketjen Black / sulfur (IKB/S) by synthesizing the IKB secondary particles with sizes ranging from 5-100  $\mu\text{m}$ . The team used them to study particle-size correlation of  $< 20 \mu\text{m}$  and  $> 70 \mu\text{m}$  IKB powders with the electrode microstructure and electrochemical properties. The electrode with  $> 70 \mu\text{m}$  particle size shows an initial discharge capacity of  $\sim 950 \text{ mAh g}^{-1}$  at lean electrolyte conditions of  $4 \mu\text{L mg}^{-1}$ , while the  $< 20\text{-}\mu\text{m}$  particle size electrode gives an initial discharge capacity of  $\sim 850 \text{ mAh g}^{-1}$  under similar conditions. These results show the influence of particle size, with further work in progress.

Dr. Cui’s group at Stanford University has developed a facile *in situ* encapsulation strategy to fabricate transition metal dichalcogenides (TMDs) coated lithium sulfide ( $\text{Li}_2\text{S@TMDs}$ ) cathodes. Coin cells were fabricated utilizing the combination of  $\text{Li}_2\text{S@TMDs}$  cathode, polymer-polymer composite solid-state electrolyte, and Li-metal anode. The cells exhibit a discharge capacity of  $\sim 860 \text{ mAh g}^{-1} \text{ Li}_2\text{S}$  at 0.1C rate, which is double that of the bare uncoated  $\text{Li}_2\text{S}$  electrode. These preliminary results demonstrate feasibility of an ASSB using  $\text{Li}_2\text{S}$ .

Dr. Qu's group at University of Wisconsin has collaborated with BNL to synthesize new polymer compounds of sulfur and has characterized them with XAS and XRF imaging. Together, XAS and XRF indicate that the sulfur is bonded to the carbon with sulfur in general uniformly distributed on the electrode. Initial electrochemical cycling tests indicate that the polymer sulfur electrode retains ~80% of capacity over 400 cycles. The results show the promise of the polymer sulfur compounds.

Dr. Liu's group at UC Berkeley has synthesized and purified amphiphilic electrolyte additives exhibiting dual functionalities having fluorocarbon moiety at one end and polar ethylene oxide moiety at the other. These additives significantly improve solubility of Li-ion salts in the fluorocarbon solvents such as 1,1,2,2-Tetrafluoroethyl 2,2,2-Trifluoroethyl Ether (TTE) while enabling formation of Li-salt micelles with amphiphilic properties. They have used small angle X-ray scattering (SAXS) to validate and measure the micelles formation. Results show that LiFSI with the smallest size anion form large sized micelles of ~80-100 nm, while LiTFSI forms much smaller micelles of ~5-30 nm. Results show potential of these amphiphilic additives with dual functionality.

## Task 5.1 – Novel Chemistry: Lithium Selenium and Selenium Sulfur Couple (Khalil Amine, Argonne National Laboratory)

**Project Objective.** The project objective is to develop a novel  $S_xSe_y$  cathode material for rechargeable lithium batteries with high energy density and long life, as well as low cost and high safety.

**Project Impact.** Development of a new battery chemistry is promising to support the goal of PHEV and EV applications.

**Approach.** The dissolution of lithium polysulfides in nonaqueous electrolytes has been the major contribution to the low energy efficiency and short life of Li-S batteries. In addition, insulating characteristics of both end members during charge/discharge (sulfur and  $Li_2S$ ) limit their rate capacity. To overcome this problem, sulfur or  $Li_2S$  is generally impregnated in a carbon-conducting matrix for better electronic conductivity. However, this makes it difficult to increase the loading density of practical electrodes. It is proposed to solve these barriers using the following approaches: (1) partially replace sulfur with selenium, (2) nano-confine the  $S_xSe_y$  in a nanoporous conductive matrix, and (3) explore advanced electrolytes with suppressed shuttle effect.

**Out-Year Goals.** This new cathode will be optimized with the following goals:

- A cell with nominal voltage of 2 V and energy density of 600 Wh/kg.
- A battery capable of operating for 500 cycles with low capacity fade.

**Collaborations.** This project engages in collaboration with the following: Prof. C. Wang at UMD, Dr. Y. Ren and Dr. C. Sun of Advanced Photon Source (APS) at ANL, Dr. L. A. Curtiss at ANL, and Prof. A. X. Sun at Western University, Canada.

### Milestones

1. Synthesized new carbon materials to prepare  $SeS_x$ /carbon composites with high sulfur loading in the composite. (Q1, FY 2020; Completed)
2. Optimizing cathode structures to increase  $SeS_x$  areal loading and improving battery performance. (Q2, FY 2020)
3. Interface understanding on the cycled  $SeS_x$  cathode using TOF-SIMS and XPS. (Q3, FY 2020)
4. Interface understanding on the cycled lithium metal using TOF-SIMS and XPS. (Q4, FY 2020)

## Progress Report

This quarter, the team has designed a new carbon host and investigated the effect of selenium doping on sulfur utilization and cycling performance of Li-S batteries. They have compared electrochemical performance in previously developed fluorinated ether electrolytes with conventional DOL/DME electrolytes.

The new carbon host is hollow carbon (HC) spheres, which has a BET surface area of  $520.12 \text{ m}^2 \text{ g}^{-1}$  and a pore size of 3-4 nm (Figure 91a) as well as a diameter of  $\sim 400 \text{ nm}$  (Figure 91b). Such a hollow structure can enable a very high  $\text{SeS}_x$  loading in the composite. The  $\text{SeS}_x$ -HC composites were prepared by a facile strategy, which involved a simple heat treatment of the mixture of selenium powder, sulfur powder, and HC. As shown in Figure 91c,  $\text{SeS}_x$  was well encapsulated into the HC spheres after thermal infusion, and the structure of HC was still well maintained. Figure 91d shows the XRD patterns of  $\text{SeS}_x$ -HC composites with different amounts of selenium doping ranging from 0% to 20%. They all exhibited strong diffraction peaks, which arises from  $\text{SeS}_x$ . The loading of  $\text{SeS}_x$  in the  $\text{SeS}_x$ -HC composites was very high, which was controlled at 80 wt%, as confirmed by TGA. XPS was further conducted to understand the interaction between selenium and sulfur in the composite. As shown in Figure 91f, the spectrum of S 2p and Se 3p confirmed strong interaction between selenium and sulfur, reflecting that selenium and sulfur are bonded simultaneously in the chain-like Se-S molecules, rather than remaining as individual selenium and sulfur.

The effect of selenium doping on sulfur utilization and cycling stability of sulfur cathode was investigated in the fluorinated ether electrolytes. Figure 91g shows cycling performance of  $\text{SeS}_x$  cathode with different selenium doping and a  $\text{SeS}_x$  loading of  $2.5 \text{ mg cm}^{-2}$ . As shown clearly, selenium doping can significantly increase reversible capacity of  $\text{SeS}_x$  cathode, which is due to enhanced electronic conductivity by selenium doping. With a 10 wt% selenium doping, the composite can have a reversible capacity of  $\sim 1000 \text{ mAh g}^{-1}$  with stable cycle life, while pure S-HC composite can only deliver a capacity of  $\sim 400 \text{ mAh g}^{-1}$ . With further increase in the content of selenium to 20 wt%, reversible capacity dropped to  $\sim 700 \text{ mAh g}^{-1}$ , indicating that the optimal amount of selenium doping is 10 wt%. In addition to the effect of selenium doping, the team also investigated the effect of fluorinated ether electrolytes. When compared with conventional DOL/DME based electrolytes, it is clearly seen that 10% Se-doped  $\text{SeS}_x$ -HC cathode demonstrates much better cycle stability and CE in the fluorinated ether electrolytes than DOL/DME based electrolytes. As shown in Figure 91h, the  $\text{SeS}_x$ -HC composite can maintain a capacity of  $\sim 900 \text{ mAh g}^{-1}$  with CE of  $\sim 100\%$  with 100 cycles, indicating the shuttle effect has been significantly suppressed.

Overall, by integration of new carbon host, selenium doping, and fluorinated ether electrolytes, the team can achieve high reversible capacity, stable cycle performance, and high CE in Li-S batteries.

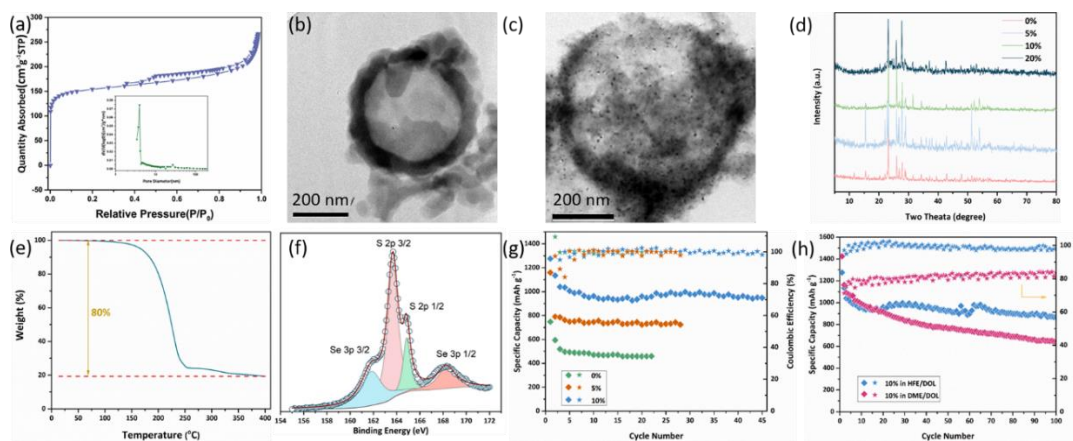


**Figure 91.** (a) Brunauer–Emmett–Teller result. (b) Transmission electron microscopy (TEM) image of new carbon host for  $\text{SeS}_x$  cathode. (c) Representative TEM image. (d) X-ray diffraction patterns. (e) Thermogravimetric analysis curve. (f) S 2p X-ray photoelectron spectroscopy result of  $\text{SeS}_x$ -C composite. (g) Cycling performance of  $\text{SeS}_x$ -C composites of  $\text{SeS}_x$  with different selenium doping. (h) Cycling performance of  $\text{SeS}_x$ -C with 10 wt% selenium doping in HFE and DME electrolytes, respectively, at  $200 \text{ mA g}^{-1}$  with  $2.5 \text{ mg cm}^{-2}$  sulfur loading.

## Patents/Publications/Presentations

The project has no patents, publications, or presentations to report this quarter.

## Task 5.2 – Development of High-Energy Lithium-Sulfur Batteries (Dongping Lu and Jun Liu, Pacific Northwest National Laboratory)

**Project Objective.** The project objective is to develop high-energy, low-cost Li-S batteries with long lifespan. All proposed work will employ thick sulfur cathode ( $\geq 2$  mAh/cm<sup>2</sup> of sulfur) at a relevant scale for practical applications. The diffusion process of soluble polysulfide out of thick cathode will be revisited to investigate cell failure mechanism at different cycling. The fundamental reaction mechanism of polysulfide under the electrical field will be explored by applying advanced characterization techniques to accelerate development of Li-S battery technology.

**Project Impact.** The theoretical specific energy of Li-S batteries is  $\sim 2300$  Wh/kg, which is almost three times higher than that of state-of-the-art Li-ion batteries. The proposed work will design novel approaches to enable Li-S battery technology and accelerate market acceptance of long-range EVs required by the EV Everywhere Grand Challenge.

**Approach.** The project proposes to (1) identify and address key issues of applying high-energy sulfur cathodes including materials, binders, electrode architectures, and functional electrode additives, (2) advance mechanism study of sulfur cathode and electrolyte by using *in situ/ex situ* techniques and custom-designed hybrid cell setup, and (3) verify effectiveness of the new approaches with coin/pouch cells by using high-loading electrodes ( $> 4$  mg/cm<sup>2</sup>), limited lithium ( $< 200\%$  lithium excess), and lean electrolyte ( $E/S < 4$   $\mu$ L/mg).

**Out-Year Goals.** This project has the following out-year goals:

- Fabricate Li-S pouch cells with thick electrodes to understand sulfur chemistry/electrochemistry in environments similar to real application.
- Leverage the Li-metal protection project funded by the DOE and PNNL advanced characterization facilities to accelerate development of Li-S battery technology.
- Develop Li-S batteries with a specific energy of 400 Wh/kg at cell level, 1000 deep-discharge cycles, improved abuse tolerance, and less than 20% capacity fade over a 10-year period to accelerate commercialization of EVs.

**Collaborations.** This project engages in collaboration with the following: Dr. X-Q. Yang (BNL), Dr. D. Qu (University of Wisconsin at Madison), Dr. G. Zhang (University of Alabama), and Dr. J. Tao (PNNL).

### Milestones

1. Synthesis of IKB with controlled secondary particles from 5 to 100  $\mu$ m for high-loading sulfur electrodes ( $> 4$  mg S/cm<sup>2</sup>). (Q1, FY 2020; Completed)
2. Realize sulfur utilization rate  $> 1200$  mAh/g in dense sulfur electrodes ( $S > 4$  mg/cm<sup>2</sup>, porosity  $\leq 50\%$ ) at an  $E/S \leq 4$   $\mu$ L/mg through electrode architecture control. (Q2, FY 2020; In progress)
3. Demonstrate  $> 80$  cycles (80% capacity retention) in dense sulfur electrodes at  $E/S \leq 4$   $\mu$ L/mg through the hybrid electrode design. (Q3, FY 2020; In progress)
4. Complete evaluation of high-loading sulfur electrodes at  $E/S \leq 3$   $\mu$ L/mg and transfer sufficient materials to Battery500 for high-energy pouch cell demonstration. (Q4, FY 2020; In progress)

## Progress Report

Li-S pouch cells with practical energies  $> 300$  Wh/kg have been successfully demonstrated with the use of PNNL developed IKB/S cathode materials, although cell cycle life needs improvement. The degradation mechanism study reveals that the failure of Li-S pouch cell is mainly due to reaction heterogeneity of a high-loading electrode under lean electrolyte conditions. The slow electrolyte diffusion/redistribution through the high-tortuosity electrode nanochannels is the root reason for cathode reaction heterogeneity, which causes gradual electrode failure propagating from the center of the electrode to the edge, ultimately leading to failure of cells. To address the electrolyte diffusion problems associated with high-loading electrodes, electrode architecture should be optimized to achieve low tortuosity at a low porosity.

The active material holds the biggest volume/mass proportion in electrode; thus, its morphology plays a key role on electrode tortuosity for a given electrode porosity. This quarter, the team synthesized IKB secondary particles with size ranging from 5 to  $\approx 100$   $\mu\text{m}$  and used them to study correlation of particle size with electrode microstructure and electrochemical properties. The particle size control was realized through control of stoichiometry of precursors and the synthesis conditions. Figure 92a-b shows SEM images of the IKB particles with typical size of  $< 20$   $\mu\text{m}$  and  $> 70$   $\mu\text{m}$ , respectively. Typical morphologies of integrated secondary particles with irregular shapes were observed. The 70- $\mu\text{m}$  powder has a tap density two-fold higher than that of the 20- $\mu\text{m}$  one, which is beneficial for improvement of electrode energy density. Before loading sulfur, the measured BET surfaces are  $1001$   $\text{m}^2/\text{g}$  and  $1155$   $\text{m}^2/\text{g}$  for 20- $\mu\text{m}$  and 70- $\mu\text{m}$  IKB powders, respectively (Figure 92c). This means that integration of particles does not cause significant reduction in electrode surface area, which ensures sufficient contact of sulfur with conductive carbon. After sulfur loading, corresponding surfaces of IKB/S were reduced to 24 and  $15$   $\text{m}^2/\text{g}$ , respectively. High-loading sulfur electrodes ( $> 4$   $\text{mg}/\text{cm}^2$ ) were prepared with these two types of materials and calendered into 60- $\mu\text{m}$  thick electrodes. The estimated electrode porosity is 44.7%, which is among the lowest porosities in a sulfur cathode reported in the literature. The purpose of reducing electrode porosity is to study the effects of particle size on electrode tortuosity and sulfur reaction kinetics. Additional benefits of using a low-porosity electrode are not only to improve cell volumetric energy density, but to also conserve more electrolyte to support cell cycling, rather than filling the electrode pores. The dense electrode was tested under lean electrolyte conditions of  $E/S = 4$   $\mu\text{L}/\text{mg}$ . A significant difference was observed for the cathodes with different IKB/S particles. The electrode using  $> 70$ - $\mu\text{m}$  particle size shows much better performance compared to the  $< 20$ - $\mu\text{m}$  particle size in terms of electrochemical polarization, reversible capacity, and cycling performance (Figure 92e-f), which indicates crucial effects of particle size on cell reaction at realistic low-porosity electrode and lean electrolyte conditions. Further experimental study and theoretical simulation of the sulfur reaction processes using different-sized cathode particles are in progress.

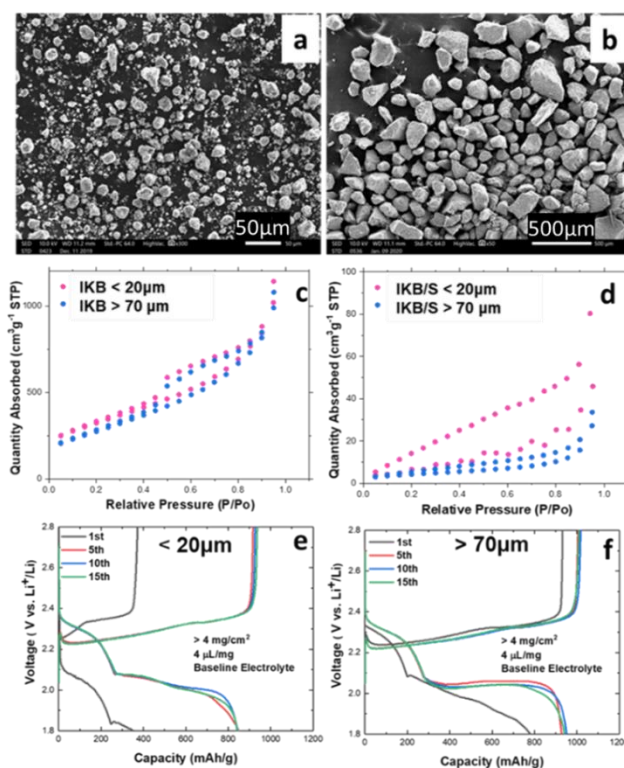


**Figure 92.** Scanning electron microscopy images of integrated Ketjen Black (IKB) particles with different particle sizes: (a)  $< 20$   $\mu\text{m}$  and (b)  $> 70$   $\mu\text{m}$ . Brunauer–Emmett–Teller absorption isotherms of (c) IKB and (d) IKB/S particles with different particle sizes. Electrochemical properties of sulfur cathode using IKB particles with size (e)  $< 20$   $\mu\text{m}$ , and (f)  $> 70$   $\mu\text{m}$ . Sulfur electrode loading  $> 4$   $\text{mg}/\text{cm}^2$ ,  $E/S = 4$   $\mu\text{L}/\text{mg}$ ,  $I = 0.1\text{C}$ , and electrolyte:  $1$   $\text{M}$   $\text{LiTFSI}/\text{DOL}/\text{DME} + 0.3$   $\text{M}$   $\text{LiNO}_3$ .

## Patents/Publications/Presentations

The project has no patents, publications, or presentations to report this quarter.

## Task 5.3 – Nanostructured Design of Sulfur Cathodes for High-Energy Lithium-Sulfur Batteries (Yi Cui, Stanford University)

**Project Objective.** The charge capacity limitations of conventional TM oxide cathodes are overcome by designing optimized nano-architected sulfur cathodes. This study aims to enable sulfur cathodes with high capacity and long cycle life by developing sulfur cathodes from the perspective of nanostructured materials design, which will be used to combine with Li-metal anodes to generate high-energy Li-S batteries. Novel sulfur nanostructures as well as multi-functional coatings will be designed and fabricated to overcome issues related to volume expansion, polysulfide dissolution, and the insulating nature of sulfur.

**Project Impact.** The capacity and cycling stability of sulfur cathode will be dramatically increased. This project's success will make Li-S batteries to power EVs and decrease the high cost of batteries.

**Approach.** The approach involves three main parts:

- Advanced nanostructured sulfur cathodes design and synthesis, including (1) engineer empty space into sulfur cathode to solve problem of electrode volume expansion, (2) develop novel sulfur nanostructures with multi-functional coatings for confinement of S/Li polysulfides to address issues of active materials loss and low conductivity, (3) develop/discover optimal nanostructured materials that can capture the polysulfide dissolved in the electrolyte, (4) develop space-efficiently-packed nanostructured sulfur cathode to increase volumetric energy density and rate capability, and (5) identify interaction mechanism between sulfur species and different types of oxides/sulfides, and find optimal material to improve capacity and cycling of sulfur cathode.
- Structure and property characterization, including *ex situ* SEM, XPS analysis, and *in operando* XRD and optical microscopy.
- Electrochemical testing including coin cells and pouch cells as well as a set of electrochemical techniques.

**Out-Year Goals.** The cycle life, capacity retention, and capacity loading of sulfur cathodes will be greatly improved (200 cycles with 80% capacity retention, > 0.3 mAh/cm<sup>2</sup> capacity loading) by optimizing material design, synthesis, and electrode assembly.

**Collaborations.** This project collaborates with the following: BMR PIs; SLAC: Dr. M. Toney (*In situ* X-ray); and Stanford: Prof. Nix (mechanics) and Prof. Bao (materials).

### Milestones

1. Understanding the mechanism of liquid sulfur on the surface of 3D materials. (Q1 FY 2020; Completed)
2. Demonstrate improvement by utilizing liquid sulfur in Li-S batteries. (Q2, FY2020; In progress)
3. Develop high sulfur loading cathode based on understanding of liquid sulfur. (Q3, FY 2020)
4. Enable Li-S batteries with high sulfur loading, low E/S ratio, and fast kinetics. (Q4, FY 2020)

## Progress Report

Last quarter, the team systematically investigated morphology changes of the sulfur species on different substrates during charging and discharging. This quarter, the team reports on developing a facile *in situ* encapsulation strategy to fabricate TMDs coated lithium sulfide ( $\text{Li}_2\text{S@TMDs}$ ) cathodes for high-energy all-solid-state Li-S battery (Figure 93a).

TMDs were intimately coated on the  $\text{Li}_2\text{S}$  surface by *in situ* and direct reaction of  $\text{Li}_2\text{S}$ . The typical particle size of as-prepared  $\text{Li}_2\text{S@TMDs}$  was 1-5  $\mu\text{m}$ , with an average size of 2  $\mu\text{m}$ . The team then prepared  $\text{Li}_2\text{S@TMDs}$  cathodes by coating the as-prepared slurry onto aluminum foils. Bare  $\text{Li}_2\text{S}$  cathodes were also made in the same way for comparison. Coin cells were fabricated by combination of  $\text{Li}_2\text{S@TMDs}$  cathode, polymer-polymer composite solid-state electrolyte, and Li-metal anode. Figure 93b shows the cross-sectional SEM image of the whole cell. The zoomed-in image shows the intimate contact between both electrodes and electrolyte (Figure 93c). Finally, the team carried out the galvanostatic charge-discharge process to evaluate preliminary electrochemical performance of as-prepared cathodes for all-solid-state Li-S battery. As shown in Figure 93d, a discharge capacity as high as  $\sim 860 \text{ mAh g}^{-1} \text{ Li}_2\text{S}$  at 0.1 C ( $1 \text{ C} = 1,166 \text{ mA g}^{-1} \text{ Li}_2\text{S}$ ) was realized by coating  $\text{Li}_2\text{S}$  with TMDs, which is more than twice as high as that of the bare one.

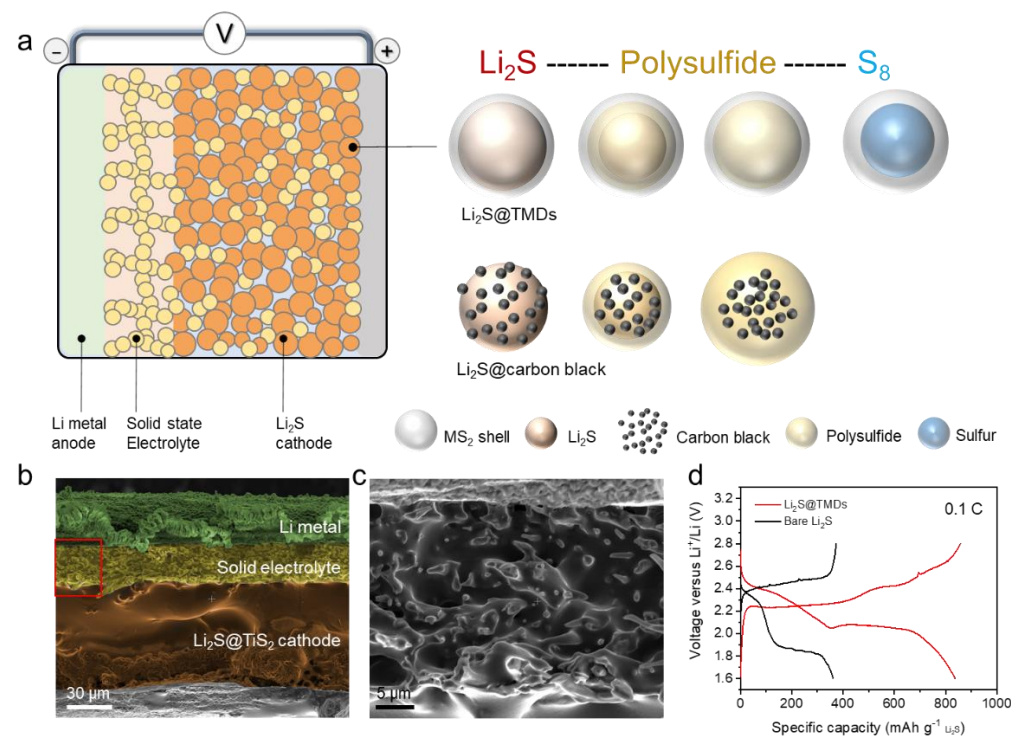


**Figure 93. Design of high-performance all-solid-state Li-S battery. (a) Schematic diagram of battery architecture and cycling reaction for the solid-state Li-S battery with Li-metal anode, polymer solid electrolyte, and  $\text{Li}_2\text{S}$  composite cathode. (b) Cross-sectional scanning electron microscopy images of as-prepared solid-state  $\text{Li}_2\text{S}$ -Li cell. (c) Zoomed-in image of polymer-polymer composite electrolyte and cathode/electrolyte interface. (d) Charge-discharge voltage profiles of  $\text{Li}_2\text{S@TMDs}$  and bare  $\text{Li}_2\text{S}$  cathodes at 0.1 C ( $1 \text{ C} = 1,166 \text{ mA g}^{-1} \text{ Li}_2\text{S}$ ).**

## Patents/Publications/Presentations

The project has no patents, publications, or presentations to report this quarter.

## Task 5.4 – Investigation of Sulfur Reaction Mechanisms (Enyuan Hu, Brookhaven National Laboratory; Deyang Qu, University of Wisconsin at Milwaukee)

**Project Objective.** The primary objectives are as follows:

- To continue conducting focused fundamental research on the mechanism of “shuttle effect” inhibition for rechargeable Li-S batteries.
- To continue developing the polymeric sulfur electrode, adequate anode, and corresponding electrolyte to achieve high-energy-density, long-cycle Li-S batteries.
- To carry out spatially resolved XRF image and S-K edge XAS [including X-ray absorption near edge structure (XANES) and X-ray absorption fine structure (XAFS)] studies of polymeric sulfur compounds.
- To investigate the alternative anode materials so they will not react with dissolved polysulfide ions.
- To continue developing and optimizing creative electrode-making processes to improve processability and aerial capacity, for example, dry process and thick electrode.

**Project Impact.** Further understanding of the mechanisms of all reactions in a Li-S cell will lead to mitigation of the “shuttle effect.” The project results will thus guide development of sulfur cathode and Li-S designs with significant increase of energy density and of cycle life and with reduction of cost. This will greatly accelerate deployment of EVs and reduce carbon emission associated with fossil fuel consumption.

**Approach.** This project will use not only *in situ* electrochemical high-performance liquid chromatography (HPLC)/MS, XPS and TXM, but also synchrotron-based *in situ* X-ray diagnostic tools such as XRD and XAS to study sulfur electrodes. The team will continue to develop thicker sulfur electrode with high areal capacity using dry process.

**One-Year Goals.** The major goal this fiscal year is to extend successful investigation of dissolved polysulfides to the polysulfides in the solid phase. This includes the following actions: (1) synthesize cross-linked polymerized sulfur compounds, (2) explore additives that can rapidly catalyze polysulfide radicals, (3) continue exploring alternative anode materials, and (4) develop *in situ* synchrotronic method to investigate sulfur and polysulfide in the solid phase.

**Collaborations.** The PI works closely with beamline scientists at synchrotron facilities to develop novel Li-S characterization tools. The PI and co-PI collaborate closely with top scientists at ANL, LBNL, and PNNL, as well as U. S. industrial collaborators at GM, Duracell, Clarios, etc. The PI and co-PI also collaborate with scientists in China, Japan, and South Korea. These collaborations will be strengthened and expanded to give this project a vision on both today’s state-of-the-art technology and tomorrow’s technology in development, with feedback from the material designer and synthesizers upstream and from industrial end users downstream.

### Milestones

1. Test the newly synthesized polymeric sulfur compounds. Conduct spatially resolved XRF image and S-K edge XAS (including XANES and XAFS) studies of polymeric sulfur compounds. (Q1, FY 2020; Completed)
2. Survey alternative anode materials and determine their interaction with dissolved polysulfide ions. Continue synthesis and testing of polymeric sulfur compounds, and optimize electrode-making processes. (Q2, FY 2020; In progress)

- Investigate radical disproportionation catalyst, and test alternative electrolytes in which the solubility of polysulfide ions is lower than ether-based electrolyte. (Q3, FY 2020; In progress)
- Complete initial design of the full cell consisting of polymeric sulfur compounds, alternative anode, and adequate additive in either coin-cell or pouch-cell format. (Q4, FY 2020; In progress)

## Progress Report

This quarter, the first milestone for the fiscal year was completed. Progress on other milestones is being made. BNL and the University of Wisconsin teams have been working together to synthesize new polymer compounds and study the polymeric sulfur compounds with XAS and XRF imaging.

**XAS and XRF of Pristine Material.** The XAS spectrum of the pristine polymeric sulfur is shown in Figure 94a. XAS corresponds to excitation of core 1s electron to the unoccupied electronic states, or in a close approximation, molecular orbitals. Unoccupied molecular orbitals corresponding to S-C interaction are labeled in Figure 94. In particular,  $\pi$  orbital, which has weaker interaction than  $\sigma$  orbital, has lower energy and corresponds to the first peak in sulfur XAS. These results indicate that sulfur is indeed bonded to carbon, which is characteristic of polymeric sulfur materials. Figure 94b shows the pristine electrode XRF images collected at selected energies. The photon flux at these energies corresponds to the concentration of polymeric sulfur species, and the intensity scale bar is shown on the right. It indicates that in general, sulfur is uniformly distributed on the electrode, with some higher sulfur concentration near the corner. Such spatial distribution may evolve as the material is cycled, and this will be studied further. The spatial resolution is  $\sim 5 \mu\text{m}$ .

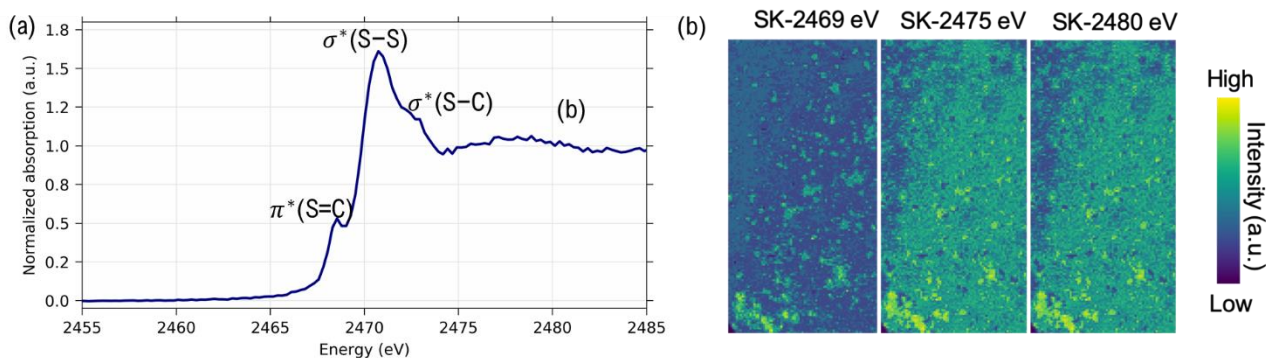


**Figure 94.** (a) X-ray absorption spectroscopy of pristine polymeric sulfur. Major peaks corresponding to characteristic unoccupied molecular orbitals are labeled. (b) X-ray fluorescence of pristine polymeric sulfur collected at energies of 2469 eV, 2475 eV, and 2480 eV.

**Synthesis and Testing of Polymeric Sulfur Materials.** Polymeric sulfur materials have been synthesized in the project's lab, and commercially available samples were also purchased from various vendors. Figure 95 shows an example of the performance of a polymeric sulfur electrode. The two-stage discharge curve becomes a one-stage flat curve, which could result from the mechanism change. The result is consistent with that reported previously.

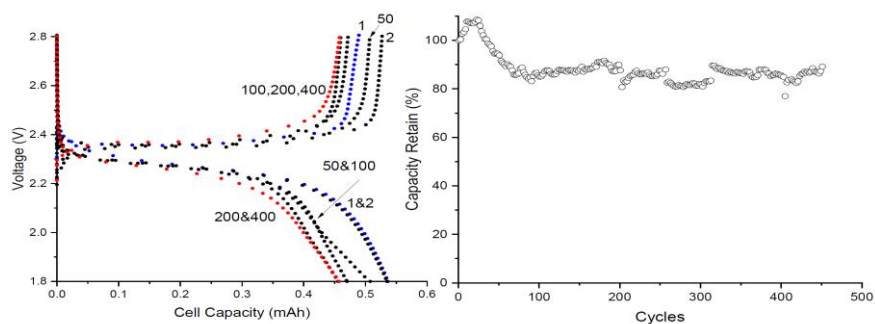


Figure 95. The charge and discharge curves of a polymeric sulfur cathode (left); cycle life (right).

### Patents/Publications/Presentations

The project has no patents, publications, or presentations to report this quarter.

## Task 5.5 – New Electrolytes for Lithium-Sulfur Battery (Gao Liu, Lawrence Berkeley National Laboratory)

**Project Objective.** The project objective is to develop new electrolytes, additives, and electrode compositions for Li-S battery with high ion-conductivity, stable toward polysulfide and promoting the polysulfide affiliation with the electrode substrate to prevent polysulfide dissolution.

**Project Impact.** This work will address the high cost and low energy density of the Li-ion rechargeable batteries. The emerging Li-S batteries could feature both high energy density and low cost. This project enables the applications of the low-cost, abundant sulfur element as a major chemical component for electrical energy storage. This project will develop new approaches for electrolytes and electrode compositions of Li-S rechargeable batteries.

**Approach.** This project aims to develop new electrolytes and additives for Li-S battery. The properties of the ideal electrolyte for sulfur electrode would be high ion conductivity, stable towards polysulfide, and promoting the polysulfide affiliation with the electrode substrate to prevent polysulfide dissolution. The project is designed to first understand the electrode substrate interaction with the polysulfides in different electrolytes. This will lead to better understandings of the polysulfide nucleation and precipitation mechanisms in common electrolytes. The second stage of the project will focus on chemically modifying the structures of the solvent and salt electrolyte molecules to increase electrolyte stability and ionic conductivity and to prevent polysulfide dissolution and promote polysulfides precipitation.

**Out-Year Goals.** The team will also investigate the contribution of Li-metal electrodes to overall Li-S battery performance and will develop methods to stabilize Li-metal surface.

**Collaborations.** This project collaborates with Dr. J. Guo and Dr. W. Yang (ALS/LBNL), Prof. A. Minor (National Center for Electron Microscopy at LBNL/UC Berkeley), Dr. L-W. Wang (LBNL), and Prof. P. B. Balbuena, TAMU.

### Milestones

1. Use the synchrotron analyses in studying new electrolytes. (Q1, FY 2020; Completed)
2. Measure and optimize compositions of the new electrolyte for conductivities, Li-ion transference numbers, and amount of polysulfide dissolution. (Q2, FY 2020)
3. Study cycling properties of lithium metal under new electrolytes. (Q3, FY 2020)
4. Select two electrolyte compositions to test in Li-S battery. (Q4, FY 2020)

## Progress Report

A series of amphiphilic electrolyte additives was synthesized and purified. Two sample structures are shown in Figure 96a. Like surfactant molecules, these synthesized additives have dual functionalities; fluorocarbon moiety is at one end of the structure, while the polar ethyleneoxide moiety is at the other. The additives significantly improve the Li-ion salt solubility in the fluorocarbon solvents (for example, TTE). In addition, the amphiphilic properties of the additives enable formation of additive molecules and Li-salt micelles in the fluorocarbon solvent, in turn facilitating solubility of the lithium salts (for example, LiTFSI) in the fluorocarbon solvent.

The TTE-based electrolytes with differing salts and amphiphilic additives were characterized by SAXS to validate and measure formation of micelles. SAXS is based on the Rayleigh scattering of X-ray. By probing the difference response in electron density, micelle size information of samples with electron contrast is revealed. The measurement was performed through ALS beamline 7.3.3 at LBNL. Three lithium salts for Li-S battery (LiFSI, LiTFSI, LiBETI) and two amphiphilic additives denoted as  $F_8EO_2$  and  $F_8EO_4$ , respectively, were used. Owing to the air-sensitive nature of the lithium salts, electrolyte samples were prepared and completely sealed in quartz capillary tubes in an Ar-filled glove box. Results for all samples were calibrated by subtracting the background of pure TTE solvent. Figure 96b summarizes results for micelle sizes as a function of lithium salts and additives. It is clearly demonstrated that micelle formation is observed in all samples with additives in the TTE solvent. From molecular- to nano-scale, these are heterogenous liquid electrolytes. Without addition of the additives, the lithium salts have infinitesimal solubility in the TTE solvent. Additives bring the lithium salts into the TTE solution. Lithium salt structure also plays an important role in micelle size. LiFSI, although it has the smallest-sized anion in the series, forms large-sized micelles. In contrast, LiTFSI and additives tend to form much smaller micelles. This quarter, the team successfully demonstrated formation of micelles based on amphiphilic additives in fluorocarbon solvent.

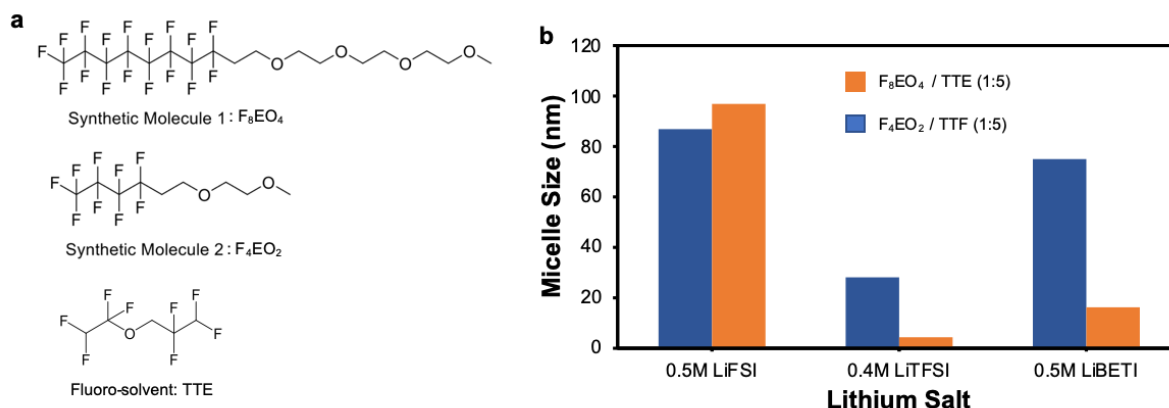


Figure 96. (a) The molecular structures of the amphiphilic additives and fluorocarbon solvent. (b) Micelle size characterized by small angle X-ray scattering as a function of lithium salts and additives.

## Patents/Publications/Presentations

### Patent

- Liu, G. Novel Electrolyte Additives for Lithium-Sulfur Rechargeable Battery. U. S. Provisional Patent 62929678, LBNL Doc# 2019-169, 2019.

## TASK 6 – AIR ELECTRODES / ELECTROLYTES

### Summary and Highlights

High-density energy storage systems are critical for EVs required by the EV Everywhere Grand Challenge. Conventional Li-ion batteries still cannot fully satisfy the ever-increasing needs because of their limited energy density, high cost, and safety concerns. As an alternative, the rechargeable lithium-oxygen (Li-O<sub>2</sub>) battery has potential to be used for long-range EVs. The practical energy density of a Li-O<sub>2</sub> battery is expected to be ~ 800 Wh kg<sup>-1</sup>. The advantages of Li-O<sub>2</sub> batteries come from their open structure; that is, they can absorb the active cathode material (oxygen) from the surrounding environment instead of carrying it within the batteries. However, the open structure of Li-O<sub>2</sub> batteries also leads to several disadvantages. The energy density of Li-O<sub>2</sub> batteries will be much lower if oxygen must be provided by an onboard container. Although significant progress has been made in recent years on fundamental properties of Li-O<sub>2</sub> batteries, research in this field is still in an early stage, with many barriers to be overcome before practical applications. These barriers include:

- Instability of electrolytes—The superoxide species generated during discharge or O<sub>2</sub> reduction process is highly reactive with electrolyte and other components in the battery. Electrolyte decomposition during charge or O<sub>2</sub> evolution process is also significant due to high over-potentials.
- Instability of air electrode (dominated by carbonaceous materials) and other battery components (such as separators and binders) during charge/discharge processes in an O-rich environment.
- Corrosion of Li-metal anode in an electrolyte saturated with oxygen.
- Low energy efficiency associated with large over-potential and poor cyclability of Li-O<sub>2</sub> batteries.
- Low power rate capability due to electrode blocking by the reaction products.
- Absence of a low-cost, high-efficiency oxygen supply system (such as oxygen selective membrane).

The main goal of this Task is to provide a better understanding on the fundamental reaction mechanisms of Li-O<sub>2</sub> batteries and identify the required components (especially electrolytes and electrodes) for stable operation of Li-O<sub>2</sub> batteries. This task will investigate several new approaches to improve stability of Li-metal anode in Li-O<sub>2</sub> batteries:

- Li-metal anodes will be protected using two approaches: (1) *in situ* formation of a stable SEI layer before Li-O<sub>2</sub> cell operation through various electrolyte formulations and treatment protocols, and (2) *ex situ* formation of stable inorganic/polymeric hybrid electrolyte layers through dip-coating or tape-casting method to coat the inorganic/polymeric hybrid electrolyte layer on Li-metal surface.
- A joint theoretical/experimental approach for design and discovery of new cathode and electrolyte materials will act synergistically to reduce charge overpotentials and increase cycle life. Synthesis methods, in combination with design principles developed from computations, will be used to make new cathode architectures. Computational studies will be used to help understand decomposition mechanisms of electrolytes and how to design electrolytes with improved stability.
- A new cathode will be developed based on high-efficiency catalyst such as two-dimensional TMDs. These cathode materials will be combined with new electrolyte blends and additives that work in synergy to reduce charge potentials and increase stability of the Li-air system.

State-of-the-art characterization techniques and computational methodologies will be used to understand charge and discharge chemistries. Success of this Task will establish a solid foundation for further development of Li-O<sub>2</sub> batteries toward practical applications for long-range EVs. The fundamental understanding and breakthrough in Li-O<sub>2</sub> batteries may also provide insight on improving performance of Li-S batteries and other energy storage systems based on chemical conversion process.

**Highlights.** The Task highlights for this quarter are as follows:

- The ANL group found a Li-O<sub>2</sub> battery that has LiOH as the predominant discharge product and enabled it by adding sodium-ions. Moreover, this strategy showed a remarkable reduction in the charging potential start from 3.3 V, in contrast to previous studies that have to use redox mediators to reduce the charging potential.
- The PNNL group developed a localized high-concentration electrolyte using 1H,1H,5H-Octafluoropentyl 1,1,2,2-tetrafluoroethyl ether (OTE) as a diluent. This electrolyte exhibits much improved electrochemical performances and higher oxygen solubility than other electrolytes. Therefore, it can largely improve the cycle life of Li-O<sub>2</sub> and Li-air batteries operating in ambient conditions.
- The ANL/UIC team compared four salts (LiNO<sub>3</sub>, LiTFSI, LiFSI, LiClO<sub>4</sub>) that can work with a LiI redox mediator in a Li-O<sub>2</sub> electrolyte to reduce the charge potential and provide lithium anode protection to extend cycle life. The best performing salt is LiNO<sub>3</sub>, and computational studies indicate that there is a surprising segregation of the ions and neutral solvent molecules in the electrolyte that may contribute to improved transport in the electrolyte.

## Task 6.1 – Rechargeable Lithium-Air Batteries (Ji-Guang Zhang and Wu Xu, Pacific Northwest National Laboratory)

**Project Objective.** The objective of this project is to develop rechargeable lithium-oxygen (Li-O<sub>2</sub>) batteries with long-term cycling stability through in-depth research on more stable electrolytes and highly efficient catalysts for air electrodes, protection of Li-metal anodes, and deeper understanding on the ORR/OER mechanisms behind the electrochemical performance of Li-O<sub>2</sub> cells. In FY 2020, the team will further investigate the stability of electrodes and electrolytes to build more stable Li-O<sub>2</sub> batteries with long-term cycling capability.

**Project Impact.** The objective of this project is to develop rechargeable Li-O<sub>2</sub> batteries with long-term cycling stability through in-depth research on more stable electrolytes and highly efficient catalysts for air electrodes, protection of Li-metal anodes, and deeper understanding on the oxygen reduction reaction / oxygen evolution reaction (ORR/OER) mechanisms behind the electrochemical performance of Li-O<sub>2</sub> cells. This fiscal year, the team will further investigate stability of electrodes and electrolytes to build more stable Li-O<sub>2</sub> batteries with long-term cycling capability.

**Approach.** Develop highly stable electrolytes, including LHCE and optimize their compositions to prevent the irreversible parasitic reactions at the electrodes (cathode and anode). The electrochemical test of Li||Li symmetric cell containing above stable electrolyte will be first measured comparatively with typical ether (TEGDME) based electrolyte to evaluate the stability of the electrolyte itself and the SEI layer. Then, the stability of proposed electrolytes at the cathode side with reactive oxygen species during ORR/OER will be further characterized in the Li-O<sub>2</sub> cells. In addition, with comparative measurements for physical properties of electrolytes, the team will find the key parameters of suitable electrolyte in Li-O<sub>2</sub> batteries.

**Out-Year-Goals.** The long-term goal of the proposed work is to enable rechargeable Li-air batteries with a specific energy of 800 Wh/kg at cell level, 1000 deep-discharge cycles, improved abuse tolerance, and less than 20% capacity fade over a 10-year period to accelerate commercialization of long-range EVs.

**Collaborations.** This project collaborates with C. Wang of PNNL on characterization of cycled air electrodes by TEM/SEM, and with Dr. P. Gao of PNNL on computational calculations and simulations.

### Milestones

1. Develop stable electrolyte to minimize parasitic reactions at the electrodes. (Q1, FY 2020; Completed, December 31, 2019)
2. Protect anodes to prevent the lithium dendrite and LiOH formation. (Q2, FY 2020; In progress)
3. Develop stable additives (solid or soluble) or methods for sustainable catalytic effect. (Q3, FY 2020)
4. Complete evaluation of cycling performance of Li-O<sub>2</sub> batteries with optimized cell components and conditions. (Q4, FY 2020)

## Progress Report

Development of stable electrolytes is critical for practical application of Li-O<sub>2</sub> batteries as well as Li-air batteries with long cycle life. This quarter, the team designed LHCE of LiTf in tetraglyme (G4) diluted by OTE, and investigated its properties and battery performances in comparison with 1 M LiTf in G4 electrolyte and HCE (2.8 M LiTf in G4). DFT simulations indicate that the activation energies of these three electrolytes against the singlet oxygen exhibit the following order: LHCE (347.8 KJ mol<sup>-1</sup>) > HCE (293.2 KJ mol<sup>-1</sup>) > 1 M LiTf/G4 (238.0 KJ mol<sup>-1</sup>). In general, higher activation energy means a reaction is more difficult to occur. In other words, LHCE is much more stable against singlet oxygen. This prediction has been verified in the project's experiment.

Li||Li symmetric cell test demonstrates excellent stability of LHCE with lithium metal, significantly superior to HCE and 1 M LiTf/G4. Linear sweep scanning results also show that LHCE has higher oxidation potential than HCE and 1 M LiTf/G4. Therefore, Li-O<sub>2</sub> cells with LHCE and an air electrode composed of carbon paper without a catalyst can be cycled stably for more than 60 cycles under the capacity limited protocol of 1.0 mAh cm<sup>-2</sup> at a current density of 0.2 mA cm<sup>-2</sup>, while similar cells with HCE and the 1 M LiTf/G4 electrolytes can only run for 16 and 36 cycles, respectively, under the same conditions (Figure 97a-c). In addition, Li-metal anode cycled in Li-O<sub>2</sub> cells using LHCE electrolyte can maintain their morphology well, but serious corrosion on Li-metal anode was observed when it was cycled in Li-O<sub>2</sub> cells using HCE and 1 M LiTf/G4 electrolytes.

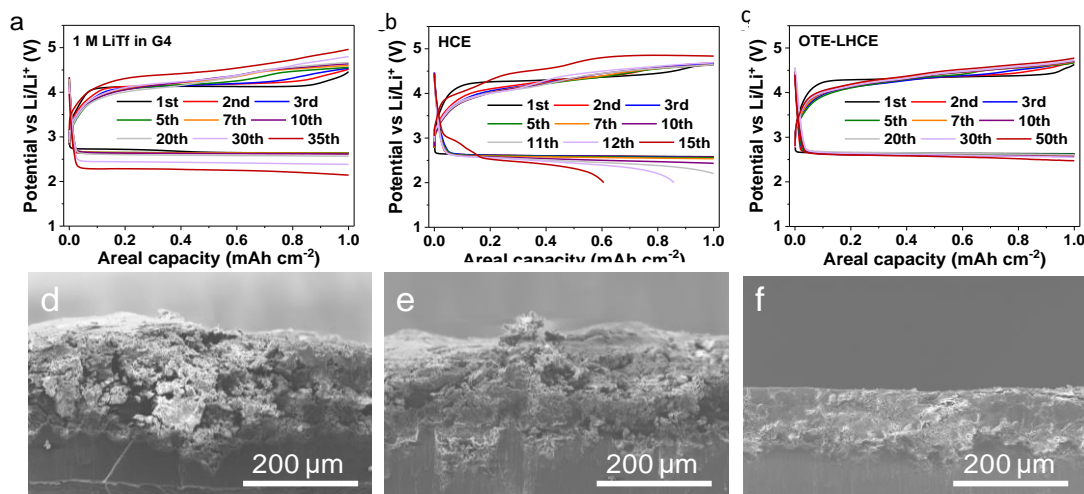


**Figure 97.** (a-c) Voltage profiles of Li-O<sub>2</sub> cells with the three electrolytes at selected cycles at a current density of 0.2 mA cm<sup>-2</sup> under a capacity limited protocol of 1.0 mAh cm<sup>-2</sup>. (d-f) Cross-sectional scanning electron microscopy images of Li-metal anodes from cycled Li-O<sub>2</sub> cells. (a/d) 1 M LiTf in G4. (b/e) HCE. (c/f) LHCE.

Another advantage of LHCE is its oxygen solubility, which is almost twice that in HCE and 1 M LiTf/G4. This advantage enables Li-air batteries with LHCE to have much higher discharge capacity and stable cycling than those using another two electrolytes under the same oxygen partial pressure. Using Zero Air gas (N<sub>2</sub>:O<sub>2</sub> = 79:21, volume ratio) containing less than 3 ppm of moisture, the capacity of Li-air cell using LHCE is about 9 mAh cm<sup>-2</sup>, which is much higher than those using 1 M electrolyte (0.353 mAh cm<sup>-2</sup>) and HCE (0.004 mAh cm<sup>-2</sup>). The Li-air cell using LHCE can be cycled more than 27 times in Zero Air gas under a capacity-limited protocol of 1.0 mAh cm<sup>-2</sup> at 0.2 mA cm<sup>-2</sup>, but the Li-air cells using other two electrolytes can only cycle one time in the same gas. The above results demonstrate that the OTE-based LHCE is a promising electrolyte for rechargeable Li-O<sub>2</sub> and Li-air batteries thanks to its chemical/electrochemical stability, proper physical properties with low viscosity, and effective oxygen utilization due to high oxygen solubility. Further development of novel electrolytes is necessary to stabilize Li-metal anode against reactive oxygen species for more reversible and stable Li-O<sub>2</sub> and Li-air batteries.

## Patents/Publications/Presentations

The project has no patents, publications, or presentations to report this quarter.

## Task 6.2 – Lithium-Air Batteries

(Khalil Amine, Larry A. Curtiss, and Jun Lu; Argonne National Laboratory)

**Project Objective.** This project will develop new cathode materials and electrolytes for Li-air batteries for long cycle life, high capacity, and high efficiency. The goal is to obtain critical insight that will provide information on the charge and discharge processes in Li-air batteries to enable new advances to be made in their performance. This will be done using state-of-the-art characterization techniques combined with state-of-the-art computational methodologies to understand and design new materials and electrolytes for Li-air batteries.

**Project Impact.** The instability of current nonaqueous electrolytes and degradation of cathode materials limits performance of Li-air batteries. The project impact will be to develop new electrolytes and cathode materials that are stable and can increase energy density of electrical energy storage systems based on lithium.

**Approach.** The project is using a joint theoretical/experimental approach for design and discovery of new cathode and electrolyte materials that act synergistically to reduce charge overpotentials and increase cycle life. Synthesis methods, in combination with design principles developed from computations, are used to make new cathode architectures. Computational studies are used to help understand decomposition mechanisms of electrolytes and how to design electrolytes with improved stability. The new cathodes and electrolytes are tested in Li-O<sub>2</sub> cells. Characterization, along with theory, is used to understand the performance of materials used in the cell and to make improved materials.

**Out-Year Goals.** The out-year goals are to find catalysts that promote discharge product morphologies that reduce charge potentials and find electrolytes for long cycle life through testing and design.

**Collaborations.** This project engages in collaboration with Prof. K. C. Lau (UC at Norridge), Prof. Y. Wu (Ohio State University), Dr. D. Zhai (China), and R. Shahbazian-Yassar (UIC).

### Milestones

1. Investigation of effect of salt modification on discharge product and charge overpotentials. (Q1, FY 2020; Completed)
2. Development of electrolyte blends for Li-anode protection for longer cycle life. (Q2, FY 2020)
3. Investigation of new alloys for templating LiO<sub>2</sub> discharge products with low charge potentials. (Q3, FY 2020)
4. Development of novel electrocatalysts for low charge potentials in synergy with new electrolyte blends. (Q4, FY 2020)

## Progress Report

The team is exploring the effect of modification of electrolytes on discharge products in Li-O<sub>2</sub> batteries as a possible way to increase efficiency and cycle life. Specifically, they have been investigating the effect of using mixtures of sodium and lithium salts. They have found that formation of LiOH as the predominant discharge product is enabled by adding sodium ions. Moreover, this strategy showed a remarkable reduction in charging potential. Previous studies of batteries based on a LiOH product have relied on redox mediators such as LiI for decomposing the LiOH; in contrast, this study does not rely on redox mediators.

Using pure carbon paper as the cathode, galvanostatic discharge/charge of a pure Li-ion based electrolyte shows a typical high charging voltage of > 4.0 V (Figure 98a). A SEM image (Figure 98b, red) reveals a toroid-like structure for pure carbon paper, indicative of Li<sub>2</sub>O<sub>2</sub> formation. Employing the same pure carbon paper cathode cell setup, the team finds that a simple addition of Na<sup>+</sup> into the electrolyte results in dramatic changes in the final discharge product morphology and electrochemistry. With an electrolyte composition of 1 M Li<sup>+</sup>/0.1 M Na<sup>+</sup> triflate salts, irregularly shaped solids are found. In 1 M Li<sup>+</sup>/0.5 M Na<sup>+</sup>, spherical solids are produced. XRD (Figure 98c) and Raman studies (Figure 98d) clearly show that LiOH is the dominant discharge product in the Na<sup>+</sup>-containing electrolyte (1 M Li<sup>+</sup>/0.5 M Na<sup>+</sup>). More importantly, the charge overpotential is found to progressively decrease (> 4.0 V → ~ 3.8 V → ~ 3.4 V) as the concentration of Na<sup>+</sup> is increased (0 M → 0.1 M → 0.5 M Na<sup>+</sup>).

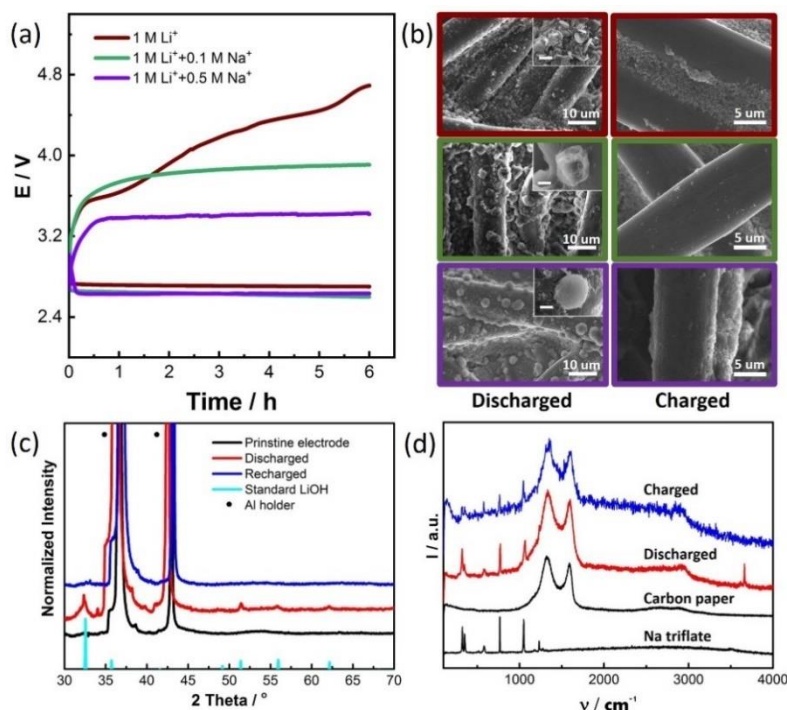


Figure 98. (a) Galvanostatic test of the Li-O<sub>2</sub> batteries with Na<sup>+</sup> additives. The cell consists of a lithium anode, carbon fiber paper cathode, glass fiber separator, and metal triflate salts in TEGDME electrolytes including 1.0 M Li<sup>+</sup> (red), 1.0 M Li<sup>+</sup> + 0.1 M Na<sup>+</sup> (green), and 1.0 M Li<sup>+</sup> + 0.5 M Na<sup>+</sup> (violet). (b) Scanning electron microscopy images of the discharged and charged cathodes based on the three electrolytes. The scale bar in the inset is 1 μm. (c) X-ray diffraction of pristine carbon cathode, discharged cathode, and charged cathode. (d) Raman spectra of triflate salt, pristine carbon cathode, discharged cathode, and charged cathode.

The final discharge product is found to be a porous and fluffy LiOH particle with broad XRD peaks. It is believed that the porous and fluffy nature of the LiOH particles with low crystallinity facilitates the subsequent charge reaction, resulting in the observed low overpotential consistent with thermodynamics for LiOH decomposition. The team believes the Na-ions in the electrolyte facilitate a reaction pathway that results in TEGDME decomposition in the first step and water formation. This is based on computational studies of DME showing that Na<sup>+</sup> cations can promote reaction pathways for interactions of DME with O<sub>2</sub> and O<sub>2</sub><sup>-</sup> and can result in decomposition to formate anion, OH, and OOH. Subsequently, the OH and OOH products can lead to H<sub>2</sub>O formation. The generated water molecules are known to play a critical role in LiOH formation, which will be favored over NaOH formation. This can explain the LiOH being present in the discharge product.

The charge mechanism was studied by differential electrochemical mass spectrometry (DEMS) and found to be primarily a 4-electron process that can be explained by dissolution of the LiOH. This discovery represents an alternative battery system that can charge LiOH at a low voltage. Because these findings are solely based on altering cation composition and do not include redox mediators, this represents an entirely separate instance of LiOH cyclability. By enabling a reversible LiOH cell chemistry, a higher reversible capacity (and subsequent energy density) can be obtained.

### Patents/Publications/Presentations

#### Publication

- Halder, A., A. T. Ngo, X. Luo, H-H. Wang, J. G. Wen, P. Abbasi, M. Asadi, C. Zhang, D. Miller, D. Zhang, J. Lu, P. C. Redfern, K. C. Lau, R. Amine, R. S. Assary, Y. J. Lee, A. Salehi-Khojin, S. Vajda, K. Amine, and L. A. Curtiss. “*In Situ* Formed Ir<sub>3</sub>Li Nanoparticles as Active Cathode Material in Li-Oxygen Batteries.” *Journal of Physical Chemistry A* 123, no. 46 (2019): 10047–10056.

## Task 6.3 – Lithium Oxygen Battery Design and Predictions (Larry A. Curtiss/Anh Ngo, Argonne National Laboratory; Amin Salehi-Khojin, University of Illinois at Chicago)

**Project Objective.** The objective of this work is to develop new materials for Li-O<sub>2</sub> batteries that give longer cycle life and improved efficiencies in an air environment. New electrolyte blends and additives will be investigated that can reduce clogging and at the same time promote the cathode functionality needed to reduce charge overpotentials. New cathode and anode materials will be investigated that can work in conjunction with the electrolytes to improve cycle life in the presence of air components.

**Project Impact.** Li-air batteries are considered as a potential alternative to Li-ion batteries for transportation applications due to their high theoretical specific energy. The major issues with the existing Li-O<sub>2</sub> systems include degradation of the anode electrode, reactions with air components, clogging of the cathode, and electrolyte instability. Thus, this project is using a comprehensive approach to improve cycle life and efficiency through development of new materials for electrodes, anodes, and electrolytes that work in synergy.

**Approach.** The experimental strategy is to use cathode materials based on 2D TMDs that the team has found to be among the best oxygen reduction and evolution catalysts. These cathode materials will be combined with new electrolyte blends and additives that work in synergy to reduce charge potentials and increase stability of the Li-air system. DFT and AIMD simulations are used to gain insight at the electronic structure level of theory of the electrolyte structure and function both in the bulk and at interfaces with the cathode, anode, and discharge product. Classical MD is used to obtain understanding at longer length and time scales of processes occurring in the electrolyte and growth mechanisms of discharge products. The team will also utilize a high-throughput screening strategy based on experiment and theory to develop a large database of properties and outcomes of electrolyte combinations that can be analyzed using machine learning to predict electrolytes and additives that will have the best performance.

**Out-Year Goals.** The out-year goals are to find electrolytes that give high capacities and long cycle life in an air atmosphere using high-throughput screening.

**Collaborations.** This project engages in collaboration with R. Assary and J. G. Wen of ANL, B. Narayanan of University of Louisville, Tao Li of Northern Illinois University, and F. Khalili-Araghi and R. Klie of UIC.

### Milestones

1. Investigate various salt combinations for Li-O<sub>2</sub> electrolytes for both lithium anode protection and low charge potentials for the performance of Li-O<sub>2</sub> batteries with use of computations to provide understanding. (Q1, FY 2020; Completed)
2. Investigate bromine-based redox mediators by experiment and theory for comparison with iodine-based redox mediators with MoS<sub>2</sub> cathode materials. (Q2, FY 2020; Initiated)
3. Develop method for screening of additive and electrolytes by experiment and theory to develop a database of properties and performance data for optimizing Li-O<sub>2</sub> batteries by machine learning. (Q3, FY 2020; Initiated)
4. Investigate electrolytes and cathodes that can greatly increase Li-O<sub>2</sub> coin cell capacities compared to current capacities through optimization of ORRs. (Q4, FY 2020; Initiated)

## Progress Report

Li-O<sub>2</sub> batteries are regarded as an advanced energy storage system that could provide a much higher specific energy than Li-ion batteries for transportation applications due to use of chemical transformations. Thus far, research on the Li-O<sub>2</sub> battery has been largely limited to the short life cycle in a pure oxygen environment (Li-O<sub>2</sub> batteries). In this project, the team is exploring new avenues to develop a Li-O<sub>2</sub> battery that can lower the charge potential for two-dimensional TMD-based cathodes. Last fiscal year, they reported that LiI in combination with LiNO<sub>3</sub> could lower the charge potential and increase cycle life. In this work, they found that the LiI serves as a redox mediator to reduce charge potential and that the LiNO<sub>3</sub> provides lithium anode protection to extend cycle life. In this report, the team presents results on use of different salts in place of LiNO<sub>3</sub> and on some computational studies of the distribution of ions in the electrolyte that provide understanding of the LiI/LiNO<sub>3</sub> results.

The team investigated three salts (that is, LiClO<sub>4</sub>, LiTFSI, and LiTF) for comparison with LiNO<sub>3</sub> in an electrolyte composed of TEGDME and EMIM-BF<sub>4</sub> ionic liquid as well as LiI as the redox mediator. Figure 99 shows the charge-discharge profiles for 1 M LiI – 1 M LiClO<sub>4</sub> and 1 M LiI – 1 M LiNO<sub>3</sub> after 100 cycles using the same electrolyte.

The LiClO<sub>4</sub> discharge profile shows a plateau around 3.3 V in the beginning of discharge, which is not present in the LiNO<sub>3</sub> profile. The other two salts (LiTFSI and LiTF) also show a similar plateau. This has been attributed to reduction of triiodide to iodide during discharge process leading to a decrease in the capacity

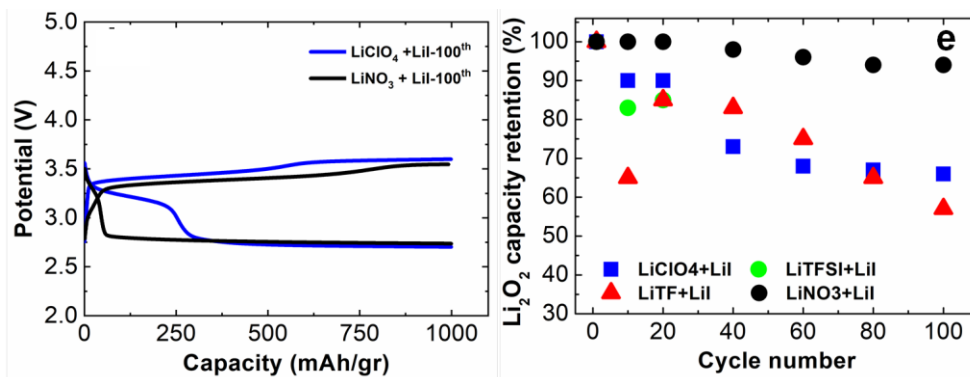


Figure 99. (left) Charge and discharge profiles comparing LiClO<sub>4</sub> and LiNO<sub>3</sub> in the 100<sup>th</sup> cycle. (right) Comparison of battery capacity retention with four salts over 100 cycles.

due to Li<sub>2</sub>O<sub>2</sub> formation. The results in Figure 99 show that the Li<sub>2</sub>O<sub>2</sub> discharge capacity retention after 100 cycles for LiClO<sub>4</sub> is around 65%, whereas when using LiNO<sub>3</sub>, 95% of Li<sub>2</sub>O<sub>2</sub> capacity is retained. The capacity retention as a function of cycle number for the four salts is shown in Figure 99. It shows that LiNO<sub>3</sub> has much better capacity retention than the other three salts.

These results raise the question as to what property of the LiI/LiNO<sub>3</sub> system reduces capacity loss observed during discharge compared to the other salts. One possible explanation is that the other three salts (LiClO<sub>4</sub>, LiTFSI, and LiTF) result in too slow of utilization of the LiI<sub>3</sub> for the chemical decomposition of Li<sub>2</sub>O<sub>2</sub> on charge and, thus, there is unused LiI<sub>3</sub> available during discharge. The team's DFT calculations indicate that the reduction potential of LiI<sub>3</sub> is around 3.3 V, so it could be what is reduced initially during discharge (the first plateau) and therefore account for the lower capacity retention (occurring at 2.7 V) for the three salts (LiClO<sub>4</sub>, LiTFSI, and LiTF) in Figure 99. The efficacy of the LiNO<sub>3</sub> salt system for LiI<sub>3</sub> utilization in contrast to the other three salts may be due to the protection of the lithium anode by the reaction of LiNO<sub>3</sub> with the surface to form a protective coating. An amorphous coating containing 3:1 O:N has been detected on the lithium anode surface. This coating seems able to reduce electrolyte decomposition and side reactions with the iodide species.

The team has conducted classical MD simulations and X-ray studies of the LiNO<sub>3</sub>/LiI system to investigate the nature of the distribution of species in the electrolyte that may have important effect on how the Li-O<sub>2</sub> battery operates. The main result from the classical MD simulations is that there are ionic and neutral domains in the electrolyte. The ionic domain contains largely the salts LiNO<sub>3</sub> and LiI with the EMIM-BF<sub>4</sub> ionic liquid. There

is also a small amount of neutral solvent species (TEGDME) present in the ionic domain. The neutral domains contain largely TEGDME. These surprising results from computation suggesting the formation of different domains in the electrolyte were confirmed by X-ray studies of the electrolyte with variation of salt content. The classical MD simulations indicate the neutral domain will have a significantly higher O<sub>2</sub> concentration and faster O<sub>2</sub> diffusion rates than the ionic domain. The transport properties of O<sub>2</sub> in the IL/TEGDME along with the high oxygen reduction rate of the MoS<sub>2</sub> catalyst in this electrolyte may be factors in the high charge rates (0.5 mA/g) attainable in this system. Another interesting result of the classical MD simulations is that in the presence of an electric field such as would be present in the battery, part of the ionic domain is found concentrated near the surface of the MoS<sub>2</sub>. This concentration near the cathode surface may contribute to the efficacy of the discharge and charge reactions found for the LiI/LiNO<sub>3</sub> system and contribute to the large capacity retention. Further studies of domain formation in this electrolyte, as well as others, are being conducted to understand this important finding in more detail.

### Patents/Publications/Presentations

#### Publication

- Ahmadiparidari, A., S. Fuladi, L. Majidi, S. Plunkett, E. Sarnello, Z. Hemmat, S. Rastegar, S. Misal, P. C. Redfern, J. Wen, T. Li, A. T. Ngo, F. Khalili-Araghi, L. A. Curtiss, and A. Salehi-Kojin. “Lowering Charge Potentials with Negligible Capacity Loss in High Rate Lithium Oxygen Batteries.” Submitted.

## TASK 7 – SODIUM-ION BATTERIES

### Summary

During FY 2019, the BMR added new projects, including several in the area of Na-ion batteries. Four of these projects are continuously funded into FY 2020. Progress on these four projects is described in this report. The Na-ion battery will require investigations to identify optimal electrode materials, electrolytes, separators, and binders to reach full potential. The BMR program will therefore have a limited effort directed toward identifying Na-ion battery materials that have potential value for vehicle applications. More detailed information on this BMR Task will be provided in upcoming reports.

**Highlights.** The highlights for this quarter are as follows:

- The BNL team has been focused on studies of titanium, chromium, and sulfur K-edge XAS for  $\text{NaTi}_{1/3}\text{Cr}_{2/3}\text{S}_2$  cathode material at different SOCs. Their results show that chromium ions do not participate in electrochemical redox reactions, while changes at sulfur K-edge during charge correspond to newly formed localized electronic states on sulfur, that is, the anionic redox process for charge compensation is accompanied with the formation of S-S dimers.
- The ANL team studied the (de)sodiation reaction mechanism of phosphorus anodes using *in situ* high energy x-ray diffraction (HEXRD), 31-P solid-state NMR, and electrochemical methods. The reversibility is tied to a nanostructure stable amorphous state that is amiable to volume changes. A full cell with the phosphorus anode and a P<sub>2</sub>-type Zn-doped Ni-Mn layered cathode shows very good cycling reversibility and life demonstrating 100 cycles with less than 10% capacity loss.
- The LBNL team studied electrochemical properties of a series of lepidocrocite titanates. These materials have sloping voltage profiles with average discharge potentials of about 0.5 V versus  $\text{Na}^+/\text{Na}$  and exhibit excellent reversibility and rate capabilities.
- The PNNL team has optimized the nonflammable phosphate based LHCE with a composition of NaFSI:TEP:TTE (1:1.5:2 in molar ratio), which leads to a high CE of 99.78% for sodium deposition/stripping.

## Task 7.1 – Exploratory Studies of Novel Sodium-Ion Battery Systems (Xiao-Qing Yang and Enyuan Hu, Brookhaven National Laboratory)

**Project Objective.** The objective of this project is to develop new advanced *in situ* material characterization techniques and apply these techniques to explore the potentials, challenges, and feasibility of new rechargeable battery systems beyond the Li-ion batteries, namely, the Na-ion battery systems for EVs, such as PHEV and BEV. To meet the challenges of powering PHEVs and BEVs, new rechargeable battery systems with high energy and power density, low cost, good abuse tolerance, and long calendar and cycle life need to be developed. This project will use the synchrotron-based *in situ* X-ray diagnostic tools, combined with TEM and STEM imaging techniques developed at BNL, to evaluate the new materials and redox couples to obtain fundamental understanding of the reaction mechanisms of these materials aiming for improvement of and guidance for new material and new technology development regarding Na-ion battery systems.

**Project Impact.** In the VTO MYPP, the goals for battery were described: “Specifically, lower-cost, abuse-tolerant batteries with higher energy density, higher power, better low-temperature operation, and longer lifetimes are needed for the development of the next-generation of HEVs, PHEVs, and EVs.” The knowledge learned from diagnostic studies and collaborations with U. S. industries through this project will help U. S. research institutions and industries to develop new materials and processes for a new generation of rechargeable battery systems, namely, Na-ion battery system, in their efforts to reach these VTO goals.

**Approach.** This project will use the synchrotron-based *in situ* X-ray diagnostic tools developed at BNL to evaluate the new materials and redox couples to enable a fundamental understanding of the mechanisms governing performance of these materials and provide guidance for new material and new technology development regarding Na-ion battery systems.

**Out-Year Goals.** Complete the synchrotron-based *ex situ* XRD, PDF, XAS, and XRF studies of novel anion redox-based cathode materials  $\text{NaTi}_{1/3}\text{Cr}_{2/3}\text{S}_2$  and  $\text{NaCrSeS}$  at different SOCs.

**Collaborations.** The BNL team has been closely working with top scientists on new material synthesis at ANL, LBNL, and PNNL and with U. S. industrial collaborators at General Motors and Johnson Controls, as well as with international collaborators.

### Milestones

1. Complete chromium, titanium, and sulfur K-edge XAS (including XANES and EXAFS) studies of  $\text{NaTi}_{1/3}\text{Cr}_{2/3}\text{S}_2$  cathode material at different SOCs. (Q1, FY 2020; Completed)
2. Complete synchrotron-based *ex situ* XRD and PDF analysis of novel anion redox-based cathode material  $\text{NaCrSeS}$  at different SOCs. (Q2, FY 2020; In progress)
3. Complete the chromium and selenium K-edge XAS study and analysis of  $\text{NaCrSeS}$  cathode material at different SOCs. (Q3, FY 2020; In progress)
4. Complete the sulfur K-edge XANES and EXAFS studies of  $\text{NaCrSeS}$  cathode material at different SOCs. (Q4, FY 2020; In progress)

## Progress Report

This quarter, the first milestone for FY 2020 was completed. BNL has been focused on studies of titanium, chromium, and sulfur K-edge XAS for  $\text{NaTi}_{1/3}\text{Cr}_{2/3}\text{S}_2$  cathode material at different SOC. Figure 100a-c shows a set of selected *in situ* XAS spectra for titanium, chromium, and sulfur during the charge and discharge process of  $\text{NaCr}_{2/3}\text{Ti}_{1/3}\text{S}_2/\text{Na}$  battery cycled at C/10. It can be seen that during the whole charge process, the chromium K-edge XAS is hardly changed, indicating that chromium ions do not participate in electrochemical redox reactions. In contrast, the titanium K-edge XAS spectra change in the first stage: the 4977.8 eV peak shifts continuously toward high energy and finally reaches 4978.8 eV. The gradually increasing intensity of pre-edges at 4970 eV indicates the oxidation process from  $\text{Ti}^{3+}$  to  $\text{Ti}^{4+}$  in the first stage of charge, but no further oxidation reaction for titanium in later stages. The most significant spectral variations at different SOC are found in the XAS spectra of sulfur K-edge: during the first stage, the sulfur K-edge spectrum is hardly changed. In the second stage, the pre-edge located at  $\sim 2468$  eV is gradually grown. Such a pre-edge is attributed to the hybridization between the Cr 3d and S 3p orbitals. The growth of a new peak appearing at 2470.7 eV can be clearly seen on the third stage of charging process, which is consistent with the changes previously reported for  $\text{NaCrS}_2$ . It corresponds to newly formed localized electronic states on sulfur, probably stand for S-S  $\sigma^*$ , resulting from the occurrence of  $2\text{S}^{2-}/(\text{S}_2)^{n-}$  ( $n < 4$ ), that is, the anionic redox process for charge compensation accompanied with the formation of S-S dimers.

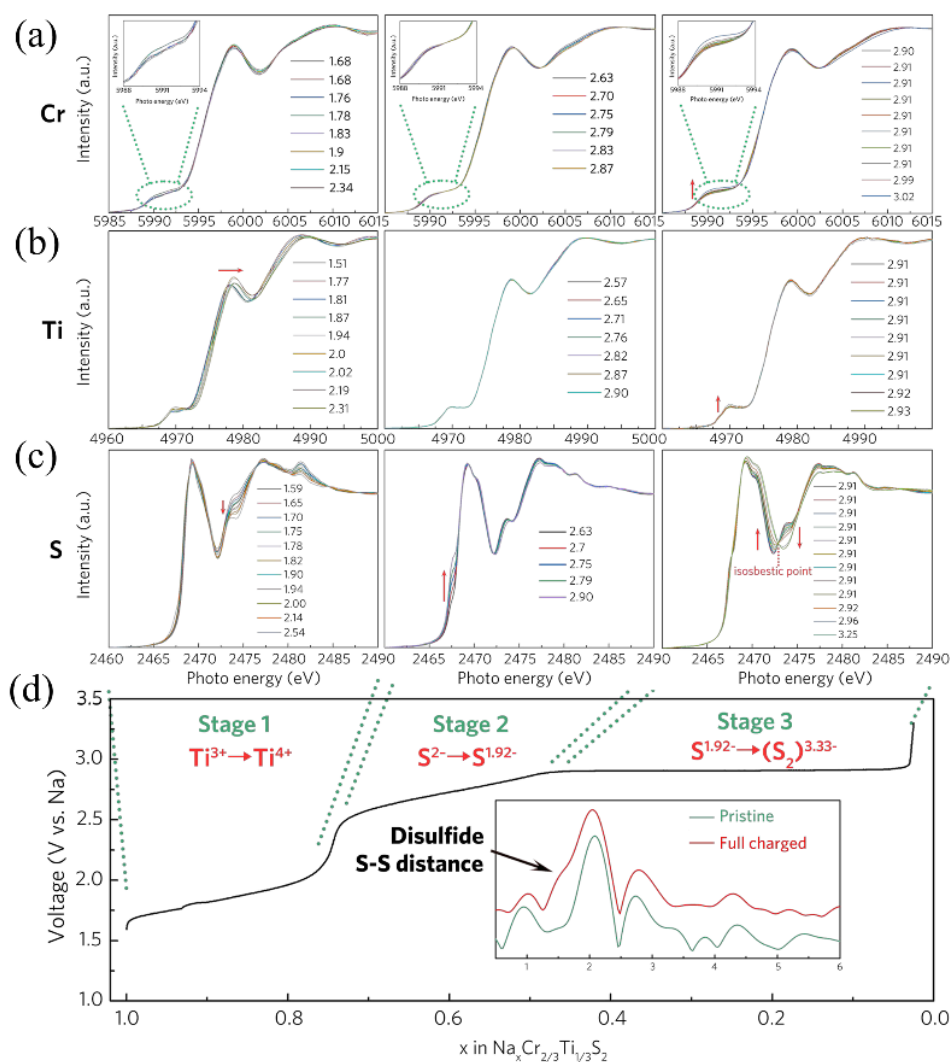


**Figure 100.** *In situ* X-ray absorption spectrum (XAS) of  $\text{NaCr}_{2/3}\text{Ti}_{1/3}\text{S}_2$  at (a) chromium, (b) titanium, and (c) sulfur K-edges. (d) Corresponding voltage profiles for the first charge. The divided *in situ* XAS K-edge XAS spectra of three stages as marked in the bottom inset during the first charge process. The inset in the bottom part is converted R space of *ex situ* sulfur K-edge extended X-ray absorption fine structure (EXAFS) for pristine and full charged samples.

## Patents/Publications/Presentations

### Publication

- Wang, T., G-X. Ren, Z. Shadik, J-L. Yue, M-H. Cao, J-N. Zhang, M-W. Chen, X-Q. Yang, S-M. Bak, P. Northrup, P. Liu, X-S. Liu,\* and Z-W. Fu.\* “Anionic Redox Reaction in Layered  $\text{NaCr}_{2/3}\text{Ti}_{1/3}\text{S}_2$  through Electron Holes Formation and Dimerization of S–S.” *Nature Communications* 10 (2019). Article number: 4458. Publication Date (Web): October 1, 2019.

## Task 7.2 – Development of a High-Energy Sodium-Ion Battery with Long Life (Chris Johnson and Khalil Amine, Argonne National Laboratory)

**Project Objective.** The project objective is to develop a high-energy Na-ion battery with long life. Moreover, the battery chemistry should utilize low-cost materials. The energy density target is 200 Wh/kg and/or 500 Wh/L, wherein the anode and cathode capacity targets are 600 mAhg<sup>-1</sup> and 200 mAhg<sup>-1</sup>, respectively.

**Project Impact.** A Na-ion battery on par with the energy density of a Li-ion battery can have a high impact in the transportation sector with the assumption that the cost is significantly below \$85/kWh and the battery pack provides a 300-mile range. The consumer is not concerned about the battery chemistry employed if these metrics can be met. Development of these battery chemistries will situate the United States in a strong position as relates to new low-cost energy storage systems beyond lithium ion.

**Approach.** In a team approach, the Na-ion battery group will create a versatile Na-ion battery chemistry with beneficial advantages such as low cost, safety, recycling, and sustainability of materials used. The team will work synergistically so that the final design is the culmination of advances in phosphorus carbon composites mated with optimized lead or other highly dense metalloids, such as tin and/or antimony and derivatives thereof, for the recyclable anode. Synthesis and optimization of such blended composite anodes will be conducted in parallel to diagnostic characterization of structures, phase formation, and cycling stability. Cathode work will begin at the end of the first year and will involve gradient cathodes consisting of Fe-Mn compositions, as well as intergrowths of layer stacking sequenced oxides. If resources allow, the team also will attempt to stabilize cathode surfaces using ALD methods, particularly for the benefit of staving off dissolution of manganese and iron/electrolyte reactivity. Electrolytes will be partly procured from Dr. H. Li at PNNL.

**Out-Year Goals.** The state-of-the-art Na-ion battery in the literature has now been surpassed by this team, but performance is still too low for commercialization. Thus, the goal is to move forward and continually invent the most superior Na-ion battery chemistry that can compete worldwide through work output from this project.

**Collaborations.** Researchers from PNNL who are developing electrolytes for Na-ion batteries will provide this project with formulations to test with the various electrode combinations investigated at ANL. The team also exchanges commercial samples with Dr. J. Barker of Faradion Ltd. in the United Kingdom.

### Milestones

1. Investigate reaction mechanism of P- and Pb-based anode. (Q1, FY 2020; Completed)
2. Synthesize high-performance layered oxide cathodes using continuous stirred tank reactor (CSTR) method. (Q2, FY 2020; In progress)
3. Optimize the interface of P- and Pb-based anode for long cycle life and high initial CE. (Q3, FY 2020; In progress)
4. Develop composition-gradient oxide cathodes. (Q4, FY 2020; In progress)

## Progress Report

The sodiation/de-sodiation mechanism of P-based anode was investigated this quarter using complementary techniques to unravel the high structural stability of this anode during charge/discharge.

To understand the superior sodium storage performance of black phosphorus-Ketjenblack (BPC) composite, a series of techniques was used to characterize its sodiation/de-sodiation process. Figure 101a illustrates CV data for the first five cycles of the BPC anode, which is almost overlapped after the first two cycles, indicating high sodiation/de-sodiation reversibility. *In situ* synchrotron HEXRD was further used to investigate the phase changes of the BPC anode. As shown in Figure 101b, no crystalline phase is present at the beginning of discharge, indicating the reaction intermediate at this stage is in an amorphous state. When the cell was discharged to around 0.3 V, crystalline Na<sub>3</sub>P phase first appeared, and its intensity gradually increased with sodiation. During the de-sodiation process, the Na<sub>3</sub>P intensity gradually decreased and completely disappeared at about 1.4 V. The HEXRD patterns at the beginning of discharge and at the end of charge are quite similar, confirming the highly reversible sodiation/de-sodiation process of the BPC anode. This result was further confirmed by *ex situ* HEXRD characterization on the BPC electrode at different charge/discharge states (Figure 101c). To further reveal the structures of sodiation/de-sodiation intermediates and/or products, especially those in amorphous states, the team conducted solid-state <sup>31</sup>P magic angle spinning (MAS) NMR spectroscopy. Figure 101d shows the mass-normalized <sup>31</sup>P MAS NMR spectra of the BPC anode at different charge/discharge states. The result illustrated that the BP nanocrystalline was transformed to crystalline Na<sub>3</sub>P through an amorphous NaP intermediate during the sodiation process, and then converted back to amorphous phosphorus with a small amount of amorphous NaP remaining during the de-sodiation process. Considering the volumetric expansion of forming Na<sub>3</sub>P is up to around 500%, this result implies that an effective integration of nanostructured composite can be a practical solution to develop high capacity and high-energy-density metallic anode. To further confirm the excellent performance of the BPC anode, the team further applied it in full-cell study using a P<sub>2</sub>-type Zn-doped Na<sub>0.66</sub>Ni<sub>0.26</sub>Zn<sub>0.07</sub>Mn<sub>0.67</sub>O<sub>2</sub> cathode. As shown in Figure 102, the assembled Na<sub>0.66</sub>Ni<sub>0.26</sub>Zn<sub>0.07</sub>Mn<sub>0.67</sub>O<sub>2</sub>/BPC full cell demonstrates excellent cycle and rate performance. The specific capacity of the BPC/NNZMO cell is limited by the NNZMO cathode. When the BPC composite anode is coupled with other sodium cathode materials such as Na[Li<sub>0.05</sub>(Ni<sub>0.25</sub>Fe<sub>0.25</sub>Mn<sub>0.5</sub>)<sub>0.95</sub>]O<sub>2</sub>, the specific capacity and energy density of the corresponding full cell could be further increased. Thus, the nanostructured BPC composite proposed here has potential to be a promising anode material for room-temperature Na-ion battery.

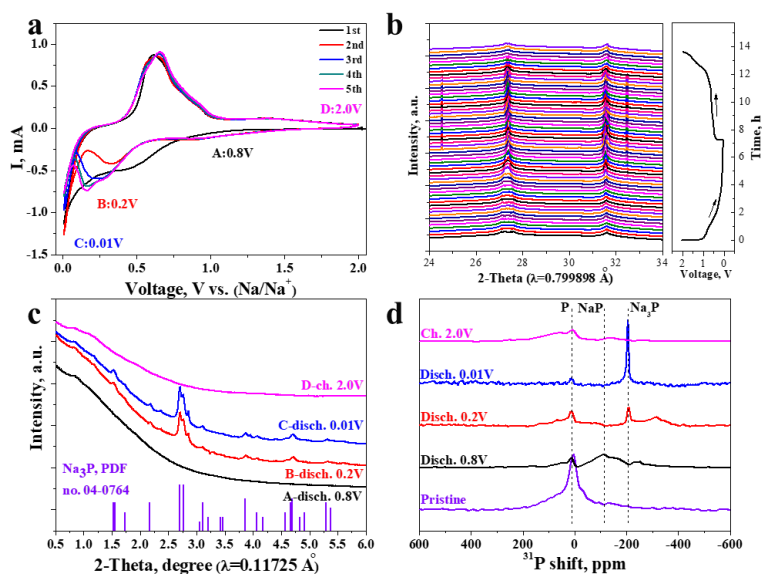


**Figure 101.** (a) Cyclic voltammogram at 0.1 mV s<sup>-1</sup>. (b) *In situ* high-energy X-ray diffraction (HEXRD) in the first cycle at 0.1 C of black phosphorus-Ketjenblack (BPC) anode. (c) *Ex situ* HEXRD. (d) <sup>31</sup>P nuclear magnetic resonance spectra of BPC anode at different charge/discharge states.

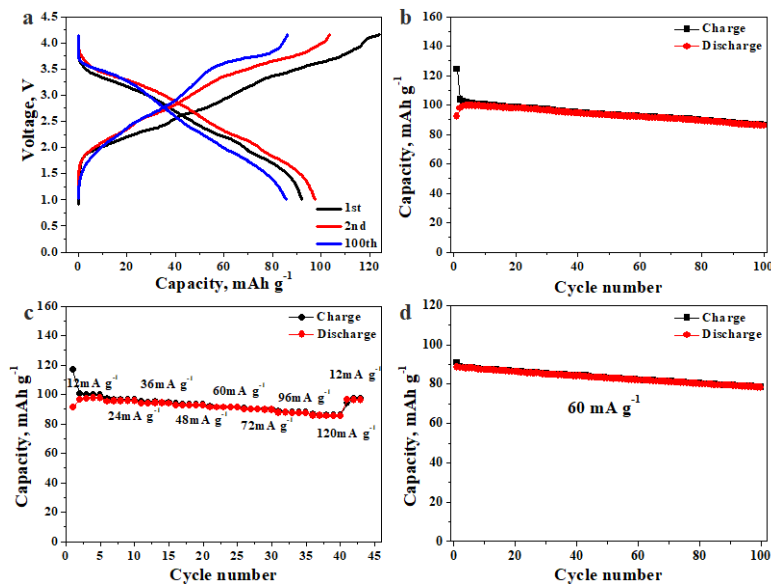


Figure 102. Representative charge/discharge curves. (b) Cycle performance at 12 mA g<sup>-1</sup>. (c-d) Rate performance of Na<sub>0.66</sub>Ni<sub>0.26</sub>Zn<sub>0.07</sub>Mn<sub>0.67</sub>O<sub>2</sub>/P cell with electrolyte of 1 M NaPF<sub>6</sub>/PC with 2 vol% fluorinated ethylene carbonate additive.

## Patents/Publications/Presentations

### Patent

- Xu, G-L., Z. Chen, and K. Amine. High Performance Layered Cathode Materials for High Voltage Sodium-Ion Batteries. US10325730B2.

### Publications

- Xiao, B., K. Wang, G-L. Xu, J. Song, Z. Chen, K. Amine, D. Reed, M. Sui, V. Sprenkle, Y. Ren, P. Yan, and X. Li. *Advanced Materials* 31 (2019): 1805889.
- Sun, D., D. Huang, H. Wang, G-L. Xu, X. Zhang, R. Zhang, Y. Tang, D. A. EI-Hady, W. Alshitari, A. S. AL-Bogami, K. Amine, and M. Shao. *Nano Energy* 61 (2019): 361–369.
- Zhuang, M., G-L. Xu, L-Y. Gan, Y. Dou, C-J. Sun, X. Qu, Y. Xie, Z. Liu, Y. Cai, Y. Ding, I. H. Abidi, A. Tyagi, K. Amine, and Z. Luo. *Nano Energy* 58 (2019): 660–668.

### Presentations

- International Conference on Sodium Batteries (ICNaB), Naperville, Illinois (November 4–7, 2019): “Challenges and Strategies to Advance Sodium-Ion Battery towards Higher Energy Density”; G-L. Xu and K. Amine.
- 236<sup>th</sup> ECS Meeting, Atlanta, Georgia (October 12–17, 2019): “An Evaluation of Electrochemical Properties for a Series of Sodium-Ion Battery Anodes”; C. Johnson.
- 236<sup>th</sup> ECS Meeting, Atlanta, Georgia (October 12–17, 2019): “Pb-Based Nanocomposite Anodes for Li- and Na-Ion Batteries”; J. Han, J. Park, Y. Kim, S. Ahmed, E. Lee, and C. Johnson.

## Task 7.3 – High-Capacity, Low-Voltage Titanate Anodes for Sodium-Ion Batteries (Marca Doeff, Lawrence Berkeley National Laboratory)

**Project Objective.** The objectives are to understand differences in the sodium intercalation mechanism of various sodium titanate anodes through an array of synthetic, electrochemical, and structural characterization techniques, and to overcome practical impediments to their use, such as the high first-cycle Coulombic inefficiencies that are currently observed. The ultimate goal is to produce a 200-250 mAh/g anode that cycles reversibly.

**Project Impact.** Although several suitable cathode materials for Na-ion batteries exist, there are few suitable anode materials due to low potential instabilities. Therefore, sodium titanate variations will be synthesized through different routes to develop materials with various morphologies and dopants. Decreasing the first-cycle inefficiencies and improving cycling performance will allow enabling technology for a practical high-energy Na-ion battery.

**Approach.** Candidate stepped layered titanates will be synthesized by appropriate routes (hydrothermal, solid-state routes, etc.). Materials will then be characterized electrochemically and physically. Structure-function relationships will be built to correlate the effect of changing structure (for example, step size) on electrochemical properties.

**Out-Year Goals.** A series of synchrotron characterization techniques will be used to further develop sodium titanate anode materials with stable cycling while delivering high capacities.

**Collaborations.** TXM is done in collaboration with Dr. Y. Liu (SSRL). Synchrotron hard, sXAS, and X-ray Raman efforts are in collaboration with Dr. D. Nordlund and Dr. D. Sokaras (SSRL). Electrolyte design is done in collaboration with Dr. K. Xu (ARL).

### Milestones

1. Conduct SEI studies. (Q1, FY 2020; In progress, pending beam time at SSRL)
2. Synthesize lepidocrocite titanates. (Q2, FY 2020; In progress)
3. Select best electrolyte solution. (Q3, FY 2020)
4. *Go/No-Go Decision:* On sodium nonatitanate, stop if problems are not solved. (Q4, FY 2020)

## Progress Report

Last quarter, the team focused on sodium nonatitanate electrodes, and they are in the early stages of preparing a paper. Lepidocrocite-structured titanates are also potentially very attractive low-voltage, high-capacity candidates for use as Na-ion battery anodes. These corrugated layered structures can be synthesized readily via solid-state or solution methods over a wide range of compositions and then ion-exchanged. The team's previous computational and experimental work revealed that vacancies or mobile cations in the titanate layers provide additional diffusional pathways for lithium ions and are beneficial for rate capability [Markus, et al., *Chemistry of Materials* 28 (2016): 4284.] Based on this observation, they opted to study electrodes based on the  $\text{Cs}_x\text{Ti}_{2-x/4}\text{O}_4$ ;  $x = 0.67-0.73$  system, which contains  $x/4$  vacancies in the titanate layers. The electrochemical properties of two compositions were studied after exchange of cesium with Na/ $\text{Na}_{0.7}\text{Ti}_{1.825}\text{O}_4$  and  $\text{Na}_{0.73}\text{Ti}_{1.8174}\text{O}_4$  (a third is planned, that of  $\text{Na}_{0.67}\text{Ti}_{1.8325}\text{O}_4$ , to complete the entire solid solution range). Both materials studied so far exhibited sloping and featureless discharge profiles with mid-point potentials of 0.5 V versus  $\text{Na}^+/\text{Na}$ , and delivered capacities of about 160-175 mAh/g from the second cycle on at moderate current densities. Figure 103 shows typical results for  $\text{Na}_{0.7}\text{Ti}_{1.825}\text{O}_4$  (slightly lower capacities were obtained for  $\text{Na}_{0.73}\text{Ti}_{1.8174}\text{O}_4$ ). Both electrodes exhibited excellent rate capabilities and cycling behavior (Figure 104).

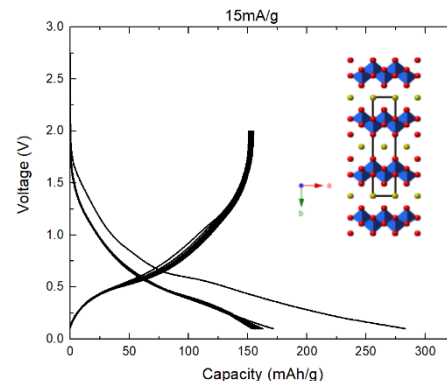


Figure 103. Initial charge and discharge profiles of a  $\text{Na}/\text{Na}_{0.7}\text{Ti}_{1.825}\text{O}_4$  cell. The structure of the material is shown in the inset.

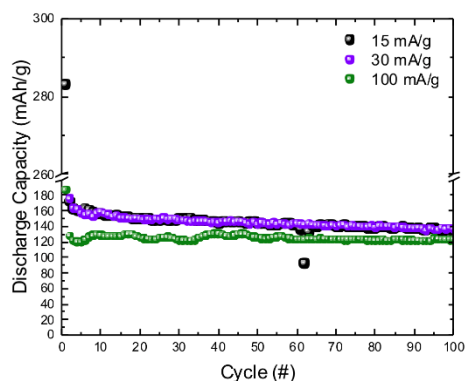


Figure 104. Capacity as a function of cycle number for  $\text{Na}/\text{Na}_{0.7}\text{Ti}_{1.825}\text{O}_4$  cells cycled at different current densities.

Work next quarter will focus on understanding the SEI chemistry, using surface-sensitive synchrotron radiation techniques including sXAS and XPS, with a goal of reducing the first cycle inefficiencies of the lepidocrocite and sodium nonatitanate electrodes. Part of this work will entail studying electrode behavior as a function of electrolytic solution composition (with and without additives, for example) as well as type of carbon additive in the electrodes. A new postdoc is scheduled to arrive early next quarter to carry out this work.

## Patents/Publications/Presentations

The project has no patents, publications, or presentations to report this quarter.

## Task 7.4 – Electrolytes and Interfaces for Stable High-Energy Sodium-Ion Batteries (Ji-Guang Zhang, Pacific Northwest National Laboratory)

**Project Objective.** This project will develop innovative electrolytes and enable fundamental understanding on the interface between electrode and electrolyte for stable operation of high-energy Na-ion batteries. The proposed research will enhance the achievable capacities of both anode and cathode for Na-ion battery and improve the stability of electrodes/electrolyte interface, establish correlation (electrolyte design rule) between electrochemical performances of Na-ion batteries and the electrolyte/interface properties, and enable long cycle life and safe operation of high-energy Na-ion batteries.

**Project Impact.** Success of this project will provide a solid understanding on the electrolyte/electrode interphase of Na-ion batteries and significantly improve their energy density, cycle life, and safety. It will also accelerate the practical application of Na-ion batteries in both EV and stationary energy storage.

**Approach.** This project will optimize the electrolyte components and concentrations to develop innovative electrolytes and additives with improved electrochemical and physical properties. *In situ* and *ex situ* spectroscopy methods will be used to unravel the origin of the SEI at the dynamic interface, providing guidance for the electrolyte and interface design and enabling high capacity and long life of Na-ion batteries.

**Out-Year Goals.** This project will select the electrolyte compounds and identify the formation of interfacial SEI layer on hard carbon and CEI layer on layer oxide cathode and its effect on the electrode materials. It will also provide guidance to electrolyte optimization and improve CE of sodium deposition/stripping to be more than 99%.

**Collaborations.** This project will collaborate with ANL and LBNL and other leading scientists in the field of cathode and anode materials for Na-ion batteries. It will also collaborate with Dr. C. Wang and Dr. M. Engelhard of PNNL for TEM and XPS characterization.

### Milestones

1. Optimize electrolyte composition: Na-based LHCE will be developed to improve cycling stability. (Q1, FY 2020; Completed)
2. Develop electrolyte additives to improve stability of SEI on anode and of CEI layer on cathode. (Q2, FY 2020; In progress)
3. Develop compatible polymer separator (or polymer electrolyte) to stabilize long-term cycling and provide a stable/adequate interphase. (Q3, FY 2020; In progress)
4. Apply the new electrolytes and additives in Na-ion batteries to improve CE to more than 99%. (Q4, FY 2020; In progress)

## Progress Report

This quarter's milestone was accomplished. The composition of nonflammable-phosphate-based LHCE is optimized by choosing selected NaFSI salt concentration, desired diluent, and the molar ratio of the salt:solvent:diluent. Layered  $\text{Na}||\text{O}_3\text{-NaCu}_{1/9}\text{Ni}_{2/9}\text{Fe}_{1/3}\text{Mn}_{1/3}\text{O}_2$  (Na-CNFM) cells were used to evaluate the triethyl phosphate (TEP)-based electrolytes (Na-CNFM weight ratio in cathode: 93.5%, mass loading: 13-16  $\text{mg cm}^{-2}$ ). All cells were cycled at 0.1 C for the first three cycles and 0.2 C for the later cycles ( $1\text{ C} = 100\text{ mAh g}^{-1}$ ). First, the team evaluated the effect of the NaFSI salt concentration in TEP solvent. As the NaFSI/TEP molar ratio increased from 1:1.8 to 1:1.3, the cycling stability and CE changed significantly. The highest solubility of NaFSI salt in TEP solvent occurred when NaFSI/TEP molar ratio reached 1:1.3. Although CE of this electrolyte was  $\sim 99\%$ , it is unstable, which may be due to the high viscosity and low ion conductivity of the electrolyte. The capacity retention of the Na-CNFM cell after 100 cycles is only 57.1%. When the salt-to-solvent ratio was reduced to 1:1.5 and 1:1.8, the capacity retention and CE were much improved. After 100 cycles, the discharge capacity of the Na-CNFM cells with a NaFSI/TEP molar ratio of 1:1.5 and 1:1.8 was 102.4 and 100.1  $\text{mAh g}^{-1}$ , respectively. Therefore, the NaFSI/TEP molar ratio of 1:1.5 was chosen as the baseline to further optimize LHCEs.

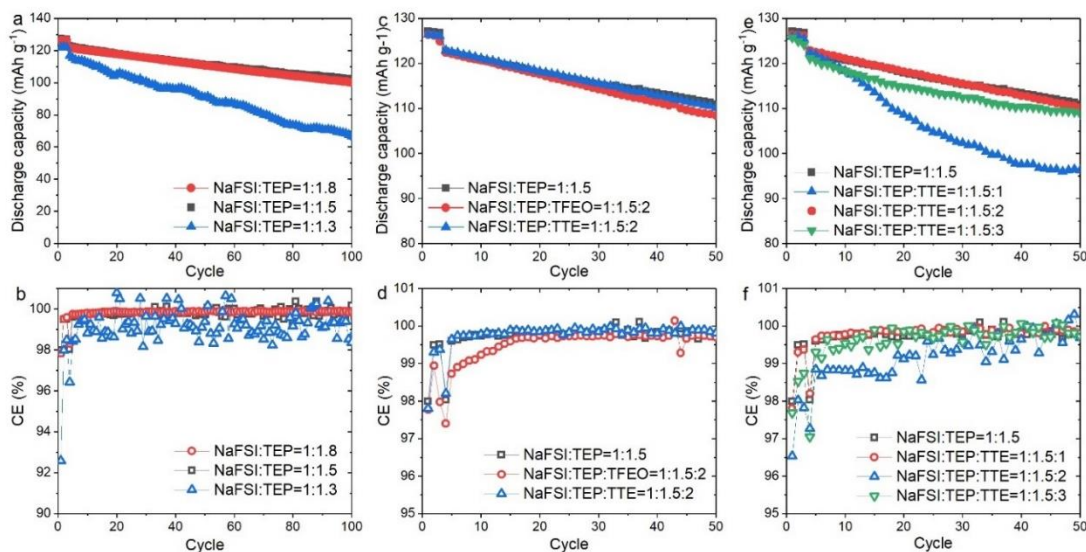


**Figure 105.** (a) Cycling stability and (b) Coulombic efficiency (CE) of  $\text{Na}||\text{O}_3\text{-NaCu}_{1/9}\text{Ni}_{2/9}\text{Fe}_{1/3}\text{Mn}_{1/3}\text{O}_2$  cells with different molar ratio of NaFSI / triethyl phosphate (TEP) electrolyte. (c) Cycling stability and (d) CE of  $\text{Na}||\text{O}_3\text{-NaCu}_{1/9}\text{Ni}_{2/9}\text{Fe}_{1/3}\text{Mn}_{1/3}\text{O}_2$  cells with different diluents at the same TEP to diluent ratio. (e) Cycling stability and (f) CE of  $\text{Na}||\text{O}_3\text{-NaCu}_{1/9}\text{Ni}_{2/9}\text{Fe}_{1/3}\text{Mn}_{1/3}\text{O}_2$  cells with different amount of TTE diluent in NaFSI/TEP/TTE electrolyte.

Although HCE can stabilize cathode, high viscosity and high cost may hinder its real application. Therefore, a non-solvating diluent was added to HCE to form LHCE, which can still retain Na-ion-solvation structure; however, the overall molar concentration of the electrolyte will be much lower. Two fluorinated solvents were used as diluent. One is TTE and the other is tris(2,2,2-trifluoroethyl)orthoformate (TFEO). By comparing the cycling performance of Na-CNFM cells in HCE and LHCE, it was found that the CE of the cells using TTE diluent is better than those using TFEO diluent, especially during initial cycles (see Figure 105d). The CE of the cells at the 10<sup>th</sup> cycles was 99.74% (NaFSI:TEP = 1:1.5), 99.78% (NaFSI:TEP:TTE = 1:1.5:2), and 99.23% (NaFSI:TEP:TFEO = 1:1.5:2). The discharge capacity after 50 cycles is 110.9 (NaFSI:TEP = 1:1.5), 110.1 (NaFSI:TEP:TTE = 1:1.5:2), and 108.4 (NaFSI:TEP:TFEO = 1:1.5:2). At last, the team tested the diluent molar ratio effect in TTE-based LHCE to optimize electrochemical performance. It is found that at a NaFSI:TEP:TTE molar ratio of 1:1.5:2, cells demonstrated the best capacity retention and CE. Therefore, the optimized composition of LHCE is NaFSI:TEP:TTE (1:1.5:2 in molar ratio) and will be used in further investigation.

## Patents/Publications/Presentations

### Presentation

- ICNaB, Naperville, Illinois (November 5–7, 2019): “Non-Flammable Localized High Concentration Electrolytes for Stable High Voltage and High Loading Sodium Batteries.” Y. Jin,\* H. Pan, P. Le, T. D. Vo, and J.-G. Zhang.

## Innovation Center for Battery500

(Jun Liu, Pacific Northwest National Laboratory; Yi Cui, Stanford University)

**Project Objective.** The project aims to develop commercially viable lithium battery technologies with a cell-level specific energy of 500 Wh/kg through innovative electrode and cell designs that enable the extraction of the maximum capacity from advanced electrode materials. In addition to achieving high specific energy, the project aims to be able to achieve 1,000 cycles for the developed technologies.

**Project Impact.** The Battery500 Consortium will develop next-generation lithium battery technologies that will significantly increase energy density, improve cycle life, and reduce cost. This will greatly accelerate deployment of EVs and reduce carbon emission associated with fossil fuel consumption. The consortium will utilize first-class expertise and capabilities in battery research in the United States and develop an integrated and multi-disciplinary approach to accelerate development and deployment of advanced electrode materials in commercially viable high-energy batteries. The advances made in this consortium will also benefit the improvement of current Li-ion battery technologies.

**Approach.** This project will utilize an assortment of national resources located at the national laboratory level and university level. The lithium anode combined with a compatible electrolyte system and two cathodes—one high-Ni  $\text{LiNi}_x\text{Mn}_y\text{Co}_z\text{O}_2$  and another sulfur—will be studied and developed to reach high-energy density. The project focus is to design novel electrode and cell architectures to meet the 500 Wh/kg goal. The consortium will work closely with R&D companies, battery/materials manufacturers, and end users/OEMs to ensure that the developed technologies are aligned with industry needs and can be transitioned to production.

**Out-Year Goals.** This project aims for the following out-year goals. (1). Fabricate and test a pouch cell capable of 350 Wh/kg and 350 cycles. (2). Fabricate and test a pouch cell capable of 400 Wh/kg and 100 cycles.

**Collaborations.** Collaboration among consortium team members will be well coordinated by the leadership team, which includes the keystone project leads and co-leads along with PIs at all member institutions. Collaboration with the community outside of this consortium and with industry will be facilitated by the executive committee, the advisory board, and the industry committee.

## Milestones

1. Deliver pouch-cell design and pouch-cell parameters for over 400 Wh/kg pouch cells. (Q1, FY 2020; Completed)
2. Develop new 3D anode structures; test and validate such using coin-cell standard protocols. (Q2, FY 2020; In progress)
3. Fabricate and test 350 Wh/kg Li-S pouch cells with over 50 stable cycles. (Q3, FY 2020; In progress)
4. Fabricate and test a pouch cell capable of 400 Wh/kg and 100 cycles. (Q4, FY 2020; In progress)

## Progress Report

## Keystone Project 1: Materials and Interfaces

The goal of Keystone 1 is to provide the materials and chemistry support for Keystone projects 2 and 3. This quarter, a niobium-oxide cathode coating identified in previous reports was further refined, a multi-functional polymer binder was shown to remarkably improve stability of ultrahigh-nickel cathodes, and 3D XANES tomography offered additional insight into the failure mechanisms of high-nickel cathodes.

In the Q3 FY 2019 report, Binghamton University showed that a Li-Nb-O coating on NMC-811 could give improved electrochemical performance, including a reduced first cycle loss. However, the coating did not improve the thermal stability of the material. As NMC-811 has a strong tendency to form a Li-rich layer on the surface due to reactivity with the environment, a Li-free precursor was investigated that could simultaneously form a protective layer and scavenge the residual lithium species. In the initial studies, the Nb-O coating showed a better thermal stability than pristine 811. Furthermore, coating effectiveness was found to be a function of annealing temperature (Figure 106). Intermediate temperatures of 400-500°C resulted in the highest first-cycle CE, with higher temperatures showing shifts in lattice parameters due to niobium doping. Extended cycling is now under way with optimized coating.

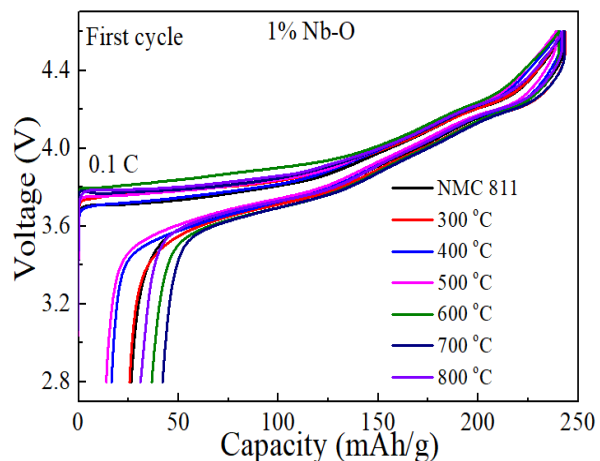


Figure 106. Charge/discharge curves of pristine NMC-811 and Nb-O modified NMC-811 heated from 300°C to 800°C.

The UT Austin team used a conductive polymer polyaniline (PANI) with numerous benefits as an additive/binder in ultrahigh-nickel, NMC-900505 cells. To fully delineate its effect on cathode performance during long-term cycling, pouch full cells with a graphite anode were assembled to avoid cell failure due to Li-metal anode. When PANI was mixed with PVDF in a 5:1 ratio as a binder for both the electrodes, capacity retention improved remarkably from 47% to 81% after 1,000 cycles (Figure 107). The cells also showed improved average CE (99.5% versus 98.5%) and discharge voltage (3.6 V versus 3.2 V at 1,000 cycles). Unlike other modifications such as dopants and coatings, which can often sacrifice capacity to improve cycle life, conductive PANI maintains the same capacity at C/2 rate and further improves rate capability (200 mAhg<sup>-1</sup> versus 180 mAhg<sup>-1</sup> at 3C rate). Even when applied to only one electrode, cell stability is greatly enhanced.

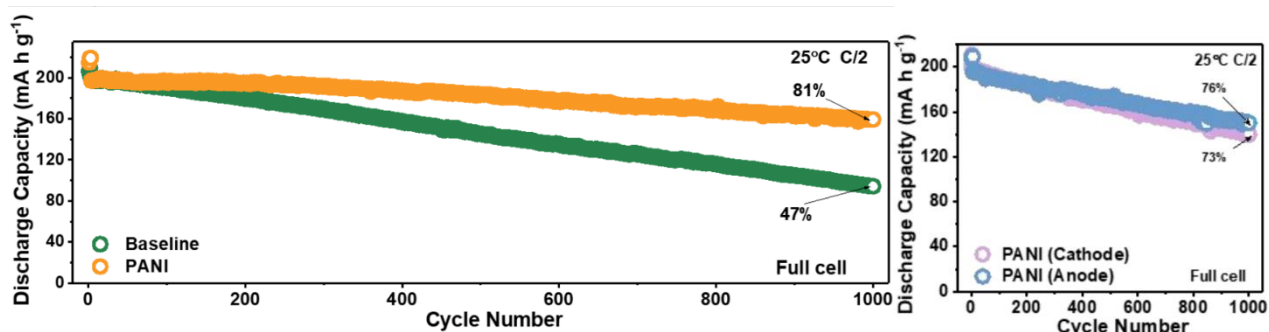


Figure 107. Cycling stability of a cell with PVDF-only binder (baseline) and a 5:1 PVDF:PANI binder blend (left) in both the cathode and anode and (right) in the cathode only or anode only.

The ability of PANI to function when applied to either electrode is due to its role as an HF scavenger. HF generated via  $\text{LiPF}_6$  decomposition can leach TM ions from the cathode particle, generating resistive spinel and rock-salt phases, releasing reactive oxygen from the lattice, and causing crossover that can damage the anode SEI. PANI in its deprotonated phase can react with and consume HF in the electrolyte, drastically reducing HF attack. Within only a few seconds of HF exposure, a blue sheet of deprotonated PANI protonates and becomes green, visually demonstrating its capability (Figure 108). In addition, TOF-SIMS on cycled electrodes (both anode and cathode) shows substantially reduced signal from deposited TM fluorides.

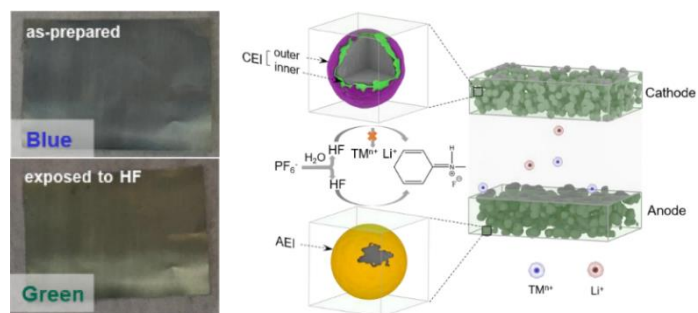


Figure 108. PANI changing color after HF exposure (left). HF scavenging and improved SEI formation (right).

TOF-SIMS on cycled electrodes (both anode and cathode) shows substantially reduced signal from deposited TM fluorides.

TOF-SIMS is also able to reveal information regarding the effect of PANI on the cathode-electrolyte interface (CEI). The depth of the maximum  $\text{NiO}^-$  yield is much lower in the PANI-modified sample, indicating a much thinner CEI (Figure 109). Additionally, the CEI is simplified into a two-layer structure with an outer layer composed of phosphorous compounds and an inner layer composed of organic species from electrolyte decomposition, as well as  $\text{CNO}^-$  from PANI itself. A third layer heavy in dissolved and re-deposited TM compounds is found only in the baseline sample without the HF scavenging effect. The combined effects of the HF scavenging and stable-CEI formation protect the cathode, leading to much-improved crystallinity after cycling as indicated by *ex situ* XRD (Figure 109).

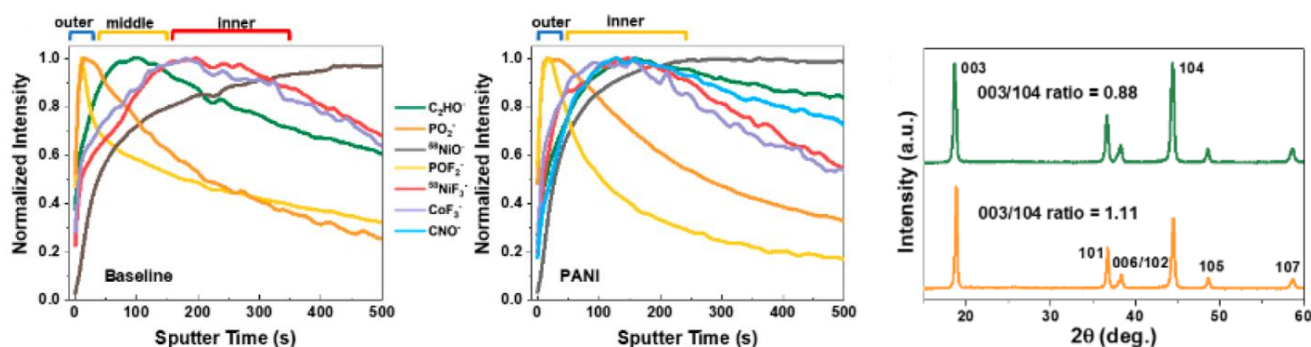


Figure 109. Cathode time-of-flight secondary ion mass spectrometry (TOF-SIMS) data with normalized signal intensities for cells with (left) no PANI and (middle) PANI after 1,000 cycles. (Right) *Ex situ* X-ray diffraction (XRD) patterns of the cathode (top) without PANI and (bottom) with PANI after 1,000 cycles. Both the TOF-SIMS and XRD characterizations were performed on pouch-cell electrodes.

This quarter, in collaboration with UT Austin, the BNL team focused on applying synchrotron based XAS, 3D XANES tomography, as well as synchrotron-XPS with depth-profiling functionality to conduct comparison studies on Ni-rich  $\text{LiNi}_{0.94}\text{Co}_{0.06}\text{O}_2$  (NC) and  $\text{LiNi}_{0.92}\text{Co}_{0.06}\text{Al}_{0.02}\text{O}_2$  (NCA) cathodes. It was found that during high-voltage cycling, many micro-cracks were developed and propagated through the  $\text{LiNi}_{0.94}\text{Co}_{0.06}\text{O}_2$  particles (Figure 110). In contrast, for the  $\text{LiNi}_{0.92}\text{Co}_{0.06}\text{Al}_{0.02}\text{O}_2$  particles, no such cracks were developed after 70 cycles at a cut-off voltage of 4.8 V. In addition, the distribution of nickel valence states in  $\text{LiNi}_{0.92}\text{Co}_{0.06}\text{Al}_{0.02}\text{O}_2$  looks much more homogeneous than in  $\text{LiNi}_{0.94}\text{Co}_{0.06}\text{O}_2$  particles. These results provide valuable insights on the origin of superior performance after doping.

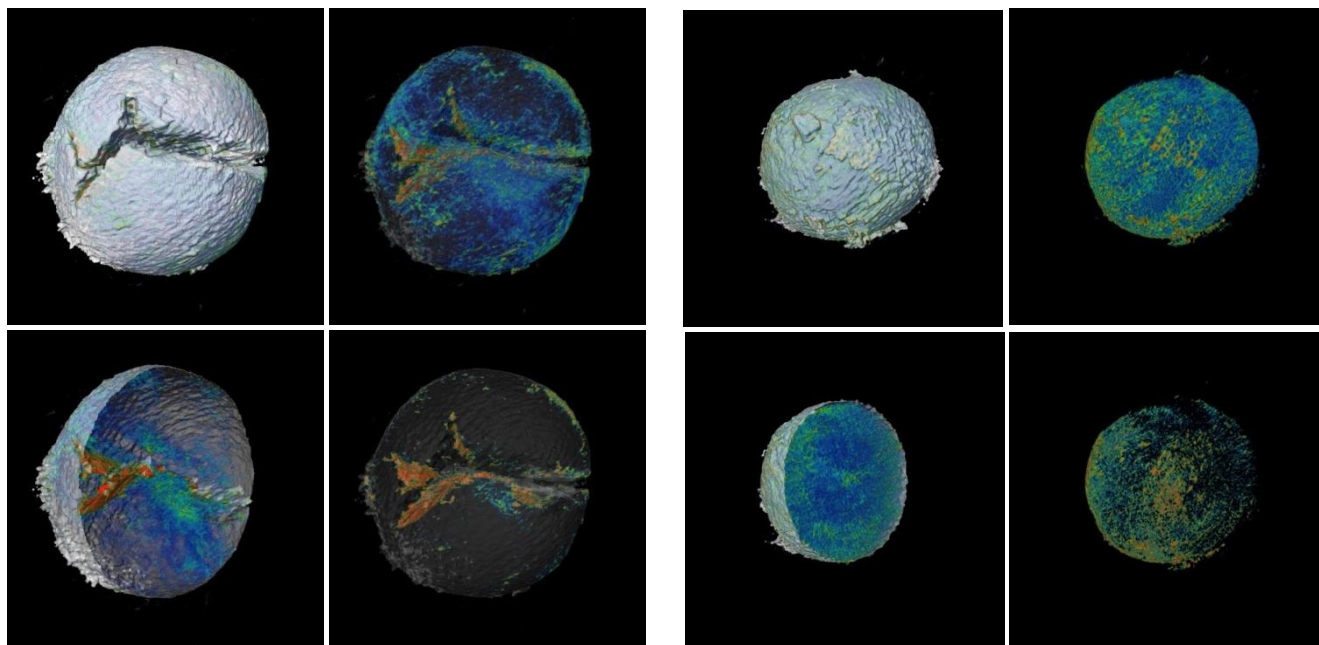


Figure 110. Three-dimensional X-ray absorption near-edge structure tomography of (left)  $\text{LiNi}_{0.92}\text{Co}_{0.06}\text{O}_2$  (NC) and (right)  $\text{LiNi}_{0.92}\text{Co}_{0.06}\text{Al}_{0.02}\text{O}_2$  (NCA) after 70 cycles at a cut-off voltage of 4.8 V.

### Highlights of Keystone Project 1

The highlights for this quarter are as follows:

- A niobium oxide cathode coating was further refined to minimize first cycle lithium loss and improve thermal stability (Binghamton University).
- Cells with an ultrahigh-nickel cathode and a composite PANI-PVDF binder display substantial improvement in CE, cycle life, and voltage hysteresis (UT at Austin).
- Three-dimensional XANES tomography of NC and NCA after high-voltage cycling shows reduced cracking and a more even distribution of nickel valence states in the Al-doped cathode (BNL).

## *Keystone Project 2: Electrode Architecture*

The goal of Keystone 2 is to design, model, fabricate, and characterize the effect of electrode architecture on electrode and cell performance in support of reaching the project goal of 500 Wh/kg cell specific energy. Included in this Keystone are architecture design of thick cathodes (UCSD), Li-metal electrode architectures (PNNL, UCSD, and Stanford), inorganic (UT-Austin) and polymer (Stanford) electrolytes, and electrode performance modeling (UW). Highlighted this quarter are recent advancements at multiple institutions in understanding the design and optimization of sulfur architecture and developing approaches to address the failure mechanisms.

This quarter, the PNNL team has made significant progress in understanding the electrolyte distribution along the large-size and porous electrode during cell cycling. A multi-physics simulation coupling Darcy porous flow and species transportation was performed. The reaction rate was estimated based on the electrolyte amount and the cycle life of the Li-S pouch cell. The electrolyte transfer process was modeled by solving the time-dependent diffusion equation for the spare volume. For electrolyte diffusion in the porous cathode and separator, an effective diffusion coefficient considering porosity and tortuosity was adopted. For simplicity, one quarter of the cathode area (Figure 111a) was simulated, and the corresponding results are depicted in Figure 111. After electrolyte injection and on a long rest period (24 h), the electrolyte diffuses through the interconnected nanopores to wet the nanosized domains of the electrode (Figure 111b). The excess portion of electrolyte is stored along the edge area after vacuum sealing the cell. On cell cycling, electrolyte depletion starts because of the unavoidable side reactions on both the cathode and lithium anode. According to Lewis' theory, as driven by electrolyte concentration gradient, the electrolyte will redistribute to replenish the electrolyte loss. However, such diffusion is hindered by the high tortuosity of the nanoporous electrodes, especially when stacking pressure is applied. Note that the 100% electrolyte content means that all the pores are filled with electrolyte. As long as the content is less than 100%, the electrode may suffer from electrolyte deficiency, that is, pores are not fully wetted by electrolyte. Simulation results indicate that the electrolyte content maintains > 95% of its original volume and is sufficient to promote the sulfur reaction in the first 50 hours of cycling (Figure 111c), which agrees well with the high sulfur utilization rate in the first cycle, as reported earlier. During the 100–150 hours of cycling (2–3 cycles) as shown in Figure 111d-e, the electrolyte amount keeps decreasing with a steeper electrolyte concentration gradient. Because of the low current density, the decreasing electrolyte will not yet cause significant cell polarization at such low rates and few cycles. However, after 200 hours of cycling, the continuous electrolyte consumption triggers the electrolyte deficiency emerging from the center (Figure 111f). More than half of the electrodes (65%) have an electrolyte content less than 85% (Figure 111g-h). The electrolyte distribution inhomogeneity deteriorates over time and imposes electrochemical polarization on sulfur conversion, and eventually discontinues the electrochemical reactions starting from the center regions. This is supported by the experimental observation that the exaggerated energy decay was observed starting during the sixth cycle (reported earlier and not shown here). The electrolyte distribution inhomogeneity is attributed to the competition between the electrolyte diffusion across the nanoporous electrode and the chemical consumption. Therefore, if the electrolyte diffusion during cycling is enhanced, the electrolyte inhomogeneity problem will be significantly reduced.

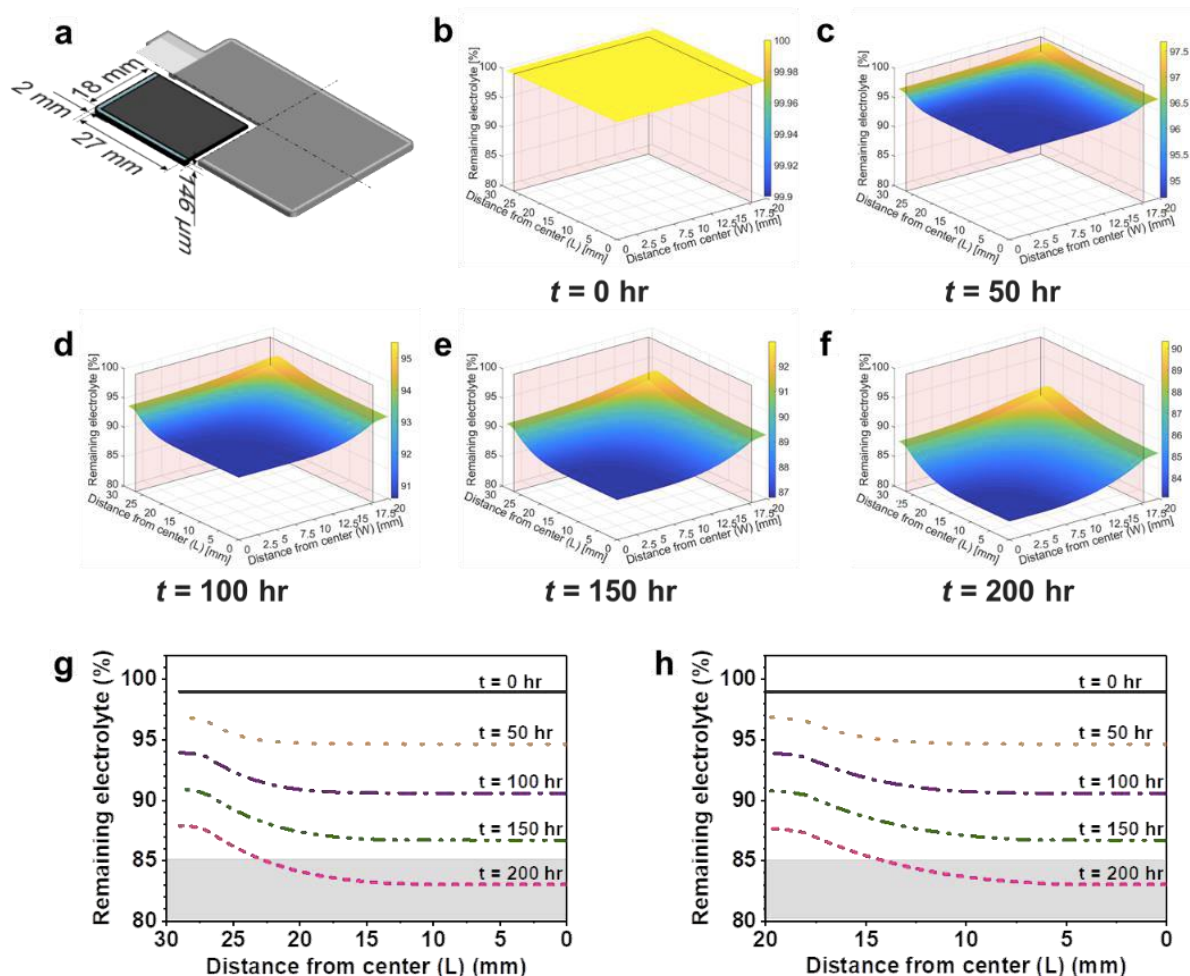


**Figure 111.** The transient simulation of electrolyte diffusion and redistribution in a large-size pouch cell on cycling. (a) Schematic illustration of the electrode dimension selected for the simulation with an electrolyte diffusion coefficient of  $1 \times 10^{-10} \text{ m}^2 \text{ s}^{-1}$ . Electrolyte distribution at half of the electrode thickness (0.073 mm) after different reaction time: (b)  $t = 0 \text{ h}$ , (c)  $t = 50 \text{ h}$ , (d)  $t = 100 \text{ h}$ , (e)  $t = 150 \text{ h}$ , and (f)  $t = 200 \text{ h}$ . Electrolyte content (%) variation at different times and locations: (g) at long line of (x, 0 mm, 0.073 mm) and (h) at short line of (0 mm, y, 0.073 mm).

The UCSD team demonstrated that sulfurized polyacrylonitrile (SPAN) is a promising cathode due to limited polysulfide dissolution in carbonate electrolytes arising from the physical confinement of the small molecular sulfur in the conductive polymer network that provides a high specific capacity of  $> 550 \text{ mAh g}^{-1}$  and an average discharge potential of  $\sim 1.8 \text{ V}$ . However, the Li-metal CEs in carbonate electrolytes are still unsatisfied. Although other electrolytes provide much better Li-metal CEs, the SPAN is known to cycle poorly in common ether-based electrolytes due to generation of soluble polysulfides, in which the reaction mechanism resembles that of elemental sulfur with poor cycling stability. The Liu group discovered a novel ether electrolyte, which is compatible with both lithium metal and SPAN. The cycling performance of thin SPAN electrodes ( $1 \text{ mAh cm}^{-2}$ ) in different electrolytes was compared. When cycled in the novel ether electrolyte, the Li||SPAN cell displayed a capacity of  $579 \text{ mAh g}^{-1}$ , and excellent cycling performance. As displayed by the voltage profiles, no capacity decay was observed over 1200 cycles (5000 hours of testing). To achieve a Li||SPAN pouch cell with energy density of  $> 250 \text{ Wh kg}^{-1}$ , the areal capacity of the SPAN electrode should be larger than  $5 \text{ mAh cm}^{-2}$ . By increasing the areal mass loading of SPAN material to  $10 \text{ mg cm}^{-2}$ , the reversible capacity of SPAN electrode reaches  $5.8 \text{ mAh cm}^{-2}$  (Figure 112a). The Li||SPAN cells were cycled using 1M LiPF<sub>6</sub> in EC/EMC (vol. ratio 1:1) at C/5 between 1.0 and 3.0 V. The Li||SPAN cell with high SPAN loading showed fast degradation (Figure 112b). After 90 cycles, the capacity of the Li||SPAN cell with  $10 \text{ mg cm}^{-2}$  of

SPAN degraded from 5.98 mAh cm<sup>-2</sup> to 2.43 mAh cm<sup>-2</sup>, which retains only 40.6% of its original capacity. As a comparison, the Li||SPAN cell using the novel ether electrolyte showed much better capacity retention with little capacity decay, which maintained a high capacity of 4.43 mAh cm<sup>-2</sup> (Figure 112c). These Li/SPAN coin cell results will enable the team to reach 250 Wh/kg energy density in 2-Ah pouch design.

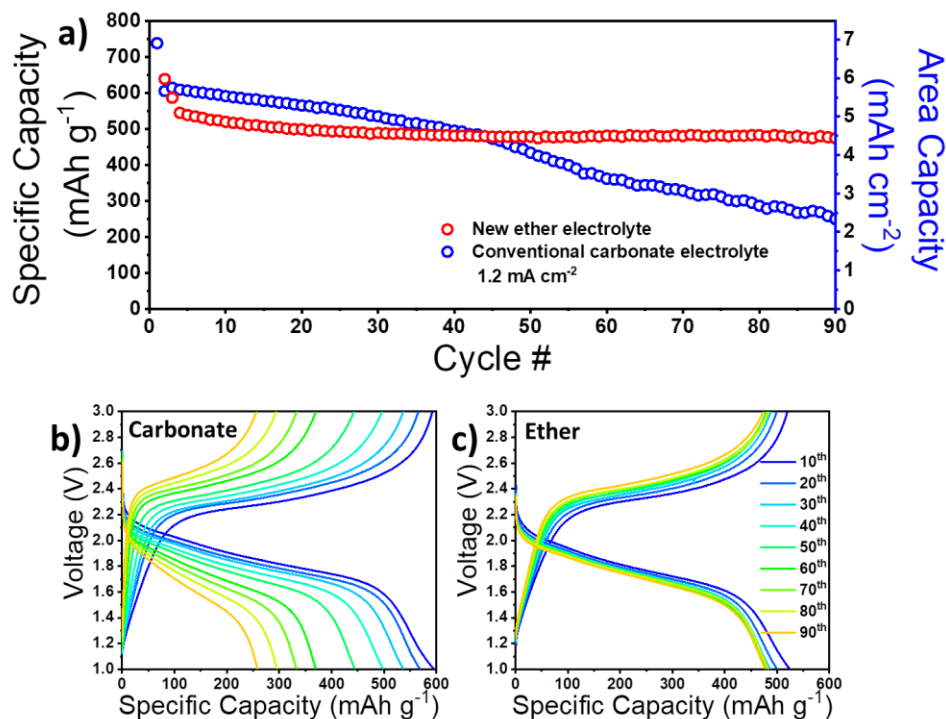


Figure 112. Comparison of cycling performance of SPAN electrodes in different electrolytes. (a-c) Thick SPAN electrode with areal capacity loading of 6 mAh cm<sup>-2</sup>, at 1.2 mA cm<sup>-2</sup> (C/5). (b) Voltage profiles of thick SPAN electrode in conventional carbonate electrolyte. (c) Voltage profiles of thick SPAN electrode in novel ether electrolyte. See reference.<sup>[1]</sup>

#### Reference

- [1] Xing, X., Y. Li, X. Wang, V. Petrova, H. Liu,\* and P. Liu.\* “Cathode Electrolyte Interface Enabling Stable Li-S Batteries.” *Energy Storage Materials* 21 (2019): 474–480.

## Highlights of Keystone Project 2

The highlights for this quarter are as follows:

- The simulation of lithium deposition at three rates using reactive MD captured the evolving morphological development of Li-metal deposits. The sensitivity of the impact from the deposition rate on morphological features, including film density, surface roughness, porosity, defect (1-D dislocations, 2-D GBs, to 3D voids) formation and density was well captured.
- A continuum model and an efficient simulation scheme have been developed for simulating Li-S batteries. This model can be used to study the effect of design parameters (thickness of electrodes, initial sulfur loading) on the performance of batteries. A new approach has been developed that enables the team to robustly simulate discharge curves for different rates and design parameters.

### Keystone Project 3: Cell Fabrication, Testing, and Diagnosis

With the significant increase in research associated with Li-metal batteries, it has become more important for researchers to understand the safety-related issues for all stages of research and development. In a manuscript published this quarter,<sup>[2]</sup> Battery500 researchers consolidated knowledge on the use of lithium metal for preparation, testing, and disposal of battery cells and cell materials. As shown in Figure 113, several types of possible safety risks were identified throughout the research procedures, from personnel training to materials handling and testing. Key recommendations from that paper include the following: proper tools and materials to be used to handle lithium metal and to disassemble cells; personnel trainings needed for new researchers, and appropriate measures and methods for disassembly and disposal of used cells. In addition to this paper, the lessons learned and knowledge gained were shared within the Battery500 Consortium through several discussions involving both senior and junior researchers. This is critical to achieve development of new high-energy battery technologies.

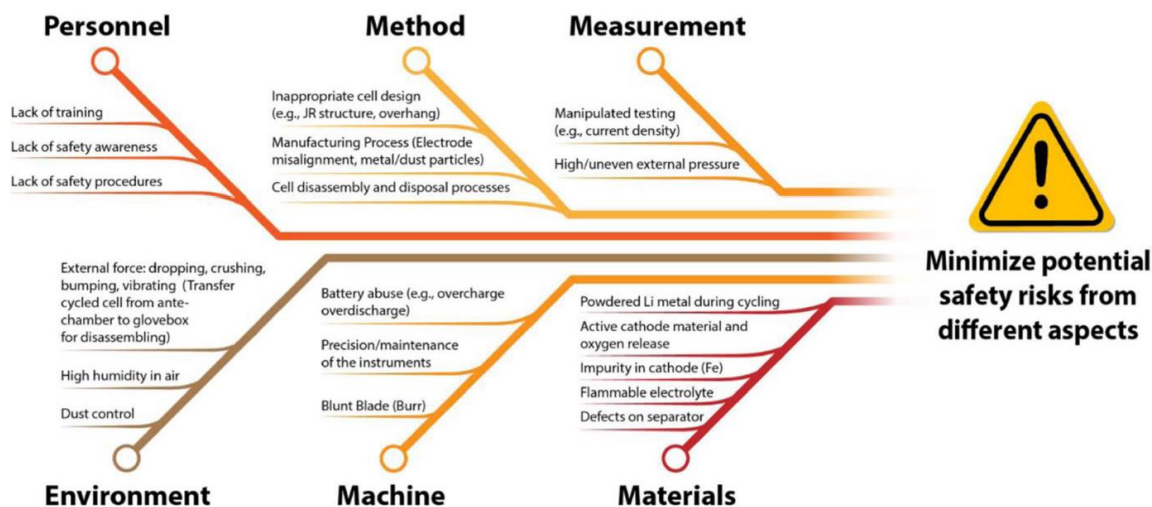
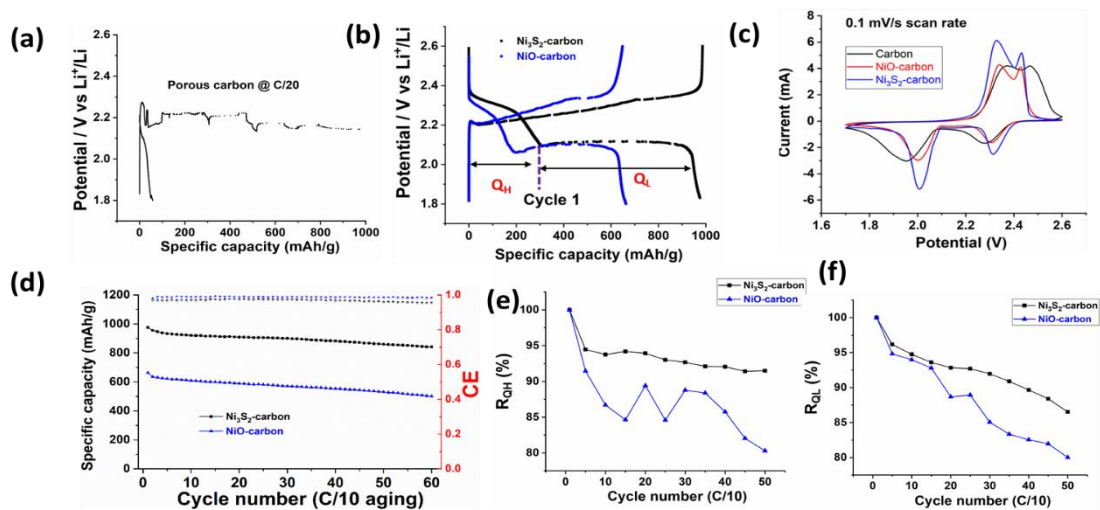


Figure 113. Schematic showing different types of risk associated with use of lithium metal, preparation of Li-metal batteries, and cycling of Li-metal batteries.<sup>[2]</sup>

In work related to increasing the understanding of Li-S battery experiments, looking at characterizing and identifying failure of different sulfur cathode support structures was also undertaken this quarter. In this work, a modified Pechini method was used to synthesize an assortment of porous carbon host materials that included core-shell structured NiO@Ni/Ni<sub>3</sub>S<sub>2</sub>@Ni materials on the carbon surfaces. The work helped identify key differences in electrode kinetics. As shown in Figure 114, without the Ni-based core-shell materials, performance is rather poor. With the addition of core-shell structures, electrode kinetics significantly improved, and higher capacity was gained in the cathode. The inclusion of core-shell structures also reduces rate of capacity fade of the cell.



**Figure 114.** (a) Cells using carbon-only cathode cannot reach the upper cutoff potential and only deliver a very limited amount of discharge capacity under the lean electrolyte condition, even during C/20 formation. (b) Discharge/charge profiles of NiO-carbon and Ni<sub>3</sub>S<sub>2</sub>-carbon materials at the first cycle under the lean electrolyte condition; their discharge capacities are 690 and 1128 mAh/g, respectively. (c) CV curves shown for various cathode materials. (d) Cycling performance. (e-f) Retention (normalized to discharge capacity of first aging cycle) of capacities for upper-plateau (Q<sub>H</sub>) and lower-plateau (Q<sub>L</sub>) regions of the NiO@Ni-carbon and Ni<sub>3</sub>S<sub>2</sub>@Ni-carbon cells.

To better understand the difference in performance of the electrodes that were all tested using lean electrolyte, more direct analysis of the charge and discharge profiles (Figure 114b) was performed. The Ni<sub>3</sub>S<sub>2</sub>-carbon cathode exhibits a much lower polarization compared with the NiO-carbon cathodes, demonstrating that the surface transformation from NiO to Ni<sub>3</sub>S<sub>2</sub> in cathode design significantly enhances the kinetics and reversibility of the electrochemical redox reaction of sulfur, which is consistent with the voltammetry results in Figure 114c. While both the Ni<sub>3</sub>S<sub>2</sub>@Ni-carbon and the NiO@Ni-carbon cells produced similar CEs, the Ni<sub>3</sub>S<sub>2</sub>@Ni-carbon cells had a significantly lower fade rate of 0.18% per cycle. To further investigate the cause for the enhanced performance of the Ni<sub>3</sub>S<sub>2</sub>@Ni-carbon cell, the discharge curves were separated into an upper and lower regime, where the upper regime corresponds to the reduction of S<sub>8</sub> to Li<sub>2</sub>S<sub>4</sub> and the lower regime corresponds to lithium polysulfides being transformed to Li<sub>2</sub>S. In both regions, Ni<sub>3</sub>S<sub>2</sub>@Ni-carbon cell displays less significant capacity fade, highlighting increased, prolonged utilization of the sulfur in the cathode. Using DFT analysis, it becomes evident that the binding energies with Ni<sub>3</sub>S<sub>2</sub> are significantly stronger, which suggests better wetting and ultimately enhanced sulfur utilization. Combining these methods provides a clearer performance analysis to guide cell design and to quantify performance fade for Li-S cells.

#### Reference

- [2] Wu, B., et al. “Good Practices for Rechargeable Lithium Metal Batteries.” *Journal of the Electrochemical Society* 166, no. 16 (2019): A4141–4149.

### Highlights of Keystone Project 3

The highlights for this quarter are as follows:

- Recommendations on safely handling for lithium metal have been published and discussed.
- Combined analysis enables discrete evaluation of sulfur electrode benefits.
- Methods to evaluate capacity fade based on discharge profile provide benefit in characterizing cell failure.

## Patents/Publications/Presentations

### Patent

- Cao, X., J-G. Zhang, and W. Xu of PNNL. Electrolyte for Stable Cycling of Rechargeable Alkali Metal and Alkali Ion Batteries. U. S. patent filed; November 2019.

### Publications

- Wu, B., Y. Yang, D. Liu, C. Niu, M. Gross, L. Seymour, H. Lee, P. Le, T. D. Vo, Z. D. Deng, E. J. Dufek, M. S. Whittingham, W. J. Liu, and J. A. Xiao. “Good Practices for Rechargeable Lithium Metal Batteries.” *Journal of the Electrochemical Society* 166 (2019): A4141–A4149. doi: 10.1149/2.0691916jes. Publication Date (Web): December 19, 2019.
- Xiao, J.\* “How Lithium Dendrites Form in Liquid Batteries.” *Science* 366 (2019): 426–427. Publication Date (Web): October 25, 2019.
- Dong, Z., Q. Wang, R. Zhang, N. A. Chernova, F. Omenya, D. Ji, and M. S. Whittingham. “The Reaction Mechanism of Sn<sub>2</sub>Fe Anode in Lithium-Ion Batteries.” *ACS Omega* 4 (2019): 22345–22355. doi: 10.1021/acsomega.9b02417. Publication Date (Web): December 18, 2019.
- Zheng, Y., F. A. Soto, V. Ponce, J. M. Seminario, X. Cao, J-G. Zhang, and P. B. Balbuena. “Localized High Concentration Electrolyte Behavior near a Lithium–Metal Anode Surface.” *Journal of Materials Chemistry A* 7 (2019): 25047–25055. Publication Date (Web): October 14, 2019.
- He, Y., X. Ren, Y. Xu, M. H. Engelhard, X. Li, J. Xiao, J. Liu, J-G. Zhang, W. Xu, and C. Wang. “Origin of Lithium Whisker Formation and Growth under Stress.” *Nature Nanotechnology* 14, no. 11 (2019): 1042–1047. Publication Date (Web): October 14, 2019.
- Xie, Q., W. Li, A. Dolocan, and A. Manthiram. “Insights into Boron-Based Polyanion-Tuned High-Nickel Cathodes for High-Energy-Density Lithium-Ion Batteries.” *Chemistry of Materials* 31 (2019): 8886–8897. doi: 10.1021/acs.chemmater.9b02916. Publication Date (Web): October 3, 2019.
- Luo, L., J. Li, and A. Manthiram. “A Three-Dimensional Lithiophilic Mo<sub>2</sub>N-Modified Carbon Nanofiber Architecture for Dendrite-Free Lithium-Metal Anodes in a Full Cell.” *Advanced Materials* 31 (2019): 1904537. doi: 10.1002/adma.201904537. Publication Date (Web): November 25, 2019.
- Li, J., and A. Manthiram. “A Comprehensive Analysis of the Interphasial and Structural Evolution over Long-Term Cycling of Ultrahigh-Nickel Cathodes in Lithium-Ion Batteries.” *Advanced Energy Materials* 9 (2019): 1902731. doi: 10.1002/aenm.201902731. Publication Date (Web): December 6, 2019.
- Li, J., C-H. Chang, and A. Manthiram. “Towards Long-Life, Ultrahigh-Nickel Layered Oxide Cathodes for Lithium-Ion Batteries: Optimizing the Interphase Chemistry with a Dual-Functional Polymer.” *Chemistry of Materials*. doi: 10.1021/acs.chemmater.9b04102. Publication Date (Web): December 31, 2019.
- Subramaniam, A., J. Chen, T. Jang, N. R. Geise, R. M. Kasse, M. F. Toney, and V. R. Subramanian. “Analysis and Simulation of One-Dimensional Transport Models for Lithium Symmetric Cells.” *Journal of the Electrochemical Society* 166, no. 15 (2019): A3806–A3819. doi: 10.1149/2.0261915jes. Publication Date (Web): November 15, 2019.
- Subramaniam, A., S. Kolluri, C. D. Parke, M. Pathak, S. Santhanagopalan, and V. R. Subramanian. “Properly Lumped Lithium-ion Battery Models: A Tanks-in-Series Approach.” *Journal of The Electrochemical Society* 167, no. 1 (2020): 013534. doi: 10.1149/2.0342001jes. Publication Date (Web): December 19, 2019.
- Wang, H., Y. Liu, Y. Li, and Y. Cui. “Lithium Metal Anode Materials Design: Interphase and Host.” *Electrochemical Energy Reviews* 2, no. 4 (2019): 509–517. Publication Date (Web): October 12, 2019.

- Mackanic, D. G., X. Yan, Q. Zhang, N. Matsuhisa, Z. Yu, Y. Jiang, T. Manika, J. Lopez, H. Yan, K. Liu, X. Chen, Y. Cui, and Z. Bao. “Decoupling of Mechanical Properties and Ionic Conductivity in Supramolecular Lithium Ion Conductors.” *Nature Communications* 10, article no. 5384 (2019). doi.org/10.1038/s41467-019-13362-4. Publication Date (Web): November 26, 2019.
- Weng, Y-T., H-W. Liu, A. Pei, F. Shi, H. Wang, C-Y. Lin, S-S. Huang, L-Y. Su, J-P. Hsu, C-C. Fang, Y. Cui, and N-L. Wu. “An Ultrathin Ionomer Interphase for High Efficiency Lithium Anode in Carbonate Based Electrolyte.” *Nature Communications* 10, article no. 5824 (2019). Publication Date (Web): December 20, 2019.
- Zhou, G., S. Zhao, T. Wang, S-Z. Yang, B. Johannessen, H. Chen, C. Liu, Y. Ye, Y. Wu, Y. Peng, C. Liu, S. P. Jiang, Q. Zhang, and Y. Cui. “Theoretical Calculation Guided Design of Single-Atom Catalysts towards Fast Kinetic and Long-Life Li-S Batteries.” *Nano Letters* (2019). Publication Date (Web): December 30, 2019.

#### Presentations

- Nobel Lecture, Stockholm, Sweden (December 8, 2019): “The Origins of The Lithium Battery”; M. S. Whittingham.
- Uppsala University, Uppsala, Sweden (December 13, 2019): “The Origins of the Lithium Battery: From an Idea to Domination of Energy Storage”; M. S. Whittingham. Invited.
- Advanced Lithium Batteries for Automobile Applications (ABAA) 12, Ulm, Germany (October 9, 2019): “What are the Ultimate Limitations of Intercalation-Based Cathodes for Lithium (or Sodium) Batteries”; M. S. Whittingham. Invited.
- ECS Fall Meeting, Atlanta, Georgia (October 16, 2019): “Beta Alumina – Prelude to a Revolution in Solid State Electrochemistry”; M. S. Whittingham. Invited.
- Scialog, Tucson, Arizona (November 16, 2019): “From an Idea to Domination of Energy Storage: A Long but Satisfying Journey”; M. S. Whittingham. Invited.
- Materials Science, University of Washington, Seattle, Washington (November 19, 2019): “From an Idea to Domination of Energy Storage”; M. S. Whittingham. Invited.
- University of Washington, Seattle, Washington (November 5, 2019): “Li Metal Batteries”; J-G. Zhang. Invited.
- MRS Fall Meeting, Boston, Massachusetts (December 4, 2019): “New Electrolyte for Lithium-Metal Batteries with High-Voltage NMC811 Cathode”; X. Cao, W. Xu, and J. Zhang. Invited.
- ABAA 12, Ulm, Germany (October 7, 2019): “Orthoformate (TFEO)-Based Localized High Concentration Electrolytes for Li Metal Batteries”; X. Cao, X. Ren, W. Xu, and J. Zhang.\* Invited.
- 236<sup>th</sup> ECS Meeting, Atlanta, Georgia (October 14, 2019): “Enabling High-Energy Lithium Metal Batteries through Electrolyte Strategy”; W. Xu,\* J-G. Zhang, X. Ren, X. Cao, and S. Jiao. Invited.
- Sustainable Power and Energy Center Seminar, University of California, San Diego, California (October 2, 2019): “Lithium Metal Anodes: Origin of Lithium Dendrites and their Implications in Rechargeable Lithium Metal Batteries”; J. Xiao. Invited.
- Seminar, University of Washington, Seattle, Washington (November 19, 2019): “Materials Science and Electrochemistry in Li-S Batteries”; J. Xiao. Invited.
- International Conference for Advanced Cathodes in Lithium & Sodium Ion Batteries (ICAC), Seoul, South Korea (November 13, 2019): “Effective Cathode Thickness in High-Energy Li-ion Batteries”; J. Xiao. Invited.
- 236<sup>th</sup> ECS Meeting, Atlanta, Georgia (October 15, 2019): “Understanding Lithium Sulfur Batteries at Different Scales”; J. Xiao. Invited.

- ABAA 12, Ulm, Germany (October 8, 2019): “Battery500 Consortium: Addressing the Fundamental Challenges to Enable Next-Generation Battery Technologies”; J. Xiao. Invited.
- Missouri University of Science and Technology, Rolla, Missouri (October 21, 2019): “Next-Generation Battery Technologies”; A. Manthiram. Invited.
- Clark Doctoral Fellows Distinguished Speaker Series, University of Maryland, College Park, Maryland (October 18, 2019): “Electrical Energy Storage: Near-Term and Long-Term Perspectives”; A. Manthiram Invited.
- World University Forum on Materials Science & Engineering Leadership, Wuhan, China (October 9–12, 2019): “Where are We Headed with Electrical Energy Storage?”; A. Manthiram. Invited keynote talk.
- Energy@UT Research Expo, Energy Institute, University of Texas, Austin, Texas (October 2, 2019): “Where are We Headed with Battery Technologies?”; A. Manthiram. Invited.
- 236<sup>th</sup> ECS Meeting, Atlanta, Georgia (October 15, 2019): “Processing & Operation under Extreme Conditions: Insights from *In Situ* X-Ray Scattering & Spectroscopy”; M. F. Toney. Invited.
- University of Houston, Materials Science Colloquium, Houston, Texas (October 11, 2019): “X-Rays Show Operating Principles of Energy Storage Materials”; M. F. Toney. Invited.
- VIPER Rover Development, Johnson Space Center, Houston, Texas (October 23, 2019): “Model-Based Battery Management System”; V. R. Subramanian. Invited.
- Nobel Lecture, Stockholm, Sweden (December 8, 2019): “Designing Lithium-ion Battery Cathodes”; John B. Goodenough (delivered by A. Manthiram).
- ABAA 12, Ulm, Germany (October 6–9, 2019): “Lithium Metal Anodes: Materials Design, Interface, and Characterization”; Y. Cui. Invited plenary.
- 236<sup>th</sup> ECS Meeting, Atlanta, Georgia (October 13-17, 2019): “Materials and Interface Design of Lithium Metal Anodes”; Y. Cui. Invited.
- Materials Science Seminar, University of California, Los Angeles, California (October 25, 2019): “Materials and Interface Design for Batteries”; Y. Cui. Invited seminar.
- Materials Science Seminar, University of Washington, Seattle, Washington (October 29, 2019): “Materials and Interface Design for Batteries”; Y. Cui. Invited seminar.
- University of Technology Sydney (UTS), Sydney, Australia (November 19, 2020): “Materials and Interface Design for Batteries”; Y. Cui. Invited seminar.
- Second International Symposium on Advanced Electron Microscopy and Spectroscopy (SAEMS), University of California, Irvine, California (December 9–11, 2019): “*In Situ* and Cryogenic Electron Microscopy for Energy Materials”; Y. Cui. Invited.
- Battery Safety Council Forum #8, Washington, D. C. (November 19–20, 2019): “From Battery Failure Analysis to Safety Mitigation”; Y. Zhang and B. Liaw. Invited.
- Department of Chemistry Seminar, Temple University, Philadelphia, Pennsylvania (November 11, 2019): “Lithium Metal Electrode — Understanding its Characteristics”; B. Liaw. Invited.